

Physics Area - PhD course in Theoretical Particle Physics

SISSA, Trieste

Tracing New Physics Across scales: From Collider Signatures to Cosmological Probes

Candidate:
Alfredo Stanzione

Supervisor:
David Marzocca

Co-Supervisor:
Aleksandr Azatov

ACADEMIC YEAR 2024/2025

Abstract

The Standard Model (SM) of particle physics is a remarkably successful and well-tested theory, with predictions that align closely with a wide range of experimental results. Nevertheless, certain observations and theoretical puzzles remain unexplained within this framework, strongly indicating the presence of new degrees of freedom beyond the SM. Uncovering the energy scale and nature of this new physics (NP) is today a central goal in particle physics. To this end, complementary approaches are pursued: precision measurements at colliders, studies of early-universe phenomena, explorations of weakly coupled or hidden sectors, advances in formal quantum field theory, and more. This thesis contributes to this broader effort by focusing on the study of heavy new physics potentially residing at energy scales above the electroweak scale, combining diverse theoretical and phenomenological inputs.

We start with an overview of the Standard Model, focusing on electroweak symmetry breaking, the Higgs mechanism, and the flavor puzzle. In addition, we review the thermal history of Standard Model particles in the context of cosmology. Then, we explore how current experimental data can serve as indirect probes of high-energy scales, using the bottom-up approach provided by effective field theories. Within this framework, we discuss scenarios in which new physics is predominantly coupled to the third generation of the Standard Model fermions. Next, we discuss the theoretical challenges and opportunities at future colliders seeking to push the boundaries of energy reach, with a focus on the modelling of initial-state radiation phenomena at lepton colliders. In particular, we discuss the origin and the phenomenological impact of the mixed Z/γ Parton Distribution Function. With an interest in the various signatures that may be hiding at the high-energy frontier, in the last part we consider the cosmological implications of Beyond the Standard Model scenarios that involve supercooled first-order phase transitions, with a particular focus on dark matter and the potential phenomenological signatures.

The aim of this Thesis is to contribute to our understanding of the current experimental landscape in particle physics, emphasizing the interplay between existing experimental hints, future collider prospects, and early universe signals of new physics.

List of Publications

I hereby declare that, except where specific reference is made to the work of others, the contents of this thesis are original and have not been submitted in whole or in part for consideration for any other degree or qualification in this or any other university.

The discussion is based on the following works:

- Francesco Garosi, David Marzocca, Antonio Rodrìguez Sanchez, Alfredo Stanzione, *Indirect constraints on top quark operators from a global SMEFT analysis.* JHEP 12 (2023) 129 [arXiv: 2310.00047][1].
- David Marzocca, Marco Nardecchia, Alfredo Stanzione, Claudio Toni, *Implications of $B \to K\nu\bar{\nu}$ under Rank-One Flavor Violation hypothesis.* Eur. Phys. J. C 84, 1217 (2024) [arXiv: 2404.06533][2].
- David Marzocca, Alfredo Stanzione, *On the impact of the mixed Z/γ PDF at muon colliders.* JHEP 03 (2025) 171 [arXiv: 2408.13191][3].
- L. Allwicher, M. Bordone, G. Isidori, G. Piazza, A. Stanzione, *Probing third generation New Physics with $K \to \pi\nu\bar{\nu}$ and $B \to K^{(*)}\nu\bar{\nu}$.* Phys.Lett.B 861 (2025) 139295 [arXiv:2410.21444][4].
- D. Racco, A. Stanzione, *Dark Matter Production around a Supercooled Epoch*, in preparation

In addition to the research presented in this thesis, I have contributed to the following works during my PhD, which are not included herein:

- Massimo D'Elia, Lorenzo Maio, Francesco Sanfilippo and Alfredo Stanzione *Phase diagram of QCD on a magnetic background.* Phys. Rev. D 105, 034511 [arXiv: 2111.11237][5]
- Massimo D'Elia, Lorenzo Maio, Francesco Sanfilippo, and Alfredo Stanzione *Confining and chiral properties of QCD in extremely strong magnetic fields.* Phys. Rev. D 104, 114512 [arXiv: 2109.07456][6].

Contents

Abstract i
List of Publications iii

0 Introduction **2**

1 Fundamentals **6**
1.1 The Standard Model 6
1.1.1 The gauge and the higgs sectors 7
1.1.2 Fermionic sector 9
1.1.3 CKM sector 12
1.1.4 Approximate symmetries 13
1.1.5 Running couplings 14
1.2 The Standard Model as an Effective Theory 16
1.2.1 EFT approach 16
1.2.2 4-Fermi theory from the SM 18
1.2.3 The SMEFT lagrangian 19
1.2.4 Flavor Symmetries in SMEFT 21
1.3 Early Universe toolkit 24
1.3.1 Friedmann equations 24
1.3.2 Thermodynamics at equilibrium 26
1.3.3 Freeze-out and Dark Matter 28

2 Indirect Constraints on New Physics Scenarios **33**
2.1 Constraints on top quark operators 35
2.1.1 EFT setup 35
2.1.2 Methodology 37
2.1.3 Observables 38
2.1.4 Global analysis 46
2.1.5 Applications for UV models 54
2.1.6 Summary 58
2.2 Implications of $B \to K\nu\bar{\nu}$ under Rank-One Flavor Violation hypothesis . . . 59
2.2.1 $B \to K^{(*)}\nu\bar{\nu}$ and rank-one correlations in LEFT 60
2.2.2 Implications in the SMEFT 63
2.2.3 Simplified Models 65
2.2.4 Summary 74
2.3 Probing third-generation New physics with $K \to \pi\nu\bar{\nu}$ and $B \to K^{(*)}\nu\bar{\nu}$ . . . 76
2.3.1 EFT setup and the $U(2)_q$ breaking spurion 76

2.3.2 Numerical Analysis . . . 79
2.3.3 Comparison with explicit models . . . 82
2.3.4 Summary . . . 84

3 Theoretical Tools for Future Colliders 87
3.1 Parton Distribution Functions at Muon Colliders . . . 89
3.1.1 The equivalent photon approximation . . . 89
3.1.2 The Standard Model PDFs . . . 92
3.2 The mixed Z_T/γ PDF . . . 96
3.2.1 Z_T/γ PDF at NLO . . . 97
3.3 Compton scattering . . . 100
3.4 Associated Higgs plus W production . . . 103
3.5 ALP single production . . . 107
3.6 Summary . . . 109

4 Cosmological probes of BSM scenarios 112
4.1 Cosmological first order phase transitions . . . 113
4.2 Supercooling . . . 117
4.3 DM relic in a supercooled universe . . . 119
4.3.1 Freeze-out . . . 120
4.3.2 Implications on Direct Searches . . . 125
4.3.3 Freeze-out in secluded Dark Sector . . . 127
4.4 Discussion . . . 128

Conclusions and outlook 131

Appendix A 134
A.1 Observables . . . 134
A.1.1 $P \to M\nu_\alpha\nu_\beta$ . . . 135
A.1.2 $B_s \to \ell^-_\alpha\ell^+_\beta$ and $K_{L,S} \to \ell^-_\alpha\ell^+_\beta$ . . . 137
A.1.3 $B \to K^{(*)}\ell^+\ell^-$ . . . 138
A.1.4 $K_L \to \pi^0\ell^+\ell^-$ . . . 139
A.1.5 $P \to M\ell^-_\alpha\ell^+_\beta$ . . . 139
A.1.6 $B \to X_s\gamma$ . . . 140
A.1.7 $R(D^{(*)})$ . . . 140
A.1.8 LFU in τ decays . . . 141
A.1.9 Charged lepton flavor violation . . . 142
A.1.10 Matching relations for the Cabibbo angle observables . . . 145
A.1.11 Higgs basis used for EWPT and Higgs fit . . . 146
A.1.12 High-p_T tails . . . 147
A.1.13 Direct constraints from LHC . . . 147
A.1.14 LEFT Operator Basis . . . 148
A.2 Four-quark operators and $\Delta F = 2$ observables . . . 149
A.3 Fits of $b \to s\nu\bar{\nu}$ . . . 150
A.3.1 LEFT . . . 151
A.3.2 SMEFT and simplified models . . . 151

A.3.3 LNV operators 153

Appendix B **156**
B.1 Derivation of the Z/γ PDF at order α^2 156
B.2 Differential cross section 160
B.2.1 Partonic cross sections for Compton scattering 160

Chapter 0

Introduction

The Standard Model (SM) of particle physics provides a consistent and predictive framework for successfully describing the known fundamental particles and the electromagnetic, weak, and strong interactions. Its formulation was completed in the 1970s, following the development of quantum electrodynamics, the unification of the electroweak interaction, and the establishment of quantum chromodynamics as the theory of the strong force. Over the subsequent decades, the SM became the central framework for high-energy physics and has since undergone extensive experimental scrutiny across a vast range of energy scales.

The agreement between theoretical predictions and experimental data has been extraordinary. Precision measurements at colliders such as LEP, SLC, thee Tevatron, and the LHC, as well as low-energy observables from flavor physics and electroweak precision tests, have confirmed the validity of the SM to remarkable accuracy. The discovery of the Higgs boson at the LHC in 2012 filled in the last big missing component. Since then, detailed measurements of Higgs production and decay rates have shown consistency with SM expectations within current experimental uncertainties.

Despite this success, it is widely understood that the SM cannot be the ultimate theory of fundamental interactions. Several observed phenomena lack explanation within the SM framework. The existence of neutrino masses, established through oscillation experiments, requires physics beyond the SM. The presence of dark matter, inferred from astrophysical and cosmological observations, has no particle candidate within the SM particle content. The baryon asymmetry of the universe cannot be generated in sufficient quantity by SM processes. The origin of the SM flavor structure, the strong CP problem, and the naturalness of the Higgs mass further point to the need for an extended theoretical framework. In addition, the SM lacks a quantum description of gravity and is agnostic about the initial conditions and evolution of the early universe.

These conceptual and observational limitations have motivated a wide range of Beyond the Standard Model (BSM) scenarios, aiming to resolve some or all of these issues. Supersymmetry, extra-dimensional theories, composite Higgs models, and various extensions of the gauge and flavor sectors are among the many proposed frameworks. A recurring feature of these models is the prediction of new states, symmetries, or dynamics at energy scales that are, in principle, accessible to collider experiments or to cosmological probes.

For many years, expectations were high that new physics would manifest at the TeV scale, accessible to the LHC. The discovery of the Higgs boson reinforced this expectation, especially in light of the naturalness problem and the sensitivity of scalar masses to ultraviolet physics.

However, more than a decade after the Higgs discovery, the LHC has not discovered any new particles beyond those already present in the SM (and its predicted bound states). While these results have imposed strong constraints on many BSM models, they have not ruled out the possibility of new physics altogether. Instead, the ongoing High-Luminosity LHC (HL-LHC) phase, with its increased integrated luminosity, is expected to further improve the sensitivity to rare processes and subtle deviations, and remains a critical component of this effort. Today, theoretical and experimental efforts are diversifying.

The absence of direct discoveries at the LHC has emphasized the importance of indirect probes—especially those based on precision measurements, flavor observables, and electroweak processes. The Standard Model Effective Field Theory (SMEFT) has emerged as a central tool in this context. It provides a systematic and model-independent approach to parameterizing deviations from the SM within a bottom-up approach. In this way, it enables global analyses of data from a wide range of processes, yielding constraints on BSM physics that can be derived even in the absence of direct production of new particles.

At the same time, the community is actively pursuing the design and development of next-generation experimental facilities. Proposed future colliders, including high-energy proton–proton machines such as the Future Circular Collider (FCC-hh), electron–positron machines like the ILC or CEPC, Muon Colliders, and FCC-ee, offer the possibility of significantly extending the reach of experimental searches. These facilities are expected to probe deeper into the structure of the Higgs sector, test the electroweak scale with greater precision, and explore energies well beyond the current capabilities of the LHC, up to $\mathcal{O}(100)\,\text{TeV}$. The exploration of both the energy and precision frontiers remains a key strategy for uncovering BSM effects.

Beyond terrestrial experiments, cosmology offers a complementary perspective on fundamental physics. The early universe acts as a natural high-energy laboratory where new particles and interactions can leave observable imprints that can be used to test or constrain specific particle physics scenarios. Observables such as the cosmic microwave background, large-scale structure, primordial element abundances, and stochastic gravitational wave backgrounds provide increasingly sensitive probes of new physics, marking the connection between particle physics and cosmology. As experimental and observational frontiers continue to advance, the convergence of these different probes is expected to play an increasingly central role in the search for new physics.

The present thesis is situated within this broad context. It aims to contribute to the understanding of fundamental physics through a combination of theoretical and phenomenological studies, with a focus on current indirect hints, future opportunities, and the link with cosmological observations. The structure of the thesis reflects this perspective:

- **Chapter 1** In the first part, the foundational elements of the Standard Model are reviewed. We discuss the gauge and Higgs sectors, the matter content, and the Higgs mechanism, with an emphasis on the flavor structure and the approximate symmetries of the theory. Following this, we review the Effective Field Theory approach and the SMEFT framework. Finally, we discuss the standard thermal history of the universe, briefly reviewing the evolution of the SM thermal bath and the decoupling of visible and Dark Matter particles.

- **Chapter 2** In this chapter, we discuss the power of the SMEFT framework in analyzing collider data and constraining new physics scenarios. In detail, we discuss a SMEFT

analysis of top-philic new physics scenarios, under the assumption that NP particles predominantly couple to third-generation fermions. In addition, we provide an effective analysis of the recently measured decay modes of mesons into neutrinos.

- **Chapter 3** In the third chapter, we discuss the theoretical challenges of future machines, focusing on Muon Colliders. We begin by detailing the techniques used to model initial-state radiation and by introducing the lepton parton distribution functions (PDFs). Then, we highlight the often-overlooked mixed Z/γ PDF, provide an improved higher-order analytic calculation, and emphasize its significance for processes at muon colliders.

- **Chapter 4** In this part, we explore the connections between particle physics and cosmology, focusing in particular on scenarios where early-universe phenomena, such as phase transitions and gravitational wave production, can serve as signatures of BSM dynamics. We review the possible occurrence of some epochs of inflation, often denoted as supercooling, and discuss their implications on the dynamics of dark sectors.

At the end, conclusions are drawn and an outlook on the results of this thesis is provided.

Chapter 1

Fundamentals

The main focus of this thesis is to explore the presence of new physics at the high-energy frontier, namely at energy scales above the electroweak scale of the Standard Model (SM). In this chapter, we introduce the key theoretical concepts that will underlie the work presented in the rest of the thesis. We begin by reviewing the SM Lagrangian, its particle content, the Higgs mechanism, and the flavor structure of the theory. We then discuss the SM from the perspective of an effective field theory, illustrating how higher-dimensional operators can be systematically added to parameterize potential effects of heavy new physics. Finally, we turn to cosmological considerations, reviewing the thermal history of the Standard Model in the early universe and examining the thermodynamics of the primordial plasma. Particular emphasis is given to the freeze-out mechanism, which governs the decoupling of both visible and dark sector particles as the universe expands and cools.

1.1 The Standard Model

The Standard Model is a renormalizable quantum field theory that successfully describes the strong, weak, and electromagnetic interactions. Its structure is determined by the gauge group

$$G_{\rm SM} = SU(3)_C \times SU(2)_L \times U(1)_Y \,, \tag{1.1}$$

where the first factor is the QCD gauge symmetry group, while the other two are often denoted as the electroweak gauge group $G_{\rm EW}$.

As the most general renormalizable theory constructed from $G_{\rm SM}$, the Standard Model contains a rich set of ingredients. Its gauge sector consists of the gluons $G_A\,(A = 1, .., 8)$, which mediate the strong interaction, and the weak and the hypercharge bosons $W_a\,(a = 1, 2, 3)$ and B, which mediate the electroweak interaction. The last boson is the complex Higgs doublet H, which is the only scalar field in the SM Lagrangian. Then, the matter content consists of the SM fermions f_i, that are grouped into three generations, that we label by the flavor index i. They are charged under the gauge group $G_{\rm SM}$ and obtain their masses via Yukawa interactions with the Higgs. Overall, the complete lagrangian of the SM can be sketched as:

$$\mathcal{L}_{\rm SM} = \mathcal{L}_{\rm gauge} + \mathcal{L}_{\rm matter} + \mathcal{L}_{\rm higgs} + \mathcal{L}_{\rm yukawa} \tag{1.2}$$

In the following sections, we will not attempt to cover all of the theoretical aspects and phenomenological implications of the SM lagrangian in eq. (1.2). We will provide a mini-

review of the mechanism of electroweak symmetry breaking and its consequences for the gauge and Higgs sectors. Then, we move on to the fermionic sector, emphasizing the generation of masses and the observed flavor structure. We follow ref.s [7, 8], where a complete introduction to the Standard Model can be found.

1.1.1 The gauge and the higgs sectors

The Yang–Mills part of the SM Lagrangian is given by

$$\mathcal{L}_{\text{gauge}} = -\frac{1}{4}G^A_{\mu\nu}G_A^{\mu\nu} - \frac{1}{4}W^a_{\mu\nu}W_a^{\mu\nu} - \frac{1}{4}B_{\mu\nu}B^{\mu\nu}\,, \tag{1.3}$$

where the corresponding field strength tensors take the general form

$$V^i_{\mu\nu} = \partial_\mu V^i_\nu - \partial_\nu V^i_\mu + i g_V f^{ijk} V^j_\mu V^k_\nu\,,$$

with f^{ijk} denoting the structure constants of the non-Abelian gauge group. In the QCD sector, one could also add the topological θ-term, $\theta_{\text{QCD}}\,\tilde{G}_{\mu\nu}G^{\mu\nu}$. Although this is a total derivative, it has physical consequences due to non-perturbative properties of the QCD vacuum, and it is related to the well-known strong CP problem. However, this term will not be discussed further in this thesis.

The Higgs sector of the SM is described by

$$\mathcal{L}_{\text{higgs}} = |D_\mu H|^2 - V(H^\dagger H) = |D_\mu H|^2 - \lambda\left(H^\dagger H - \frac{v^2}{2}\right)^2\,, \tag{1.4}$$

where the Higgs doublet H acquires a nonzero vacuum expectation value, breaking the electroweak symmetry. The measured value $v \simeq 246$ GeV is determined precisely from the muon decay rate. To describe fluctuations around this vacuum, we parametrize the Higgs field as

$$\langle H\rangle = \begin{pmatrix} 0 \\ \frac{v}{\sqrt{2}} \end{pmatrix}, \qquad H' = H - \langle H\rangle = \begin{pmatrix} G^+ \\ \frac{h - iG_3}{\sqrt{2}} \end{pmatrix}, \tag{1.5}$$

where h denotes the CP-even physical Higgs scalar, G^+ is the charged would-be Goldstone boson, and G_3 is the neutral CP-odd would-be Goldstone. As will be discussed below, these G^i fields are "eaten" by the gauge bosons after symmetry breaking, providing them with longitudinal components. By convention, the vacuum is taken real and aligned along the neutral component of the doublet without loss of generality.

In order to derive the pattern of electroweak symmetry breaking and the resulting spectrum of gauge boson masses, we note that the Higgs doublet transforms as $(\mathbf{1},\mathbf{2})_{1/2}$ under the electroweak group G_{SM}. Its covariant derivative then reads

$$D_\mu H = \partial_\mu H - i g_2 W^a_\mu t_a H - i\frac{1}{2}g_1 B_\mu H\,, \tag{1.6}$$

where $t_a = \sigma^a/2$ are the $SU(2)_L$ generators (with σ^a the Pauli matrices), and g_1, g_2 are the gauge couplings associated with $U(1)_Y$ and $SU(2)_L$, respectively. Substituting the Higgs

vacuum expectation value v into the kinetic term $|D_\mu H|^2$, we find

$$\begin{aligned} |D_\mu H|^2 &= g_2^2 \frac{v^2}{8} (0\ 1) \begin{pmatrix} \frac{g_1}{g_2} B_\mu + W_\mu^3 & W_\mu^1 - i W_\mu^2 \\ W_\mu^1 + i W_\mu^2 & \frac{g_1}{g_2} B_\mu - W_\mu^3 \end{pmatrix}^2 \begin{pmatrix} 0 \\ 1 \end{pmatrix} = \\ &= g_2^2 \frac{v^2}{8} \left[(W_\mu^1)^2 + (W_\mu^2)^2 + \left(\frac{g_1}{g_2} B_\mu - W_\mu^3 \right)^2 \right] . \end{aligned} \tag{1.7}$$

This expression gives the mass terms for the gauge bosons. First, we identify the charged vectors

$$W_\mu^\pm = \frac{W_\mu^1 \mp i W_\mu^2}{\sqrt{2}} . \tag{1.8}$$

Then, to diagonalize the neutral sector, we introduce the Weinberg angle θ_W, defined by $\cos\theta_W = g_2/\left(\sqrt{g_1^2 + g_2^2}\right)$, and rotate the fields as

$$\begin{pmatrix} Z_\mu \\ A_\mu \end{pmatrix} = \begin{pmatrix} \cos\theta_W & -\sin\theta_W \\ \sin\theta_W & \cos\theta_W \end{pmatrix} \begin{pmatrix} W_\mu^3 \\ B_\mu \end{pmatrix} . \tag{1.9}$$

This identifies the massive Z_μ boson and the massless photon A_μ. Overall, the Higgs kinetic term gives

$$|D_\mu H|^2 = \frac{g_2^2 v^2}{4} W_\mu^+ W^{\mu -} + \frac{(g_1^2 + g_2^2) v^2}{8} Z_\mu Z^\mu + \text{ interactions} , \tag{1.10}$$

leading to the mass relations

$$m_W^2 = \frac{g_2^2 v^2}{4} , \quad m_Z^2 = \frac{(g_1^2 + g_2^2) v^2}{4} = \frac{m_W^2}{\cos^2\theta_W} , \quad m_A = 0 . \tag{1.11}$$

By inserting the Higgs vev into the scalar potential, we can also obtain the mass of the physical Higgs scalar:

$$V(H^\dagger H) \ = \ \lambda v^2 h^2 + \text{interactions} , \tag{1.12}$$

from which we identify

$$m_h^2 = 2\lambda v^2 , \qquad m_{G^\pm}^2 = m_{G_3}^2 = 0 . \tag{1.13}$$

Experimentally, the Higgs mass is measured to be $m_h \simeq 125$ GeV while the vectors have mass $m_W \simeq 80$ GeV and $m_Z \simeq 91$ GeV.

In summary, the Higgs vacuum expectation value breaks the electroweak gauge symmetry as $SU(2)_L \times U(1)_Y \to U(1)_{\text{e.m.}}$. The three massless degrees of freedom G^i are the Goldstone bosons associated with the three broken generators. These would-be Goldstones are "eaten" by the $W^\pm$ and Z gauge bosons, becoming the longitudinal components of these now massive vector fields. Indeed, in unitary gauge, they disappear entirely from the Lagrangian. Expanding the covariant derivative also reveals all interactions among the Higgs h and gauge fields. In addition, the SM Lagrangian also contains the gauge-fixing part

$$\mathcal{L}_{\text{g.f.}} = -\frac{1}{2\xi} \sum_V \left(\partial_\mu V^\mu + g_V \, \xi \, H'^\dagger \, i T \, \langle H \rangle + \text{h.c.} \right)^2 , \tag{1.14}$$

as well as the corresponding ghost terms arising in a general R_ξ-gauge. We do not discuss these terms in this introduction, and refer the reader to, e.g., [7, 8] for a complete discussion.

Having diagonalized the gauge sector and determined the mass spectrum, it is also useful to introduce the combinations of broken generators $t_\pm = t_1 \pm i\, t_2$, and the unbroken electric charge operator

$$Q = t_3 + Y\,. \tag{1.15}$$

The elementary electric charge is given by $e = g_2\, s_W = g_1\, c_W$, which can, for example, be checked by studying the commutators $g_2[A_\mu, W_\mu^\pm]$, verifying that the $W^\pm$ bosons have electric charge ± 1 in units of e.

Finally, we can write the generic covariant derivative acting on any SM fermion:

$$D_\mu = \partial_\mu - i g_s G_\mu^A T_A - i\frac{g_2}{\sqrt{2}}\left(W_\mu^+\, t_+ + W_\mu^-\, t_-\right) - ieQA_\mu - i\frac{g_2}{c_W}\left(t_3 - Q\, s_W^2\right) Z_\mu\,, \tag{1.16}$$

where $T^A = \lambda^A/2$ $(A = 1, \ldots, 8)$ are the $SU(3)_C$ generators and λ^A are the Gell-Mann matrices. Importantly, since the Higgs is color-neutral, the QCD sector and its gauge fields are unaffected by electroweak symmetry breaking.

1.1.2 Fermionic sector

In the Standard Model, the left-handed leptons $(\nu_{eL}, e_L,\ \nu_{\mu L}, \mu_L,\ \nu_{\tau L}, \tau_L)$ and left-handed quarks $(u_L, d_L,\ c_L, s_L,\ t_L, b_L)$ transform as doublets under the $SU(2)_L$ chiral gauge group:

$$l^i = \begin{pmatrix}\nu_{eL}\\ e_L\end{pmatrix}, \begin{pmatrix}\nu_{\mu L}\\ \mu_L\end{pmatrix}, \begin{pmatrix}\nu_{\tau L}\\ \tau_L\end{pmatrix}, \qquad q^i = \begin{pmatrix}u_L\\ d_L\end{pmatrix}, \begin{pmatrix}c_L\\ s_L\end{pmatrix}, \begin{pmatrix}t_L\\ b_L\end{pmatrix}. \tag{1.17}$$

For convenience, we will often use the shorthand ν_L^i, e_L^i for the lepton components and u_L^i, d_L^i for the quark components, where $i = 1, 2, 3$ denotes the family index. The right-handed fermions,

$$e_R^i = (e_R,\ \mu_R,\ \tau_R)\,, \quad u_R^i = (u_R,\ c_R,\ t_R)\,, \quad d_R^i = (d_R,\ s_R,\ b_R)\,, \tag{1.18}$$

are all singlets under $SU(2)_L$. In addition, all quarks carry color charge under $SU(3)_C$, and all Standard Model fermions have appropriate hypercharges under $U(1)_Y$, as summarized in table 1.1. The interactions between SM fermions and the gauge bosons follow directly from expanding the covariant derivative in the fermionic kinetic terms. Using the explicit expression of the covariant derivative given in eq. (1.16), these interactions can be compactly written as:

$$\mathcal{L}_{\text{matter}} = \sum_f i\,\bar{f}\,\gamma^\mu\,\partial_\mu f + g_s\, G_\mu^A\, j_{sA}^\mu + e\, A_\mu\, j_{\text{em}}^\mu + \frac{g_2}{c_W}\, Z_\mu\, j_n^\mu + \frac{g_2}{\sqrt{2}}\left(W_\mu^+\, j_-^\mu + \text{h.c.}\right), \tag{1.19}$$

where we have defined the corresponding fermionic currents (color, electromagnetic, neutral, charged):

$$\begin{aligned} j_{sA}^\mu &= \bar{u}\,\gamma^\mu\, T_A\, u + \bar{d}\,\gamma^\mu\, T_A\, d\,,\\ j_{\text{em}}^\mu &= \sum_f Q_f\, \bar{f}\,\gamma^\mu\, f\,,\\ j_n^\mu &= \sum_f Q_f^Z\, \bar{f}\,\gamma^\mu\, f\,,\\ j_-^\mu &= (j_+^\mu)^\dagger = \bar{u}_L\,\gamma^\mu\, d_L + \bar{\nu}_L\,\gamma^\mu\, e_L\,, \end{aligned} \tag{1.20}$$

	Field	$SU(3)_c$	$SU(2)_L$	$U(1)_Y$	Lorentz
Left-handed quark doublets	$q^i = \begin{pmatrix} u_L^i \\ d_L^i \end{pmatrix}$	**3**	**2**	$\frac{1}{6}$	$\left(\frac{1}{2}, 0\right)$
Left-handed lepton doublets	$l^i = \begin{pmatrix} \nu_L^i \\ e_L^i \end{pmatrix}$	**1**	**2**	$-\frac{1}{2}$	$\left(\frac{1}{2}, 0\right)$
Right-handed up quarks	u_R^i	**3**	**1**	$\frac{2}{3}$	$\left(0, \frac{1}{2}\right)$
Right-handed down quarks	d_R^i	**3**	**1**	$-\frac{1}{3}$	$\left(0, \frac{1}{2}\right)$
Right-handed leptons	e_R^i	**1**	**1**	-1	$\left(0, \frac{1}{2}\right)$
Higgs doublet	H	**1**	**2**	$\frac{1}{2}$	$(0, 0)$

Table 1.1: Quantum number and Lorentz irreps of the Standard Model fermions and Higgs boson.

with $Q_f^Z \equiv t_3 - Q\, s_W^2$, and an implicit sum over fermion generations.

Next, we discuss the Yukawa interactions of the SM fermions, which generate their masses after electroweak symmetry breaking. The Yukawa part of the SM Lagrangian is

$$\mathcal{L}_{\text{yukawa}} = -Y_{ij}^u\, \bar{q}^i\, u_R^j\, \tilde{H} - Y_{ij}^d\, \bar{q}^i\, d_R^j\, H - Y_{ij}^e\, \bar{l}^i\, e_R^j\, H + \text{h.c.}, \tag{1.21}$$

where we have introduced the conjugate Higgs field $\tilde{H} \equiv \epsilon\, H^*$, with $\epsilon = i\sigma_2$, the antisymmetric 2×2 matrix. Substituting the Higgs vacuum expectation value into this expression, we obtain:

$$\mathcal{L}_{\text{yukawa}} = -\frac{v}{\sqrt{2}} \left(Y_{ij}^u\, \bar{u}_L^i\, u_R^j + Y_{ij}^d\, \bar{d}_L^i\, d_R^j + Y_{ij}^e\, \bar{e}_L^i\, e_R^j \right) + \text{h.c.} + (\text{interactions})\,. \tag{1.22}$$

We see that the fermion mass matrices are given by $m_{ij}^X = \frac{v}{\sqrt{2}}\, Y_{ij}^X$ for each species $X = u, d, e$, with mixing determined by the corresponding Yukawa couplings. Importantly, in the minimal SM there are no right-handed neutrinos, so neutrinos remain massless at this level.

Each Yukawa matrix can be diagonalized by a bi-unitary transformation. Specifically, for each fermion species $X = u, d, e$, we can introduce unitary matrices U_L^X and U_R^X such that:

$$Y^X = (U_L^X)^\dagger\, Y_{\text{diag}}^X\, U_R^X\,, \tag{1.23}$$

where Y_{diag}^X is the diagonalized Yukawa matrix for the species X. Using these unitary rotations, we can redefine the fermion fields without changing the kinetic terms. In particular, we define the mass eigenstate fields (denoted by a prime) as:

$$u'_{L,R} = U_{L,R}^u\, u_{L,R}\,, \quad d'_{L,R} = U_{L,R}^d\, d_{L,R}\,, \quad e'_{L,R} = U_{L,R}^e\, e_{L,R}\,. \tag{1.24}$$

In this basis, the Yukawa interactions and corresponding mass terms are already diagonal, so the fermions have physical masses

$$m_i^X = \frac{v}{\sqrt{2}}\, y_i^X \,, \tag{1.25}$$

where y_i^X denotes the diagonal entries of the Yukawa matrix Y^X_{diag}. Concretely:

$$Y^u_{\text{diag}} = \text{diag}(y_u, y_c, y_t)\,, \quad Y^d_{\text{diag}} = \text{diag}(y_d, y_s, y_b)\,, \quad Y^e_{\text{diag}} = \text{diag}(y_e, y_\mu, y_\tau)\,. \tag{1.26}$$

Numerical estimates based on the measured fermion masses give [9]:

$$\begin{aligned} (y_u, y_c, y_t) &\approx (10^{-5},\ 7\times 10^{-3},\ 1)\,, \\ (y_d, y_s, y_b) &\approx (3\times 10^{-5},\ 5\times 10^{-4},\ 2.4\times 10^{-2})\,, \\ (y_e, y_\mu, y_\tau) &\approx (3\times 10^{-6},\ 6\times 10^{-4},\ 10^{-2})\,. \end{aligned} \tag{1.27}$$

This pattern exhibits a pronounced hierarchical structure across the three generations. Understanding the origin of these hierarchies — and the smallness of most Yukawa couplings - is known as the *flavor puzzle* of the Standard Model.

We can now examine how the gauge interactions introduced in eq. (1.19) appear when working in the fermion mass-eigenstate basis. The electromagnetic, color, and neutral-current interactions remain completely unchanged – and hence diagonal in flavor space – under these unitary rotations, because they involve fermion bilinears with the same unitary transformation acting on both fermion and antifermion. A direct consequence is the absence of tree-level flavor-changing neutral currents (FCNCs) in the Standard Model, an important feature that we will revisit in the next chapters when discussing potential channels to discover New Physics signatures.

In contrast, the charged-current interactions with the $W^\pm$ bosons do change under rotation to the mass basis. On the lepton side, since neutrinos are assumed massless in the SM, we are free to redefine the left-handed neutrino fields by an arbitrary unitary rotation without affecting the kinetic terms or the Yukawa interactions. Hence, we can choose $\nu'_L = U^e_L\, \nu_L$, i.e. use the same unitary rotation as for the charged leptons. With this choice, the leptonic charged-current interaction is unchanged:

$$\bar\nu^i_L\, \gamma^\mu\, e^i_L \ \to\ \bar\nu'^{\,i}_L\, \gamma^\mu\, e'^{\,i}_L\,. \tag{1.28}$$

On the other hand, the quark charged-current interaction becomes

$$\bar u_L\, \gamma^\mu\, d_L \ \to\ \bar u'_L\, \gamma^\mu\, (U^u_L\, U^{d\dagger}_L)\, d'_L \ \equiv\ \bar u'_L\, \gamma^\mu\, V\, d'_L\,, \tag{1.29}$$

where

$$V \equiv U^u_L\, U^{d\dagger}_L$$

is the unitary Cabibbo–Kobayashi–Maskawa (CKM) matrix. Henceforth, we will drop the primes and assume all SM fermion fields are expressed in the mass-eigenstate basis unless specified otherwise.

1.1.3 CKM sector

The CKM matrix $V \equiv U_L^u U_L^{d\dagger}$ is a 3×3 complex unitary matrix. In general, a 3×3 unitary matrix is specified by $n^2 = 9$ real parameters: 3 rotation angles and 6 complex phases. However, not all of these parameters are physical. The SM Lagrangian is invariant under independent global phase rotations of the left- and right-handed quark fields,

$$f^i_{L,R} \to e^{i\alpha^i_{L,R}} f^i_{L,R} \quad \text{for} \quad f = u,\, d\,,$$

which allows us to remove 5 of the 6 phases appearing in the CKM matrix (a common rephasing does not yield any effect and cannot be used to absorb any further phase). Hence, after fixing this freedom, we are left with 3 real mixing angles and a single CP-violating phase δ. These 4 parameters completely determine the CKM matrix. It is customary to write the CKM as

$$\begin{aligned} V &= \begin{pmatrix} 1 & 0 & 0 \\ 0 & \cos\theta_{23} & \sin\theta_{23} \\ 0 & -\sin\theta_{23} & \cos\theta_{23} \end{pmatrix} \\ &\times \begin{pmatrix} \cos\theta_{13} & 0 & \sin\theta_{13} e^{i\delta} \\ 0 & 1 & 0 \\ -\sin\theta_{13} e^{i\delta} & 0 & \cos\theta_{13} \end{pmatrix} \begin{pmatrix} \cos\theta_{12} & \sin\theta_{12} & 0 \\ -\sin\theta_{12} & \cos\theta_{12} & 0 \\ 0 & 0 & 1 \end{pmatrix} \\ &= \begin{pmatrix} c_{12}c_{13} & s_{12}c_{13} & s_{13}e^{-i\delta} \\ -s_{12}c_{23} - c_{12}s_{23}s_{13}e^{i\delta} & c_{12}c_{23} - s_{12}s_{23}s_{13}e^{i\delta} & s_{23}c_{13} \\ s_{12}s_{23} - c_{12}c_{23}s_{13}e^{i\delta} & -c_{12}s_{23} - s_{12}c_{23}s_{13}e^{i\delta} & c_{23}c_{13} \end{pmatrix}, \end{aligned} \tag{1.30}$$

where $c_{ij} = \cos(\theta_{ij})$ and $s_{ij} = \sin(\theta_{ij})$. The numerical values for the angles and phase, according to the last experimental review [9], are:

$$\begin{aligned} s_{12} &= 0.22501 \pm 0.00068, \quad & s_{13} &= 0.003732^{+0.000090}_{-0.000085}\,, \\ s_{23} &= 0.04183^{+0.00079}_{-0.00069}, & \delta &= 1.147 \pm 0.026\,. \end{aligned} \tag{1.31}$$

Since all the measured CKM mixing angles are small, it is often useful to work with the Wolfenstein parametrization, which provides a transparent and accurate approximation of the flavor structure. To $\mathcal{O}(\lambda^3)$, the CKM matrix is written as

$$V = \begin{pmatrix} V_{ud} & V_{us} & V_{ub} \\ V_{cd} & V_{cs} & V_{cb} \\ V_{td} & V_{ts} & V_{tb} \end{pmatrix} = \begin{pmatrix} 1 - \frac{\lambda^2}{2} & \lambda & A\lambda^3(\bar\rho - i\bar\eta) \\ -\lambda & 1 - \frac{\lambda^2}{2} & A\lambda^2 \\ A\lambda^3(1 - \bar\rho - i\bar\eta) & -A\lambda^2 & 1 \end{pmatrix} + \mathcal{O}\left(\lambda^4\right), \tag{1.32}$$

where the Wolfenstein parameters take the experimentally measured values [9]:

$$\begin{aligned} \lambda &= 0.22501 \pm 0.00068, \quad & A &= 0.826^{+0.016}_{-0.015}, \\ \bar\rho &= 0.1591 \pm 0.0094, & \bar\eta &= 0.3523^{+0.0073}_{-0.0071}. \end{aligned} \tag{1.33}$$

These parameters can be directly related to the three rotation angles and CP-violating phase that define the CKM matrix. For instance, $\lambda = \sin\theta_{12}$[1] approximately matches the Cabibbo angle θ_{12}.

[1]We point out that the letter λ, according to common conventions, is used for both the Higgs quartic coupling and for describing the Cabibbo angle in Wolfenstein parametrization.

1.1.4 Approximate symmetries

To investigate physics beyond the Standard Model (BSM), it is crucial to first understand the symmetries that characterize the SM itself. These symmetries provide valuable guidance for identifying observables and processes where new physics effects are most likely to manifest. Moreover, they offer important clues about the possible symmetry structure and dynamics of the heavy degrees of freedom that lie beyond the SM.

A natural starting point is to identify the largest group of global symmetries acting on the SM fermions that is compatible with the gauge symmetries. Neglecting the Yukawa interactions, the SM Lagrangian exhibits an accidental global flavor symmetry group:

$$\mathcal{G}_f = \mathrm{U}(3)_\ell \times \mathrm{U}(3)_q \times \mathrm{U}(3)_e \times \mathrm{U}(3)_u \times \mathrm{U}(3)_d \,, \tag{1.34}$$

which acts independently on the three generations of each type of fermion field. This symmetry is explicitly broken by the Yukawa interactions, which reduce $\mathcal{G}_f$ to:

$$\mathcal{G}_f \xrightarrow{Y_{e,u,d}\neq 0} \mathrm{U}(1)_B \times \mathrm{U}(1)_{L_e} \times \mathrm{U}(1)_{L_\mu} \times \mathrm{U}(1)_{L_\tau} \times \mathrm{U}(1)_Y \,, \tag{1.35}$$

where we identify the gauged hypercharge group $U(1)_Y$, and the global baryon and individual lepton numbers B and L_i. These are accidental symmetries of the renormalizable SM Lagrangian and can be violated at perturbative level only by higher-dimensional operators.

As discussed in previous sections, the breaking of $\mathcal{G}_f$ by the Yukawa matrices introduces a highly hierarchical structure in flavor space, with all quark flavor violation encoded in the CKM matrix. This structure has far-reaching phenomenological implications.

Consider, for instance, FCNC processes such as $d_i \to d_j$ transitions. These are forbidden at tree level in the SM and only arise at loop level through box or penguin diagrams. Remarkably, they are subject, beyond the loop factor, to strong suppressions. In particular, the relevant amplitudes usually involve sums over CKM combinations of the form $f(k)V_{ik}^\dagger V_{kj}$, where $f(k)$ are loop functions depending on quark masses. If we neglect the difference between masses, these terms would satisfy unitarity relations of the type $\sum_k V_{ik}^\dagger V_{kj} = 0$ and lead to the cancellation among contributions from different up-type quarks in the loops. The actual contribution is then proportional to mass differences among the virtual quarks, suppressed anyway by small off-diagonal CKM elements. Interestingly, the dominant contribution in many cases arises from top-quark loops ($k = t$), not because the CKM elements $V_{ti}^\dagger V_{tj}$ are large, but because the large top mass enhances the loop function.

The exceptional suppression of FCNC transitions within the SM makes them particularly sensitive to new physics. New heavy states, even at scales far above the electroweak scale, can induce contributions that are comparable to the SM expectations. This sensitivity turns rare FCNC processes into powerful indirect probes of BSM dynamics.

At the same time, the observed suppression of flavor-violating effects suggests that the flavor structure of any BSM extension must be highly non-generic. This motivates the study of approximate flavor symmetries, such as $U(3)^5$, and specific breaking patterns that could explain both the SM flavor structure and the suppression of dangerous BSM effects. We will return to these ideas in Sec. 1.2.4, where we discuss how the SMEFT framework can be organized according to flavor symmetry assumptions, such as Minimal flavor Violation (MFV) or $U(2)^n$-based approaches.

In analogy with the approximate global symmetries acting on fermions, the Higgs sector of the Standard Model also enjoys an approximate global symmetry structure. In particular, in

the limit of vanishing hypercharge and degenerate Yukawa couplings, the Higgs interactions exhibit an enhanced $SU(2)_L \times SU(2)_R$ symmetry, whose properties and phenomenological consequences we now briefly review.

It is useful to recast the Higgs doublet in a 2×2 matrix representation, defined as

$$\Phi(x) = G_i(x)\sigma^i + h(x)\mathbb{I}_{2\times 2}, \tag{1.36}$$

so that the Higgs sector of the Standard Model Lagrangian can be written as

$$\mathcal{L}_{\text{Higgs}} = \frac{1}{4}\text{Tr}\left[D_\mu \Phi^\dagger D^\mu \Phi\right] - \lambda\left(\frac{1}{4}\text{Tr}\left[\Phi^\dagger\Phi\right] - \frac{v^2}{2}\right)^2, \tag{1.37}$$

where the covariant derivative takes the form

$$D_\mu \Phi = \partial_\mu \Phi - i\frac{g_2}{2}W_\mu^a \sigma^a \Phi + i\frac{g_1}{2}B_\mu \Phi \sigma^3. \tag{1.38}$$

In the limit where the hypercharge coupling $g_1 \to 0$, the Higgs Lagrangian exhibits an enhanced global symmetry $SU(2)_L \times SU(2)_R$, under which the Higgs field transforms as $\Phi \to U_L \Phi U_R^\dagger$. This symmetry is only broken explicitly by the gauging of hypercharge, which corresponds to gauging only the third generator of $SU(2)_R$, and by the difference in the Yukawa couplings between up- and down-type fermions.

The Higgs vacuum expectation value (VEV) spontaneously breaks $SU(2)_L \times SU(2)_R \to SU(2)_C \sim SO(3)_C$, known as the *custodial* symmetry. The three Nambu–Goldstone bosons associated with this breaking pattern correspond, as usual, to the degrees of freedom that are eaten to give mass to the $W^\pm$ and Z gauge bosons through the Higgs mechanism.

A direct consequence of custodial symmetry is that the tree-level relation between the electroweak gauge boson masses and couplings:

$$\rho \equiv \frac{m_W^2}{m_Z^2 \cos^2\theta_W} = 1\,, \tag{1.39}$$

which is only modified by loop contributions. In addition, in the SM, radiative corrections to the ρ parameter vanish in the limit of degenerate up- and down-type fermion masses and zero hypercharge. In contrast, many new physics scenarios—particularly those involving non-minimal Higgs sectors—explicitly break custodial symmetry at tree level and typically induce corrections to the ρ parameter. Precision measurements, especially from LEP, have placed stringent bounds on deviations from the SM value of ρ, thus severely constraining the parameter space of new physics models that do not respect custodial symmetry.

1.1.5 Running couplings

We conclude this review of the Standard Model by discussing an important feature common to all interacting QFTs: the running of couplings.

A well-known result of renormalization theory is that coupling constants acquire a dependence on the energy scale μ. In terms of the squared couplings $\alpha_i = g_i^2/(4\pi)$, the evolution is governed by the corresponding β-functions:

$$\beta(\alpha_i) \equiv \mu\frac{d\log\alpha_i}{d\mu} = -\beta_0\alpha_i + \mathcal{O}(\alpha_i^3)\,. \tag{1.40}$$

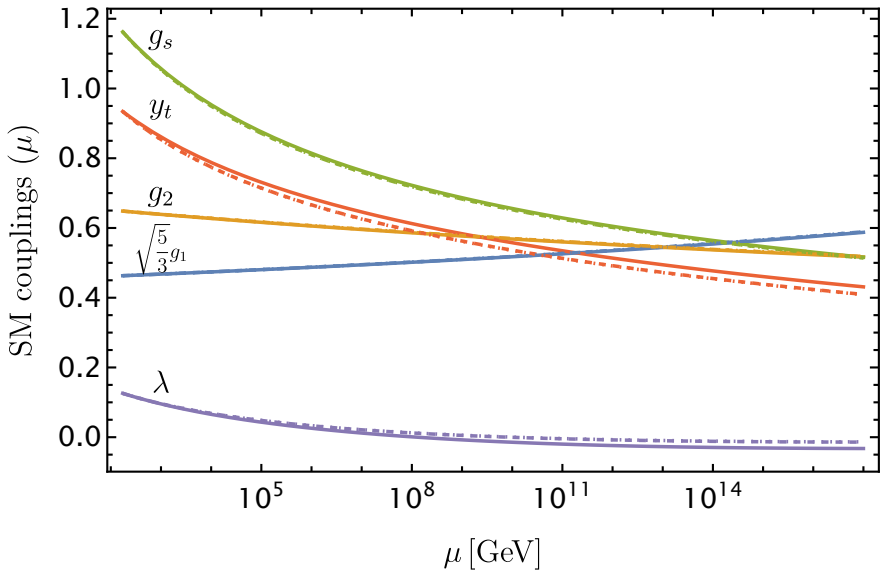


Figure 1.1: Running of the SM couplings g_1, g_2, g_s, y_t, and λ. Solid, dashed, and dotted lines show the evolution obtained using the 1-loop, 2-loop, and 3-loop β-functions, respectively.

Here, β_0 is the one-loop coefficient of the β-function, which is scheme-independent.

In the SM, we are typically interested in the evolution of the gauge couplings g_s, g_2, and g_1, corresponding to the gauge groups $SU(3)_c \times SU(2)_L \times U(1)_Y$. At low energies, we may also be concerned with the running of the electromagnetic coupling e.

In the presence of n_s complex scalars and n_f chiral fermions transforming in the fundamental representation of a non-abelian group, the general one-loop expression for β_0 reads:

$$\beta_0^{SU(N)} = \frac{1}{6\pi}\left(11N - n_f - \frac{n_s}{2}\right) , \tag{1.41}$$

while for $U(1)$ groups, denoting by Q_f and Q_s the charges of fermions and scalars respectively, the coefficient is given by:

$$\beta_0^{U(1)} = -\frac{1}{6\pi}\left(2\sum_f Q_f^2 + \sum_s Q_s^2\right) . \tag{1.42}$$

Applying these formulas to the field content of the Standard Model yields:

$$\beta_0^{U(1)_Y} = -\frac{41}{12\pi} , \quad \beta_0^{SU(2)_L} = \frac{19}{12\pi} , \quad \beta_0^{SU(3)_c} = \frac{7}{2\pi} . \tag{1.43}$$

Using these results, the one-loop running of the coupling constant can be obtained by integrating eq. (1.40):

$$\alpha^{(1)}(\mu) = \frac{\alpha(\mu_0)}{1 + \beta_0 \alpha(\mu_0) \ln(\mu/\mu_0)} . \tag{1.44}$$

It is well known that the behavior of the coupling evolution depends on the sign of β_0. In particular, QCD exhibits asymptotic freedom at high energies and becomes strongly coupled at low energies $E \leq \Lambda_{\rm QCD}$.

For completeness, we also present the one-loop β-functions for the top Yukawa coupling y_t and the Higgs quartic coupling λ. These couplings are of particular importance as they dominate many processes within and beyond the SM and play a key role in studies of vacuum stability and the naturalness of the weak scale.

At one-loop, the β-functions for λ and y_t are:

$$\begin{aligned} 16\pi^2\beta_\lambda &= 24\lambda^2 - 3\lambda\left(g_1^2 + 3g_2^2\right) + \frac{3}{4}\left(\frac{1}{2}g_1^4 + g_1^2 g_2^2 + \frac{3}{2}g_2^4\right) + 12y_t^2\lambda - 6y_t^4\,, \\ 16\pi^2\beta_{y_t} &= y_t\left[\frac{9}{2}y_t^2 - \left(\frac{17}{12}g_1^2 + \frac{9}{4}g_2^2 + 8g_s^2\right)\right]\,. \end{aligned} \tag{1.45}$$

The evolution of the five couplings discussed in this section is shown in fig. 1.1. For completeness, we also display the numerical solutions using two-loop and three-loop β-functions, represented by dashed and dotted curves, respectively.

1.2 The Standard Model as an Effective Theory

We now turn to the discussion of the Standard Model Effective Field Theory (SMEFT). After introducing the general philosophy of effective field theories and motivating their use, we present a few illustrative examples[2] of how they can be applied within the Standard Model framework. Finally, we introduce the SMEFT Lagrangian up to dimension-six operators, which will play a central role in the analyses carried out in the subsequent chapters of this thesis.

1.2.1 EFT approach

The concept of an effective theory, or an effective description of a physical phenomenon, can actually be traced back long before the formulation of quantum field theories. The core idea is that physics often simplifies when viewed at large distances (low energies), where the short-distance (high-energy) degrees of freedom become irrelevant. One can illustrate this with a simple example from classical electrostatics: the potential generated by a localized, static distribution of electric charges. If we denote by d the characteristic size of this charge distribution, then the electric potential measured at a distance r can be expanded in powers of d/r. Intuitively, if we are very far from the source ($r \gg d$), we cannot resolve its structure and only need the leading terms of this expansion. More explicitly, the potential can be written as a multipole series:

$$V(r) = \frac{a}{r} + b_i\,\nabla_i\frac{1}{r} + c_{ij}\,\nabla_i\nabla_j\frac{1}{r} + \cdots\,. \tag{1.46}$$

The higher-order terms incorporate details of the short-distance structure of the charge distribution. Indeed, by dimensional analysis, these terms are suppressed by powers of $(d/r)^n$, becoming negligible at large distances. On the other hand, the first term corresponds to the monopole contribution. Taking the far-field limit $r \gg d$, we recognize this as the potential generated by a point-like source with total charge Q, allowing us to match the effective coefficient $a = Q/(4\pi)$.

[2]The discussion is inspired by the GGI lectures on EFT by Adam Falkowski [10].

This example shows that effective descriptions can be naturally built from power counting, dimensional analysis, scale separation, and matching to known behaviors in the appropriate limits. In general, the accuracy of the effective description depends on the scale separation: as we approach the UV regime ($r \lesssim d$, or energies $E \gtrsim \Lambda \equiv 1/d$), the effective expansion breaks down and the full microscopic theory is required.

These ingredients also underlie the logic of effective field theories in QFT context. Similarly to the toy electrostatic example, the idea is to construct the most general Lagrangian that respects Lorentz invariance and the gauge and global symmetries of the theory, using the assumed low-energy field content:

$$\mathcal{L}_{\text{eff}} = \mathcal{L}^{(d\leq 4)} + \sum_d C_d \, \frac{\mathcal{O}_d}{\Lambda^{d-4}} \,, \tag{1.47}$$

where $\mathcal{L}^{(d\leq 4)}$ is the renormalizable part of the Lagrangian (with all operators of dimension ≤ 4) and the $\mathcal{O}_d$ denotes the set of higher d-dimensional operators suppressed by powers of the cutoff scale Λ, which characterizes the energy where the effective description breaks down. The corresponding expansion parameter is $(E/\Lambda)^n$, where E is the typical energy scale of the process under consideration.

Before applying this logic to the Standard Model, let us illustrate the concept with a simple quantum field theory example: the effective theory of light-by-light scattering as an IR effective description of QED. Treating for the moment the UV physics as unknown, we can parametrize the low-energy theory just writing all the gauge-invariant operators built from the photon field. Therefore, the so-called Euler-Heisenberg effective Lagrangian reads

$$L_{EH} = -\frac{1}{4} F_{\mu\nu} F^{\mu\nu} + \mathcal{L}_{EH}^{(D=8)} + \mathcal{L}_{EH}^{(D=12)} + \cdots \,. \tag{1.48}$$

Gauge invariance requires that the photon field A_μ appears only through the field strength $F_{\mu\nu}$ or its dual $\tilde{F}_{\mu\nu}$. Moreover, odd-dimensional operators vanish identically by Lorentz and permutation symmetries, so the leading corrections appear at dimension 8. The most general set of independent operators at dimension 8 is

$$\mathcal{L}_{EH}^{(D=8)} = \frac{c_1}{16} \, (F_{\mu\nu} F^{\mu\nu})(F_{\rho\sigma} F^{\rho\sigma}) + \frac{c_2}{16} \, (F_{\mu\nu} \tilde{F}^{\mu\nu})(F_{\rho\sigma} \tilde{F}^{\rho\sigma}) \,. \tag{1.49}$$

Any other gauge-invariant operator at this order can be rewritten in terms of this minimal basis. The Wilson coefficients c_1 and c_2 can be determined by matching to the UV theory. This can be done by computing the 2-to-2 photon scattering both in full QED, via loop box diagram involving electrons, and in our effective description via tree level vertices. This matching yields:

$$c_1 = \frac{8\alpha^2}{45\, m_e^4} \,, \qquad c_2 = \frac{14\alpha^2}{45\, m_e^4} \,, \tag{1.50}$$

where m_e is the electron mass and α is the fine-structure constant. This demonstrates that the cutoff scale Λ is set by the heavy particle scale, in this case, the electron. The EFT is valid for processes with $E \ll m_e$.

Although this example is based on a well-established theory, QED, the power of the EFT approach actually lies in its generality. Consider, for instance, that we want to discriminate between two different UV completions: standard QED with a Dirac electron or scalar QED

with a charged scalar of mass m_s. In the scalar case one finds $c_1^s = 0$, $c_2^s = \alpha^2/(90\, m_s^4)$. Hence, a precise low-energy measurement of c_1 and c_2 would allow us to discriminate the correct underlying theory, within a bottom-up approach and even without direct access to the heavy states.

1.2.2 4-Fermi theory from the SM

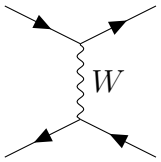
We now illustrate the general principles of effective field theories with a relevant example: the four-fermion (Fermi) theory as the low-energy limit of the Standard Model. Specifically, we focus on four-quark interactions that contribute to kaon physics. At low energies, the most general effective Lagrangian describing these interactions can be written as

$$\mathcal{L}_{\text{eff}} \supset -c_1\, \mathcal{O}_1 - c_2\, \mathcal{O}_2 + \text{h.c.} = -c_1\, (\bar{u}_L \gamma^\mu s_L)(\bar{d}_L \gamma_\mu u_L) - c_2\, (\bar{u}_L \gamma^\mu u_L)(\bar{d}_L \gamma_\mu s_L) + \text{h.c.}\,, \quad (1.51)$$

where the Wilson coefficients c_1 and c_2 encode the effects of the heavy Standard Model degrees of freedom. From the ultraviolet perspective, these operators originate from the charged-current interaction in the SM:

$$\mathcal{L}_{\text{SM}} \supset \frac{g_2}{\sqrt{2}}\, W_\mu^+\, (V_{ud}\, \bar{u}_L \gamma^\mu d_L + V_{us}\, \bar{u}_L \gamma^\mu s_L) + \text{h.c.}\,. \quad (1.52)$$

Indeed, the Wilson coefficients c_i can be determined by computing the tree-level diagram



$$= \left(\frac{i g_2}{\sqrt{2}}\right)^2 (V_{us} \bar{u}_L \gamma^\mu s_L)\, \frac{-i\left(g_{\mu\nu} - \frac{p_\mu p_\nu}{m_W^2}\right)}{p^2 - m_W^2}\, \left(V_{ud}^\star \bar{d}_L \gamma^\nu u_L\right)\,.$$

and expanding the propagator of the W boson for $p^2 \ll m_W^2$. We obtain the matching condition

$$c_1 = \frac{4 G_F}{\sqrt{2}} V_{us} V_{ud}^\star = \frac{g_2^2}{2\, m_W^2} V_{us} V_{ud}^\star\,, \qquad c_2 = 0\,. \quad (1.53)$$

This procedure, namely removing the heavy W boson propagator and replacing it by a local four-fermion operator, is what we mean by *integrating out* the heavy degrees of freedom. Although $\mathcal{O}_2$ is not generated at tree level, there is no symmetry that forbids its appearance. Indeed, we can expect radiative corrections to generate $\mathcal{O}_2$, e.g. from the loop diagrams in fig. 1.2

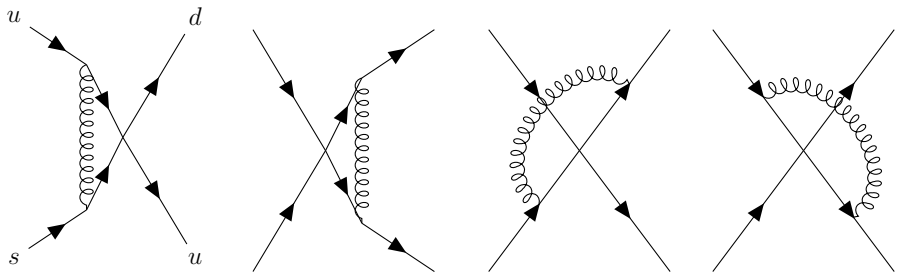


Figure 1.2: QCD radiative contributions to low energy four-fermion operators. It is not necessary to consider other diagrams thanks to current conservation.

We recall that, in the context of renormalization theory, we can define the anomalous dimension associated to an operator $\mathcal{O}_i$

$$\gamma^{\mathcal{O}_i} = \mu \frac{d\log Z^{\mathcal{O}_1}}{d\mu} \,, \tag{1.54}$$

where $Z^{\mathcal{O}_i}$ is the renormalization costant of $\mathcal{O}_i$. More in general, if the lowest dimensional irrelevant operator is not unique, as in this case, we can have a set of operators that mix under renormalization. The anomalous dimension consequently becomes a matrix, and we can study the mixings due to radiative corrections by solving the differential equations:

$$\mu \frac{d \log c_i}{d\mu} = \gamma_{ij}(\{g\})\, c_j \,, \tag{1.55}$$

where, by dimensional grounds, γ_{ij} depends on the marginal couplings of the theory $\{g\}$.

In the case under examination, the most important radiative corrections come from QCD effects. Without entering into the details of the calculation, it can be shown that the anomalous-dimension matrix at one-loop level is:

$$\gamma_{ij} = \frac{\alpha_s}{4\pi} \begin{pmatrix} -2 & 6 \\ 6 & -2 \end{pmatrix} . \tag{1.56}$$

For convenience, we can define the diagonal basis[3] $\mathcal{O}_{1/2} = (\mathcal{O}_1 - \mathcal{O}_2)/2$ and $\mathcal{O}_{3/2} = (\mathcal{O}_1 + \mathcal{O}_2)/2$, which has anomalous dimensions $\gamma_{1/2} = -8\,\alpha_s/(4\pi)$ and $\gamma_{3/2} = 4\,\alpha_s/(4\pi)$, respectively. In this basis, the renormalization group (RG) equation in eq. (1.55) can be solved straightforwardly, running the scale from m_W, where the operators are generated, down to m_K, the scale relevant for kaon phenomenology. Taking the Wilson coefficients to be $c_{1/2}(m_W) = c_{3/2}(m_W) = c_0$, we find numerically that $c_{1/2}(m_K) \simeq 2\, c_0$ and $c_{3/2}(m_K) \simeq 0.7\, c_0$. The latter can be eventually used to compute the amplitudes relevant for IR processes as, for example, non-leptonic decays.

This example illustrates the key steps involved in applying the effective field theory framework when studying the impact of heavy degrees of freedom on low energy phenomenology. In practice, starting from a UV Lagrangian, whether it be the Standard Model or one of its extensions, we integrate out heavy fields at their characteristic mass thresholds and use the renormalization group to evolve the effective operators down to the scale of interest. These tools are essential for interpreting precise low-energy measurements as indirect probes of new physics. We will use these techniques in the analyses provided in chapter 2 within the SMEFT framework, that we introduce in the next section.

1.2.3 The SMEFT lagrangian

We now introduce the formulation of the Standard Model Effective Field Theory. The SMEFT is defined as the effective theory containing all the Standard Model (SM) degrees of freedom — namely the gauge bosons G^A, W^a, and B, the Higgs doublet H, and the three generations of fermions — with interactions governed by the SM Lagrangian $\mathcal{L}_{\rm SM}$,

[3] In general, γ_{ij} is not necessarily a symmetric matrix, so a basis in which it is diagonal does not always exist.

supplemented by a tower of higher-dimensional operators. These operators are constructed solely from SM fields and respect Poincaré invariance as well as the full SM gauge symmetry $SU(3)_c \times SU(2)_L \times U(1)_Y$. They are suppressed by powers of a large UV scale Λ, which sets the cutoff of the effective theory and the scale at which new heavy states are expected to appear. A key assumption of the SMEFT is the existence of a significant mass gap separating the electroweak scale from the unknown high-energy physics, allowing a controlled expansion valid in the energy range $v < E < \Lambda$.

The resulting Lagrangian is non-renormalizable in the traditional sense, as it contains operators of dimension greater than four. However, this is not a limitation: the SM is simply the low-energy limit of a more fundamental UV-complete theory. The higher-dimensional operators provide a systematic parametrization of possible heavy-physics effects on infrared dynamics, much like the familiar Fermi theory of weak interactions (in section 1.2.2) or the chiral Lagrangian that describes low-energy QCD.

The most general SMEFT Lagrangian can then be written as

$$\mathcal{L}_{\text{SMEFT}} = \mathcal{L}_{\text{SM}} + \mathcal{L}^{d=5} + \mathcal{L}^{d=6} + \mathcal{L}^{d=7} + \dots , \tag{1.57}$$

where $\mathcal{L}^d$ denotes the terms involving gauge-invariant operators of mass dimension d, built solely out of SM fields. In the following, we focus on the dimension-5 and dimension-6 operators of the SMEFT, which are most relevant for low-energy phenomenology. Moreover, we will illustrate throughout the thesis how such operators can arise either at tree level, by integrating out heavy states, or through radiative corrections, in close analogy with the 4-Fermi theory as the effective low-energy limit of charged-current interactions.

Let us begin with the dimension-5 terms. Given the SM particle content and symmetries, there is a single operator at this order, the L-violating Weinberg operator:

$$\mathcal{L}^{d=5}_{\text{SMEFT}} = -\sum_{i,j=1}^{3} \frac{c^{(5)}_{ij}}{\Lambda} \, \varepsilon^{ak} \, \varepsilon^{bl} \, H_k \, H_l \, (l^c_i)_a \, (l_j)_b \, , \tag{1.58}$$

which generates Majorana neutrino masses after electroweak symmetry breaking.

The tiny observed neutrino masses imply that this operator must originate at a very high scale $\Lambda \sim 10^{14-15}$ GeV. If all higher-dimensional operators arose at this same scale, then any other effects of new physics would also be enormously suppressed and phenomenologically irrelevant. This suggests that this operator, if present, originates at scales much higher than the typical scale where other SMEFT operators are generated. In general, it is often assumed that B and L violating effects, tightly constrained by experiments, arise from scales $\Lambda_{\not{B},\not{L}}$ larger than the typical SMEFT scale Λ. Therefore, in this thesis we restrict attention to the $B-L$ preserving sector. Concretely, we work with the SMEFT truncated at dimension-6:

$$\mathcal{L}^{d\leq 6}_{\text{SMEFT}} = \mathcal{L}_{\text{SM}} + \sum_i c^{(6)}_i \, \frac{\mathcal{O}^{(6)}_i}{\Lambda^2} \, , \tag{1.59}$$

which will be the basis for the phenomenological analyses discussed in the following chapters.

In general, one can write down a large number of independent dimension-6 operators built from Standard Model fields. These include four-fermion interactions of the schematic form $(\bar{\psi}\psi)(\bar{\psi}\psi)$, purely bosonic structures like $(H^\dagger H)\,\Box(H^\dagger H)$ or $H^\dagger H \, B_{\mu\nu}B^{\mu\nu}$, and many others. However, not all such operators are truly independent. Operators that look different at the Lagrangian level can produce identical on-shell amplitudes and thus observable effects.

To obtain a physically meaningful parametrization of new physics effects, we need to work with a complete and non-redundant operator basis. Redundant operators can be systematically eliminated using integration by parts, field redefinitions (or classical equations of motion), and algebraic identities like Fierz identities and Dirac structure reduction. A well-known example of such a non-redundant operator set is the so-called Warsaw basis, introduced in [11], which provides a complete basis for the dimension-6 SMEFT Lagrangian. Overall, neglecting flavor indices we can count 63 operators (59 B and L conserving). They are shown explicitely in tables 1.2 and 1.3. When including the flavor structure, they amount to 1350 CP-even and 1149 CP-odd independent coefficients for the dimension-six operators.

$\boldsymbol{1:V^3}$	
Q_G	$f^{ABC}G^{A\nu}_{\mu}G^{B\rho}_{\nu}G^{C\mu}_{\rho}$
$Q_{\widetilde{G}}$	$f^{ABC}\widetilde{G}^{A\nu}_{\mu}G^{B\rho}_{\nu}G^{C\mu}_{\rho}$
Q_W	$\epsilon^{IJK}W^{I\nu}_{\mu}W^{J\rho}_{\nu}W^{K\mu}_{\rho}$
$Q_{\widetilde{W}}$	$\epsilon^{IJK}\widetilde{W}^{I\nu}_{\mu}W^{J\rho}_{\nu}W^{K\mu}_{\rho}$

$\boldsymbol{2:H^6}$	
Q_H	$(H^\dagger H)^3$

$\boldsymbol{3:H^4D^2}$	
$Q_{H\Box}$	$(H^\dagger H)\Box(H^\dagger H)$
Q_{HD}	$\left(H^\dagger D^\mu H\right)^*\left(H^\dagger D_\mu H\right)$

$\boldsymbol{5:\psi^2H^3+h.c.}$	
Q_{eH}	$(H^\dagger H)(\bar{l}_p e_r H)$
Q_{uH}	$(H^\dagger H)(\bar{q}_p u_r \widetilde{H})$
Q_{dH}	$(H^\dagger H)(\bar{q}_p d_r H)$

$\boldsymbol{4:V^2H^2}$	
Q_{HG}	$H^\dagger H\, G^A_{\mu\nu}G^{A\mu\nu}$
$Q_{H\widetilde{G}}$	$H^\dagger H\, \widetilde{G}^A_{\mu\nu}G^{A\mu\nu}$
Q_{HW}	$H^\dagger H\, W^I_{\mu\nu}W^{I\mu\nu}$
$Q_{H\widetilde{W}}$	$H^\dagger H\, \widetilde{W}^I_{\mu\nu}W^{I\mu\nu}$
Q_{HB}	$H^\dagger H\, B_{\mu\nu}B^{\mu\nu}$
$Q_{H\widetilde{B}}$	$H^\dagger H\, \widetilde{B}_{\mu\nu}B^{\mu\nu}$
Q_{HWB}	$H^\dagger\tau^I H\, W^I_{\mu\nu}B^{\mu\nu}$
$Q_{H\widetilde{W}B}$	$H^\dagger\tau^I H\, \widetilde{W}^I_{\mu\nu}B^{\mu\nu}$

$\boldsymbol{6:\psi^2VH+h.c.}$	
Q_{eW}	$(\bar{l}_p\sigma^{\mu\nu}\tau^I e_r)HW^I_{\mu\nu}$
Q_{eB}	$(\bar{l}_p\sigma^{\mu\nu}e_r)HB_{\mu\nu}$
Q_{uG}	$(\bar{q}_p\sigma^{\mu\nu}T^A u_r)\widetilde{H}\, G^A_{\mu\nu}$
Q_{uW}	$(\bar{q}_p\sigma^{\mu\nu}\tau^I u_r)\widetilde{H}\, W^I_{\mu\nu}$
Q_{uB}	$(\bar{q}_p\sigma^{\mu\nu}u_r)\widetilde{H}\, B_{\mu\nu}$
Q_{dG}	$(\bar{q}_p\sigma^{\mu\nu}T^A d_r)H\, G^A_{\mu\nu}$
Q_{dW}	$(\bar{q}_p\sigma^{\mu\nu}\tau^I d_r)H\, W^I_{\mu\nu}$
Q_{dB}	$(\bar{q}_p\sigma^{\mu\nu}d_r)H\, B_{\mu\nu}$

$\boldsymbol{7:\psi^2H^2D}$	
$Q^{(1)}_{Hl}$	$(H^\dagger i\overleftrightarrow{D}_\mu H)(\bar{l}_p\gamma^\mu l_r)$
$Q^{(3)}_{Hl}$	$(H^\dagger i\overleftrightarrow{D}^I_\mu H)(\bar{l}_p\tau^I\gamma^\mu l_r)$
Q_{He}	$(H^\dagger i\overleftrightarrow{D}_\mu H)(\bar{e}_p\gamma^\mu e_r)$
$Q^{(1)}_{Hq}$	$(H^\dagger i\overleftrightarrow{D}_\mu H)(\bar{q}_p\gamma^\mu q_r)$
$Q^{(3)}_{Hq}$	$(H^\dagger i\overleftrightarrow{D}^I_\mu H)(\bar{q}_p\tau^I\gamma^\mu q_r)$
Q_{Hu}	$(H^\dagger i\overleftrightarrow{D}_\mu H)(\bar{u}_p\gamma^\mu u_r)$
Q_{Hd}	$(H^\dagger i\overleftrightarrow{D}_\mu H)(\bar{d}_p\gamma^\mu d_r)$
$Q_{Hud}+h.c.$	$i(\widetilde{H}^\dagger D_\mu H)(\bar{u}_p\gamma^\mu d_r)$

Table 1.2: The dimension-six operators in SMEFT that involve at least one scalar H or vector V bosonic field. Operators with $+h.c.$ have Hermitian conjugates. The subscripts p, r, s, t are weak-eigenstate indices.

1.2.4 Flavor Symmetries in SMEFT

The proliferation of independent coefficients at dimension $d = 6$ does not imply that, in a bottom-up approach, we must remain fully agnostic and consider all 2499 operators. In fact, many of these couplings, as for example those contributing at tree level to flavor-violating observables, are already strongly constrained. In some cases, experimental bounds push the corresponding scale Λ above $\mathcal{O}(10^5\,\text{TeV})$. If we consider this as the scale of the whole EFT construction, then it would not be that interesting.

On the other hand, we know from the structure of the SM Yukawa couplings that flavor is highly non-generic in the renormalizable ($d = 4$) sector. It is therefore reasonable to assume an underlying non-generic structure that gives rise to approximate flavor symmetries also at

$\mathbf{8:(\bar{L}L)(\bar{L}L)}$	
Q_{ll}	$(\bar{l}_p\gamma^\mu l_r)(\bar{l}_s\gamma_\mu l_t)$
$Q_{qq}^{(1)}$	$(\bar{q}_p\gamma^\mu q_r)(\bar{q}_s\gamma_\mu q_t)$
$Q_{qq}^{(3)}$	$(\bar{q}_p\gamma^\mu \tau^I q_r)(\bar{q}_s\gamma_\mu \tau^I q_t)$
$Q_{lq}^{(1)}$	$(\bar{l}_p\gamma^\mu l_r)(\bar{q}_s\gamma_\mu q_t)$
$Q_{lq}^{(3)}$	$(\bar{l}_p\gamma^\mu \tau^I l_r)(\bar{q}_s\gamma_\mu \tau^I q_t)$

$\mathbf{8:(\bar{R}R)(\bar{R}R)}$	
Q_{ee}	$(\bar{e}_p\gamma^\mu e_r)(\bar{e}_s\gamma_\mu e_t)$
Q_{uu}	$(\bar{u}_p\gamma^\mu u_r)(\bar{u}_s\gamma_\mu u_t)$
Q_{dd}	$(\bar{d}_p\gamma^\mu d_r)(\bar{d}_s\gamma_\mu d_t)$
Q_{eu}	$(\bar{e}_p\gamma^\mu e_r)(\bar{u}_s\gamma_\mu u_t)$
Q_{ed}	$(\bar{e}_p\gamma^\mu e_r)(\bar{d}_s\gamma_\mu d_t)$
$Q_{ud}^{(1)}$	$(\bar{u}_p\gamma^\mu u_r)(\bar{d}_s\gamma_\mu d_t)$
$Q_{ud}^{(8)}$	$(\bar{u}_p\gamma^\mu T^A u_r)(\bar{d}_s\gamma_\mu T^A d_t)$

$\mathbf{8:(\bar{L}L)(\bar{R}R)}$	
Q_{le}	$(\bar{l}_p\gamma^\mu l_r)(\bar{e}_s\gamma_\mu e_t)$
Q_{lu}	$(\bar{l}_p\gamma^\mu l_r)(\bar{u}_s\gamma_\mu u_t)$
Q_{ld}	$(\bar{l}_p\gamma^\mu l_r)(\bar{d}_s\gamma_\mu d_t)$
Q_{qe}	$(\bar{q}_p\gamma^\mu q_r)(\bar{e}_s\gamma_\mu e_t)$
$Q_{qu}^{(1)}$	$(\bar{q}_p\gamma^\mu q_r)(\bar{u}_s\gamma_\mu u_t)$
$Q_{qu}^{(8)}$	$(\bar{q}_p\gamma^\mu T^A q_r)(\bar{u}_s\gamma_\mu T^A u_t)$
$Q_{qd}^{(1)}$	$(\bar{q}_p\gamma^\mu q_r)(\bar{d}_s\gamma_\mu d_t)$
$Q_{qd}^{(8)}$	$(\bar{q}_p\gamma^\mu T^A q_r)(\bar{d}_s\gamma_\mu T^A d_t)$

$\mathbf{8:(\bar{L}R)(\bar{R}L)+h.c.}$	
Q_{ledq}	$(\bar{l}_p^j e_r)(\bar{d}_s q_{tj})$

$\mathbf{8:(\bar{L}R)(\bar{L}R)+h.c.}$	
$Q_{quqd}^{(1)}$	$(\bar{q}_p^j u_r)\epsilon_{jk}(\bar{q}_s^k d_t)$
$Q_{quqd}^{(8)}$	$(\bar{q}_p^j T^A u_r)\epsilon_{jk}(\bar{q}_s^k T^A d_t)$
$Q_{lequ}^{(1)}$	$(\bar{l}_p^j e_r)\epsilon_{jk}(\bar{q}_s^k u_t)$
$Q_{lequ}^{(3)}$	$(\bar{l}_p^j \sigma_{\mu\nu} e_r)\epsilon_{jk}(\bar{q}_s^k \sigma^{\mu\nu} u_t)$

$\mathbf{\Delta B=\Delta L=1+h.c.}$	
Q_{duql}	$\epsilon^{\alpha\beta\gamma}\epsilon^{ij}(d_{\alpha p}^T C u_{\beta r})(q_{\gamma is}^T C l_{jt})$
Q_{qque}	$\epsilon^{\alpha\beta\gamma}\epsilon^{ij}(q_{\alpha ip}^T C q_{\beta jr})(u_{\gamma s}^T C e_t)$
Q_{qqql}	$\epsilon^{\alpha\beta\gamma}\epsilon^{i\ell}\epsilon^{jk}(q_{\alpha ip}^T C q_{\beta jr})(q_{\gamma ks}^T C l_{\ell t})$
Q_{duue}	$\epsilon^{\alpha\beta\gamma}(d_{\alpha p}^T C u_{\beta r})(u_{\gamma s}^T C e_t)$

Table 1.3: The dimension-six four-fermion operators in SMEFT. Operators with $+\,h.c.$ have Hermitian conjugates. The subscripts p, r, s, t are weak-eigenstate indices.

the level of $d = 6$ operators and beyond. These assumptions allow for a significant reduction in the number of relevant operators, making the EFT construction more predictive and phenomenologically interesting. One possibility to organise the EFT expansion is to think about the approximate flavor symmetries discussed in section 1.1.4. With this respect, only 47 dimension-6 operators (including flavor indices) are consistent with exact $\mathrm{U}(3)^5$ symmetry. All other dimension-6 operators can be viewed as additional sources of flavor symmetry breaking.

A popular and systematic approach to encode this structure is the framework of *Minimal Flavor Violation* (MFV), which assumes that the SM Yukawa couplings are the only sources of $\mathrm{U}(3)^5$ breaking, even beyond the renormalizable level. In this approach, the exact $\mathrm{U}(3)^5$-symmetric limit corresponds to leading order in a symmetry-breaking expansion. Going beyond this order, the Yukawa matrices are treated as spurion fields, i.e. non-dynamical background fields transforming under $\mathcal{G}_f$ as:

$$\begin{aligned} Y_u &\sim (\mathbf{1}, \mathbf{3}, \mathbf{1}, \overline{\mathbf{3}}, \mathbf{1})\,, \\ Y_d &\sim (\mathbf{1}, \mathbf{3}, \mathbf{1}, \mathbf{1}, \overline{\mathbf{3}})\,, \\ Y_e &\sim (\mathbf{3}, \mathbf{1}, \overline{\mathbf{3}}, \mathbf{1}, \mathbf{1})\,. \end{aligned} \tag{1.60}$$

With these transformation properties, the SM Yukawa sector becomes formally invariant under $\mathcal{G}_f$. Higher-dimensional operators can then be organized as a power series in the spurion fields, ensuring formal $\mathcal{G}_f$ invariance of the full EFT. For instance, fermion bilinears

can be constructed as

$$q_i\gamma^\mu q_i\,, \quad q_i(Y_uY_u^\dagger)_{ij}\gamma^\mu q_j\,, \quad q_i(Y_dY_d^\dagger)_{ij}\gamma^\mu q_j\,, \ldots \tag{1.61}$$

where $i,j=1,2,3$ denote flavor indices. This approach, motivated by the observed structure of flavor in the SM, leads to a significant reduction in the number of independent operators, overall by at least two orders of magnitude.

Another well-motivated idea is to impose a $\mathrm{U}(2)^5$ flavor symmetry, a subgroup of the full $\mathcal{G}_f$, which treats the first two light generations as indistinguishable and distinguishes them from the third generation. This setup effectively captures a broad class of Standard Model extensions in which the third generation plays a special role, as is often the case in theories addressing the hierarchy of fermion masses or flavor anomalies.

In this framework, the Yukawa structures are reproduced by introducing a minimal set of symmetry-breaking spurions. These spurions are sufficient to organize the expansion of the SMEFT Lagrangian in a way consistent with the observed fermion masses and mixings. A minimal and commonly used set includes:

$$\begin{aligned} V_\ell &\sim (\mathbf{2},\mathbf{1},\mathbf{1},\mathbf{1},\mathbf{1})\,, \qquad V_q \sim (\mathbf{1},\mathbf{2},\mathbf{1},\mathbf{1},\mathbf{1})\,, \\ \Delta_e &\sim (\mathbf{2},\mathbf{1},\overline{\mathbf{2}},\mathbf{1},\mathbf{1})\,, \quad \Delta_{u(d)} \sim (\mathbf{1},\mathbf{2},\mathbf{1},\overline{\mathbf{2}}(\mathbf{1}),\mathbf{1}(\overline{\mathbf{2}}))\,. \end{aligned} \tag{1.62}$$

Here, the spurions V_q and V_ℓ parametrize the mixing between the light generations and the third one, while the Δ spurions account for the breaking of the residual $\mathrm{SU}(2)$ flavor symmetry within the light generations. Within this framework, fermion bilinears can be systematically expanded using the spurions. Some representative examples are:

$$\bar{q}_3\gamma^\mu q_3\,, \quad \bar{q}_i\gamma^\mu q_i\,, \quad \bar{q}_i(V_q)_i\gamma^\mu q_3 + \text{h.c.}\,, \quad \bar{q}_i(V_q)_i\gamma^\mu(V_q^\dagger)_j q_j\,, \ldots \tag{1.63}$$

where $i=1,2$ now runs only over the first two generations. We will not elaborate further on this formalism here, as it will be applied explicitly in the following chapters. For complete reviews and systematic treatments of the $\mathrm{U}(2)^n$ approach and its implications, we refer the reader to [12, 13].

A final comment is in order regarding basis choices in flavor space. In general, through appropriate redefinitions of the fermion fields and the Yukawa matrices, one can always choose a flavor basis in which the Yukawa couplings are entirely expressed in terms of fermion masses and the CKM matrix. Two commonly adopted choices are the *down-type basis* and the *up-type basis*. In the former case, the down-type quark and charged lepton Yukawas are diagonal:

$$\begin{aligned} Y_e &= \mathrm{diag}(y_e,y_\mu,y_\tau)\,, \quad Y_d = \mathrm{diag}(y_d,y_s,y_b)\,, \\ Y_u &= V_{\mathrm{CKM}}^\dagger\cdot\mathrm{diag}(y_u,y_c,y_t)\,. \end{aligned} \tag{1.64}$$

In contrast, in the up-type basis the up-type quark Yukawa matrix is diagonal:

$$\begin{aligned} Y_e &= \mathrm{diag}(y_e,y_\mu,y_\tau)\,, \quad Y_u = \mathrm{diag}(y_u,y_c,y_t)\,, \\ Y_d &= V_{\mathrm{CKM}}\cdot\mathrm{diag}(y_d,y_s,y_b)\,. \end{aligned} \tag{1.65}$$

In either of these bases, the quark doublets q^i can be written in terms of mass eigenstates as:

$$q^i = \begin{pmatrix} u_L^i \\ V_{ij}d_L^j \end{pmatrix}\,, \quad q^i = \begin{pmatrix} V_{ji}^* u_L^j \\ d_L^i \end{pmatrix}\,, \tag{1.66}$$

in the down- and up-type bases respectively.

1.3 Early Universe toolkit

The predictive power of the Standard Model extends well beyond collider experiments and terrestrial observations. Its particle content plays a central role in cosmology, where it shapes the thermal history of the early universe. Indeed, many key features of modern cosmological observations, from primordial nucleosynthesis to the cosmic microwave background, can be successfully described using the known particle spectrum and interactions of the SM. In general, the early universe provides a unique laboratory for probing physics at high energies, testing the SM content and offering complementary hints to physics Beyond the SM.

In this section, we will not attempt a discussion of primordial inflation, nor will we explore the full complexity of the universe's earliest moments. Instead, we will focus on the post-inflationary evolution of the thermal bath and discuss the cosmological history of the SM species as the universe expands and cools. Following this thermal history, we establish the basic picture of how the known (and unkown) particles interact, decouple, and contribute to the energy and entropy budget of the universe, providing a complete simple toolkit of the early universe physics. These concepts will be essential and extensively used in chapter 4, when discussing non-standard thermal histories and the freeze-out of Dark Matter candidates in these scenarios.

1.3.1 Friedmann equations

The starting point to understand the large-scale evolution of the Universe are the Einstein's field equations, which relate the curvature of spacetime to its matter and energy content:

$$G_{\mu\nu} + \Lambda g_{\mu\nu} = 8\pi G_N \, T_{\mu\nu} \, . \tag{1.67}$$

Here, $G_{\mu\nu}$ is the Einstein tensor encoding the curvature of spacetime, Λ is the cosmological constant and $T_{\mu\nu}$ is the total stress-energy tensor describing the distribution of matter and energy components. Under the assumption of an homogeneous and isotropic universe, it can be shown that the general solutions to the Einstein equations take the form of the Friedmann–Robertson–Walker (FRW) metric,

$$ds^2 = dt^2 - a(t)^2 \left(\frac{dr^2}{1 - \kappa r^2} + r^2 d\Omega^2 \right) , \tag{1.68}$$

where $a(t)$ is the scale factor and κ characterizes the spatial curvature ($\kappa = 0, \pm 1$, corresponding to flat, closed, and open universe, respectively), r is just a radial coordinate while $d\Omega$ represents the angular part of the metric. Treating the contents of the Universe as a perfect fluid with energy density ρ and pressure P, the stress-energy tensor can be simply written as

$$T^{\mu\nu} = (\rho + P) \, u^\mu u^\nu - P \, g^{\mu\nu} \, , \tag{1.69}$$

where u is the 4-velocity of the fluid. We stress that ρ and P are the total energy and pressure densities, which take into account all the components of the universe: matter, radiation, etc. Substituting these expressions for the stress energy tensor and the FRW metric into Einstein's

equations then leads to the well-known two Friedmann equations:

$$\left(\frac{\dot{a}}{a}\right)^2 = \frac{8\pi G_N}{3}\rho - \frac{\kappa}{a^2} + \frac{\Lambda}{3}\,, \tag{1.70}$$

$$\frac{\ddot{a}}{a} = -\frac{4\pi G_N}{3}(\rho + 3P) + \frac{\Lambda}{3}\,, \tag{1.71}$$

which describe the evolution of the scale factor $a(t)$ and thus determine the expansion history of the Universe. As customary, the expansion rate of the Universe can be described in terms of the Hubble parameter, defined as $H(t) \equiv \dot{a}(t)/a(t)$.

Using the conservation of the stress-energy tensor $\nabla_\mu T^{\mu\nu} = 0$, one can derive the continuity equation

$$\dot{\rho} + 3\frac{\dot{a}}{a}(\rho + P) = \dot{\rho} + 3H(\rho + P) = 0\,, \tag{1.72}$$

which drives the dilution of the energy as the Universe expands. In general, different components of the universe are characterized by different equations of state, which relate the pressure and the density. However, for any given equation of state $P = \omega\rho$, it is straightforward to find the general solution to the continuity equation

$$\rho \propto a^{-3(1+w)}\,. \tag{1.73}$$

Depending on the value of w, it describes different types of energy, for example:

- $w = 1/3$: this describes pure radiation. The energy density of radiation scales as $\rho \propto a^{-4}$.
- $w = 0$: this describes non-relativistic matter (dust), where the pressure is negligible compared to the energy density, $P \approx 0$. The energy density of matter scales as $\rho \propto a^{-3}$.
- $w = -1$: this describes a dark energy component (cosmological constant), the pressure is $P = -\rho$, where $\rho \propto$ const. The dark energy density remains constant as the Universe expands.

In principle, ω could take other values between -1 and $+1$, but we do not consider other cases here. We just mention that $\omega = -1/3$ corresponds to the case of a curvature component, as it reproduces the scaling that characterizes the curvature term in the first Friedmann equation in (1.70). However, we measure a nearly flat space $\kappa \approx 0$.

According to eq. (1.70), the Hubble parameter $H(t)$ evolves differently depending on what is the dominant component of the Universe. In particular, we can write the contributions from curvature and cosmological constant as

$$\rho_\kappa = -\frac{3\kappa}{8\pi G_N a^2}\,, \qquad \rho_\Lambda = \frac{\Lambda}{8\pi G_N}\,, \tag{1.74}$$

so that eq. (1.70) can be recast as follows

$$H^2 = \sum_i \frac{8\pi G_N}{3}\rho_i\,, \tag{1.75}$$

Given the dependence of each component on the universe scale factor $a(t)$, as in eq. (1.73), we can write the Hubble rate at any time t as a function of the energy components and the Hubble rate that we observe today:

$$H^2 = H_0^2 \left(\Omega_{0,r}\, a^{-4} + \Omega_{0,m}\, a^{-3} + \Omega_{0,\kappa}\, a^{-2} + \Omega_{0,\Lambda}\, a^{0} \right), \tag{1.76}$$

where we have defined the ratio of the energy densities with the critical energy density ρ_c:

$$\Omega_{0,i} \equiv \frac{\rho_i}{\rho_c}, \qquad \rho_c \equiv \frac{3H_0^2}{8\pi G_N}, \tag{1.77}$$

and where the subscript '0' refers to the present epoch, having normalized $a_0 = 1$. The precise value of H_0 is still under debate, but it is measured to be roughly $H_0 \sim 70\ \mathrm{km\,s^{-1}Mpc^{-1}}$. As clear from eq. (1.76), the sum of all the fractional energy densities is $\Omega_{\rm tot} = 1$. According to the most recent cosmological observations, the energy budget in our Universe is approximately:

$$\Omega_{0,\Lambda} \simeq 0.68\,, \quad \Omega_{0,m} \simeq 0.32\,, \tag{1.78}$$

with a very small radiation component and negligible curvature κ. Remarkably, we observe that a large fraction of the matter component $\Omega_{0,m}$ is actually made of Dark Matter, i.e. a fraction of matter that is not involved in electromagnetic interactions. Its presence is inferred only through its gravitational effects on visible matter, light, and the large-scale structure of the Universe. The current abundance of Dark Matter is about 5 times larger than the visible Baryon abundance, precisely

$$\Omega_{\rm DM} \simeq 0.27\,, \quad \Omega_b \simeq 0.05\,. \tag{1.79}$$

Despite playing a fundamental role in the formation and evolution of cosmic structures, the Standard Model lacks of a DM candidate. This is indeed a strong need for physics beyond the SM.

In the following section, and in most of this thesis, we will be interested in the early stages of our universe when the energy was dominated by the radiation energy density of the thermal bath, scaling as a^{-4}. In chapter 4, we will also discuss some non-standard thermal histories featuring the presence of a large cosmological constant component.

1.3.2 Thermodynamics at equilibrium

We focus on the thermal history of the Universe starting after reheating, once the Standard Model relativistic plasma has been established and builds the dominant energy componant of the universe. At this stage, all particle species are in thermal equilibrium, which is ensured by their interaction rates $\Gamma_{\rm int}$ being much larger than the Hubble expansion rate H, so that interactions occur on timescales much shorter than the cosmic expansion. Indeed, we can easily estimate by dimensional analysis that the thermal average cross section, in the high temperature limit, scales as $\sigma \sim \alpha^2/T^2$ while the number density of particles scales as $n \sim T^3$. Therefore, we can compute the ratio $\Gamma_{\rm int}/H \sim n\sigma/H \sim \alpha^2 m_{\rm Pl}/T$, implying that equilibrium is ensured for temperatures lower than the Hubble scale (but much larger than the SM mass scales).

As the Universe expands and cools, $\Gamma_{\rm int}$ generally decreases faster than H. Eventually, for each particle species, the condition $\Gamma_{\rm int} \approx H$ is satisfied, and that species decouples from

the thermal bath. Since different particles have different interaction rates, they freeze out at different times. To describe this process quantitatively, it is essential to first establish the thermodynamic properties of the plasma in thermal equilibrium, which will serve as the baseline for analyzing the subsequent decoupling of each species.

At the microscopic level, when a system of particles is in kinetic equilibrium, the number of particles per unit volume in phase space is determined by the equilibrium distribution function. According to standard statistical mechanics, this is given by

$$f_i^{\rm eq}(p) = \frac{1}{\exp\left(\frac{E_i-\mu_i}{T_i}\right) \pm 1}, \qquad n_i^{\rm eq} = \frac{g_i}{(2\pi)^3}\int d^3p\, f_i^{\rm eq}(p), \tag{1.80}$$

where $E_i = \sqrt{p^2+m_i^2}$ is the particle energy, T_i denotes the temperature of species i, and μ_i its chemical potential. The $+(-)$ sign applies to fermions (bosons), and g_i denotes the number of internal degrees of freedom (spin, color, etc). Since the chemical potentials in the early universe are generally negligible, we will set $\mu_i \simeq 0$ in what follows. For each particle species, we can then define the corresponding energy density and pressure as

$$\rho_i = \frac{g_i}{(2\pi)^3}\int d^3p\, f_i^{\rm eq}(p)\, E_i(p)\,, \qquad P_i = \frac{g_i}{(2\pi)^3}\int d^3p\, f_i^{\rm eq}(p)\, \frac{p^2}{3E_i(p)}\,, \tag{1.81}$$

Two limiting regimes are particularly relevant for cosmology. These are determined by the relative size of the particle's mass m_i and its temperature T_i:

- **Non-relativistic limit** ($m_i \gg T_i$):

$$\begin{aligned} n_i &= g_i \left(\frac{m_i T_i}{2\pi}\right)^{3/2} e^{-m_i/T_i}\,, \\ \rho_i &= m_i\, n_i\,, \qquad P_i = T_i\, n_i\,, \end{aligned} \tag{1.82}$$

- **Relativistic limit** ($m_i \ll T_i$):

$$\begin{aligned} n_i &= c_i\, g_i\, \frac{\zeta(3)}{\pi^2}\, T_i^3\,, \\ \rho_i &= d_i\, g_i\, \frac{\pi^2}{30}\, T_i^4\,, \qquad P_i = \frac{\rho_i}{3}\,, \end{aligned} \tag{1.83}$$

where $c_i = 1\,(3/4)$ and $d_i = 1\,(7/8)$ for bosons (fermions). When the particles in the plasma are in thermal (kinetic and chemical) equilibrium, they all share the same temperature T. Therefore, it is often useful to introduce the total energy density of all relativistic species as

$$\rho_{\rm rad}(T) = g_\star(T)\, \frac{\pi^2}{30}\, T^4\,, \tag{1.84}$$

with the effective number of degrees of freedom defined by

$$g_\star(T) = \sum_{i\in B} g_i \left(\frac{T_i}{T}\right)^4 + \frac{7}{8}\sum_{j\in F} g_j \left(\frac{T_j}{T}\right)^4\,. \tag{1.85}$$

Here, the sums run over all relativistic bosonic and fermionic species, taking into account both relativistic particles in thermal equilibrium and relativistic species that have decoupled and may have a temperature $T_i \neq T$. As an example, we can compute the relativistic degrees of freedom for the SM at $T \geq 100$ GeV $\gtrsim m_W$, where all the species are non-decoupled, i.e. all the $T_i = T$, then

$$\begin{aligned} g_\star^{\rm SM}(T \gg m_W) \;=\; & \underbrace{2\cdot 8}_{\text{gluons}} \;+\; \underbrace{3\cdot 3}_{W^\pm,Z} \;+\; \underbrace{2}_{A} \;+\; \underbrace{1}_{h} \;+ \\ & + \frac{7}{8}\left(\underbrace{4\cdot 6\cdot 3}_{\text{quarks}} \;+\; \underbrace{4\cdot 3}_{\text{leptons}} \;+\; \underbrace{2\cdot 3}_{\text{neutrinos}}\right) \;=\; 106.75\,, \end{aligned} \tag{1.86}$$

Having established the scaling of the energy density with temperature, we can also write the corresponding Hubble rate as a function of the bath temperature. Substituting $\rho_{\rm rad}(T)$ into the first Friedmann equation in eq. (1.70) yields:

$$H(T) = \sqrt{\frac{\pi^2}{90}\, g_\star(T)}\, \frac{T^2}{m_{\rm Pl}}\,. \tag{1.87}$$

where $m_{\rm Pl} \equiv (8\pi)^{-1/2} M_{\rm Pl} = (8\pi G_N)^{-1/2} \simeq 2.4 \times 10^{18}\,\text{GeV}$ is the reduced Planck mass.

Another important quantity describing the evolution of the Universe is the entropy density. Specifically, we define the entropy density as

$$s \equiv \frac{S}{V} = \frac{\rho + P}{T} = \frac{2\pi^2}{45}\, g_{\star,s}(T)\, T^3\,, \tag{1.88}$$

where

$$g_{\star,s}(T) = \sum_{i\in B} g_i \left(\frac{T_i}{T}\right)^3 + \frac{7}{8}\sum_{j\in F} g_j \left(\frac{T_j}{T}\right)^3\,. \tag{1.89}$$

In general, $g_\star \neq g_{\star,s}$, except in the special case where all relativistic species are in thermal equilibrium and thus share the same temperature. The conservation of the total entropy S implies that $s \propto a^{-3}$, and thus it is often combined with the number density n_i in defining the yield:

$$Y_i \equiv \frac{n_i}{s}\,, \tag{1.90}$$

that remains constant as long as particles of type i are neither produced or destroyed (nor entropy injections in the bath take place). This is the case of the baryon asymmetry $Y_B \equiv (n_B - n_{\bar B})/s$.

1.3.3 Freeze-out and Dark Matter

If equilibrium had persisted until the present epoch, the Universe would consist almost entirely of photons, as all massive species would be exponentially Boltzmann suppressed unless protected by additional symmetries or conserved charges. Understanding how deviations from equilibrium lead to the *freeze-out* of massive particles is therefore essential.

As discussed earlier, a given particle species drops out of equilibrium when its interaction rate $\Gamma_{\rm int}(T)$ falls below the cosmic expansion rate $H(T)$. To illustrate this, let us focus on electroweak interactions. Well below the electroweak scale, gauge bosons are heavy, and the

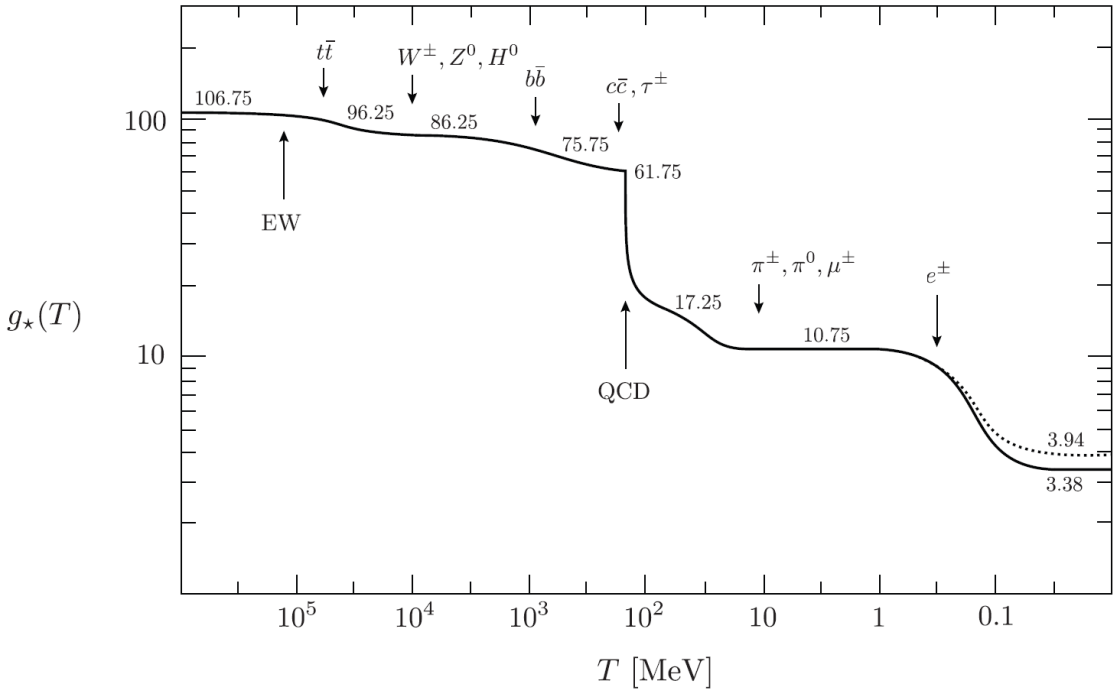


Figure 1.3: Number of total degrees of freedom g_* of the Standard Model as a function of temperature. The entropy effective number g_{s*} becomes different below the electron positron annihilation, after neutrino freeze-out. Image taken from [14].

cross section for weak processes can be estimated as $\sigma \sim (\alpha/m_V^2)^2\, T^2$, yielding an interaction rate $\Gamma_{\rm int} \sim n\,\sigma \sim \alpha^2 T^5/m_V^4$. Comparing this to the Hubble rate,

$$\frac{\Gamma_{\rm int}}{H} \sim \frac{\alpha^2\, m_{\rm Pl}\, T^3}{m_V^4} \sim \left(\frac{T}{1\ \text{MeV}}\right)^3 . \tag{1.91}$$

This implies that neutrinos, which only couple via weak interactions, decouple at a temperature of order $T \sim 1$ MeV, in good agreement with the more refined value $T_{\rm dec} \simeq 0.8$ MeV.

More generally, as the Universe expands and cools, different species decouple sequentially, reducing the effective number of relativistic degrees of freedom. This process is sketched in fig. 1.3, where we show the Standard Model effective degrees of freedom in the energy density ($g_\star$) and in the entropy ($g_{\star,s}$), following the evolution of the universe. A convenient and really quantitative way to describe the departure from equilibrium is through the Boltzmann equation, which governs the time evolution of the number density n_i of a particle species i:

$$\frac{1}{a^3}\frac{d(n_i a^3)}{dt} = C(\{n_j\})\,, \tag{1.92}$$

where the right-hand side, referred to as the collision term, encodes all the interactions that produce or destroy particles i. In the absence of interactions, the collision term vanishes and the comoving number density is conserved.

For example, for a generic $2 \to 2$ process involving four different species, we can write

$$\frac{1}{a^3}\frac{d(n_i a^3)}{dt} = -\langle\sigma v\rangle \left[n_1 n_2 - \left(\frac{n_1 n_2}{n_3 n_4}\right)_{\rm eq} n_3 n_4\right], \tag{1.93}$$

where $\langle\sigma v\rangle$ is the thermally averaged cross section. The structure of the collision term is fixed by requiring that it vanishes in equilibrium. In the special case of scatterings like $X_{\rm DM}\,\bar{X}_{\rm DM} \to \ell\,\bar{\ell}$, relevant for the discussion of freeze-out in many Dark Matter models, we can assume $n_1 = n_2 = n$, $n_3 = n_4 = n_\ell$, and that the light species ℓ stays in equilibrium ($n_\ell \simeq n_\ell^{\rm eq}$). The Boltzmann equation then simplifies to

$$\frac{1}{a^3}\frac{d(na^3)}{dt} = -\langle\sigma v\rangle\left(n^2 - n_{\rm eq}^2\right)\,, \tag{1.94}$$

or, in terms of the yield $Y = n/s$,

$$\frac{dY}{dt} = -s\langle\sigma v\rangle\left(Y^2 - Y_{\rm eq}^2\right)\,. \tag{1.95}$$

To make the evolution more transparent, it is conventional to introduce the dimensionless variable $x \equiv m/T$, where m is the particle's mass and T is the bath temperature. In terms of x, the Boltzmann equation becomes

$$\frac{dY}{dx} = \frac{\langle\sigma v\rangle\, s}{xH}\left(Y^2 - Y_{\rm eq}^2\right)\,. \tag{1.96}$$

During the radiation-dominated era, $H \propto T^2/m_{\rm Pl}$, so this can be rewritten as

$$\frac{dY}{dx} = \frac{\lambda}{x^2}\left(Y^2 - Y_{\rm eq}^2\right), \qquad \lambda \equiv \frac{2\pi^2}{45}\,g_{\star,s}\,\frac{m^3\langle\sigma v\rangle}{H(m)}\,, \tag{1.97}$$

where $g_{\star,s}$ denotes the effective number of entropic degrees of freedom and, in principle, depends on x. Eq. 1.97 can be solved numerically for any value of λ. Some examples are shown in fig. 1.4.

As clear from the plot, the larger the cross secton σ, hence λ, the longer the particle species under examination stays in thermal equilibrium with the bath before decoupling, as expected. Thus, the first consequence of eq. (1.97) is that the final yield is smaller for larger couplings and, viceversa, larger for smaller couplings (as long as our working assumptions, like being in a radiation dominated universe, are satisfied).

Even though there is no analytic solution to the Boltzmann equation, it is possible to derive some approximate analytic solutions in two opposite regimes: the *Hot Relic* limit and the *Cold Relic* limit. The former correspond to the case in which freeze-out occurs when the particle is still relativistic. This scenario can occur when the particle is very weakly coupled to the plasma. In other words, the condition $n\langle\sigma v\rangle < H$ is satisfied well before $n(T)$ enters the non-relativistic suppressed regime of the Boltzmann distribution, since the smallness of the l.h.s. is due to a small thermal cross section. In this case, we simply get:

$$Y_\infty = Y_{\rm EQ}\,(x_f) = 0.278 g_{\rm DM}/g_{*s}\,(x_f) \quad (x_f \lesssim 3)\,, \tag{1.98}$$

where x_f is the value of x at freeze-out. On the other hand, the Cold Relic scenario correspond to freeze-out occuring when the particle is in the non-relativistic regime. In this case, it can be proved that the final yield is well approximated by:

$$Y_\infty = \frac{3.79(n+1)x_f^{n+1}}{\left(g_{\star,s}/g_\star^{1/2}\right)M_{\rm Pl} m\sigma_0} \quad (x_f \gtrsim 3)\,, \tag{1.99}$$

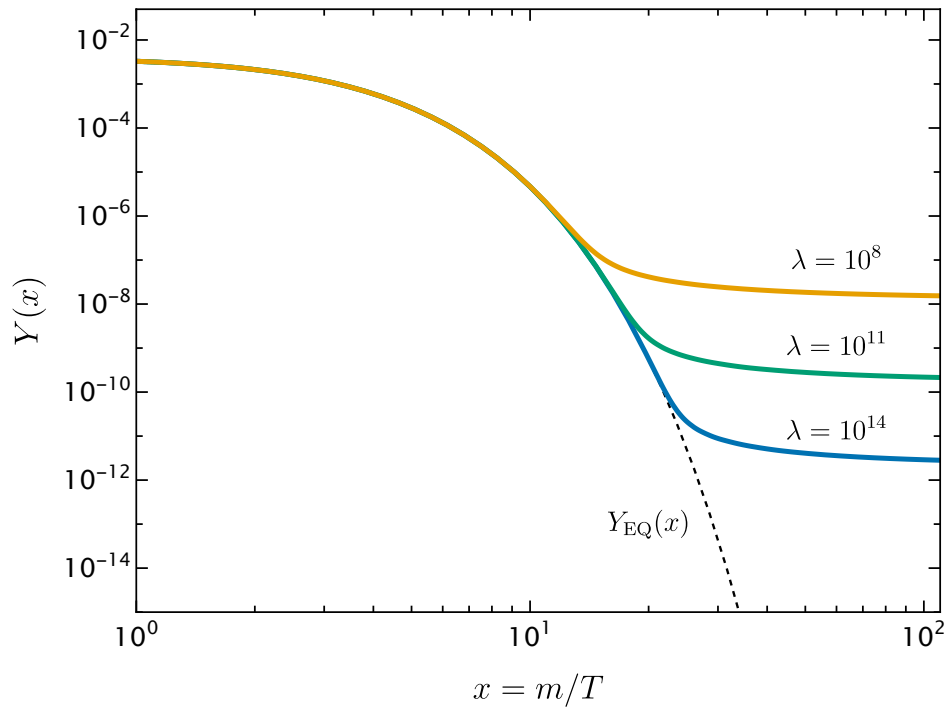


Figure 1.4: Dark Matter Freeze Out for several values of the parameter λ. The dashed line is the equilibrium Boltzmann distribution. As clear from the three solid curves, larger cross section (larger λ) allows the particles to stay in equilibrium in the plasma for longer times, hence the smaller freeze-out relic abundance.

where σ_0 is the first term in the expansion of the thermally averaged cross section $\langle\sigma v\rangle \simeq \sigma_0 x^{-n}(1-bx^{-m})$, where $n = 0(1)$ correspond to s(p)-wave annihilation, and additional coefficients depend on the specific model. The moment at which freeze-out occurs typically scales as $x_f \propto \log\lambda$ for cold relic.

Finally, if we want to compare the freeze-out yield to the Dark Matter abundance that we observe today, we still need to multiply Y_∞ by the present entropy density $s_0 = 2.97\,\mathrm{cm}^{-3}$, by the mass of the species m, and divide it by the critical density ρ_c to obtain the fractional component $\Omega_{\rm DM}$. Putting all together we get, respectively for Hot and Cold relics:

$$\begin{aligned}\Omega^{\rm hot}_{\rm DM}h^2 &\simeq 0.075\cdot\left(\frac{m}{\rm eV}\right)\cdot\left(\frac{g_{\rm DM}}{g_{\star s}}\right)\\ \Omega^{\rm cold}_{\rm DM}h^2 &\simeq 1.07\cdot 10^9\frac{(n+1)x_f^{n+1}\mathrm{GeV}^{-1}}{\left(g_{\star s}/g_*^{1/2}\right)M_{\rm Pl}\sigma_0}.\end{aligned} \tag{1.100}$$

These formulae will be used in chapter 4, where we will discuss the interplay of non-standard cosmologies driven by BSM (visible) physics on dark sectors and the dynamics of Dark Matter particles.

Chapter 2

Indirect Constraints on New Physics Scenarios

The structure of the flavor sector described in sections 1.1.2 and 1.1.3 leads to a rich set of phenomenological implications. First, due to its large mass - or equivalently, its $\mathcal{O}(1)$ Yukawa coupling to the Higgs — the top quark plays a special role both within the Standard Model and in many of its extensions. In the SM, thanks to the GIM mechanism [15], the top quark provides dominant loop contributions to many low-energy flavor-changing neutral-current processes. It also induces some of the leading radiative corrections in the electroweak sector, drives the renormalization group evolution of the Higgs quartic coupling, and plays a central role in the (meta)stability of the Higgs potential.

The top quark also generates the largest corrections to the Higgs mass, therefore going beyond the SM it is a crucial actor in all New Physics scenarios that aim at addressing the naturalness problem of the EW scale. For instance, the so-called top partners are expected to be some of the lightest new particles in such scenarios, both in supersymmetric (stops) and in composite Higgs (vectorlike top partners) models. This expectation is reinforced by the fact that experimental constraints from direct searches of these particles are generally weaker than for the partners of the lighter quarks.

Furthermore, due to the large top mass, its couplings to the EW gauge bosons are still not tightly constrained, allowing the possibility of sizable NP effects in this sector. For all these reason, many NP models predict new states that couple predominantly to the top quark. See Ref. [16] for a recent review.

In contrast, the remarkable accuracy of SM predictions and the absence of significant deviations in flavor-changing processes involving light quarks suggest that the new dynamics may couple more weakly to the first two generations of fermions. This experimental scenario often finds consistency with models that are approximately invariant under $U(2)^5$ flavor symmetries acting only on the light fermions, as discussed in section 1.1.4.

In general, if the new degrees of freedom are heavy, their low-energy effects can be described using effective operators within the SMEFT framework, that we introduced in section 1.2.3. Therefore, in this chapter, we focus on the EFT analysis of scenarios like the ones described above. First, in section 2.1, we present a comprehensive study of all dimension-6 operators involving top quarks, deriving constraints from a wide set of low-energy observables and comparing them to bounds from high-energy collider searches. This discussion is mostly based on [1].

The assumption that NP predominantly couples to the third generation is further explored in sections 2.2 and 2.3, where we carefully examine the implications of recent measurements of rare di-neutrino modes, $B \to K\bar{\nu}\nu$ and $K \to \pi\bar{\nu}\nu$. In detail, in section 2.2, we show that the third-generation-philic framework naturally emerges from the general hypothesis of rank-one flavor violation. Then, in section 2.3, we discuss in more detail the breaking structure of an approximate $U(2)_q$ symmetry via a minimal set of parameters, consistent with a broad set of observables, and assess the near-future impact of dineutrino modes on such NP scenarios. These analyses are based on refs. [2, 4].

2.1 Constraints on top quark operators

2.1.1 EFT setup

We assume that at the UV scale Λ (we fix $\Lambda = 1$ TeV for concreteness) only effective operators involving the top quark are generated at the tree level and we study the indirect constraints that can be obtained on the corresponding coefficients by considering the effects they have on a large set of low energy observables, comparing these to the direct constraints that have been obtained by studying top quark processes at the LHC.

We work in the Standard Model Effective Field Theory (SMEFT) and choose the Warsaw basis [11] of dimension-six operators:[1]

$$\mathcal{L}_{\text{SMEFT}} = \mathcal{L}_{\text{SM}} + \sum_i \frac{c_i^{(6)}}{\Lambda^2} \mathcal{O}_i^{(6)} + \dots \,, \tag{2.1}$$

that we discussed in section 1.2.3. As stated above, we focus on top-quark operators, i.e. operators that among quarks involve only the third generation quark doublet q^3 and right-handed top u^3, assuming that all other vanish. The lepton sector is instead left completely general, since we want to consider also tests of lepton flavor universality (LFU) and lepton flavor violation (LFV). The set of SMEFT operators is then reduced to the list in table 2.1. In the following, the superscripts '3' for quark indices in SMEFT coefficients are omitted, as they are in the Table. We work with the rescaled coefficients $C_i \equiv \frac{c_i^{(6)}}{\Lambda^2}$ in TeV^{-2} units.

While in the limit where only the top quark mass is considered the gauge and mass bases are the same, we want to describe also the mixing with light generations via the Cabibbo-Kobayashi-Maskawa (CKM) matrix and therefore we must consider all quark masses. In this case, the flavor basis at the scale Λ is in general different than the quark mass bases, forcing us to make a flavor assumption at the high scale. Two common choices in the literature are the up or down quark mass bases. If only the operators listed above are considered, then the results of the fit will of course depend on this choice.[2] Since we are assuming that new physics is mostly coupled to the top quark, it is logical to work in the up-quark and charged-lepton mass basis, where $q^i = (u_L^i,\, V_{ij} d_L^j)$, $l^\alpha = (\nu_L^\alpha,\, \ell_L^\alpha)$, and V is the CKM matrix. This will induce CKM-suppressed operators involving first and second generation left-handed down quarks.

We aim at deriving indirect constraints on all these operators by considering a large set of low-energy observables in a global analysis. We include rare B-meson and kaon decays, meson mixing observables, all the processes used to measure the Cabibbo angle, anomalous magnetic moments of the electron and muon, lepton flavor universality tests in charged-current lepton decays, charged lepton flavor-violating processes, and precision electroweak and Higgs measurements.

Several groups studied indirect constraints on top anomalous interactions or top quark operators. Refs. [21–25] analyzed anomalous top couplings to W and Z bosons, and top quark flavor violation, considering rare meson decays and electroweak precision data. Dipole

[1] We assume baryon and lepton number conservation at the scale Λ.

[2] One alternative could be to introduce a consistent flavor symmetry, for instance $U(2)_q \times U(2)_u \times U(2)_d$ [17–19], and symmetry-breaking spurions, and consider then also the operators suppressed by the spurions, see e.g. Ref. [20]. This would however increase greatly the number of coefficients to fit and goes beyond the purpose of our work.

Semi-leptonic		Four quarks	
$\mathcal{O}_{lq}^{(1),\alpha\beta}$	$(\bar{l}^a\gamma_\mu l^\beta)(\bar{q}^3\gamma^\mu q^3)$	$\mathcal{O}_{qq}^{(1)}$	$(\bar{q}^3\gamma^\mu q^3)(\bar{q}^3\gamma_\mu q^3)$
$\mathcal{O}_{lq}^{(3),\alpha\beta}$	$(\bar{l}^a\gamma_\mu\tau^a l^\beta)(\bar{q}^3\gamma^\mu\tau^a q^3)$	$\mathcal{O}_{qq}^{(3)}$	$(\bar{q}^3\gamma^\mu\tau^a q^3)(\bar{q}^3\gamma_\mu\tau^a q^3)$
$\mathcal{O}_{lu}^{\alpha\beta}$	$(\bar{l}^\alpha\gamma^\mu l^\beta)(\bar{u}^3\gamma_\mu u^3)$	$\mathcal{O}_{uu}$	$(\bar{u}^3\gamma^\mu u^3)(\bar{u}^3\gamma_\mu u^3)$
$\mathcal{O}_{qe}^{\alpha\beta}$	$(\bar{q}^3\gamma^\mu q^3)(\bar{e}^\alpha\gamma_\mu e^\beta)$	$\mathcal{O}_{qu}^{(1)}$	$(\bar{q}^3\gamma^\mu q^3)(\bar{u}^3\gamma_\mu u^3)$
$\mathcal{O}_{eu}^{\alpha\beta}$	$(\bar{e}^\alpha\gamma^\mu e^\beta)(\bar{u}^3\gamma_\mu u^3)$	$\mathcal{O}_{qu}^{(8)}$	$(\bar{q}^3\gamma^\mu T^A q^3)(\bar{u}^3\gamma_\mu T^A u^3)$
$\mathcal{O}_{lequ}^{(1),\alpha\beta}$	$(\bar{l}^\alpha e^\beta)\epsilon(\bar{q}^3 u^3)$	Higgs-Top	
$\mathcal{O}_{lequ}^{(3),\alpha\beta}$	$(\bar{l}^\alpha\sigma_{\mu\nu}e^\beta)\epsilon(\bar{q}^3\sigma^{\mu\nu}u^3)$	$\mathcal{O}_{Hq}^{(1)}$	$(H^\dagger i\overleftrightarrow{\mathcal{D}}_\mu H)(\bar{q}^3\gamma^\mu q^3)$
Dipoles		$\mathcal{O}_{Hq}^{(3)}$	$(H^\dagger i\overleftrightarrow{\mathcal{D}}^a_\mu H)(\bar{q}^3\gamma^\mu\tau^a q^3)$
$\mathcal{O}_{uG}$	$(\bar{q}^3\sigma^{\mu\nu}T^A u^3)\tilde{H}G^A_{\mu\nu}$	$\mathcal{O}_{Hu}$	$(H^\dagger i\overleftrightarrow{\mathcal{D}}_\mu H)(\bar{u}^3\gamma^\mu u^3)$
$\mathcal{O}_{uW}$	$(\bar{q}^3\sigma^{\mu\nu}u^3)\tau^a\tilde{H}W^a_{\mu\nu}$	$\mathcal{O}_{uH}$	$(H^\dagger H)(\bar{q}^3 u^3\tilde{H})$
$\mathcal{O}_{uB}$	$(\bar{q}^3\sigma^{\mu\nu}u^3)\tilde{H}B_{\mu\nu}$		

Table 2.1: The 19 dimension-six operators considered in this work. They can be split in four classes, depending on the fields coupled to the Top quark. We keep the lepton flavor structure arbitrary.

and scalar SMEFT operators with top quarks have been considered in Refs. [26, 27], where indirect bounds from $b \to s\gamma$ and electric dipole moments have been derived after the RG evolution down to the low scale. More recently, Ref. [28] performed a more global analysis, where several top quark operators have been considered and the indirect constraints from B-meson observables and $Z \to b\bar{b}$ have been derived and compared with direct limits from LHC. In our work we go beyond these previous analyses by considering a much larger set of top quark operators (all the ones that involve top quarks) and by substantially enlarging the scope of the observables considered.

This study is structured as follows. In section 2.1.2 we review the methodology employed for this work, discussing briefly the RGEs and matching procedures. Section 2.1.3 contains an overview of all the observables we take into account, divided into different classes. In section 2.1.4 we employ the global likelihood to derive fits in some simplified scenarios and discuss the results: one coefficient at a time, interesting pairs of coefficients, and a Gaussian fit with all coefficients except those of semileptonic operators. To showcase some other applications of our analysis, in section 2.1.5 we study two specific UV models that we match to the SMEFT. The first contains a scalar leptoquark coupled only to the third generation quark and lepton doublets. The second simplified model, inspired by the Cabibbo anomaly, contains a scalar and a vector leptoquark. Finally, we conclude in section 3.6. Appendix A.1 contains details on all the observables included in our analysis.

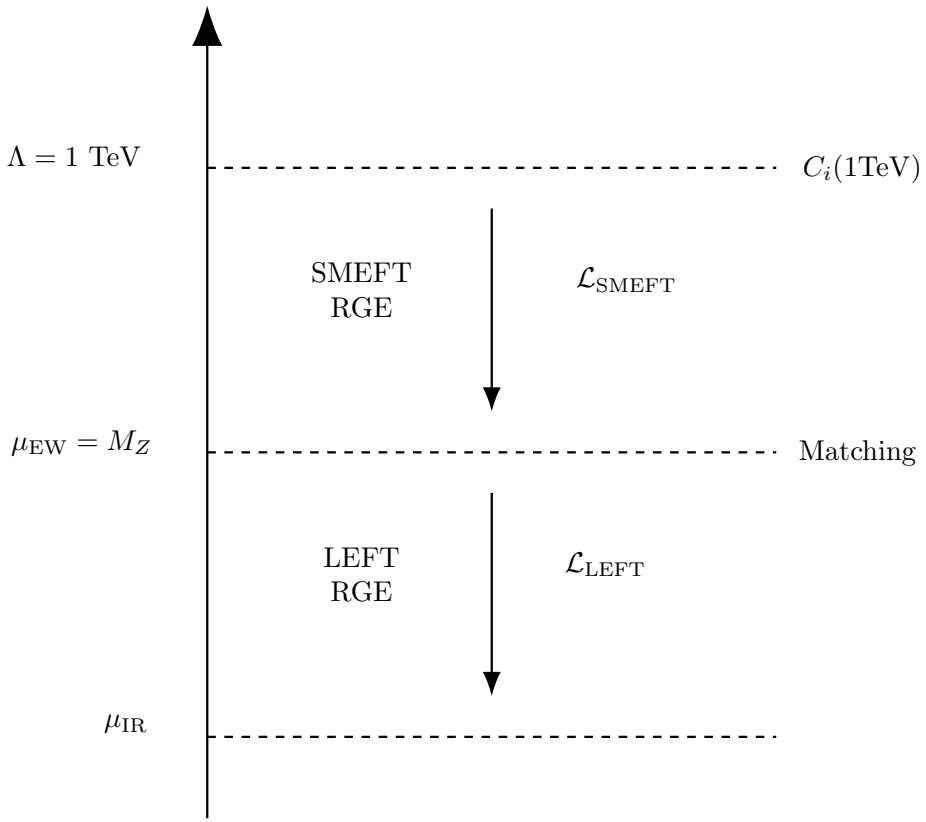


Figure 2.1: Sketch of the EFT analysis procedure adopted in this work. μ_{IR} is the scale relevant to the low energy observable under consideration.

2.1.2 Methodology

Our goal is to constrain TeV-scale top-philic scenarios deriving bounds from a large set of low-energy observables. The EFT approach represents a suitable framework for this task, as it allows us to consistently study and keep track of the scale dependence of the operators in a multi-step procedure. In practice, RGEs connect different energy scales within the range of validity of the EFT, while matching procedures allow us to integrate out heavy degrees of freedom, linking EFTs valid above or below the threshold (see also the 4-Fermi example of section 1.2.2).

The description of low energy observables below the electroweak scale relies on the LEFT Lagrangian defined in Ref. [29]:

$$\mathcal{L}_{\text{LEFT}} = \mathcal{L}_{\text{QED+QCD}} + \sum_i L_i^{(5)} O_i^{(5)} + \sum_i L_i^{(6)} O_i^{(6)} \,, \tag{2.2}$$

where the Higgs, W and Z bosons and the top quark have been integrated out, leaving the QCD sector with only two up-type quarks. Higher-dimension non-renormalizable operators are generated both by the SM heavy particles and by SMEFT contributions, again in a model-independent EFT framework. The complete list of LEFT operators is provided in table A.4.

After having defined our set of top-quark operators at the UV scale $\Lambda = 1$ TeV, as in eq. (2.1), the matching to the whole set of observables is done through the following steps:

- We evolve the SMEFT coefficients C_i from Λ down to the electroweak matching scale, that we fix to $\mu_{\rm EW} = m_Z \simeq 91.2$ GeV. We perform this running procedure numerically using the DSixTools package [30, 31], which implements the RG equations provided in [32–34].

- As discussed in Ref. [35], we combine the one-loop matching with one-loop RG evolution. For the matching between the SMEFT and the LEFT we use the results computed in Ref. [36] and refer to its ancillary files for the complete expressions (see also Ref. [37]).

- The LEFT coefficients [38] are then evolved from the electroweak scale down to the energy scales $\mu_{\rm IR}$ relevant to the specific experiment, e.g. $\mu_{\rm IR} = 4.2$ GeV for B decays, again using the DSixTools numerical routines.

- We express the low-energy observables in terms of the LEFT Wilson coefficients generated by the previous steps.

The whole process is sketched in fig. 2.1, where the main steps and the corresponding energy scales are outlined. QCD effects are known to be relevant, especially at low energies, and a resummation beyond the leading order is required. So, as an exception, we use the five-loop QCD correction for quark Yukawas and the gauge coupling from Refs. [39–41] and the four-loop strong coupling beta function and quark mass anomalous dimension from Ref. [42]. These QCD corrections are implemented in DSixTools as well as the three-loop SM RGEs from Refs. [43–46].

The procedure depicted in fig. 2.1 does not apply to the observables defined above/at the EW scale, when running the SMEFT coefficients up to $\Lambda_{\rm UV}$ is the only necessary step. In some cases, previous studies and results in the literature allowed us to partially or completely skip some steps. These cases will be mentioned and discussed in the following.

Once we have expressed the low energy observables and pseudo-observables in terms of SMEFT Wilson coefficients, we can build the log-likelihood:

$$-2\log\mathcal{L}(C_k) \equiv \chi^2(C_k) = \sum_{i,j}(\mathcal{O}_i(C_k) - \mu_i)\,(\sigma^2)^{-1}_{ij}\,(\mathcal{O}_j(C_k) - \mu_j)\,, \tag{2.3}$$

where $\mathcal{O}_i$ are the observables, C_k are the Wilson coefficients defined at the TeV scale, μ_i are the experimental values and $(\sigma^2)^{-1}_{ij}$ the corresponding covariance matrix. The likelihood is maximized by looking at the minimum of the chi-square, χ^2_0, so that the quantity $\Delta\chi^2 = \chi^2 - \chi^2_0$ allows to define the 68% or 95% CL regions. We use our global likelihood to perform individual, pairwise and global fits on Wilson coefficients. In practice, we allow only one, two or a subset of parameters in the global $\chi^2(C_i)$ to vary and set to zero all the remaining ones. Results and applications are discussed in section 2.1.4 and 2.1.5.

2.1.3 Observables

The up quark basis we employ for the left-handed quark doublet makes several top quark operators, such as the ones from table 2.1, contribute to FCNC $d^i_L \to d^j_L$ transitions even at tree-level, only suppressed by $V^*_{tj}V_{ti}$ factors. Very strong bounds to such BSM contributions can be obtained from rare B and K decays as well as meson mixing observables. Operators with top quarks are also expected to give relevant contributions, via loop effects, to anomalous

magnetic moments of leptons, tau decays, electroweak precision data, Higgs measurements and precision measurements entering in Cabibbo-angle analyses. Finally, operators that violate lepton flavor are constrained by LFV tests in lepton and meson decays. In the following subsections we provide some more details on these observables, postponing more detailed discussions to Appendix A.1.

B physics

SM-suppressed FCNC $b \to s$ transitions are powerful channels to probe new physics, in particular in those observables for which the SM prediction is free from poorly-known long-distance QCD effects. Among these, after the recent update by LHCb [47], the lepton flavor universality ratios R_K and R_{K^*} provide stringent constraints on NP coupled to light leptons:

$$\begin{aligned} R_K[1.1,6] &= 0.949 \pm 0.047\,, \\ R_{K^*}[1.1,6] &= 1.027 \pm 0.077\,. \end{aligned} \tag{2.4}$$

Other powerful decay channels for testing new physics are the so-called *golden-channel* decays[3], for which it can be useful to define the ratios with the SM predictions as

$$R^{\nu}_{K^{(*)}} \equiv \frac{\mathcal{B}(B \to K^{(*)}\nu\bar{\nu})}{\mathcal{B}(B \to K^{(*)}\nu\bar{\nu})_{\rm SM}}\,, \tag{2.5}$$

using the updated SM predictions from Ref. [48]. Notably, the Belle-II experiment recently presented the first evidence for a signal in the $B^+ \to K^+\nu\bar{\nu}$ channel: $\mathcal{B}(B^+ \to K^+\nu\bar{\nu})_{\rm Belle-II} = (2.3 \pm 0.5^{+0.5}_{-0.4}) \times 10^{-5}$ [49]. Once combined with previous upper limits, this becomes $\mathcal{B}(B^+ \to K^+\nu\bar{\nu})_{\rm Comb.} = (1.3 \pm 0.4) \times 10^{-5}$, to be compared with the SM prediction $\mathcal{B}(B^+ \to K^+\nu\bar{\nu})_{\rm SM} = (0.444 \pm 0.030) \times 10^{-5}$.[4] The corresponding value for R^{ν}_K is reported in table 2.2. On the other hand, the strongest upper limit on the K^* mode comes from Belle, with $R^{\nu}_{K^*} < 3.21$ at 95%CL [50] after combining the different modes. Several NP models affect these decay modes as a rescaling of the SM short-distance amplitude, that involves only $V-A$ currents, in such a way that $R^{\nu}_K = R^{\nu}_{K^*}$. In this case it is interesting to combine the two modes, obtaining:

$$R^{\nu}_{K^{(*)}} = 2.16 \pm 0.70\,, \tag{2.6}$$

compatible with the SM value of 1 at 1.7σ. We emphasize that, since we are not assuming lepton flavor number conservation, the inclusive sum on neutrino final states takes into account LFV cases:

$$\mathcal{B}(B \to K^{(*)}\nu\bar{\nu}) = \sum_{\alpha,\beta=1}^{3} \mathcal{B}(B \to K^{(*)}\nu_\alpha\bar{\nu}_\beta)\,. \tag{2.7}$$

We conclude the list of B decays by including $B_s \to X_s\gamma$, the leptonic $B_s \to \ell_\alpha\ell_\beta$ decays as well as semileptonic and leptonic LFV modes. The complete list of B-physics observables we consider is displayed table 2.2, together with measurements provided by the LHCb, Belle(-II) and BaBar experiments.

Theoretical predictions are extensively discussed in Appendix A.1, where branching ratios expressed in terms of low energy EFT coefficients are given. Here, we limit ourselves to show, in table 2.3, a comprehensive sketch of SMEFT contributions to the observables considered in the work. We briefly discuss WC's relevance and interplay in the rest of this Section.

[3] Rare decays of mesons into neutrinos will be deeply discussed in section 2.2 and 2.3.

[4] This is the SM prediction with the long-distance $B^+ \to \bar{\nu}_\tau\tau^+ \to K^+\bar{\nu}_\tau\nu_\tau$ removed, since the experimental collaboration treats this as background.

Observable	Experimental value
$B \to X_s\gamma$	$(3.49 \pm 0.19) \times 10^{-4}$ [51]
R_K^ν	2.93 ± 0.90 [48, 49]
$R_{K^*}^\nu$	< 3.21 [48, 50]
$R_K[1.1, 6]$	0.949 ± 0.047 [47]
$R_{K^*}[1.1, 6]$	1.027 ± 0.077 [47]
$\mathcal{B}(B \to Ke\mu)$	$< 4.5 \times 10^{-8}$ [52]
$\mathcal{B}(B \to Ke\tau)$	$< 3.6 \times 10^{-5}$ [53]
$\mathcal{B}(B \to K\mu\tau)$	$< 4.5 \times 10^{-5}$ [54]

Observable	Experimental value
$\mathcal{B}(B_s \to ee)$	$< 11.2 \times 10^{-9}$ [55]
$\mathcal{B}(B_s \to \mu\mu)$	$(3.01 \pm 0.35) \times 10^{-9}$ [56]
$\mathcal{B}(B_s \to \tau\tau)$	$< 6.8 \times 10^{-3}$ [57]
$\mathcal{B}(B_s \to e\mu)$	$< 6.3 \times 10^{-9}$ [58]
$\mathcal{B}(B_s \to \mu\tau)$	$< 4.2 \times 10^{-5}$ [59]
$\mathcal{B}(B_d \to ee)$	$< 3.0 \times 10^{-9}$ [55]
$\mathcal{B}(B_d \to \mu\mu)$	$< 2.6 \times 10^{-10}$ [56]
$\mathcal{B}(B_d \to \tau\tau)$	$< 2.1 \times 10^{-3}$ [57]
$\mathcal{B}(B_d \to e\mu)$	$< 1.3 \times 10^{-9}$ [58]
$\mathcal{B}(B_d \to \mu\tau)$	$< 1.4 \times 10^{-5}$ [59]

Table 2.2: Experimental values for B-physics observables included in this work. Bounds are given at 95% CL. In the last column, prospects of future precision are included.

The semileptonic C_{qe} and the combination $(C_{lq}^{(1)} + C_{lq}^{(3)})$ contribute at tree level to $b(d) \to s\ell_\alpha\ell_\beta$ processes, getting constrained by both rare meson $B_{s,d} \to \ell_\alpha\ell_\beta$ and semileptonic $B \to K\ell_\alpha\ell_\beta$ decays. Within these cases, the recent analysis of $R_{K^{(*)}}$ provides strong constraints on light lepton operators (see discussion in section 2.1.4 and figures therein) up to the $|C_i| \leq 10^{-2}\,\text{TeV}^{-2}$ level. These bounds on semileptonic current-current operators are completed and complemented by dineutrino modes $B \to K\nu\bar{\nu}$, which are sensitive at tree level to the combination $(C_{lq}^{(1)} - C_{lq}^{(3)})$ and to the Higgs-top operators $C_{Hq}^{(1)}$ and $C_{Hq}^{(3)}$.

In general, contributions from 4-quark operators arise in radiative corrections, from both the one-loop matching and the RG evolution. Similarly, the up-type dipole operators C_{uG}, C_{uB} and C_{uW} enter the one-loop matching expression for down-type dipoles, contributing then to the $B \to X_s\gamma$ decays. Inclusive radiative decays and rare $B \to \ell_\alpha\ell_\beta$ decays also constrain the $C_{Hq}^{(1/3)}$ coefficients, making B physics bounds almost comparable to the EW precision tests (see fig. 2.4).

Remarkably, the lack of direct limits on semileptonic dimension-six operators from top-quark measurements, such as inclusive $t\bar{t}$ and single top productions, makes indirect bounds from B mesons crucial in interpreting top-philic NP scenarios. At the same time, these flavor observables provide competitive or stronger constraints on 4-quark and Higgs-top operators, testing the robustness of global fits.

Kaon physics

Analogously to B physics, several operators in table 2.1 induce $s \to d$ transitions, driving FCNC decays of kaons. The list of observables we considered in this work and the corresponding experimental measurements are reported in table 2.4, while more details can be found in Appendix A.1. The discussion for kaon physics follows the same lines as the one above for B decays: the relevant coefficients constrained by each observables are reported in table 2.3. Bounds on WC from rare kaon decays involving leptons are less relevant then the corresponding ones of B mesons, mainly due to the strong constraints from $R_{K^{(*)}}$ and

	Tree level matching	RG and 1-loop matching
$B \to X_s\gamma$		$C_{Hq}^{(1,3)},\ C_{uB},\ C_{uW},\ C_{uG}$
$R_{K^{(*)}}^{\nu}$ $K \to \pi\nu\bar{\nu}$	$C_{Hq}^{(1,3)},\ C_{lq}^{(1,3),\alpha\beta}$	$C_{Hu},\ C_{qq}^{(1,3)},\ C_{lu}^{\alpha\beta},\ C_{qe}^{\alpha\beta}$ $C_{qu}^{(1,8)},\ C_{uu},\ C_{uW}$
$B \to K^{(*)}\ell_\alpha\ell_\beta$ $B_{s,d} \to \ell_\alpha\ell_\beta$ $K \to \pi\ell_\alpha\ell_\beta$ $K \to \ell_\alpha\ell_\beta$	$C_{lq}^{(1,3),\alpha\beta},\ C_{qe}^{\alpha\beta},\ C_{Hq}^{(1,3)}$	$C_{lu}^{\alpha\beta},\ C_{eu}^{\alpha\beta},\ C_{qq}^{(1,3)}$
$R_{K^{(*)}}$	$C_{lq}^{(1,3),\ell\ell},\ C_{qe}^{\ell\ell}$	$C_{lu}^{\ell\ell}$

Table 2.3: Most relevant WC to B-physics observables. The operators that contribute at tree level are displayed in the left column, while operators generated by radiative corrections are listed in the right column. The indices take values α, β=1,2,3 and $\ell = e, \mu$. Transpose conjugate operators are not listed since related to the already mentioned ones, e.g. $C_{lq}^{(1),\beta\alpha} = C_{lq}^{(1),\alpha\beta\,*}$.

$B_s \to \mu\mu$, while $K \to \pi\nu\bar{\nu}$ gives competitive bounds on $C_{lq}^{(1/3),33}$, see the relevant discussions in section 2.1.4.

$\Delta F = 2$

Meson mixing observables offer some of the most stringent constraints for several scenarios of beyond the SM physics. Among the top quark operators we consider, $\mathcal{O}_{qq}^{(1,3)}$ induce tree-level contributions to these processes, while many more contribute at the loop level.

Model-independent expressions of new physics contributions to $\Delta F = 2$ amplitudes in terms of SMEFT coefficients have been derived in Ref. [71]. The authors considered hadronic matrix elements of the various LEFT operators at the low scale, the RG evolution to the electroweak scale, the matching to SMEFT coefficients in the Warsaw basis (and the up quark mass basis), and finally the SMEFT RG evolution up to a scale $\Lambda = 5\,\text{TeV}$. We neglect the small mismatch in the RG evolution between this scale and the scale at which we define our coefficients, 1 TeV, as this can be well included among the theory uncertainties of working with the LL RG evolution. For the predictions of the SM contribution to meson mixing we use the results of Ref. [70], specifically the values obtained with the exclusive V_{cb} measurements and the inclusive V_{ub} one (so-called hybrid scenario). Finally, we take the experimental values for ϵ_K, ΔM_s, and ΔM_d from the PDG combination [51]. In table 2.5 we collect the values employed in our analysis, where experimental and theory uncertainties are added in quadrature.

Cabibbo angle decays

Nuclear beta, baryon, pion, kaon decay and semileptonic tau decay data are also precise new physics probes. Since the studied decay modes in the SM are suppressed by $\mathcal{O}\left(\frac{1}{v^2}\right)$, new physics contributions to the observables are only suppressed with respect to the SM by $\mathcal{O}\left(\frac{v^2}{\Lambda^2}\right)$. Taking into account the per-mil level precision reached in some of the observables, potential new physics beyond the TeV scale is probed by these decays. Within the SM

Observable	Experimental value
$\mathcal{B}(K^+ \to \pi^+ \nu\bar{\nu})$	$(1.14^{+0.4}_{-0.33}) \times 10^{-10}$ [60] [61]
$\mathcal{B}(K_L \to \pi^0 \nu\bar{\nu})$	$< 3.6 \times 10^{-9}$ [62]
$\mathcal{B}(K_S \to \mu^+\mu^-)$	$< 2.5 \times 10^{-10}$ [63]
$\mathcal{B}(K_L \to \mu^+\mu^-)_{SD}$	$< 2.5 \times 10^{-9}$ [64]
$\mathcal{B}(K_L \to \mu^\pm e^\mp)$	$< 5.6 \times 10^{-12}$ [65]
$\mathcal{B}(K_L \to \pi^0\mu^+\mu^-)$	$< 4.5 \times 10^{-10}$ [66]
$\mathcal{B}(K_L \to \pi^0 e^+ e^-)$	$< 3.3 \times 10^{-10}$ [67]
$\mathcal{B}(K_L \to \pi^0 e^+\mu^-)$	$< 9.1 \times 10^{-11}$ [68]
$\mathcal{B}(K^+ \to \pi^+ e^+\mu^-)$	$< 7.9 \times 10^{-11}$ [69]

Table 2.4: Experimental values for kaon physics observables included in this work. Bounds are given at 95% CL.

Observable	Experimental value	SM prediction
ϵ_K	$(2.228 \pm 0.011) \times 10^{-3}$	$(2.14 \pm 0.12) \times 10^{-3}$
ΔM_s	$(17.765 \pm 0.006)\,\text{ps}^{-1}$	$(17.35 \pm 0.94)\,\text{ps}^{-1}$
ΔM_d	$(0.5065 \pm 0.0019)\,\text{ps}^{-1}$	$(0.502 \pm 0.031)\,\text{ps}^{-1}$

Table 2.5: Experimental values [51] and SM predictions [70] for meson mixing observables.

picture, this sector is known to lead to some tensions, known as Cabibbo anomalies. It is then interesting to incorporate it to the analysis and to check whether, within our BSM set-up, constraints from other observables leave room for potential new physics explanations of these anomalies.

We make use the global analysis to those observables made in Ref. [72] in terms of low-energy EFT coefficients ϵ_i, which updates the EFT analyses made in Refs. [73, 74] and incorporates hadronic tau decays. Consistently with the assumptions of that analysis, we match the ϵ_i to the LEFT and then to the SMEFT at tree-level (see A.1.10). The leading contributions induced by the studied top operators appear through leading logs in the SMEFT running proportionally to the top Yukawa squared.

In our BSM set-up, the combined fit to this set of observables translates into $\mathcal{O}(\text{TeV})$ sensitivity to $C_{lq}^{(3),\ell\ell}$. At least part of the Cabibbo tension can in principle be alleviated by a nonzero $C_{lq}^{(3),22}$ value, which can play an important role in the unitarity relation. In section 2.1.5 we discuss a UV model inspired by this anomaly. Currently, efforts in the area are focused in understanding whether the so-called Cabibbo anomalies are genuine new physics hints or due to underestimated uncertainties. Overall one may not expect any major improvement in the sensitivity to new physics with respect to the quoted precision from this sector in the short term.

Observable	Experimental value	
	$\ell = e$	$\ell = \mu$
Δa_ℓ	$(2.8 \pm 7.4) \times 10^{-13}$	$(20.0 \pm 8.4) \times 10^{-10}$
$g_\tau/g_\ell - 1$	$(2.7 \pm 1.4) \times 10^{-3}$	$(0.9 \pm 1.4) \times 10^{-3}$

Table 2.6: BSM contributions to anomalous magnetic moment of the leptons, $\Delta a_\ell \equiv a_\ell^{\rm exp} - a_\ell^{\rm SM}$, and LFU in τ decays [75], $g_\tau/g_\ell - 1$. The correlation between the g_τ/g_e and the g_τ/g_μ values is of a 51 %.

Magnetic moments and LFU in τ decays

The anomalous magnetic moments of electrons and muons, $a_\ell = (g_\ell - 2)/2$, are among the most precisely measured quantities in experimental physics,

$$\begin{aligned} a_e^{\rm exp} &= (11596521807.3 \pm 2.8) \times 10^{-13}\,, \\ a_\mu^{\rm exp} &= (11659205.9 \pm 2.2) \times 10^{-10}\,. \end{aligned} \tag{2.8}$$

Remarkably, the theoretical precision of the corresponding SM predictions is similar, making them stringent SM tests. In practice, some tensions in the associated evaluations using different inputs slightly limit the current precision. Namely, as pointed out in Ref. [76], the value of $a_e^{\rm SM}$ is sensitive to the input value of the fine-structure constant, $\alpha_{\rm QED}$, and the two most precise determinations, based on Cesium and Rubidium atomic recoils [77, 78], differ by more than $5\,\sigma$. Similarly, the SM leading-order hadronic vacuum polarization (HVP) prediction quoted in the muon $g-2$ Theory White Paper (WP) [79–99], which constitutes the dominant source of uncertainty for $a_\mu^{\rm SM}$, is 2σ below the lattice BMW value [100] and new results on related observables [100–113] suggest that the source of the difference may go beyond a mere statistical fluctuation. We then take the weighted average of the $a_e^{\rm SM}$ result obtained from $\alpha_{\rm QED}^{\rm Cs}$ and $\alpha_{\rm QED}^{\rm Rb}$ and the weighted average of the $a_\mu^{\rm SM}$ one using $a_{\mu,\rm BMW}^{\rm HVP,LO}$ and $a_{\mu,\rm WP}^{\rm HVP,LO}$ as inputs, but adding half their differences as additional sources of systematic uncertainties. The corresponding values of $\Delta a_\ell = a_\ell^{\rm exp} - a_e^{\rm SM}$ are compiled in table 2.6.

The main way to generate an extra a_ℓ contribution in our BSM set-up is through the $\mathcal{O}_{lequ}^{(3),\ell\ell}$ operator, since top-antitop annihilation will generate, through mixing, the dipole operator associated to the anomalous magnetic moment. The process has been recently studied within the LEFT-SMEFT framework in Ref. [76]. Using the results from that reference, running up to $\Lambda = 1\,$TeV and keeping only the studied operators we find, in TeV units,

$$\begin{aligned} \Delta a_e &= -4.8 \times 10^{-8}\, C_{lequ}^{(3),11} + 7.1 \times 10^{-11}\, C_{lequ}^{(1),11}\,, \\ \Delta a_\mu &= -1.0 \times 10^{-5}\, C_{lequ}^{(3),22} + 1.5 \times 10^{-8}\, C_{lequ}^{(1),22}\,. \end{aligned} \tag{2.9}$$

Thus, barring some bizarre cancellation mechanism, $|C_{lequ}^{(3),11}| \gtrsim 10^{-4}\,\text{TeV}^{-2}$ and $|C_{lequ}^{(3),22}| \gtrsim 10^{-3}\,\text{TeV}^{-2}$ at $\Lambda = 1\,$TeV can already be excluded by current g-2 measurements.

Ratios of leptonic decays of τ and μ provide very clean tests of lepton flavor universality [75, 114]. Deviation from the SM predictions are often parameterized by ratios of effective charges, $g_\ell/g_{\ell'}$, which in the SM limit are equal to 1, and whose experimental values are given

Observable	Experimental limit
$\mathcal{B}(\mu \to e\gamma)$	5.0×10^{-13} [115]
$\mathcal{B}(\mu \to 3e)$	1.2×10^{-12} [116]
$\mathcal{B}(\mu\,\mathrm{Au} \to e\,\mathrm{Au})$	8.3×10^{-13} [117]
$\mathcal{B}(\tau \to e\gamma)$	3.9×10^{-8} [118]
$\mathcal{B}(\tau \to 3e)$	3.2×10^{-8} [119]
$\mathcal{B}(\tau \to e\,\bar{\mu}\mu)$	3.2×10^{-8} [119]
$\mathcal{B}(\tau \to e\pi^0)$	9.5×10^{-8} [120]
$\mathcal{B}(\tau \to e\eta)$	1.1×10^{-7} [120]
$\mathcal{B}(\tau \to e\eta')$	1.9×10^{-7} [120]

Observable	Experimental limit
$\mathcal{B}(\tau \to e\pi^+\pi^-)$	2.7×10^{-8} [121]
$\mathcal{B}(\tau \to eK^+K^-)$	4.1×10^{-8} [121]
$\mathcal{B}(\tau \to \mu\gamma)$	5.0×10^{-8} [122]
$\mathcal{B}(\tau \to 3\mu)$	2.5×10^{-8} [119]
$\mathcal{B}(\tau \to \mu\,\bar{e}e)$	2.1×10^{-8} [119]
$\mathcal{B}(\tau \to \mu\pi^0)$	1.3×10^{-7} [123]
$\mathcal{B}(\tau \to \mu\eta)$	7.7×10^{-8} [120]
$\mathcal{B}(\tau \to \mu\eta')$	1.5×10^{-7} [120]
$\mathcal{B}(\tau \to \mu\pi^+\pi^-)$	2.5×10^{-8} [121]
$\mathcal{B}(\tau \to \mu K^+K^-)$	5.2×10^{-8} [121]

Table 2.7: Current 95% CL limits on studied LFV branching ratios.

in table 2.6. In the LEFT one has

$$\begin{aligned} \frac{g_\tau}{g_e} - 1 &= \frac{v^2}{2}\left(L^{V,LL}_{\substack{\nu e\\ \mu e e\mu}} - L^{V,LL}_{\substack{\nu e\\ \tau\mu\mu\tau}}\right), \\ \frac{g_\tau}{g_\mu} - 1 &= \frac{v^2}{2}\left(L^{V,LL}_{\substack{\nu e\\ \mu e e\mu}} - L^{V,LL}_{\substack{\nu e\\ \tau e e\tau}}\right), \end{aligned} \tag{2.10}$$

where $v \approx 246$ GeV. In our set-up this translates, for $\Lambda = 1\,\mathrm{TeV}$, into

$$\begin{aligned} \frac{g_\tau}{g_e} - 1 &= 0.0038\,(C_{lq}^{(3),33} - C_{lq}^{(3),11}), \\ \frac{g_\tau}{g_\mu} - 1 &= 0.0038\,(C_{lq}^{(3),33} - C_{lq}^{(3),22}), \end{aligned} \tag{2.11}$$

where the C_{lq} coefficients are in TeV^{-2} units.

Charged Lepton Flavor-Violating decay modes

Experimental searches of neutrinoless lepton flavor-violating decay modes of leptons are suitable to test potential BSM scenarios at energy scales beyond the reach of searches at high-energy colliders.

The very stringent limits on $\mu \to e\gamma$, $\mu \to 3e$ transitions and $\mu \to e$ conversion in nuclei, currently coming respectively from MEG at PSI and SINDRUM [115–117], constitute a BSM probe of scales of up to $\Lambda_{\mathrm{BSM}} \sim 10^3 - 10^4\,\mathrm{TeV}$ [124]. They were studied within the LEFT in Ref. [125]. For our specific SMEFT set-up, the corresponding limits translate into limits on linear combinations of Wilson coefficients involving semileptonic operators that violate lepton flavor. They are the only operators that at the same time contain the needed BSM LFV insertion and satisfy the assumed top-philic condition. If only one (but any) parameter is switched on, one is able to constrain it at the $|C_i| \lesssim 10^{-4}\,\mathrm{TeV}^{-2}$ level. Studies at PSI, MEG II [126], Mu2e [127] and Mu3e [128], are expected to significantly improve these limits in the near future. We compile the present bounds in table 2.7.

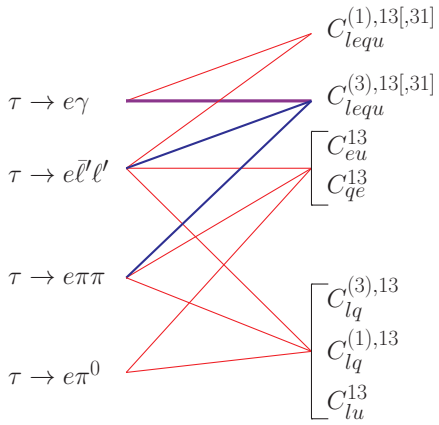


Figure 2.2: Sensitivity of the different $\tau \to e$ decay modes (similar hierarchy is observed for the $\tau \to \mu$ ones) to the different studied Wilson coefficients using the current experimental bounds. Red, blue and purple lines correspond, respectively, to upper bounds to the coefficient below 0.4, 4×10^{-3} and 4×10^{-4} (TeV units), assuming one parameter is present at a time.

While the EFT description at the SMEFT-LEFT level of the tau decays is qualitatively equivalent, leading to bounds on Wilson coefficients to the same kind of semileptonic operators for our case, the underlying LFV studies are different [129–132]. With the existing and future probes one does not expect to test new physics much higher than $\Lambda_{\rm BSM} \sim 10\,\text{TeV}$ [124]. However, many more potential decay channels can be experimentally accessed, as a consequence of a tau mass that is large enough to produce hadrons. In this sense, if charged LFV were discovered in the tau sector, the information from the different decay channels would unlock the full power of the EFT approach to stringently discriminate among different BSM scenarios, by having direct experimental access to the values of the different Wilson Coefficients. In the meantime we can use the existing limits to set bounds on different combinations of them. Current limits, coming from Belle and BaBar [51], are expected to be improved by Belle-II [133]. In fig. 2.2 the sensitivity of the different decay modes to the different studied operators is shown.

Electroweak and Higgs data

Electroweak precision data (Z and W decays) and Higgs measurements provide strong indirect constraints on new physics involving the top quark, via loop effects. The authors of Ref. [134] performed a global SMEFT analysis of Z and W pole data, WW pair production data at LEP2, and Higgs signal strength measurements from ATLAS and CMS. SMEFT contribution in the Warsaw basis are included at the tree-level except for observables that are loop-generated in the SM (such as $h \to \gamma\gamma, Z\gamma$ and $gg \to h$), in which case one-loop contributions are included as well. For our numerical analysis we use updated results for the global fit (including correlations), kindly provided by the authors of Ref. [134]. The constraints on LFV Z couplings to charged leptons are taken from the fit in Ref. [135], while those the LFV couplings to neutrinos are constrained via the measurement of the effective number of neutrinos N_ν updated in Ref. [136]. The fit is performed in terms of specific combinations of Wilson coefficients of the Warsaw basis evaluated at the weak scale shown

C_W	δc_z	$c_{z\Box}$	c_{gg}	$c_{\gamma\gamma}$	c_{zz}	$c_{z\gamma}$
$[\delta g_L^{W\ell}]_{\alpha\beta}$	$[\delta g_L^{Z\ell}]_{\alpha\beta}$	$[\delta g_R^{Z\ell}]_{\alpha\beta}$	$[\delta g_L^{Zd}]_{\alpha\alpha}$	$[\delta g_R^{Zd}]_{\alpha\alpha}$	$[\delta g_L^{Zu}]_{\alpha\alpha}$	$[\delta g_L^{Zu}]_{\alpha\alpha}$
$[C_{uH}]_{33}$	$[C_{dH}]_{33}$	$[C_{eH}]_{22}$	$[C_{eH}]_{33}$	$[C_{ll}]_{1221}$		

Table 2.8: List of Wilson coefficients used in the fit of Ref. [134]. The ones with capital C are already in the Warsaw basis, while the definition of the others is reported in App. A.1.11.

in table 2.8. Their definition is reported in App. A.1.11.

We interpret the resulting likelihood for SMEFT coefficients as evaluated at the EW scale (we fix it at M_Z for concreteness), and then include the RG evolution up to 1 TeV to obtain the final likelihood for our analysis, in terms of the coefficients of the operators listed in table 2.1. The coefficients that provide relevant constraints to our analysis are listed here, together with the TeV-scale coefficients that contribute the most to each one:

EW/Higgs coeff.		TeV-scale coefficient
$\delta g_L^{Z\ell}$	$\longleftarrow$	$C_{uB},\ C_{uW}, C_{Hu},\ C_{Hq}^{(1,3)},\ C_{lq}^{(1,3),\ell\ell},\ C_{lu}^{\ell\ell},\ \ldots$
$\delta g_L^{W\ell}$	$\longleftarrow$	$C_{uB},\ C_{uW},\ C_{Hu},\ C_{Hq}^{(1,3)},\ C_{lq}^{(3),\ell\ell},\ \ldots$
$\delta g_R^{Z\ell}$	$\longleftarrow$	$C_{uB},\ C_{uW},\ C_{Hu},\ C_{Hq}^{(1,3)},\ C_{eu}^{\ell\ell},\ C_{qe}^{\ell\ell},\ \ldots$
δg_L^{Zb}	$\longleftarrow$	$C_{Hq}^{(1,3)},\ C_{Hu},\ C_{qq}^{(1,3)},\ \ldots$
δg_R^{Zb}	$\longleftarrow$	$C_{Hq}^{(1)},\ C_{Hu},\ C_{qq}^{(1,3)},\ C_{uB},\ C_{uW},\ \ldots$
$c_{\gamma\gamma}$	$\longleftarrow$	$C_{uB},\ C_{uW},\ C_{uG}$
c_{gg}	$\longleftarrow$	C_{uG}
$[C_{eH}]_{\alpha\alpha}$	$\longleftarrow$	$C_{lequ}^{(1),\alpha\alpha}$
$[C_{uH}]_{33}$	$\longleftarrow$	$C_{uH},\ C_{uG},\ C_{Hq}^{(1,3)},\ C_{qu}^{(1,8)},\ \ldots$

(2.12)

Direct bounds from LHC

SMEFT interpretations of top quark production and decay measurements at LHC have been discussed in several works [25, 27, 137–150], providing direct bounds on 4-quark, dipole and Higgs-top operators.

The analysis by the SMEFiT collaboration [143] includes observables from the LHC Run-II dataset and studies connections with Higgs and diboson data. The SMEFiT fitting framework has been released as a Python open source package [148]. We exploit the flexibility of this toolbox to perform a SMEFT analysis of Higgs, top quark and electroweak production data (see Section 3 of Ref. [143] for details) including our operators of table 2.1, with exception of the semi-leptonic ones. The resulting constraints are reported in Appendix A.1.13. In the next section we compare these with the indirect constraints derived from our global analysis.

2.1.4 Global analysis

The observables described in the previous section, except for the direct constraints from LHC of section 2.1.3, are used to build the log-likelihood as in eq. (2.3). This provides global

indirect constraints on top quark operators, that we can compare with the direct ones from measurements at LHC. In the following we present examples of fits derived using our global likelihood. For simplicity we assume all Wilson coefficients to be real in the following.

One-parameter fits

Wilson	Global fit [TeV^{-2}]	Dominant
$C_{qq}^{(+)}$	$(-1.9 \pm 2.3) \times 10^{-3}$	ΔM_s
$C_{qq}^{(-)}$	$(-2.0 \pm 1.0) \times 10^{-1}$	$B_s \to \mu\mu$
$C_{qu}^{(1)}$	$(1.3 \pm 1.0) \times 10^{-1}$	ΔM_s
$C_{qu}^{(8)}$	$(-1.7 \pm 4.4) \times 10^{-1}$	ΔM_s
C_{uu}	$(-3.0 \pm 1.7) \times 10^{-1}$	$\delta g_{L,11}^{Ze}$
$C_{Hq}^{(+)}$	$(18.7 \pm 8.8) \times 10^{-3}$	$B_s \to \mu\mu$
$C_{Hq}^{(-)}$	$(5.8 \pm 4.5) \times 10^{-2}$	$\delta g_{L,11}^{Ze}$
C_{Hu}	$(-4.3 \pm 2.3) \times 10^{-2}$	$\delta g_{L,11}^{Ze}$
C_{uB}	$(-0.6 \pm 2.0) \times 10^{-2}$	$c_{\gamma\gamma}$
C_{uG}	$(-0.1 \pm 2.0) \times 10^{-2}$	c_{gg}
C_{uH}	$(-0.3 \pm 5.2) \times 10^{-1}$	$C_{uH,33}$
C_{uW}	$(-0.1 \pm 3.1) \times 10^{-2}$	$c_{\gamma\gamma}$

Table 2.9: Combined fit for one at a time Wilson coefficients for nonleptonic operators. The dominant observable giving the most precise bound is also displayed.

First, we perform one-parameter fits setting all the Wilson coefficients to zero except for one. While such one-parameter set-up is not a realistic low-energy description of typical UV scenarios, it can provide meaningful information about the new physics scale that can be probed if that operator is generated. It also provides a way to compare the sensitivity of different observables or, alternatively, which observables/sectors one should look at first if a specific operator is induced by the studied UV model.

The results associated to the different operators, respectively nonleptonic, semileptonic lepton-flavor conserving and semileptonic lepton-flavor violating, are shown in table 2.9, 2.10 and 2.11, together with which (isolated) single observable currently gives the most precise determination of the associated Wilson coefficient. We have defined $C_{iq}^{(\pm)} \equiv C_{iq}^{(1)} \pm C_{iq}^{(3)}$ for $i = H, q, l$. As shown in section 2.1.3, these linear combinations are typically the ones appearing at leading order in the most constraining observables.

We study next the complementarity of the indirect bounds with the direct LHC ones. In fig. 2.3 we show the results of the individual fits for Higgs-Top, Dipoles and Four Quarks operators, together with corresponding bounds derived through the SMEFiT fitting framework. We stress that, exclusively in this plot, Wilson coefficients are displayed according to

Wilson	Global fit [TeV^{-2}]	Dominant
$C_{lq}^{(+),11}$	$(2.4 \pm 3.5) \times 10^{-3}$	R_K
$C_{lq}^{(+),22}$	$(-4.0 \pm 3.4) \times 10^{-3}$	R_K
$C_{lq}^{(+),33}$	$(7.2 \pm 4.4) \times 10^{-1}$	g_τ/g_i
$C_{lq}^{(-),11}$	$(10.9 \pm 7.6) \times 10^{-2}$	$R^{\nu}_{K^{(*)}}$
$C_{lq}^{(-),22}$	$(-6.0 \pm 7.0) \times 10^{-2}$	$R^{\nu}_{K^{(*)}}$
$C_{lq}^{(-),33}$	$(-1.8 \pm 1.0) \times 10^{-1}$	$R^{\nu}_{K^{(*)}}$
C_{lu}^{11}	$(-1.7 \pm 7.0) \times 10^{-2}$	$\delta g^{Ze}_{L,11}$
C_{lu}^{22}	$(-4.3 \pm 1.8) \times 10^{-1}$	$\delta g^{Ze}_{L,22}$, R_K
C_{lu}^{33}	$(0.5 \pm 2.4) \times 10^{-1}$	$\Delta g^{Ze}_{L,33}$
C_{qe}^{11}	$(-0.7 \pm 3.9) \times 10^{-2}$	R_{K^*}
C_{qe}^{22}	$(12.1 \pm 9.2) \times 10^{-3}$	$B_s \to \mu\mu$
C_{qe}^{33}	$(2.2 \pm 2.4) \times 10^{-1}$	$\delta g^{Ze}_{R,33}$

Wilson	Global fit [TeV^{-2}]	Dominant
C_{eu}^{11}	$(5.0 \pm 8.1) \times 10^{-2}$	$\Delta g^{Ze}_{R\,11}$
C_{eu}^{22}	$(4.8 \pm 2.1) \times 10^{-1}$	$\Delta g^{Ze}_{R\,22}$
C_{eu}^{33}	$(-2.3 \pm 2.5) \times 10^{-1}$	$\Delta g^{Ze}_{R\,33}$
$C_{lequ}^{(1),11}$	$(0.4 \pm 1.0) \times 10^{-2}$	$(g-2)_e$
$C_{lequ}^{(1),22}$	$(1.8 \pm 1.6) \times 10^{-2}$	C_{eH22}
$C_{lequ}^{(1),33}$	$(8.0 \pm 9.1) \times 10^{-2}$	C_{eH33}
$C_{lequ}^{(3),11}$	$(-0.6 \pm 1.5) \times 10^{-5}$	$(g-2)_e$
$C_{lequ}^{(3),22}$	$(-19.3 \pm 8.1) \times 10^{-5}$	$(g-2)_\mu$
$C_{lequ}^{(3),33}$	$(-7.0 \pm 7.8) \times 10^{-1}$	C_{eH33}

Table 2.10: Combined fit for one at a time Wilson coefficients for semileptonic lepton-flavor-conserving operators. For reference, we also display the single observable giving the most precise bound.

Wilson	$\mu \to e$		$\tau \to \mu$		$\tau \to e$	
	Limit	Dominant	Limit	Dominant	Limit	Dominant
$C_{lequ}^{(3)}$	3.9×10^{-9}	$\mu \to e\gamma$	5.0×10^{-5}	$\tau \to \mu\gamma$	4.4×10^{-5}	$\tau \to e\gamma$
$C_{lequ}^{(1)}$	3.6×10^{-5}	$\mu \to 3e, e\gamma$	2.7×10^{-2}	$\tau \to \mu\gamma$	2.4×10^{-2}	$\tau \to e\gamma$
$C_{lq}^{(3)}$	6.7×10^{-5}	$\mu\text{Au} \to e\text{Au}$	7.1×10^{-2}	$\tau \to \mu\pi\pi$	7.4×10^{-2}	$\tau \to e\pi\pi$
$C_{lq}^{(1)}$	4.0×10^{-5}	$\mu\text{Au} \to e\text{Au}$	1.1×10^{-1}	$\tau \to \mu\pi\pi$	1.1×10^{-1}	$\tau \to e\pi\pi$
C_{lu}	4.0×10^{-5}	$\mu\text{Au} \to e\text{Au}$	1.0×10^{-1}	$\tau \to \mu\pi\pi$	1.1×10^{-1}	$\tau \to e\pi\pi$
C_{eu}	3.6×10^{-5}	$\mu\text{Au} \to e\text{Au}$	1.0×10^{-1}	$\tau \to \mu\pi\pi$	1.1×10^{-1}	$\tau \to e\pi\pi$
C_{qe}	3.6×10^{-5}	$\mu\text{Au} \to e\text{Au}$	1.0×10^{-1}	$\tau \to \mu\pi\pi$	1.0×10^{-1}	$\tau \to e\pi\pi$

Table 2.11: Upper limits (68% CL) in TeV^{-2} for the different LFV Wilson coefficients. Family superscripts are omitted (in the working approximation bounds on $C_{lequ}^{(1,3),ij}$ and $C_{lequ}^{(1,3),ji}$ are found to be the same). For reference we also display the single observable giving the most precise bound.

the SMEFiT basis (lower case c_{AB}), whose expression in terms of the Warsaw basis can be found in table A.3.

A few comments are in order concerning the comparison of these bounds. The combinations involving the coefficients $C_{qq}^{(1/3)}$ are constrained up to the 10^{-2} level, due to the $\Delta F = 2$ meson mixing observables that strongly constrain their sum. This result remarkably improves

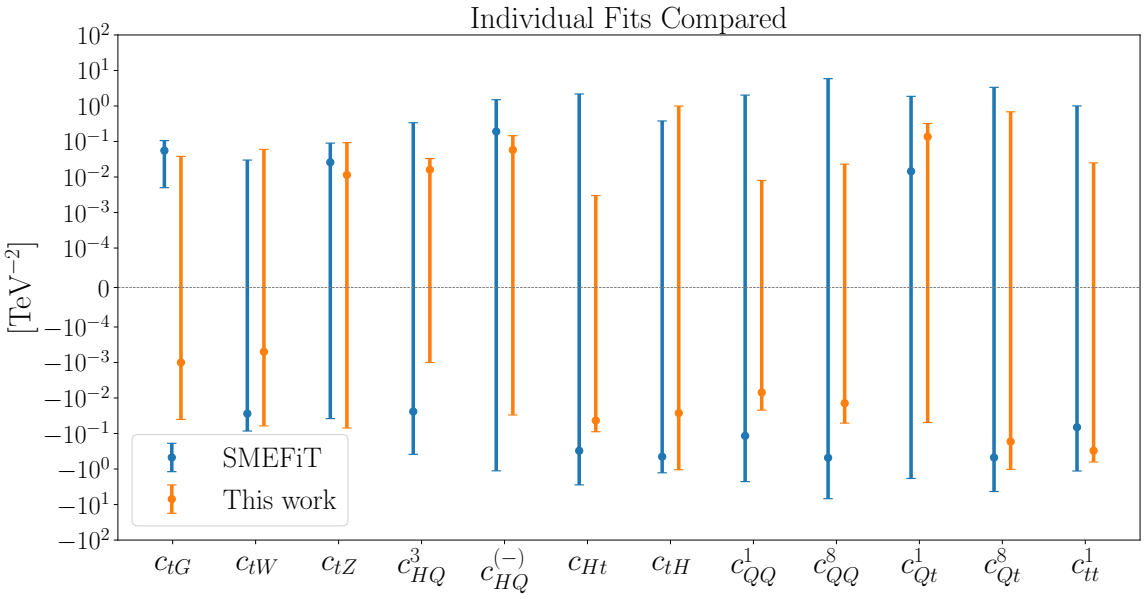


Figure 2.3: Comparison of the indirect constraints derived in this work and the direct bounds obtained through the SMEFiT toolbox. We display the 95% CL bounds for Wilson coefficients in the SMEFiT basis and notation (see table A.3 for their expression in terms of the Warsaw basis).

the bounds derived by the ATLAS and CMS direct measurements of top quark cross-sections by 2-3 orders of magnitude. An improvement is also clear for the combinations of the Higgs-Top operators $C_{Hq}^{(1/3)}$ and C_{Hu} (c_{Ht}), mostly constrained in this analysis by the electroweak and Higgs observables discussed in section 2.1.3. The C_{uG} (c_{tG}) coefficient represents the only exception to the general improvement trend observed in almost all the cases. However, as discussed in Ref. [143], the numerical fit of C_{uG} performed through the SMEFiT routine seems to be unstable, so that we do not consider this direct bound reliable (see Section 5.3 of Ref. [143] for an extended discussion).

Two-parameters fits

In this Section we carry out two-parameter fits, i.e. two Wilson coefficients at a time are allowed to vary under the assumption that they are generated at the same scale, while all the others are set to zero. These analyses can provide useful information on the interplay between pairs of coefficients, highlighting what are the most constrained combinations and giving thus intuition on their correlations. This is also the first step towards a UV interpretation, as WC's allowed regions can be contrasted with the relations predicted by specific UV scenarios. Among all the possible pairs we only show some interesting cases, e.g. when the importance of combining different sectors is highlighted and/or when the pair can be interesting from a NP perspective.

The results of two-parameters fits are illustrated in figs. 2.4 - 2.9. We display the 68%CL regions obtained when different subsets of data are taken as input and the 68% and 95%CL regions resulting from the whole set of observables. In order to better understand the underlying phenomenology, in some plots we also show single-observable 1σ contours. In this way, we can investigate the constraining power of each sector/observable on coefficients pairs.

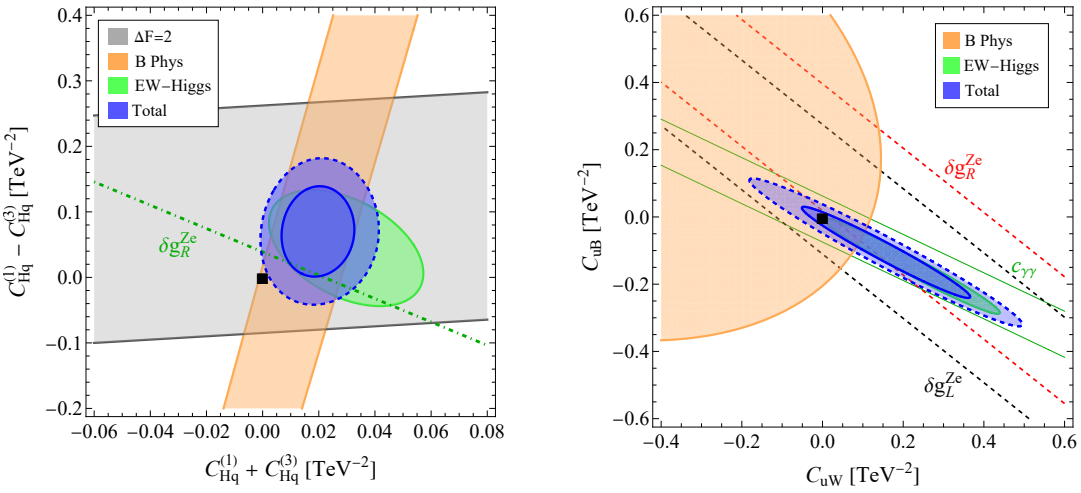


Figure 2.4: Left panel: Higgs-Top coefficients $C_{Hq}^{(+)}$ vs $C_{Hq}^{(-)}$. Right panel: dipole coefficients C_{uW} vs C_{uB}.

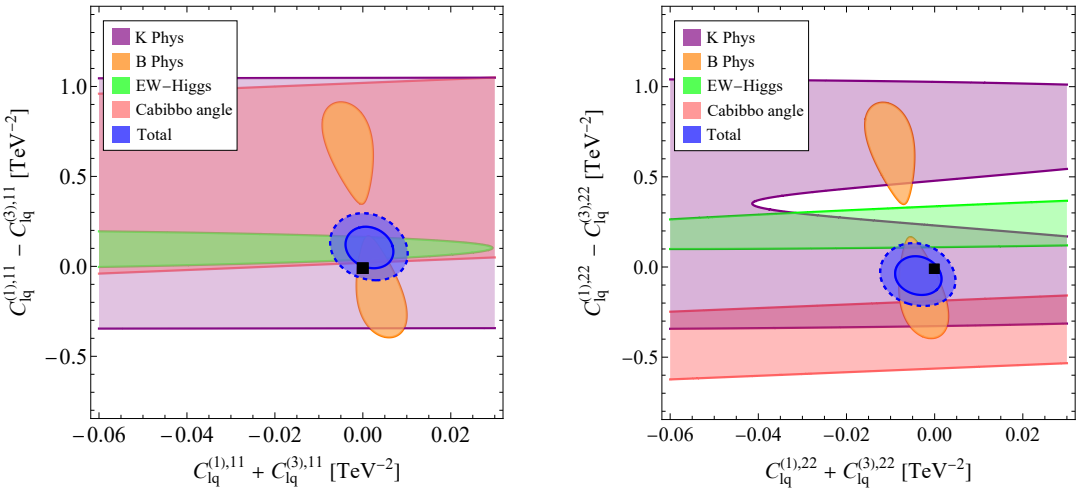


Figure 2.5: Semileptonic $C_{lq}^{(+)}$ vs $C_{lq}^{(-)}$ coefficients involving electrons and muons.

To start with, in fig. 2.4 we show the allowed regions for the $C_{Hq}^{(+)}$ and $C_{Hq}^{(-)}$ coefficients. Noteworthy, constraints from the B sector, mostly due to leptonic $B \to \ell\ell$ and radiative decays, are competitive to the EW and Higgs bounds, resulting in a (slightly more than) 2σ deviation from the SM prediction. This pull is mostly due to the Z boson coupling to right-handed electrons, $\delta g_R^{Ze} = (-7.3 \pm 4.4) \times 10^{-3}$ [134], as we show in the plot with the dot-dashed green line marking the 1σ bound. In the right panel, as an example of dipole operators, we show the C_{uW} vs C_{uB} plane. As expected, a strong constraint is set on the photon direction, whose main responsible is the $c_{\gamma\gamma}$ coefficient discussed in section 2.1.3. The dominant constraints on the orthogonal direction are set again by the electroweak sector, as a combined effect of the deviations in the Z boson coupling to leptons and other (pseudo-)observables.

In fig. 2.5 and the left panel of fig. 2.6, we show the two-parameters fits for the $C_{lq}^{(+/-),\alpha\alpha}$ coefficients. The existence of flat directions points out the importance of performing SMEFT analysis using various datasets, exploiting the complementarity between different physics

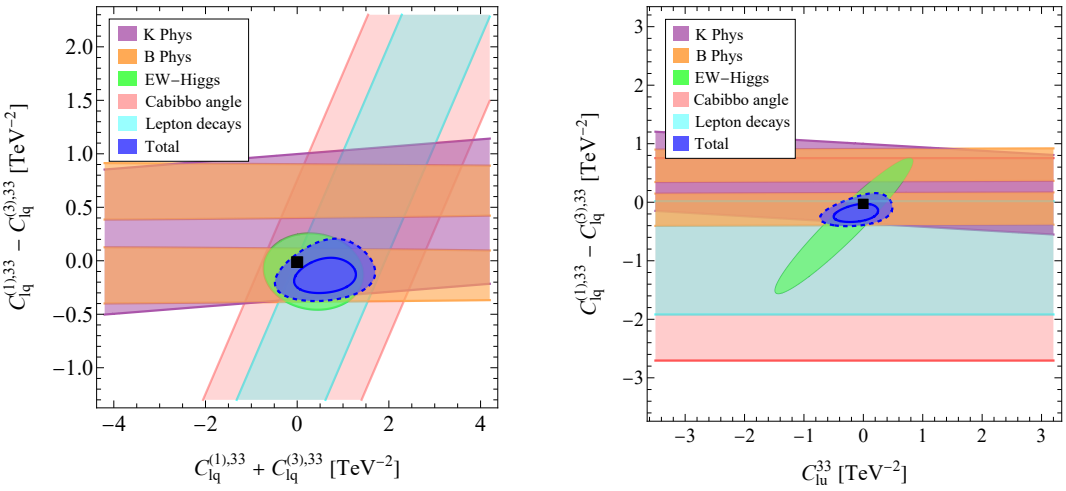


Figure 2.6: Left panel: semileptonic $C_{lq}^{(+)}$ vs $C_{lq}^{(-)}$ coefficients involving tau leptons. Bounds from the EW sector are improved by the synergy with the other sectors. Right panel: Semileptonic $C_{lq,33}^{(-)}$ vs $C_{lu,33}$ coefficients.

sectors to constraint the EFT space. Focussing on B-physics, the strong bound on the positive combinations $C_{lq}^{(+),\alpha\alpha}$, with $\alpha = 1, 2$, can be ascribed to the $R_{K^{(*)}}$ measurements. In addition, the recently announced measurement of R_K^ν, with a pull from the SM, drives the allowed region for the negative combination, splitting the allowed band in two regions depending on the interference with the SM. Interestingly, in case of electrons and muons (fig. 2.5) the deviation in R_K^ν could be compatible with the Cabibbo angle anomaly but is in some tension with the bounds from EW precision data, which drives the global fit towards the SM. In case of tau leptons (fig. 2.6), instead, the looser EW bounds and the vanishing contribution to R_K allow the global analysis to overlap with the preferred region from R_K^ν. This feature is visible also in the right panel of fig. 2.6, where we display the allowed regions in the plane $C_{lq}^{(-),33}$ vs C_{lu}^{33}. The semileptonic coefficients $C_{lq}^{(1,3),33}$ will be further discussed in section 2.1.5, where the scenario of a single scalar leptoquark S_1 coupling tau leptons and top quarks is explored. In fig. 2.7 we show the fit in the plane of C_{lu} vs. C_{qe} for both electrons (left panel) and muons (right panel). In both cases the global fit shows an interesting interplay of B and EW physics.

In fig. 2.8, we show the pairwise fits on the LFV coefficients $C_{lq,12}^{(+/-)}$ and $C_{lq,23}^{(+/-)}$. In the first case, the global fit is controlled entirely by the μAu $\to e$Au measurement, as expected from table 2.11. In the second case, the sensitivity of the coefficients is mostly driven by the tau LFV decays discussed in section 2.1.3. However, LFV decay modes of B and K mesons, as well bounds on LFV Z decays, can improve the constraints. This discussion also applies to the $C_{lq,13}^{(+/-)}$ coefficients, whose bounds are very similar to the ones derived for $C_{lq,23}^{(+/-)}$.

Regarding four-quark operators, it is clear from the left panel of fig. 2.9 that the combinations $C_{qq}^{(+)}$ and $C_{qq}^{(-)}$ are the relevant degrees of freedom in the EFT space. In particular, the sum is severely constrained by meson oscillations, while the orthogonal combination is mainly constrained by $B_s \to \mu^+\mu^-$, kaon decays and EW and Higgs observables. In the right panel we display the $C_{qu}^{(1)}$ vs $C_{qq}^{(+)}$ pair. We illustrate the effect of the δg_R^{Ze} measurement, responsible again for the main discrepancy in the EW sector. The resulting allowed region shows a tension from the SM value within of slightly more than two sigmas.

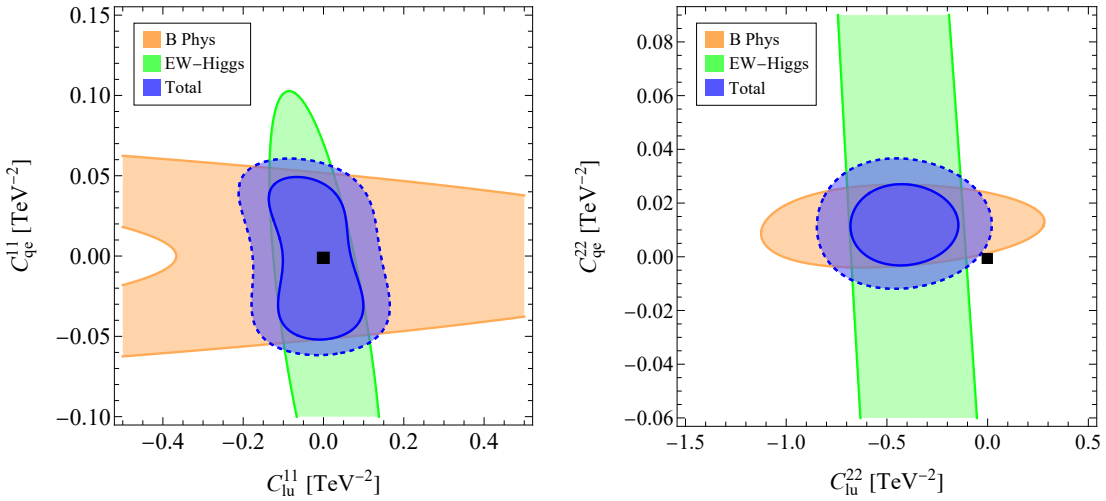


Figure 2.7: Here we show the semileptonic coefficients C_{lu} vs. C_{qe} for electrons (left) and muons (right).

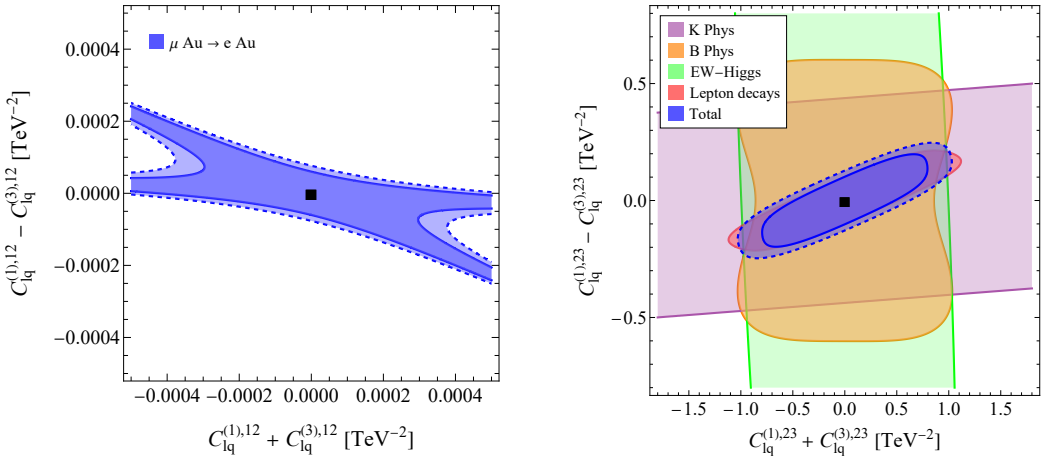


Figure 2.8: Two-parameters fit for the LFV semileptonic coefficients $C_{lq,12}^{(+/-)}$ and $C_{lq,23}^{(+/-)}$. The stronger constraints come from the LFV decay modes of tau lepton.

Gaussian fit with no semileptonic operators

Plots pose a limitation in only allowing fits to pairs of coefficients. There are two main possibilities to go beyond that: providing the complete likelihood or employing the Gaussian approximation around the global maximum of the likelihood to derive a multi-dimensional fit. While the former solution is more general, it is not a fit and the complexity of our analysis make the resulting numerical function unwieldy to publish in a paper.[5] Therefore, in this work we opt to perform a multi-dimensional Gaussian fit.

[5]However, we can provide it in electronic form upon request.

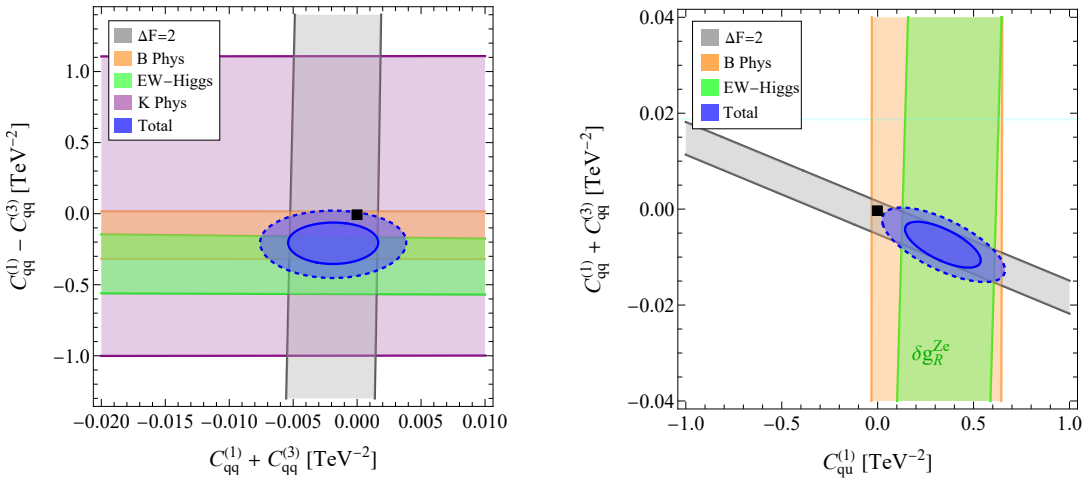


Figure 2.9: Left panel: four-quarks $C_{qq}^{(1)+(3)}$ vs $C_{qq}^{(1)-(3)}$ coefficients. $\Delta F = 2$ processes constraint the $C_{qq}^{(+)}$ combination up to the 10^{-3} level. The difference is constrained by the other sectors. Right panel: $C_{qu}^{(1)}$ and $C_{qq}^{(+)}$.

We consider all the operators in table 2.1 except the semileptonic ones:[6]

$$\vec{C} = (C_{qq}^{(+)}, C_{qq}^{(-)}, C_{uu}, C_{qu}^{(1)}, C_{qu}^{(8)}, C_{Hq}^{(+)}, C_{Hq}^{(-)}, C_{Hu}, C_{uH}, C_{uG}, C_{uW}, C_{uB}) \ . \tag{2.13}$$

The best-fit point improves the χ^2 from the SM value by $\Delta\chi^2 \equiv \chi^2_{\rm SM} - \chi^2_{\rm best-fit} \approx 10.9$. This comes mostly from the EW-Higgs sector, however it is a result in mild improvements in several observables rather than a resolution of a specific large anomaly. The fit presents some almost flat directions, which imply correlations among some coefficients very close to ± 1. For this reason, we report the result in terms of the eigenvectors of the Hessian matrix around the best-fit minimum:

$$\chi^2 = \chi^2_{\rm best-fit} + (C_i - \mu_{C_i})(\sigma^2)^{-1}_{ij}(C_j - \mu_{C_j}) = \chi^2_{\rm best-fit} + \frac{(K_i - \mu_{K_i})^2}{\sigma^2_{K_i}}. \tag{2.14}$$

The results for the best-fit values μ_{K_i} and uncertainties σ_{K_i} are reported in table 2.12, while the rotation matrix from these coefficients to our C_i is given by $\vec{K} = U_{KC}\vec{C}$, with

$$U_{KC} = \begin{pmatrix}
-1.00 & 0.000 & 0.000 & -0.016 & -0.004 & -0.004 & 0.021 & -0.001 & 0.000 & 0.000 & 0.000 & 0.000 \\
-0.005 & -0.089 & -0.015 & 0.058 & 0.000 & 0.984 & -0.004 & -0.117 & 0.000 & -0.009 & 0.044 & 0.063 \\
0.004 & 0.011 & -0.039 & 0.018 & -0.001 & -0.1 & 0.145 & -0.28 & 0.015 & -0.494 & 0.447 & 0.667 \\
-0.007 & -0.013 & 0.09 & -0.053 & -0.003 & 0.081 & -0.316 & 0.64 & 0.024 & -0.673 & -0.126 & -0.059 \\
0.005 & 0.007 & -0.074 & 0.042 & -0.002 & -0.025 & 0.259 & -0.525 & 0.025 & -0.548 & -0.213 & -0.55 \\
-0.004 & -0.041 & 0.025 & 0.067 & 0.006 & -0.004 & -0.128 & 0.084 & 0.006 & 0.022 & 0.853 & -0.492 \\
-0.006 & -0.137 & 0.078 & 0.196 & 0.96 & -0.017 & 0.09 & 0.047 & -0.065 & -0.007 & -0.017 & 0.008 \\
0.002 & -0.349 & -0.006 & 0.646 & -0.248 & -0.029 & 0.545 & 0.318 & 0.014 & 0.001 & -0.012 & 0.006 \\
0.005 & 0.007 & 0.028 & -0.138 & 0.077 & 0.017 & 0.145 & 0.06 & 0.973 & 0.037 & 0.017 & -0.003 \\
0.023 & 0.221 & 0.074 & -0.569 & 0.053 & 0.092 & 0.684 & 0.292 & -0.212 & -0.002 & 0.095 & -0.057 \\
0.006 & -0.798 & 0.451 & -0.364 & -0.071 & -0.059 & -0.038 & -0.122 & -0.039 & 0.000 & -0.012 & 0.007 \\
-0.004 & 0.404 & 0.876 & 0.235 & -0.058 & 0.025 & 0.017 & -0.093 & 0.013 & 0.000 & -0.01 & 0.006
\end{pmatrix}. \tag{2.15}$$

The last two coefficients, K_{11} and K_{12}, correspond to two flat directions with only very weak

[6] An analogous Gaussian fit including also semileptonic operators does not provide a physically meaningful result. This is due to the non-Gaussianities, that become very important in light of the mild deviations from the SM expectation present in some observables. In this case, performing a Gaussian expansion around the global minimum provides a bad approximation to the full likelihood.

Coefficient	Gaussian fit [TeV^{-2}]	Coefficient	Gaussian fit [TeV^{-2}]
K_1	0.0019 ± 0.0023	K_7	0.54 ± 0.79
K_2	0.0179 ± 0.0083	K_8	0.74 ± 0.88
K_3	-0.002 ± 0.015	K_9	-0.8 ± 1.3
K_4	-0.016 ± 0.021	K_{10}	-0.7 ± 1.8
K_5	0.044 ± 0.029	K_{11}	12 ± 13
K_6	-0.30 ± 0.38	K_{12}	-11 ± 16

Table 2.12: Result of our multidimensional gaussian fit of non-leptonic coefficients, in terms of the eigenvectors of the Hessian matrix.

constraints from our observables, given approximately by:

$$\begin{aligned} K_{11} &\approx -0.80 C_{qq}^{(-)} + 0.45 C_{uu} - 0.36 C_{qu}^{(1)} - 0.12 C_{Hu} + \dots \ , \\ K_{12} &\approx +0.40 C_{qq}^{(-)} + 0.88 C_{uu} + 0.24 C_{qu}^{(1)} - 0.09 C_{Hu} + \dots \ . \end{aligned} \tag{2.16}$$

Using the naive power counting of Ref. [151], one may estimate the allowed EFT hyper-volume spanned by the studied non-leptonic Wilson coefficients as $V_{\rm EFT} \sim \frac{\pi^6}{720} \left(\frac{(4\pi)}{\rm TeV^2}\right)^3 \left(\frac{(4\pi)^2}{\rm TeV^2}\right)^8 \left(\frac{(4\pi)^3}{\rm TeV^2}\right)$, assuming $\Lambda = 1\,$TeV. From table 2.12, experimental constraints restrict the potential SMEFT hyperspace to a very tiny fraction of its volume, $\sim 10^{-31}$.

2.1.5 Applications for UV models

In this Section we apply our global analysis to two UV scenarios of New Physics at the TeV scale, coupled mainly to the top quark. The first is a simple minimal extension of the SM by one scalar leptoquark $S_1 \sim (\bar{\mathbf{3}}, \mathbf{1})_{+1/3}$ coupled only to the third generation quark and lepton doublets. The second scenario is an application guided by the Cabibbo anomaly, it includes the scalar leptoquark $S_3 \sim (\bar{\mathbf{3}}, \mathbf{3})_{+1/3}$ as well as the vector leptoquark $U_1 \sim (\mathbf{3}, \mathbf{1})_{+2/3}$.

Single leptoquark S_1

Let us consider the scalar leptoquark $S_1 \sim (\bar{\mathbf{3}}, \mathbf{1})_{+1/3}$, coupled only to the third generation of quark and lepton $SU(2)_L$ doublets:

$$\mathcal{L} \supset \lambda_{t\tau}\, \bar{q}_3^c i\sigma_2 l_3\, S_1 + \text{h.c.} \ , \tag{2.17}$$

where $q_3 = (t_L,\, V_{tj} d_L^j)$, $l_3 = (\nu_\tau,\, \tau_L)$ and σ_i are the Pauli matrices. While the recent interest in this leptoquark stems from its ability to address the $R(D^{(*)})$ and $(g-2)_\mu$ anomalies, our setup will not address either of those since in our case S_1 doesn't couple to the charm nor the muon. Indeed, our goal is only to showcase a simple application of the global analysis.

Matching at tree level this Lagrangian to the SMEFT gives [152, 153]

$$C_{lq}^{(1),33} = -C_{lq}^{(3),33} = \frac{|\lambda_{t\tau}|^2}{4M_{S_1}^2} \ . \tag{2.18}$$

For precision studies of such scenarios, however, the tree level matching is not sufficient since one-loop contributions can be important for some observables, as discussed in Refs. [154–159].

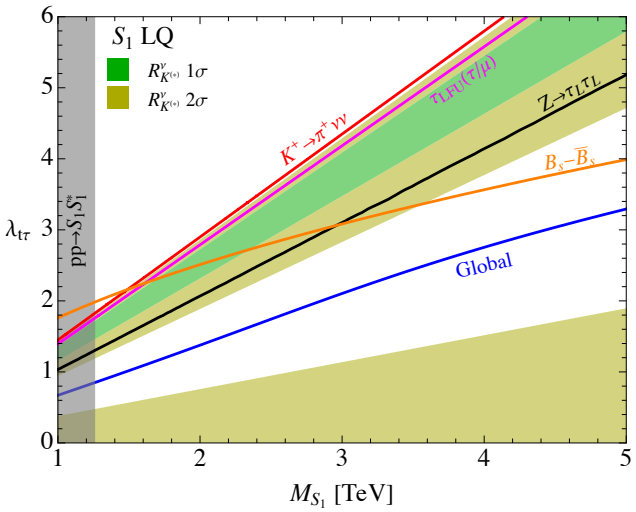


Figure 2.10: Present constraints on the S_1 leptoquark model, coupled only to third generation quark and lepton doublets. The green (yellow) region is preferred at 1σ (2σ) by $R^{\nu}_{K^{(*)}}$, while the gray region is excluded at 95%CL from direct searches at LHC. The region above each line is excluded at 95%CL by the corresponding observable, or by our global analysis (blue line).

For our goal it is sufficient to add the leading contributions to four-quark operators, which induce contributions to meson-mixing observables. From the complete one-loop matching of this scalar leptoquark to SMEFT, done in Ref. [160], we extract the relevant contribution:

$$C^{(1)}_{qq} = C^{(3)}_{qq} = -\frac{|\lambda_{t\tau}|^4}{256\pi^2 M^2_{S_1}} \ . \tag{2.19}$$

These coefficients are generated at the M_{S_1} scale, that we assume to be near 1 TeV, so that we neglect the RG evolution between M_{S_1} and 1 TeV.

The constraints from the global analysis, as well as from the most relevant observables, in the plane of the $\lambda_{t\tau}$ coupling vs. the leptoquark mass, are shown in fig. 2.10. The shaded gray region is excluded by ATLAS from leptoquark pair-production searches [161]. The regions preferred at 1σ and 2σ by the $R^{\nu}_{K^{(*)}}$ combination, eq. (2.6), are show in green and yellow, respectively. Interestingly, the intermediate white region is disfavored at the 95%CL by $R^{\nu}_{K^{(*)}}$ due to the negative interference with the SM, which suppresses the branching ratio below the 2σ level. We observe an interesting interplay of constraints from different classes of observables: electroweak precision data and τ physics, meson mixing, B and kaon rare decays, as well as direct searches from LHC.

Two leptoquarks for the Cabibbo anomaly?

In this section we illustrate how our combined likelihood may also be used to check whether experimental results in tension with the SM predictions can be partially accommodated in top-philic extensions (and which ones), taking into account the restrictions imposed by experimental results in other sectors. Here we focus on the longstanding tensions within the SM involving the determination of the inputs of the first row of the CKM matrix, known as Cabibbo anomalies.

Regardless of whether nonzero values are allowed or not for the remaining Wilson coefficients, the likelihood of the Cabibbo angle observables displays a $3\,\sigma$ preference for a nonzero value of $C_{lq}^{(3),22}$ at $\Lambda = 1\,\text{TeV}$,

$$[C_{lq}^{(3),22}]^{\text{Cabibbo}} = (0.19 \pm 0.06)\,\text{TeV}^{-2}\,. \tag{2.20}$$

Let us first develop on where this preferred nonzero value comes from. $C_{lq}^{(3),\alpha\alpha}$ induces an unusually large $C_{Hl}^{(3),\alpha\alpha}$ at the EW scale, due to a mixing that involves a double top Yukawa insertion. The leading log approximation, which one may expect to give a first approximation for $\Lambda \gtrsim$ TeV, is displayed in eq. (A.88). After EWSB $C_{Hl}^{(3),\alpha\alpha}$ induces, at tree level, a re-scaling of the corresponding lepton charged current vertices, modifying the ratios of muon, beta and kaon decays. As a consequence, the corresponding apparent unitarity relation is[7]

$$\begin{aligned}\Delta_{\text{CKM}} &\equiv |V_{ud}^{\beta}|^2 + |V_{us}^{K_{\ell 3}}|^2 - 1 \approx -2v^2\,(|V_{ud}|^2 C_{Hl}^{(3),22} - |V_{us}|^2 (C_{Hl}^{(3),\ell\ell} - C_{Hl}^{(3),11} - C_{Hl}^{(3),22}))\\ &\approx -2v^2\,C_{Hl}^{(3),22} \sim -\left[\frac{N_c}{2\pi^2}\frac{m_t^2}{\Lambda_{\text{UV}}^2}\log\frac{\Lambda_{\text{UV}}}{M_Z}\right]\Lambda_{\text{UV}}^2 C_{lq}^{(3),22}(\Lambda_{\text{UV}}^2)\,.\end{aligned} \tag{2.21}$$

Experimentally Δ_{CKM} is known beyond the per-mil level and gives the main pull behind the result of eq. (2.20).

If we set all the parameters to zero except for $C_{lq}^{(3),22}$ for the EW/Higgs likelihood, we also obtain a slight preference for nonzero values, but with the opposite sign,

$$[C_{lq}^{(3),22}]^{\text{EW/Higgs}} = (-0.11 \pm 0.06)\,\text{TeV}^{-2}\,. \tag{2.22}$$

This is to be expected, since it is well known that explaining Δ_{CKM} through increasing the muon decay matrix element is in tension with fits in other EWPOs, e.g. see Refs. [162–164]. We may yet respect CKM unitarity and decrease the muon decay rate with respect to the SM expectation by breaking LFU, with $0 < C_{Hl}^{(3),22} < -C_{Hl}^{(3),11}$. Let us then allow for nonzero values at the TeV scale for $C_{lq}^{(3),\alpha\alpha}$ for the first two lepton families and also for the corresponding $C_{lq}^{(1),\alpha\alpha}$, typically induced in UV models by the same couplings. The minimum χ^2 follows the expected pattern, plus a preference for $C_{lq}^{(1),11} \approx C_{lq}^{(3),11}$ and $C_{lq}^{(1),22} \approx 3C_{lq}^{(3),22}$. Both these relations and the obtained signs happen to match the couplings induced by top-philic U_1 and S_3 leptoquarks coupled, respectively, to the first and the second lepton family,

$$\mathcal{L} \supset \lambda_{U_1}\,\bar{q}_3\gamma_\mu l_1\,U_1^\mu + \lambda_{S_3}\,\bar{q}_3^c i\sigma_2\sigma_a l_2\,S_3^a + \text{h.c.}\,, \tag{2.23}$$

giving [152, 153]

$$C_{lq}^{(3),11} = -\frac{|\lambda_{U_1}|^2}{2M_{U_1}^2}\,, \quad C_{lq}^{(3),22} = \frac{|\lambda_{S_3}|^2}{4M_{S_3}^2}\,, \tag{2.24}$$

plus the relations with $C_{lq}^{(1)}$ above. Imposing them as strict equalities one finds, in this two-parameter scenario,

$$C_{lq}^{(3),11} = (-0.19 \pm 0.06)\,\text{TeV}^{-2}\,,\; C_{lq}^{(3),22} = (0.14 \pm 0.04)\,\text{TeV}^{-2}\,. \tag{2.25}$$

With respect to the SM, this minimum has a $\Delta\chi^2 = 8.0$ preference for the Cabibbo sector and a $\Delta\chi^2 = 5.7$ for the EW/Higgs one.

[7] V_{ub} has a completely negligible numerical role in this relation.

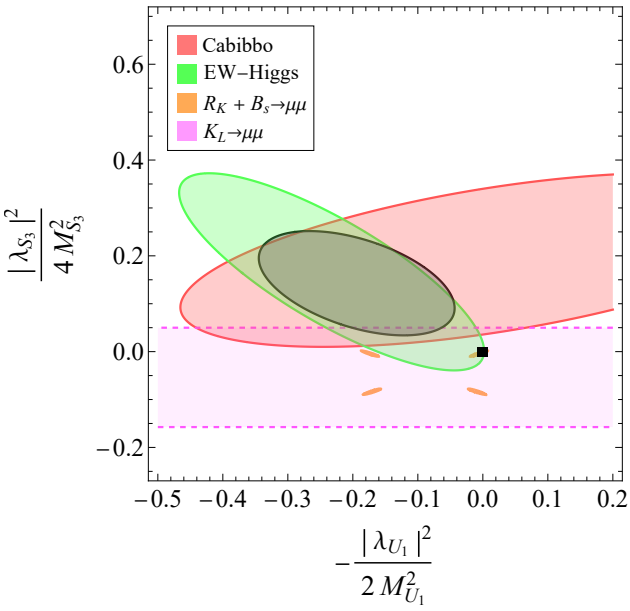


Figure 2.11: Allowed regions (95% CL) for the studied leptoquark couplings (see text) from the Cabibbo and the EW Higgs sector and combined, in black. Masses are in TeV units. The preferred nonzero values can be ruled out from B-physics and K-physics observables, unless one defines the top-philic set up in the down-quark basis.

It is only when adding constraints from B and K physics observables when this scenario becomes strongly disfavored. In a generic top-philic set-up defined in any specific flavor basis in which $C_{lq}^{(1,3),ii}$ are induced, FCNCs are generated when rotating to the mass basis. In the down sector FCNCs are very strongly constrained by the processes studied in this work, as we have explicitly shown when defining the top-philic condition in the up quark basis. Indeed we show in fig. 2.11 how including those constraints we can rule out this, and practically any, top-philic explanation to the Cabibbo anomaly.

Let us finish this section by remarking that there is, however, a possible way out to the strong constraints on FCNCs coming from K and B physics. Assuming that there exists some, admittedly bizarre from our infra-red perspective, mechanism in the UV theory to select a top-philic set-up in the only basis where this operator does not induce tree-level FCNCs in the down sector, i.e. the down-quark basis, the previous constraints from K and B physics do not hold, while the constraints on Cabibbo angle and EW/Higgs would give, in a first approximation, the same results, since the leading mechanism to modify the SM, through modifying lepton vertices, is largely independent on quark-basis rotation. In that scenario, this leptoquark model may still be a feasible (partial) solution to the Cabibbo anomaly. Complementary constraints on the space of parameters may come from $D-\bar{D}$ mixing (since FCNCs are yet induced in the up sector) and direct leptoquark searches, bounding the possible masses from below. Further studying this scenario is, however, well beyond the goals and the scope of this work.

2.1.6 Summary

We provided a global analysis of indirect constraints on SMEFT operators involving the top quark. In fact, several motivated UV scenarios predict new physics coupled mostly with the top. Our global analysis combines a large number of observables that do not involve directly the top quark. These include: B, K and τ decays, meson mixing observables, magnetic moments of leptons, measurements of the Cabibbo angle, EW precision measurements, Higgs physics, and LFV tests. Top quark operators contribute to these observables either at the tree-level via the $SU(2)_L$ connection with left-handed down quarks or via loop effects. Assuming that top quark operators are generated at the 1TeV scale, we evolve them down to the scale relevant for each observable using the relevant RG and matching equations. The result of this process is a global likelihood expressed in terms of the high-scale Wilson coefficients.

Using this likelihood we derive global indirect constraints on single coefficients, comparing the result with the bounds obtained from LHC analysis of processes involving top quarks. In all cases we find that the indirect constraints are stronger than the direct ones, often by several orders of magnitude. We then perform several 2D fits to study interesting correlations among coefficients and the complementarity between different observables, that showcase the importance of performing such global analyses. We also perform a multi-dimensional Gaussian fit of all the coefficients of non-leptonic operators, that can be useful to identify the directions in parameter space that have strongest or weakest constraints. Indeed, among these coefficients we identify two almost-flat directions.

Finally, as examples of possible applications of our analysis we study the EFT coefficients generated by two simple UV models. The first includes a scalar singlet leptoquark coupled only to the third generation of quark and lepton doublets. We show how the different indirect constraints one can derive from different sectors combine in providing strong bounds on the model, and how these are complementary to direct searches at the LHC. As a second example we study a two-leptoquark scenario inspired by the Cabibbo anomaly, with only two free couplings. This model accommodates the anomaly and improves the fit quality for the rest of EW-Higgs precision observables. However, B and kaon physics constraints are able to completely rule out this scenario unless a very specific flavor alignment is imposed.

Our results show how global indirect constraints on top quark operators can be powerful in constraining new physics scenarios coupled mainly to the top quark. Such constraints are often much stronger, or in any case complementary, to those derived from high-energy top quark physics at colliders. Furthermore, several of the observables providing the strongest indirect constraints are expected to be measured with a substantially better precision in the future: $R^{\nu}_{K^{(*)}}$ and τ decays at Belle-II, $R_{K^{(*)}}$ and $B_s \to \mu\mu$ by LHCb, ATLAS and CMS, $K \to \pi\nu\nu$ by NA62, and several experiments are expected to improve the sensitivity on $\mu \to e$ LFV by several orders of magnitude. All this will further increase the relevance of such global analysis of indirect bounds in the future.

2.2 Implications of $B \to K\nu\bar{\nu}$ under Rank-One Flavor Violation hypothesis

Rare semileptonic neutral-current decays of mesons are powerful probes of New Physics due to their loop and CKM suppression in the Standard Model. Within this class of processes, the so-called golden-channel decays to neutrinos stand out thanks to the precision of the SM predictions, a consequence of the neutrality of neutrinos under electromagnetic interactions, implying the absence of long-distance non-perturbative contributions to the decay rate [48, 165–169]. While these processes were already included in the previous sections, within the global analysis of top quark operators, we now aim at providing an in depth study under more general assumptions.

Particularly interesting is the $b \to s\nu\bar{\nu}$ transition, currently studied via several decays of B mesons into Kaons. It is useful to define the ratios with the SM prediction as

$$R^{\nu}_{K^{(*)}} = \frac{\mathcal{B}(B \to K^{(*)}\nu\bar{\nu})}{\mathcal{B}(B \to K^{(*)}\nu\bar{\nu})_{\rm SM}} \,, \tag{2.26}$$

where in the following we employ the latest SM predictions from Ref. [48], which combine results on the hadronic form factors from different lattice groups. An upper limit from the combination of all $B \to K^*\nu\bar{\nu}$ channels has been reported by the Belle experiment: $\mathcal{B}(B \to K^*\nu\bar{\nu}) < 2.7 \times 10^{-5}$ at the 90% CL [50]. Assuming the central value being the SM point (which is also motivated by the $\sim 2\sigma$ excess in the K^{*+} channel) we obtain $R^{\nu}_{K^*} = 1.0 \pm 1.1$. For the neutral channel Belle set the upper limit $\mathcal{B}(B^0 \to K^0_S\nu\bar{\nu}) < 1.3 \times 10^{-5}$ at the 90% CL [50],[8] which we translate to $R^{\nu}_{K^0_S} = 1.0 \pm 3.3$. Recently, the Belle-II experiment announced the first 3.5σ evidence for the $B^+ \to K^+\nu\bar{\nu}$ decay, showing a 2.7σ excess over the SM prediction [49]. When combined with previous upper limits on the same mode they obtain $\mathcal{B}(B^+ \to K^+\nu\bar{\nu}) = (1.3 \pm 0.4) \times 10^{-5}$, which corresponds to $R^{\nu}_{K^+} = 2.93 \pm 0.90$, a 2.1σ deviation from the SM.[9] With 5 (50) ab^{-1} of integrated luminosity, Belle-II expects to measure these rates with approximately 30% (11%) precision [170].

It is likely that the mild deviation from the SM observed in $B^+ \to K^+\nu\bar{\nu}$ is simply due to a statistical fluctuation. If the excess is instead due to a contribution of physics beyond the SM one would generically expect correlated deviations also in other measurements. Such correlations would depend on the specific assumptions on the type of NP and its flavor structure. Our goal is to study possible correlations between this excess and other processes investigated at both low and high-energy experiments, under the assumption that NP is heavier than the electroweak scale. As a consequence, we describe NP contributions in the form of Effective Field Theory (EFT) operators written in terms of SM fields. Similar investigations have already been performed by several groups [171–176], while for the opposite but complementary case of light NP see Refs. [177–188]. Regarding the flavor structure of NP, our goal is to consider a scenario that is both specific enough to induce interesting correlations while being generic enough to allow us to explore different directions in flavor space. We therefore assume that the EFT flavor structure follows the *Rank-One Flavor Violation* (ROFV)

[8] We note that in the PDG it is reported an upper limit of 2.6×10^{-5}, quoting that same Belle paper. We use the value reported by Belle.

[9] The long-distance contribution $B^+ \to \nu\tau^+ \to K^+\nu\bar{\nu}$ is removed from the SM prediction, since it is also treated as background in the experimental analysis.

hypothesis [189], where the flavor matrix of EFT coefficients of semileptonic operators is of rank-1. This flavor structure is automatically realised in several New Physics scenarios, such as all leptoquark models coupled (mostly) to a single lepton flavor, or with single vector-like quarks that mix with SM quarks. In general, it is realised in all cases where a single linear combination of quarks is coupled to NP:

$$\mathcal{L} \supset \lambda_i \bar{q}^i \mathcal{O}_{\rm NP} + \text{h.c.} \ . \tag{2.27}$$

Such structure implies correlations between operators involving different families of quarks. In the specific case discussed here, the channels most obviously correlated to $b \to s\nu\bar{\nu}$ transitions are $s \to d\nu\bar{\nu}$ and $b \to d\nu\bar{\nu}$.

The $s \to d\nu\bar{\nu}$ transition can be tested via $K^+ \to \pi^+\nu\bar{\nu}$ and $K_L \to \pi^0\nu\bar{\nu}$ decays, currently investigated at the NA62 [60, 190] and KOTO [62] experiments, respectively. While an upper limit is currently set on the neutral channel, $\mathcal{B}(K_L \to \pi^0\nu\bar{\nu}) < 2.4 \times 10^{-9}$ at the 90% CL [62], the NA62 experiments found evidence for the charged mode with significance larger than 5σ: $\mathcal{B}(K^+ \to \pi^+\nu\bar{\nu}) = \left(13.6\,(^{+3.0}_{-2.7})_{\rm stat}(^{+1.3}_{-1.2})_{\rm syst}\right) \times 10^{-11}$ [191]. A final sensitivity of about 15% is now expected by NA62 [192, 193], while KOTO should reach a 95%CL upper limit of 1.8×10^{-10} by the end of stage-I [194].[10] The $B \to \pi\nu\bar{\nu}$ and $B \to \rho\nu\bar{\nu}$ decays, measured at Belle [50], instead test the $b \to d\nu\bar{\nu}$ partonic transition.

By adding further assumptions on the gauge structure of the new physics, or by assuming specific heavy mediators, further correlations with other leptonic and semileptonic decays, involving also charged leptons, appear, as well as with electroweak or collider observables.

In section 2.2.1 we briefly review the low-energy EFT (LEFT) fit of $b \to s\nu\bar{\nu}$ transitions, introduce the ROFV hypothesis and study the correlations one can derive in the LEFT. In section 2.2.2 we study the correlations arising at the level of SMEFT. In section 2.2.3 we focus on semileptonic four-fermion operators and review single-mediator simplified models. Finally, we summarise our results and conclude in section 2.2.4. The details of all observables discussed in our analysis are collected in App. A.1. In App. A.3 we collect the fits of EFT coefficients related to $b \to s\nu\bar{\nu}$ in the various scenarios. Finally, in App. A.3.3 we study possible interpretations of the R_K^ν excess in terms of lepton-number violating operators.

2.2.1 $B \to K^{(*)}\nu\bar{\nu}$ and rank-one correlations in LEFT

Let us start by reviewing the fit of $B \to K^{(*)}\nu\bar{\nu}$ measurements in the EFT framework. The low energy effective theory relevant to the $b \to s\nu\bar{\nu}$ processes is described by the effective Lagrangian [48, 165, 166]

$$\mathcal{L}^{bs\nu\nu}_{\rm LEFT} = \sum_{\alpha\beta} \left[(L_L^{sb\alpha\beta} + L_L^{sb,\,\rm SM}\delta^{\alpha\beta})(\bar{s}_L\gamma_\mu b_L)(\bar{\nu}_L^\alpha\gamma^\mu\nu_L^\beta) + L_R^{sb\alpha\beta}(\bar{s}_R\gamma_\mu b_R)(\bar{\nu}_L^\alpha\gamma^\mu\nu_L^\beta) \right] \ , \tag{2.28}$$

where $L_L^{sb,\,\rm SM} = \frac{8G_F V_{tb}V_{ts}^*}{\sqrt{2}}\frac{\alpha}{4\pi}C_L^{\rm SM}$, with $C_L^{\rm SM} \approx -6.32$ [48], see App. A.1.1 for details. We also define the lepton flavor universal LFU coefficients as $L_{L,R}^{sb\alpha\beta} = L_{L,R}^{sb,\,\rm LFU}\,\delta^{\alpha\beta}$, and the vector/axial combinations as $L_{V,A}^{sb\alpha\beta} \equiv L_R^{sb\alpha\beta} \pm L_L^{sb\alpha\beta}$. In the top row of fig. 2.12 we plot the correlation of R_K^ν and $R_{K^*}^\nu$ while varying the effective coefficients $L_{L,R,V}^{sb}$. In the bottom row we show the

[10] The proposed HIKE experiment at CERN could reach $\mathcal{O}(5\%)$ precision on $\mathcal{B}(K^+ \to \pi^+\nu\bar{\nu})$ [193], while a stage-II upgrade at KOTO would allow a precision of about 20% in the neutral channel [194].

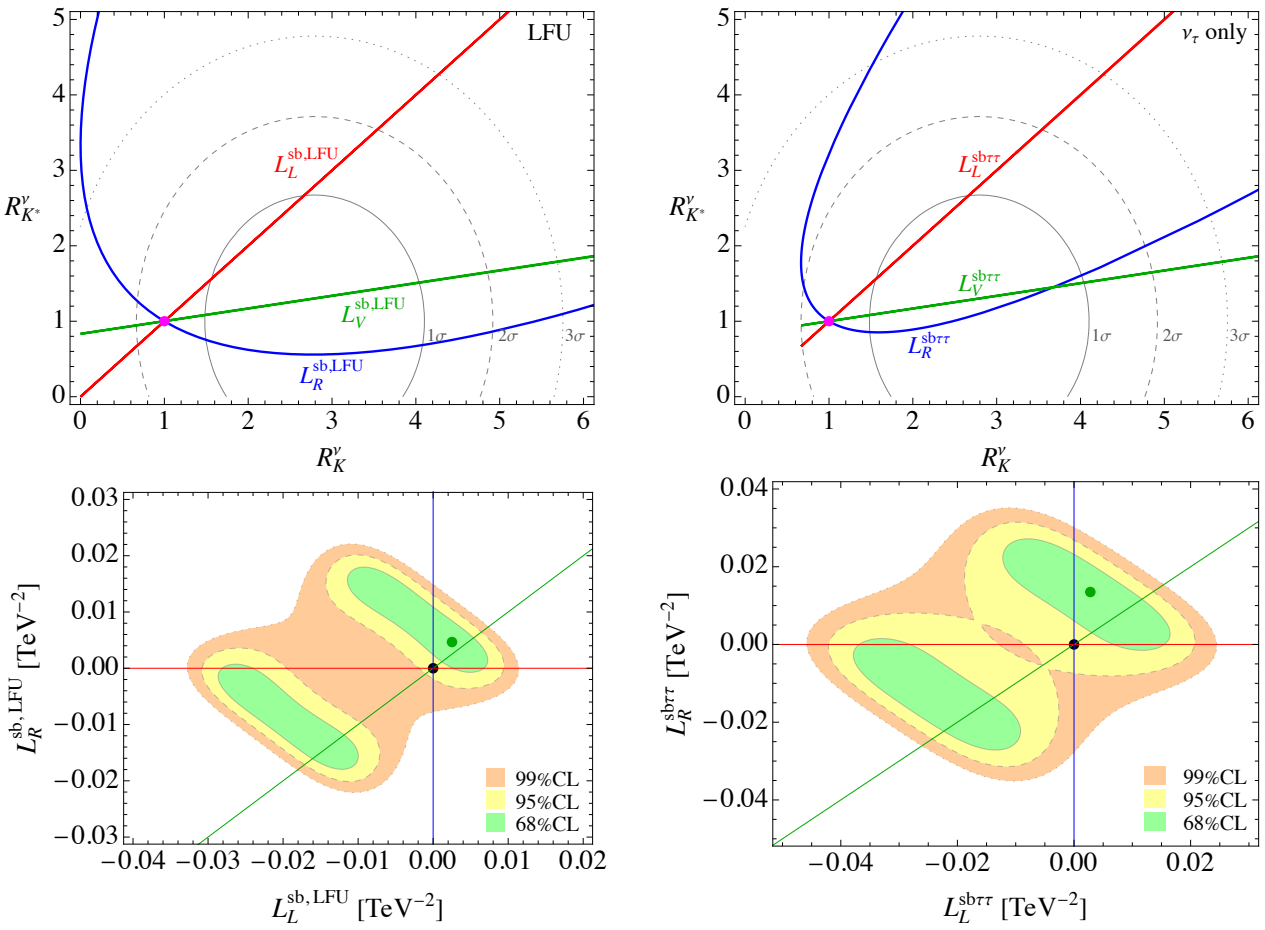


Figure 2.12: Top row: Fit of available data on all $B \to K^{(*)}\nu\bar{\nu}$ channels. Solid, dashed, and dotted gray lines represent 1σ, 2σ and 3σ contours. The magenta point represents the SM.
Bottom row: Fit in the $(L_L^{sb\alpha\beta},\ L_R^{sb\alpha\beta})$ plane assuming lepton flavor universality (left) or contributions only in the tau neutrino (right). Red, blue, and green lines represents the EFT directions as in the plots above.

fit in the plane $L_L^{sb} - L_R^{sb}$, assuming for simplicity LFU or new physics coupled only to tau neutrinos. We observe a slight preference (less than 1σ) for the right and vector currents, due to the absence of any excess in the K^* channel. Future more precise measurements will clarify whether the Belle-II excess in the K^+ channel is something more than merely a statistical fluctuation and the interplay with the K^* mode will provide more information on the chiral structure of the underlying new physics interactions. In the rest of the work we take the excess at face value and proceed with the new physics interpretation.

The two low-energy operators in eq. (2.28) are part of an effective Lagrangian involving all three quark families. Focusing on the new physics contribution one has

$$\mathcal{L}^{\rm NP}_{\rm LEFT} = \sum_{ij\alpha\beta} \left[L_L^{ij\alpha\beta} (\bar{d}^i_L \gamma_\mu d^j_L)(\bar{\nu}^\alpha_L \gamma^\mu \nu^\beta_L) + L_R^{ij\alpha\beta} (\bar{d}^i_R \gamma_\mu d^j_R)(\bar{\nu}^\alpha_L \gamma^\mu \nu^\beta_L) \right] . \tag{2.29}$$

We study scenarios with NP coupled to left, right, or vector quark currents. The key assumption of this work is that the NP sector responsible for the R^ν_K signal couples to a single

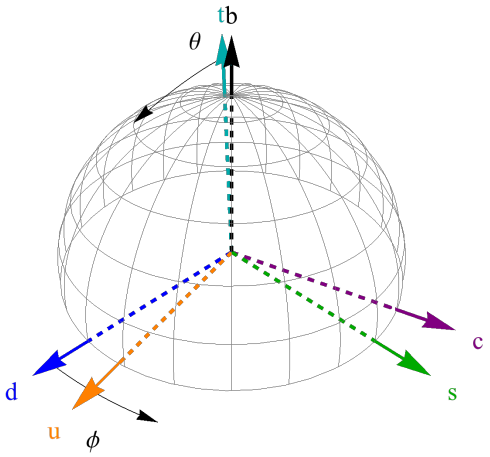


Figure 2.13: SM quark directions of the versor $\hat{n}$, shown in the semi-sphere described by the two angles (θ, ϕ). Left-handed up quarks fit in this space by writing the $SU(2)_L$ quark doublet in the down mass basis: $q_L^i = (V_{ji}^* u_L^j, d_L^i)^t$. See Ref. [189] for details.

direction in quark flavor space, inducing the ROFV structure [189]. In the lepton side we consider instead flavor universality or coupling only to the tau flavor. Under these assumptions, the Wilson coefficient matrices in eq. (2.29) have the following structure:

$$L_{L,R,V}^{ij\alpha\beta} = C_{L,R,V} \times \hat{n}_i \hat{n}_j^* \times \begin{cases} \delta^{\alpha\beta} & \text{for LFU ,} \\ \delta^{\tau\alpha}\delta^{\tau\beta} & \text{for only tau flavor ,} \end{cases} \tag{2.30}$$

where $C_{L,R,V} \in \mathbb{R}$ and $\hat{n}$ is a unitary vector in $U(3)_q$ flavor space. We can parametrize $\hat{n}$ as

$$\hat{n} = \begin{pmatrix} e^{i\alpha_{db}} \sin\theta \cos\phi \\ e^{i\alpha_{sb}} \sin\theta \sin\phi \\ \cos\theta \end{pmatrix} \tag{2.31}$$

where the angles and the phases can be chosen to lie in the following range

$$\theta \in \left[0, \frac{\pi}{2}\right] , \ \phi \in [0, 2\pi) , \ \alpha_{sb} \in \left[-\frac{\pi}{2}, \frac{\pi}{2}\right] , \ \alpha_{db} \in \left[-\frac{\pi}{2}, \frac{\pi}{2}\right] \ . \tag{2.32}$$

The directions in flavor space associated to each SM quark can be shown in the semi-sphere described by the angles (θ, ϕ) as in fig. 2.13.

For any given θ and ϕ, the overall coefficient $C_{L,R,V}$ and the phase α_{sb} can be univocally determined by the fit to $b \to s\nu\bar{\nu}$ observables. As described in detail in App. A.3.1, we find that we can set $L_{L,R,V}^{sb\alpha\beta}$ to be real and positive to be conservative. This yields $\alpha_{sb} = 0$ and

$$C_{L,R,V} \cos\theta \sin\theta \sin\phi = L_{L,R,V}^{sb}\Big|_{\text{best-fit}} \ , \tag{2.33}$$

where in the r.h.s we use the best-fit value resulting from the fit of all $B \to K^{(*)}\nu\bar{\nu}$ observables, including the Belle II excess, which is reported in table 2.13 for the various cases.

The ansatz in eq. (2.30) allows us to correlate the EFT coefficients for $b \to d\nu\bar{\nu}$ and $s \to d\nu\bar{\nu}$ transitions to the one of $b \to s\nu\bar{\nu}$, once the overall scale $C_{L,R,V}$ is fixed for any

Table 2.13: Best-fit values of sb LEFT coefficients from a fit to $B \to K^{(*)}\nu\bar{\nu}$ observables, as obtained in App. A.3.1.

	LFU	ν_τ **only**
RH	$L_R^{sb,\mathrm{LFU}} \approx (11.5\,\mathrm{TeV})^{-2}$	$L_R^{sb\tau\tau} \approx (7.7\,\mathrm{TeV})^{-2}$
LH	$L_L^{sb,\mathrm{LFU}} \approx (14.2\,\mathrm{TeV})^{-2}$	$L_L^{sb\tau\tau} \approx (9.2\,\mathrm{TeV})^{-2}$
V	$L_V^{sb,\mathrm{LFU}} \approx (11.6\,\mathrm{TeV})^{-2}$	$L_V^{sb\tau\tau} \approx (7.7\,\mathrm{TeV})^{-2}$

given θ and ϕ using eq. (2.33). For simplicity we set also $\alpha_{db} = 0$. This means that for any direction in the quark flavor space, *i.e.* any θ and ϕ, we get a precise prediction for the new physics contribution to other observables. The EFT dependence of the relevant meson decays observables is discussed in App. A.1.

The corresponding regions in the $\phi - \theta$ plane, excluded at the 95% CL, are shown in fig. 2.14 for the cases of interest. As we can see from the plots, the most severe bounds come from $K^+ \to \pi^+\nu\bar{\nu}$, which requires $\hat{n}$ to be very close to the direction of the third family. The $B \to \pi\nu\bar{\nu}$ and $B \to \rho\nu\bar{\nu}$ limits, shown together in the picture, exclude instead values of $\phi \approx 0, \pi$, *i.e.* directions of $\hat{n}$ too much aligned to the down quark d.

Among all the possible directions described by $\hat{n}$, a region that is particularly well motivated from the theoretical point of view is the one near the third generation: $\hat{n}_{3^{\mathrm{rd}}} = (\mathcal{O}(V_{td}), \mathcal{O}(V_{ts}), \mathcal{O}(1))$. Indeed, NP is expected to couple more strongly to the third generation of quarks in several explicit models, both to evade the strong flavor and direct searches constraints, that involve light quarks, as well as to address the hierarchy problem of the electroweak scale or the SM flavor puzzle. This scenario can be parametrized by [189]

$$\hat{n}_{3^{\mathrm{rd}}} \propto (a_{bd} e^{i\alpha_{bd}} |V_{td}|, a_{bs} e^{i\alpha_{bs}} |V_{ts}|, 1) \ , \tag{2.34}$$

where $a_{bd,bs}$ are $\mathcal{O}(1)$ real parameters. In fig. 2.14, and in the following of this study, we show with a meshed-red area the region with $|a_{bd,bs}| \in [0.2 - 5]$, without providing a quantitative analysis of these parameters. A detailed analysis of the $U(2)_q$ breaking spurion, in the specific third-generation-philic scenario, will be instead the content of 2.3.

In this section, we focused exclusively on operators that conserve total lepton number L. However, in App. A.3.3 we also discuss a possible interpretation in terms of operators that violate L. There, we show that dimension-six operators with $|\Delta L| = 2$ could potentially accommodate the excess. However, these operators are unlikely to fit within the ROFV framework since they involve both left- and right-handed quark chiralities, which in general couple independently to NP. As a result, these operators fall outside the scope of this analysis and are not discussed further in the main text.

2.2.2 Implications in the SMEFT

Assuming that the new physics scale lies above the electroweak scale, it is natural to work within the Standard Model EFT (SMEFT) framework. The dim-6 operators made of quark

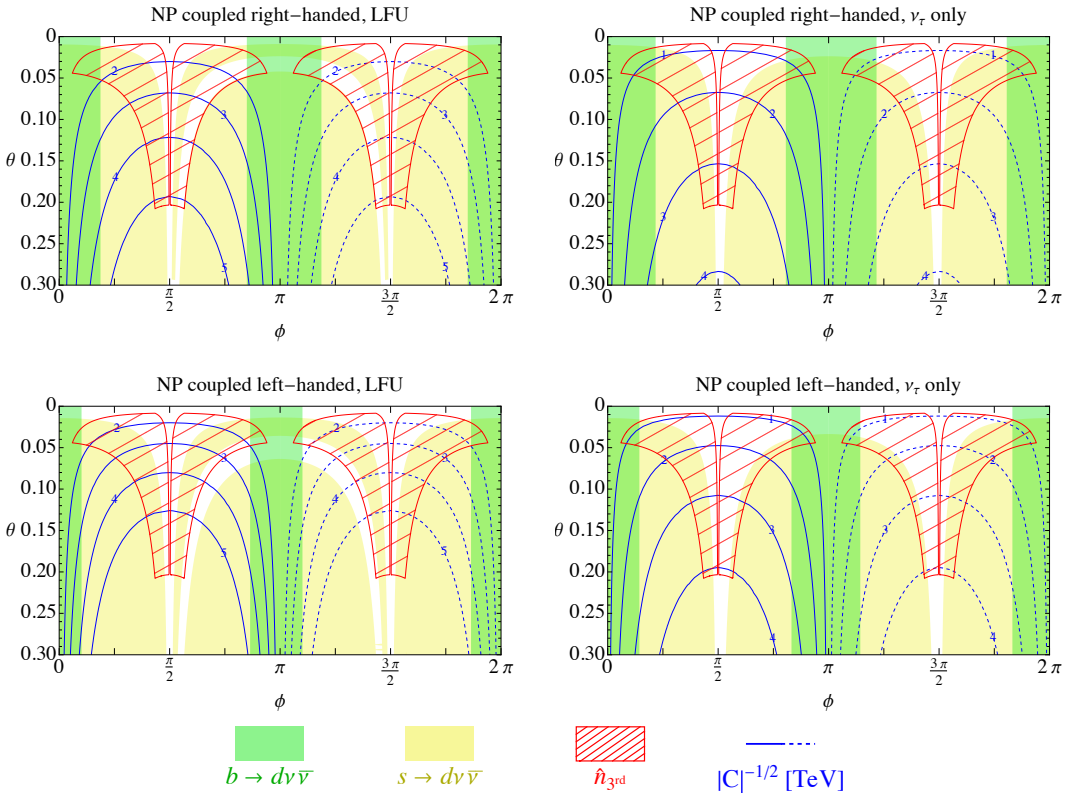


Figure 2.14: Limits in the $\phi - \theta$ plane for NP coupled to right-handed and left-handed quark currents assuming LFU (on the left) or coupling only to tau neutrinos (on the right). The case of vector-like current is very similar to the right-handed one and therefore not reported here. The solid (dashed) blue lines refer respectively to positive (negative) values of C, labelled as $|C|^{-1/2}$ [TeV]. The meshed red region correspond to the one aligned close to the third generation, eq. (2.34) with $|a_{db,sb}| \in [0.2 - 5]$.

currents and affecting the neutrino decay channels are

$$\begin{aligned}
\mathcal{O}_{lq}^{(1)\alpha\beta ij} &= \left(\bar{l}_L^\alpha \gamma_\mu l_L^\beta\right)\left(\bar{q}_L^i \gamma^\mu q_L^j\right) , & \mathcal{O}_{Hq}^{(1)ij} &= \left(H^\dagger \overleftrightarrow{D}_\mu H\right)\left(\bar{q}_L^i \gamma^\mu q_L^j\right) , \\
\mathcal{O}_{lq}^{(3)\alpha\beta ij} &= \left(\bar{l}_L^\alpha \gamma_\mu \sigma_a l_L^\beta\right)\left(\bar{q}_L^i \gamma^\mu \sigma_a q_L^j\right) , & \mathcal{O}_{Hq}^{(3)ij} &= \left(H^\dagger \sigma_a \overleftrightarrow{D}_\mu H\right)\left(\bar{q}_L^i \gamma^\mu \sigma_a q_L^j\right) , \\
\mathcal{O}_{ld}^{\alpha\beta ij} &= \left(\bar{l}_L^\alpha \gamma_\mu l_L^\beta\right)\left(\bar{d}_R^i \gamma^\mu d_R^j\right) , & \mathcal{O}_{Hd}^{ij} &= \left(H^\dagger \overleftrightarrow{D}_\mu H\right)\left(\bar{d}_R^i \gamma^\mu d_R^j\right) .
\end{aligned} \tag{2.35}$$

We choose to work in the down-type quark basis[11], so that the fermionic weak doublets in the operators above are $l_L^\alpha = (\nu_L^\alpha, \ell_L^\alpha)$ and $q_L^i = (V_{ji}^* u_L^j, d_L^i)$, where V is the CKM matrix. Being aligned with the down-quark mass basis, the matching relations between the SMEFT operators in eq. (2.35) and the LEFT ones in eq. (2.29) are, at tree level:

$$\begin{aligned}
L_L^{ij\alpha\beta} &= C_{lq}^{(1)\alpha\beta ij} - C_{lq}^{(3)\alpha\beta ij} + C_{Hq}^{(1)ij}\delta_{\alpha\beta} + C_{Hq}^{(3)ij}\delta_{\alpha\beta} , \\
L_R^{ij\alpha\beta} &= C_{ld}^{\alpha\beta ij} + C_{Hd}^{ij}\delta_{\alpha\beta} .
\end{aligned} \tag{2.36}$$

These SMEFT operators can affect a broad set of low energy observables both via tree and loop level effects, getting sizable constraints on the flavor direction space. Therefore, we

[11] We remind the reader that in section 2.1 we employed instead the up-type basis choice.

enlarge the set of observables under consideration, whose correlation to di-neutrino modes is studied under the ROFV hypothesis. In detail, we include the rare decays $B_s(K_{L,S}) \to \mu^+\mu^-$, meson-mixing constraints, the Higgs and electroweak fit from Ref. [134] (we use an updated version kindly provided by the authors), and data from high-p_T dilepton tails via the HighPT tool [195]. Details on the EFT dependence of these observables are collected in App. A.1.

We assume that the operators are induced at the UV scale $\mu_{\rm UV} \equiv 1$ TeV. The Wilson coefficients are evolved down to the EW scale $\mu_{EW} \sim m_Z$ with the RGEs from Refs. [32–34]. Going across the EW threshold, we match the SMEFT onto the LEFT at tree-level [29] and finally evolve the LEFT operators down to the low energy scales relevant for flavor observables [38]. Following this procedure, we eventually build a global likelihood expressed in terms of the UV Wilson Coefficients. The RG equations are solved numerically using the DSixTools package [31], both above and below the EW scale. Again, the whole procedure can be sketched as in fig. 2.1. In the following, unless otherwise specified, SMEFT coefficients are all understood to be evaluated at the UV scale $\mu_{\rm UV}$.

The analysis strategy for SMEFT operators follows the same steps outlined for the LEFT case. The only difference lies in the fit of the excess from Belle II, now including also the $B_s \to \mu^+\mu^-$ decay, the $R_{K^{(*)}}$ ratios and, in some specific case, the ΔM_{B_s} meson mass mixing, whose information would otherwise be lost as they are mainly affected, trough the correlations coming from the SMEFT or the underlying UV structure, by the same SMEFT coefficients related to $R^{\nu}_{K^{(*)}}$.

Let us start by discussing the Higgs-quark SMEFT operators $O^{(1)}_{Hq}$, $O^{(3)}_{Hq}$ and O_{Hd}. The Belle II excess, as well as the other neutrino channels, are sensitive to the $C^{(+)}_{Hq} \equiv C^{(1)}_{Hq} + C^{(3)}_{Hq}$ and C_{Hd} coefficients. We find that the constraints set by $B_s \to \mu^+\mu^-$ and ΔM_{B_s} do not allow to accommodate the excess in R^{ν}_K. Indeed, an enhancement above $\sim 25\%$ of the SM prediction for $B^+ \to K^+\nu\bar{\nu}$ is highly disfavoured, in agreement with what was pointed out in [172]. We report a more detailed analysis of these cases in App. A.3.2.

In the rest of this study, we focus on four-fermion semileptonic SMEFT operators, specifically $O^{(1)\alpha\beta ij}_{lq}$, $O^{(3)\alpha\beta ij}_{lq}$, and $O^{\alpha\beta ij}_{ld}$. We introduce the combinations $C^{(\pm)}_{lq} = C^{(1)}_{lq} \pm C^{(3)}_{lq}$, *i.e.* the relevant degrees of freedom affecting the observables included in the analysis. The Belle II excess is indeed sensitive to the $C^{(-)}_{lq}$ and C_{ld} coefficients, while $B_s \to \mu^+\mu^-$ provides bounds on the positive combination. Since there could be various different possible combinations of coefficients at the SMEFT level, it is useful to consider which operators are expected to be induced from UV models. Given the EFT scales resulting from fig. 2.14, scenarios that induce the desired effect at the loop level are expected to have light and relatively strongly coupled states, disfavored by direct searches at the LHC. Therefore, in the next section we present a detailed study of simplified models of single-mediator scenarios, that generate different combinations of those semileptonic operators when the heavy state is integrated out at the tree-level.

2.2.3 Simplified Models

The semileptonic operators in eq. (2.35) can be induced by integrating out at the tree-level either leptoquarks or colorless heavy vectors. The possible leptoquarks responsible for those operators are listed in table 2.14, while colorless heavy vectors can either be $Z' \sim (\mathbf{1}, \mathbf{1}, 0)$ or $V' \sim (\mathbf{1}, \mathbf{3}, 0)$. An important feature of these UV models is the generation, at tree or loop

level, of 4-quarks operators that affect $\Delta F = 2$ processes, which are highly constrained by meson-antimeson mixing measurements [196, 197] and whose bounds are so included as well in the following analysis. For details on the generation mechanisms of 4-quarks operators, see App. A.2.

As already explained in the previous Section, we first fit the $B \to K^{(*)}\nu\bar{\nu}$ decays together with the observables correlated trough the SMEFT or the underlying UV structure. The details of the fit and the resulting plots for all the models we consider have been put in App. A.3.2. In the second step we perform the global analysis in the (ϕ, θ) plane including all the other observables discussed previously. For the constraints from high-p_T tails we use the EFT approach, assuming that the mediator's mass is above a few TeV.

Vector triplet V'

First we consider a colorless spin-1 mediator V' transforming as $(\mathbf{1}, \mathbf{3}, 0)$ under the SM group $G_{\rm SM}$, whose interaction to the SM fields is given by the Lagrangian

$$\mathcal{L} \supset \sum_a \left[\sum_{ij} g_q^{ij} (\bar{q}_L^i \gamma^\mu \sigma_a q_L^j) + \sum_{\alpha\beta} g_\ell^{\alpha\beta} \bar{l}_L^\alpha \gamma^\mu \sigma_a l_L^\beta \right] V'_{a\mu} \ . \tag{2.37}$$

According to the ROFV hypothesis of this work, the rank of the quark coupling matrix g_q^{ij} is assumed equal to one, *i.e.* $g_q^{ij} = g_q \hat{n}_i \hat{n}_j^*$. A flavor structure such this could arise, for example, if the quark fields couple to V' only via mixing with a single heavy VLQ doublet Q in the form

$$\mathcal{L}_{V'} \supset g_Q V'_\mu (\bar{Q}\gamma^\mu Q) + M_Q \bar{Q} Q + (M_i \bar{Q} q_L^i + h.c.\ ) \ , \tag{2.38}$$

so that $\hat{n}_i \propto M_i$. Once V' is integrated out, the matching with semileptonic SMEFT operators reads

$$C_{lq}^{(3)\alpha\beta ij} = -\frac{1}{4} \frac{g_q^{ij} g_\ell^{\alpha\beta}}{M_{V'}^2}, \quad C_{lq}^{(1)\alpha\beta ij} = C_{ld}^{\alpha\beta ij} = 0 \ . \tag{2.39}$$

On the lepton side, we consider either LFU or only tau flavor, namely

$$g_\ell^{\alpha\beta} = \begin{cases} g_\ell \ \delta^{\alpha\beta} & \text{for LFU} \ , \\ g_\ell \ \delta^{\tau\alpha}\delta^{\tau\beta} & \text{for only tau flavor} \ . \end{cases} \tag{2.40}$$

Following this, we can write $C_{lq}^{(3)\alpha\beta ij} = C \ \hat{n}_i \hat{n}_j^* \ (g_\ell^{\alpha\beta}/g_\ell)$, where $C = g_q g_\ell / 4M_{V'}^2$. From the 2D fits of R_K^ν in App. A.3.2 (fig. A.9), we observe that $B_s \to \mu^+\mu^-$ highly disfavours any enhancement of R_K^ν in the LFU case. On the other hand, a coupling to only tau flavor allows to accommodate the Belle II result. Assuming a real and positive EFT coefficient to be conservative, we find a best-fit value

$$C_{lq}^{(-)\tau\tau sb}\Big|_{\rm best-fit} \approx (9.1\,\text{TeV})^{-2} \ . \tag{2.41}$$

Setting this value, we then plot the excluded region at 95% in the $\phi - \theta$ plane due to observables correlated trough the ROFV structure in fig. 2.15. We find again that $K \to \pi\nu\bar{\nu}$ decay is the strongest constraint, forcing $\phi \sim \frac{\pi}{2}, \frac{3\pi}{2}$ to evade the bounds, but differently from the LEFT case, the small θ region is now forbidden by high-p_T tails and EW data. With these parameters, the contribution to $b \to c\tau\nu$ transition is small and the effect in $R(D^{(*)})$ is

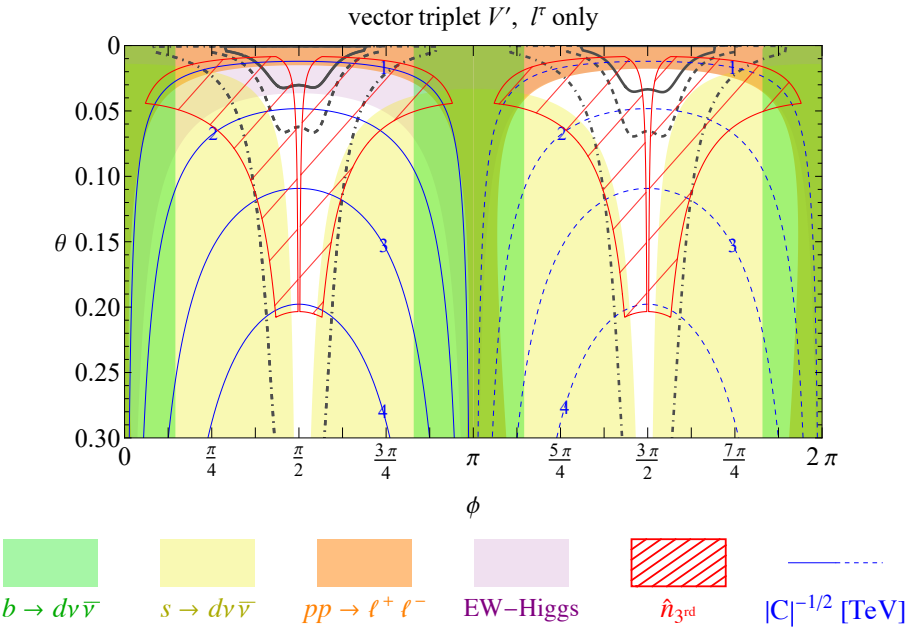


Figure 2.15: Most important limits on the $\phi - \theta$ plane for a V' mediator. Contours of the regions excluded by $\Delta F = 2$ observables are shown for $|g_q/g_\ell| = 0.1$(solid), 0.05(dashed) and 0.01(dot-dashed). The solid (dashed) blue lines refer respectively to positive (negative) values of $C = g_q g_\ell / 4M^2_{V'}$, labelled as $|C|^{-1/2}$ [TeV]. The meshed red region correspond to the to the third generation alignment, eq. (2.34) with $|a_{db,sb}| \in [0.2 - 5]$.

limited to ~ 4 percent or less. Furthermore, $\Delta F = 2$ operators are induced at the tree-level, proportionally to $g_q^2/M^2_{V'}$, see eq. (A.92). Compared to $C_{lq}^{(-)\tau\tau ij}$ they depend on the ratio $|g_q/g_\ell|$, which is an independent variable: smaller values suppress $\Delta F = 2$ effects. Contours of the region excluded by meson-antimeson mixing at 95% are shown for $|g_q/g_\ell| = 0.1$, 0.05 and 0.01. It is clear that we need a certain hierarchy between the coupling to quarks and tau, approximately $|g_q/g_\ell| \lesssim 0.05$, in order to have a viable scenario. Such maximal allowed value, combined with the constraint $g_\ell \lesssim 2.3$ coming from the tool of perturbative unitary (PU) [198] and the fixed best-fit value in eq. (2.41), imply an upper limit for the vector mass:

$$M_{V'} \lesssim 1391 \text{ GeV} \left(\frac{|g_q/g_\ell|^{\max}}{0.05}\right)^{1/2} |\sin\theta\cos\theta\sin\phi|^{\frac{1}{2}} \tag{2.42}$$
$$\approx 762 \text{ GeV} \left(\frac{|g_q/g_\ell|^{\max}}{0.05}\right)^{1/2} \left|\frac{\theta}{0.3}\right|^{1/2} ,$$

where in the last step we approximate $\sin\theta \sim \theta$ and $\cos\theta \sim \sin\phi \sim 1$ as found from our analysis. Such a light mass invalidates our use of the limits from high-p_T tails, which employ the EFT approximation for heavy mediators. Nevertheless, we can consider the resonant channel $pp \to V'^0 \to \tau\tau$, and the corresponding search by ATLAS [199, 200]. In our setup, since $|g_q/g_\ell| \ll 1$, the branching ratio to the tau pair will be $\sim 1/2$ and given the preference for having $\hat{n}$ aligned to the third generation (small θ) the production cross section will be dominated by $b - \bar{b}$ fusion (for completeness we include contributions from all quarks). Notwithstanding the large value of g_ℓ, the width of the vector is approximately

$\Gamma_{\rm tot}/M_{V'} \approx 14\%$ so we use the narrow width approximation to obtain the total cross section:

$$\sigma(pp \to V'^0 \to \tau^+\tau^-) \approx \frac{4\pi^2}{3}\mathcal{B}(V'^0 \to \tau^+\tau^-) \sum_{i,j=u,d,s,c,b} \frac{\Gamma(V'^0 \to q^i\bar{q}^j)}{M_{V'}} \frac{2}{s_0}\mathcal{L}_{q^i\bar{q}^j}(M_{V'}) \ , \quad (2.43)$$

where $s_0 = (13\ \text{TeV})^2$, $\mathcal{L}_{q^i\bar{q}^j}(E)$ is the $q^i - \bar{q}^j$ parton luminosity and $\Gamma(V'^0 \to q^i\bar{q}^j) = \frac{M_{V'}N_c}{24\pi}|g_q^{ij}|^2$. We include all neutral-current (i,j) combinations, including flavor-violating ones. For each value of $\theta - \phi$ we fix $M_{V'}$ at the upper limit from eq. (2.42), set $g_\ell = g_\ell^{\max} \approx 2.3$, and then fix g_q by imposing the best-fit value for $C_{lq}^{(-)\tau\tau sb}$. Doing so we have all parameters required to compute the cross section and we can compare with the upper limit from ATLAS [199, 200]. We find that the whole region allowed by the global fit (white region in fig. 2.15) is excluded for values $\theta \lesssim 0.22$, see fig. 2.16.

In addition to this, another possible direct-search channel for such vectors is electroweak pair-production, *i.e.* $pp \to V^+V^-$ or $V^\pm V^0$, with subsequent decays into taus and neutrinos. The analysis of Ref. [201] looked for pair-produced charginos decaying into taus and missing energy, obtaining an upper limit of about 630 GeV for light LSP. This analysis could be recasted to derive a limit on the V' mass, however the coupling to EW gauge bosons would introduce further model dependence via the presence of a possible non-minimal coupling. This analysis goes well beyond the purpose of our work, so we do not pursue it further.

Vector singlet Z'

We turn now to a colorless spin-1 mediator Z' transforming as $(\mathbf{1},\mathbf{1},0)$ under $G_{\rm SM}$, with couplings

$$\mathcal{L} \supset \left[\sum_{ij} g_L^{ij}(\bar{q}_L^i\gamma^\mu q_L^j) + \sum_{ij} g_R^{ij}(\bar{d}_R^i\gamma^\mu d_R^j) + \sum_{\alpha\beta} g_\ell^{\alpha\beta}\bar{l}_L^\alpha\gamma^\mu l_L^\beta\right] Z'_\mu \ . \quad (2.44)$$

We are interested in scenarios where the mediator couples to a quark current with only left ($g_R^{ij} = 0$), right ($g_L^{ij} = 0$) or vector ($g_L^{ij} = g_R^{ij}$) couplings, denoted respectively as $Z'_{L,R,V}$.

However, we immediately discard the vector combination scenario Z'_V as it is non trivial to justify a ROFV structure for it and furthermore it is highly disfavoured by meson-antimeson mixing constraints, as they would require a larger hierarchy among the lepton and quark couplings, namely $|g_q/g_\ell| \lesssim \mathcal{O}(10^{-3})$, with respect to the case with $Z'_{L,R}$ mediator. So we will not discuss further this option and hence focus on $Z'_{L,R}$. We then assume the quark coupling matrix for both these mediator to have the ROFV structure $g_{L,R}^{ij} = g_q\hat{n}_i\hat{n}_j^*$. New $Z'_{L,R}$s with such coupling structure are justified by UV scenarios with heavy vector-like quarks, as already pointed out for V'. The tree-level matching with the relevant semileptonic SMEFT operators reads

$$C_{lq}^{(1)\alpha\beta ij} = -\frac{g_L^{ij}g_\ell^{\alpha\beta}}{M_{Z'}^2}, \quad C_{lq}^{(3)\alpha\beta ij} = 0, \quad C_{ld}^{\alpha\beta ij} = -\frac{g_R^{ij}g_\ell^{\alpha\beta}}{M_{Z'}^2} \ , \quad (2.45)$$

where, on the lepton side we consider the same cases as done for the vector triplet, eq. (2.40).

The usual 2D fits of the Belle II result can be found in App. A.3.2. In general, we find that we can accommodate the excess in all the scenarios, expect for the case of a Z'_R with LFU couplings. However, we discard Z'_L boson with LFU coupling as well as it is highly disfavoured by the $\Delta F = 2$ constraints, which would require a larger hierarchy among the lepton and

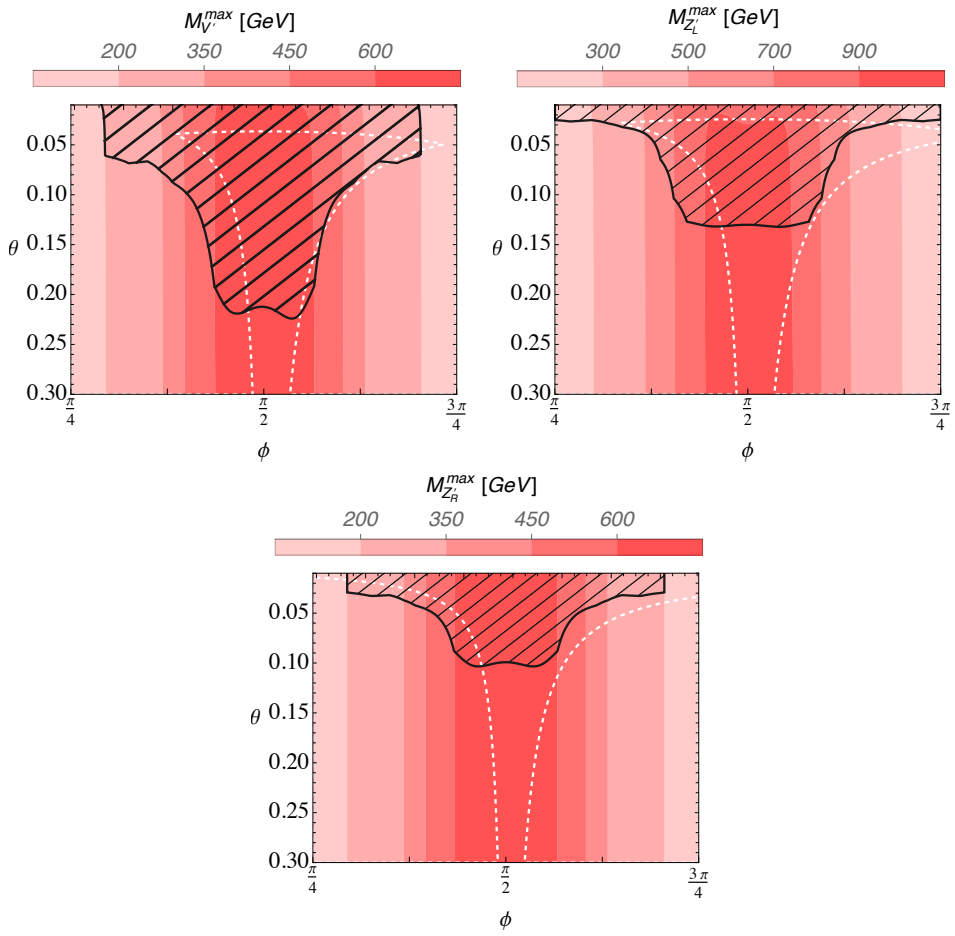


Figure 2.16: Maximal allowed values of the mediator mass in the $\phi - \theta$ around $\phi \sim \pi/2$ for V' and $Z'_{L,R}$ with couplings to only tau leptons. The meshed black region is excluded by ATLAS trough the direct search of $pp \to X \to \tau^+\tau^-$ [200]. The region outside the dashed white line is excluded at 95% by the same observables of fig. 2.15 and 2.17 except for the high-p_T dilepton tails whose constraint does not hold at such small values of the mediator mass. The results for the region around $\phi \sim 3\pi/2$ are qualitatively similar to these.

quark couplings, namely $|g_q/g_\ell| \lesssim \mathcal{O}(10^{-2})$, respect to the case with lepton coupling only to tau flavor. Assuming real coefficients, we find the best-fit values

$$C_{lq}^{(-)\tau\tau sb}\Big|_{Z_L,\text{best}-\text{fit}} \approx (9.2\,\text{TeV})^{-2}\,, \quad C_{ld}^{\tau\tau sb}\Big|_{Z_R,\text{best}-\text{fit}} \approx (7.7\,\text{TeV})^{-2}\,. \tag{2.46}$$

Using these values, the correlation with other observables under the ROFV hypothesis is displayed in fig. 2.17. We can notice that the most severe bounds come again from $K \to \pi\nu\bar{\nu}$ that requires $\hat{n}$ to be very close to the direction of the third family while, as already discussed for the V' case, the small θ region is excluded at the SMEFT level by high $-\,p_T$ tails or by EW data. Contours of the region excluded by meson-antimeson mixing at 95% are shown for $|g_q/g_\ell| = 0.1$, 0.05 and 0.01. As in the vector triplet case, a hierarchy between lepton and quark couplings, namely $|g_q/g_\ell| \lesssim 0.05$, is required.

The discussion on the upper limit on the Z' mass and corresponding direct searches follows analogously to the previous section, with the main difference that the Z' cannot

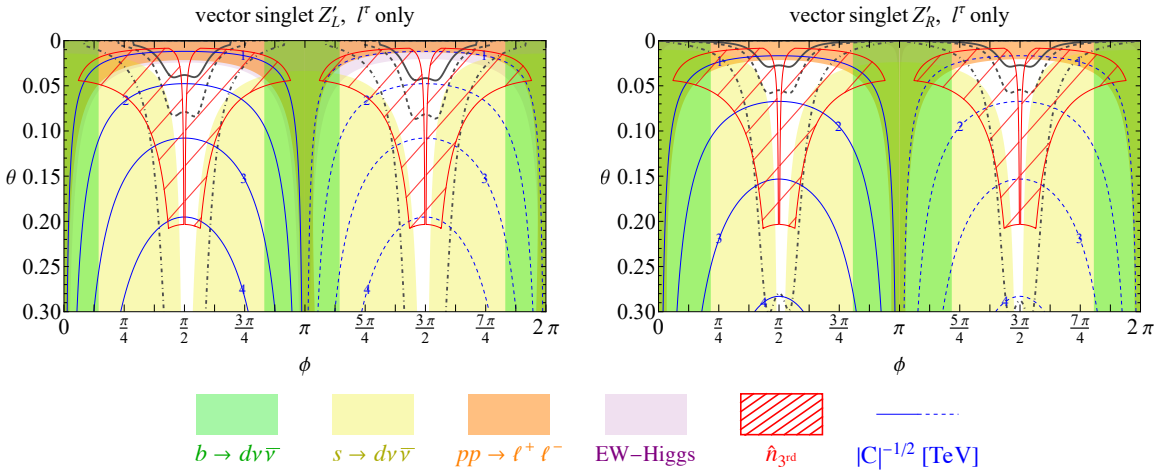


Figure 2.17: Limits in the $\phi - \theta$ plane for Z'_L and Z'_R mediators. Contours of the regions excluded by $\Delta F = 2$ observables are shown for $|g_q/g_\ell| = 0.1$(solid), 0.05(dashed) and 0.01(dot-dashed). The solid (dashed) blue lines refer respectively to positive (negative) values of $C = -g_q g_\ell / M^2_{Z'}$, labelled as $|C|^{-1/2}$ [TeV]. The meshed red region correspond to the to the third generation alignment, eq. (2.34) with $|a_{db,sb}| \in [0.2 - 5]$.

be pair-produced via electroweak interactions so $\tau^+\tau^-$ resonant production is the dominant search channel. From the maximal value of $|g_q/g_\ell|$ allowed by meson mixing we can derive an upper limit for the vector mass after setting g_ℓ at the maximal value from perturbative unitarity, $g_\ell^{\max} \approx 1.65$. In this case the branching ratio into taus is expected to be equal to 1/2 with good accuracy and we can compute the signal cross section as in eq. (2.43) after solving for g_q by imposing the best-fit values in eq. (2.46). In the case of Z'_R we do not include the contribution from u and c quarks, since it couples only to right-handed down quarks. The excluded region in the two models can be seen in fig. 2.16, corresponding to a lower limit $\theta \gtrsim 0.13$ (0.10) for Z'_L (Z'_R).

Leptoquarks

Leptoquarks (LQs) are hypothetical BSM states that mediate interactions between leptons and quarks. Since LQs interacting with lepton fields of different flavor would generate lepton flavor violating couplings once integrated out, we assume couplings only to the tau fields for these type of single-mediator simplified models. In this case they naturally yield a Rank-One structure, where the matching of the coefficient C of eq. (2.33) to the LQ coupling and mass is shown in table 2.14 while $\hat{n}_i$ is proportional to the LQ coupling to the SM fields as $\lambda_{i\tau} \equiv \lambda\ \hat{n}_i$.

In our analysis we also consider meson-antimeson mixing effects coming from loop-induced four-quark operators (see App. A.2 for details). To do so, we set $m_{LQ} = 2$ TeV as benchmark point, which is beyond the lower limit of 1.3 (1.5) TeV obtained by direct searches for scalar (minimally coupled vector) LQ coupled to third generation SM fermions [161].

The resulting 2D fits of the Belle II excess for all the LQs listed in table 2.14 can be found in App. A.3.2. Among the various leptoquarks we focus on $\tilde{R}_2$ and V_2, which give the best fit to the R^ν_K excess as shown in fig. A.10, and on S_1, whose fit is slightly worse than the former, as an example of LQ coupled to left-handed quarks. This is understood by the

LQ	Spin	$G_{\rm SM}$	Interaction term	SMEFT coeff.	C
S_1	0	$(\bar{\mathbf{3}},\mathbf{1},1/3)$	$\lambda^*_{i\tau}(\overline{q_L^{i,c}}\epsilon l_L^\tau)S_1$	$C_{lq}^{(1)}=-C_{lq}^{(3)}$	$\frac{1}{2}\frac{\lvert\lambda\rvert^2}{m_{LQ}^2}$
S_3	0	$(\bar{\mathbf{3}},\mathbf{3},1/3)$	$\lambda^*_{i\tau}(\overline{q_L^{i,c}}\epsilon\sigma_a l_L^\tau)(S_3)_a$	$C_{lq}^{(1)}=3C_{lq}^{(3)}$	$\frac{1}{2}\frac{\lvert\lambda\rvert^2}{m_{LQ}^2}$
U_3	1	$(\mathbf{3},\mathbf{3},2/3)$	$\lambda_{i\tau}(\overline{q_L^i}\gamma_\mu\sigma_a l_L^\tau)(U_3^\mu)_a$	$C_{lq}^{(1)}=-3C_{lq}^{(3)}$	$-\frac{1}{2}\frac{\lvert\lambda\rvert^2}{m_{LQ}^2}$
$\tilde{R}_2$	0	$(\mathbf{3},\mathbf{2},1/6)$	$\lambda_{i\tau}\overline{d_R^i}(l_L^\tau\epsilon\tilde{R}_2)$	C_{ld}	$-\frac{1}{2}\frac{\lvert\lambda\rvert^2}{m_{LQ}^2}$
V_2	1	$(\bar{\mathbf{3}},\mathbf{2},5/6)$	$\lambda^*_{i\tau}\overline{d_R^{i,c}}\gamma_\mu(l_L^\tau\epsilon V_2^\mu)$	C_{ld}	$\frac{\lvert\lambda\rvert^2}{m_{LQ}^2}$

Table 2.14: List of the leptoquark fields relevant for this work. Here $\epsilon\equiv i\sigma_2$ acts on the isospin indices.

fact that they induce a right-handed quark current, preferred by data over the left-handed one (see fig. 2.12). The scalar triplet S_3 performs slightly worse than S_1 due to the larger contribution to meson mixing and the vector triplet U_3 is expected to induce an even larger effect in $\Delta F=2$ observables, although for a precise computation it would be necessary to introduce a UV-completion for the vector, resulting in a model-dependent analysis. As usual, we find that we can set $C_{lq}^{(-)\tau\tau sb}$ or $C_{ld}^{\tau\tau sb}$ to be real and positive to be conservative. This yields $\alpha_{sb}=0$ while the best-fit values of $C_{lq}^{(-)\tau\tau sb}$ or $C_{ld}^{\tau\tau sb}$ are respectively

$$\begin{aligned} C_{lq}^{(-)\tau\tau sb}\big|_{S_1,\text{best}-\text{fit}} &\approx (8.5\,\text{TeV})^{-2}\,,\\ C_{ld}^{\tau\tau sb}\big|_{\tilde{R}_2,\text{best}-\text{fit}} &\approx (7.5\,\text{TeV})^{-2}\,,\\ C_{ld}^{\tau\tau sb}\big|_{V_2,\text{best}-\text{fit}} &\approx (7.5\,\text{TeV})^{-2}\,. \end{aligned} \tag{2.47}$$

Once the overall coefficient is determined from $b\to s\nu\bar{\nu}$ data, we can constrain the direction in the quark flavor space, *i.e.* θ and ϕ, using the other observables correlated to R_K^ν in the ROFV hypothesis. Again, for simplicity we set $\alpha_{db}=0$. The corresponding constrained regions in the $\phi-\theta$ plane are shown in fig. 2.18 for the cases of our interest. Since $C_{lq}^{(-)\tau\tau sb}$ or equivalently $C_{ld}^{\tau\tau sb}$ is set to be positive, the values of ϕ are restricted to $[0,\pi]$ or to $[\pi,2\pi]$ depending on if the LQ induces respectively a positive or negative overall coefficient C. From the plot we can read that for the S_1 case, the small θ region gets constrained by EW data, specifically the measurement of the $Z\to\tau\tau$ coupling, due to the mixing along the RG evolution of $C_{Hl}^{(+)}$ with $C_{lq}^{(-)}$ (see eq. (A.89)), but it is not bounded by dilepton tails as the positive combination $C_{lq}^{(+)}$ vanishes for S_1. Viceversa, $\tilde{R}_2$ and V_2 get the strongest bound at small θ from high-p_T di-tau tails. These constraints are expected to improve substantially from future measurements at (HL-)LHC. Using the projections from the HighPT tool [195], we verified that the bounds on the Wilson coefficients will improve by a factor of approximately 2. Similar improvements are expected also for the colorless vectors. As for V', also for the leptoquarks the contribution to $R(D^{(*)})$ is always negligible and cannot address the observed deviation from the SM prediction. Different values of the LQ coupling $|\lambda|$ are outlined by blue contours in fig. 2.18. Furthermore, a PU bound on

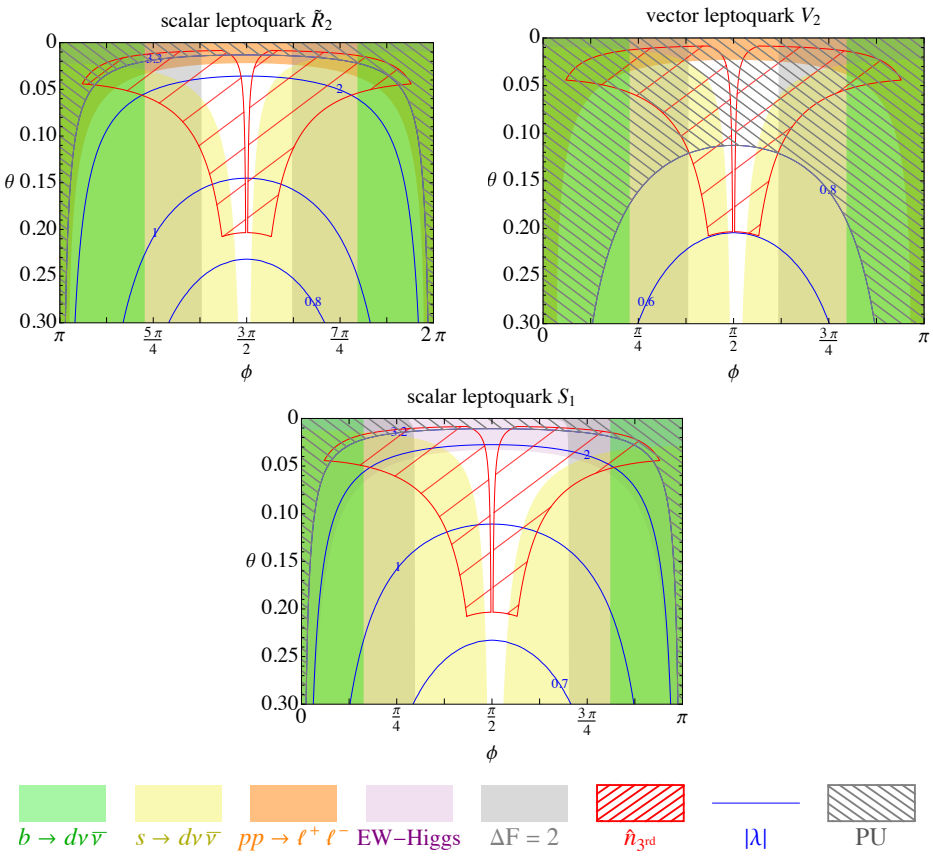


Figure 2.18: Limits in the $\phi-\theta$ plane for S_1, $\tilde{R}_2$ and V_2 leptoquarks with mass $m_{\rm LQ} = 2$ TeV. The solid blue lines refer to values of the LQ coupling $|\lambda|$. The meshed red region correspond to the one aligned to the third generation of quarks up to $\mathcal{O}$(CKM) rotations, eq. (2.34), with $|a_{db,sb}| \in [0.2 - 5]$. The dashed gray region is exclude by the argument of perturbative unitary.

λ can be computed by considering all the $2 \to 2$ scattering in the model as discussed in Refs. [198, 202]. By direct calculation one gets

$$|\lambda| \lesssim \begin{cases} 3.2 & \text{for } S_1 \ , \\ 3.3 & \text{for } \tilde{R}_2 \ , \\ 0.8 & \text{for } V_2 \ . \end{cases} \tag{2.48}$$

Such bound actually excludes a relevant portion of the parameter space in the V_2 plot, while we are safely below the PU threshold for S_1 and $\tilde{R}_2$.

We note that $\tilde{R}_2$ and V_2 generate the same semileptonic coefficient C_{ld}, albeit with opposite overall sign, and same four-quark operator (see App. A.2), so that they exhibit a similar behaviour. However, most of the allowed region for V_2 is excluded by the perturbative unitarity bound, eq. (2.48), as clear from fig. 2.18.

When compared to V' and Z' vectors, that require a large hierarchy between the couplings to quarks and to leptons in order to pass $\Delta F = 2$ constraints, leptoquarks enjoy an automatic loop suppression of flavor mixing. We therefore identify S_1 and $\tilde{R}_2$ as the most favoured single-mediator simplified models to accommodate the observed enhancement in Belle II

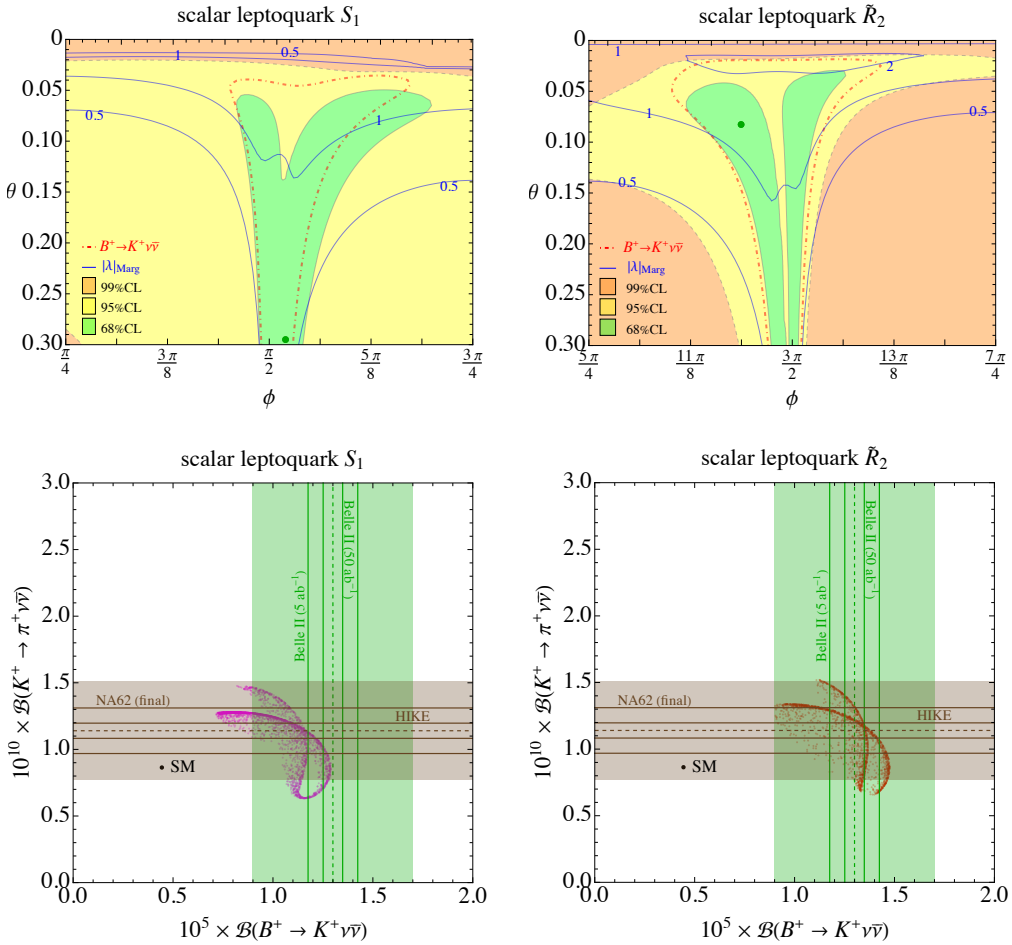


Figure 2.19: Top row: preferred region in the $\phi - \theta$ plane by the global fit for the S_1 and $\tilde{R}_2$ leptoquarks, where the value of $|\lambda|$ has been marginalised. In blue we show iso-lines of the value of $|\lambda|$ that marginalizes the fit. Bottom row: we show points taken from a random scan inside of the 1σ region of the global fit (green region in the plots above), mapped in the plane of $B^+ \to K^+\nu\bar{\nu}$ and $K^+ \to \pi^+\nu\bar{\nu}$. We overlay the present 1σ constraints as well as future prospects.

measurement of $B^+ \to K^+\nu\bar{\nu}$ decay.

Motivated by these results, we proceed with a further investigation of the region at small θ and $\phi \sim \frac{\pi}{2}$ or $\frac{3\pi}{2}$ through the following procedure. We consider the complete χ^2 of our analysis (including so both $b \to s$ transitions and all the possible correlated observables) that depends on the overall SMEFT coefficient C and on the angle variables θ, ϕ.[12] We profile the χ^2 over the C parameter, *i.e.* over $|\lambda|$ since we fix $m_{LQ} = 2$ TeV, namely at each (θ, ϕ) point we substitute the value of $|\lambda|$ that minimise the chi-square. The resulting $\chi^2_{\rm profiled}(\theta, \phi)$ is used to derive the 1σ, 2σ and 3σ regions shown in the top row of fig. 2.19. The solid blue lines correspond to the value of $|\lambda|$ that minimised the χ^2. The dot-dashed red line represents the 1σ region preferred by the excess in $B^+ \to K^+\nu\bar{\nu}$.

Finally, we map the 1σ (green) regions of the top row in fig. 2.19 into regions in the $\mathcal{B}(B^+ \to K^+\nu\bar{\nu}) - \mathcal{B}(K^+ \to \pi^+\nu\bar{\nu})$ plane, in order to show the predicted values of these

[12] We set $\alpha_{sb} = \alpha_{db} = 0$ for simplicity.

di-neutrino modes for the two simplified models under examination. We overlay the present 1σ constraints by Belle-II and NA62, as well as future prospects by the same experiments [170] as well as by the proposed HIKE experiment at CERN [193]. It is clear that future measurements will have a strong power to confirm or disprove definitely the present excess observed by Belle-II, and to resolve the specific direction in flavor space for the new physics couplings under the ROFV hypothesis.

2.2.4 Summary

Numerous groundbreaking advancements in particle physics have been achieved through the measurement of low-energy observables. It is also likely that a future discovery of physics beyond the SM will come from such experiments. In this case, correlations among these observables are crucial for establishing new physics and identifying the appropriate UV extension of the Standard Model. However, obtaining correlations requires making theoretical assumptions, particularly regarding the flavor structure of the new physics. A generic model-independent parametrization results in a complex analysis with numerous couplings, potentially obscuring the underlying UV physics and yielding generic correlations. Conversely, a model-dependent approach typically yields strong correlations but is limited in validity to the specific model.

In our study, we propose a simple and motivated ansatz for the new physics that offers a balance between predictivity and generality: the Rank One Flavor Violation (ROFV) hypothesis [189]. In this scenario, new physics couples to a specific direction in flavor space, which can be varied enabling a comprehensive exploration of this hypothesis using only a few parameters.

We specifically examine the recent hint of a potential deviation in the $B \to K\nu\bar{\nu}$ decays as observed by the Belle II collaboration.[13] Possible correlations arise from Lorentz symmetry, SM gauge symmetry, and flavor structure. While we consider the most general operators for Lorentz and gauge symmetries, we employ our ROFV hypothesis for the flavor aspect of the analysis.

At the LEFT analysis level, the minimal correlation under scrutiny is that with the decay $B \to K^*\nu\bar{\nu}$. Our primary findings are depicted in fig. 2.12. We find that right-handed and vector currents for quarks are favored over the left-handed counterpart, as the latter yields $R^\nu_{K^*} = R^\nu_K$, and currently, there is a good agreement between the observed value of $B \to K^*\nu\bar{\nu}$ and the Standard Model prediction. Our analysis using ROFV indicates that most important observable correlating with $B \to K\nu\bar{\nu}$ is the transition $K \to \pi\nu\bar{\nu}$, while from a more theoretical standpoint, the preference lies within the region aligned with the bottom quark.

Regarding the SMEFT, we have identified six potential operators that could contribute to $b \to s\nu\bar{\nu}$ at the tree level. Among them, three involve the Higgs doublet but are not considered phenomenologically viable due to constraints from $B_s \to \mu^+\mu^-$ and ΔM_{B_s}, confirming the finding of [172]. The remaining three are semileptonic four-fermion operators. Instead of conducting an exhaustive examination, we focused on simplified models of single-mediator scenarios, which yield fixed combinations of these semileptonic operators when the heavy

[13] Contrary to Refs. [171, 172] we conservatively use the combination of Belle II [49] and Belle [50], resulting in a reduced value for the central value of R^ν_K respect to the cited works.

state is integrated out at the tree level. Loop level mediator are not considered in our work because they have to be very light and strongly coupled to reproduce the anomalous effect and this scenario seems disfavoured by the present data.

Our primary phenomenological finding utilizing the ROFV hypothesis suggests the potential for significant effects in $K \to \pi\nu\bar{\nu}$. For this reason, and particularly for the most promising candidates S_1 and $\tilde{R}_2$, we conducted an analysis providing a more detailed understanding of the correlation between this observable and R_K^ν (see fig. 2.19). We emphasize the importance of obtaining better measurements for both observables and present future prospects from experiments such as Belle II and NA62.[14]

On the theoretical front, we emphasize that new physics is favored to primarily couple to the third generation, in both the quark and charged lepton flavor spaces. This strengthens the case of a potential connection between the anomalous data and the Yukawa structure of the Standard Model couplings. The role of neutrino modes in the top-philic framework with a quantitative study of the approximate $U(2)$ symmetry will be the content of the remaining sections of this chapter.

[14] We note that a proposed experiment like HIKE [193] would have been advantageous in elucidating this specific physics case.

2.3 Probing third-generation New physics with $K \to \pi\nu\bar{\nu}$ and $B \to K^{(*)}\nu\bar{\nu}$

In section 2.2, we examined the implications of the most recent measurement of the rare decay $B \to K\bar{\nu}\nu$, carefully exploring correlations with other observables arising from renormalization group evolution and from specific UV model assumptions. This allowed us to identify the most constraining observables within a broad class of scenarios. Most importantly, we showed that the general hypothesis of rank-one flavor violation, when confronted with current experimental constraints, naturally points toward a picture in which new physics, if present at high energy scales, predominantly couples to the third generation of fermions. Moreover, the viable parameter space is found to be consistent with the presence of approximate $U(2)$ flavor symmetries acting on the first two generations.

In the remaining sections of this chapter, building on the insights gained from the previous analysis, we further explore the potential of rare dineutrino modes as sensitive probes of new physics. Indeed, $K \to \pi\nu\bar{\nu}$ and $B \to K^{(*)}\nu\bar{\nu}$ are the only FCNC transitions involving third-generation leptons for which current measurements have reached the SM sensitivity. We therefore focus on the specific scenario of third-generation-philic interactions, corresponding to $\theta \approx 0$ in the language introduced earlier. We allow for the presence of effective operators involving light quarks through the insertion of a $U(2)_q$-breaking spurion $\tilde{V}$, characterized by a minimal set of parameters, ϵ and κ, which respectively quantify the size and direction of the $U(2)_q$ breaking structure. The goal of this study is to focus on these parameters, deriving constraints and quantifying the viability of a minimal $U(2)_q$ breaking scenario, *i.e.* $\kappa \approx 1$.

In section 2.3.1, for convenience, we briefly revisit the EFT setup and introduce the spurion $\tilde{V}$ relevant for this analysis, providing simplified analytic expressions that illustrate the role of the $U(2)_q$ breaking terms in flavor observables. In section 2.3.2, we perform a numerical study to determine the preferred values of the parameters ϵ and κ, along with the current and projected experimental constraints. Finally, we comment on possible explicit UV completions that realize such a structure. Conclusions are drawn in section 2.3.4.

2.3.1 EFT setup and the $U(2)_q$ breaking spurion

As anticipated, we work within an EFT framework assuming heavy NP predominantly coupled to third-generation fermions. More precisely, we assume that the only dynamical fields are the SM ones, and we neglect $U(2)^5$–invariant operators involving light fermions. On the other hand, since we are interested in describing flavor mixing in the quark sector, we consider operators built in terms of the leading $U(2)_q$–breaking spurion $\tilde{V}$ [20] which is responsible for the heavy→light mixing in the quark Yukawa couplings. The spurion, which transforms as a doublet under $U(2)_q$, is parameterized as

$$\tilde{V} = -\varepsilon V_{ts} \begin{pmatrix} \kappa V_{td}/V_{ts} \\ 1 \end{pmatrix} . \tag{2.49}$$

The parameters ε and κ are assumed to be real and $O(1)$: ε control the overall size of the spurion (the normalization is chosen such that $3 \to 2$ mixing is positive for $\varepsilon > 0$ in the standard CKM convention), while κ quantifies possible deviation from a minimal $U(2)_q$–breaking structure. The minimal framework corresponds to the limit $\kappa = 1$ [17, 20].

In this setup there is an intrinsic ambiguity on what we denote as third generation in the left-handed quark sector, or better which are the $U(2)_q$ singlet fields. For definiteness, we choose again a down-aligned basis, where the quark doublets are written as $q_L^i = (V_{ji}^\star u_L^j, d_L^i)^T$, with u_L^i and d_L^i denoting the quark mass eigenstates, such that

$$q_L^3 = \begin{pmatrix} V_{ub}^\star u_L + V_{cb}^\star c_L + V_{tb}^\star t_L \\ b_L \end{pmatrix} \tag{2.50}$$

is a $U(2)_q$ singlet. On the lepton side, we focus only on amplitudes sensitive to third-generation leptons, hence the only relevant lepton fields to consider are $l_L^3 = (\nu_\tau, \tau_L)^T$ and τ_R. With these assumptions, the leading semileptonic operators involving only $U(2)^5$–singlet fields are[15]

$$\begin{aligned} O_{lq}^{\pm} &= (\bar{q}_L^3 \gamma^\mu q_L^3)(\bar{l}_L^3 \gamma_\mu l_L^3) \pm (\bar{q}_L^3 \gamma^\mu \sigma^a q_L^3)(\bar{l}_L^3 \gamma_\mu \sigma^a l_L^3)\,, \\ O_S &= (\bar{l}_L^3 \tau_R)(\bar{b}_R q_L^3)\,. \end{aligned} \tag{2.51}$$

The Wilson Coefficients associated to these three operators are dimensionful parameters that we express in units of TeV^{-2}:

$$\mathcal{L}_{\text{eff}}^{\text{NP}} \supset \sum_k C_k O_k + \text{h.c.}\,. \tag{2.52}$$

In principle, in addition to the three operators in eq. (2.51) we should consider all terms generated by the insertion of one or two spurions in each of them, separately, via the replacement $q_L^3 \to \tilde{V}_i q_L^i$. In practice, to avoid the proliferation of free parameters, we assume that the underlying NP leads to a rank-one structure in quark flavor space, as explained in the previous section 2.2. In other words, we assume that NP is aligned to a specific direction in flavor space, and the insertion of spurions describes the misalignment of this direction relative to that of the q_L^3 field in (2.50). In practice, this condition is achieved via the replacement

$$q_L^3 \to q_L^3 + \tilde{V}_i q_L^i \tag{2.53}$$

in the three operators in eq. (2.51).

The EFT framework we are considering is then described by five independent parameters: $C_{\ell q}^+$, $C_{\ell q}^-$, C_S, ε, and κ. The list of the observables included in the analysis and the way they are affected by these parameters is summarized in table 2.15.

Flavor-changing amplitudes

Before presenting the numerical results, it is useful to discuss the implications of the $U(2)_q$ breaking assumptions on the different flavor-changing amplitudes. While the complete EFT predictions are illustrated in detail in the appendix, here we provide some simplified formulae which illustrate the main effects.

Let's start from the contributions to R_D and R_{D^*}. Here NP interfere with a tree-level SM amplitude, hence can be treated as a small correction. Considering only the vector operators

[15] Since we are interested in dineutrino modes, we focus on the semileptonic operators that provide the main tree-level contribution. However, we include a scalar operator to improve the fit to other observables.

	C_S	$C^+_{\ell q}$	$C^-_{\ell q}$	ε	κ	Exp. indication
$\sigma(pp \to \ell\ell)$	✓	✓	✓			bounds on $\mathcal{A}_{\rm NP}$
EWPO		✓	✓			bounds on $\mathcal{A}_{\rm NP}$
R_D, R_{D^*}	✓	✓	✓	✓		$\mathcal{A}_{\rm NP}/\mathcal{A}_{\rm SM} > 0$
$\mathcal{B}(B \to K^{(*)}\mu\bar{\mu})$		✓		✓		$\mathcal{A}_{\rm NP}/\mathcal{A}_{\rm SM} < 0$
$\mathcal{B}(B \to K\nu\bar{\nu})$			✓	✓		$\lvert\mathcal{A}_{\rm SM} + \mathcal{A}_{\rm NP}\rvert^2 > \lvert\mathcal{A}_{\rm SM}\rvert^2$
$\mathcal{B}(K \to \pi\nu\bar{\nu})$			✓	✓	✓	$\lvert\mathcal{A}_{\rm SM} + \mathcal{A}_{\rm NP}\rvert^2 > \lvert\mathcal{A}_{\rm SM}\rvert^2$

Table 2.15: List of observables considered in the analysis, and their sensitivity to the EFT parameters. In the last column we highlight the present hints of deviations from the SM, as emerging from data.

in (2.51) and expanding to first order in their coefficients leads to

$$\begin{aligned} \frac{R_{D^{(*)}}}{R^{\rm SM}_{D^{(*)}}} &\approx 1 + 2{\rm Re}\left(C_{V_L}\right) \\ &\approx 1 - v^2\,(1+\varepsilon)\left(C^+_{lq} - C^-_{lq}\right)\,, \end{aligned} \tag{2.54}$$

where $v = (\sqrt{2}G_F)^{-1/2} \approx 246$ GeV, the explicit expression of C_{V_L} can be found in eq. (A.66) and we have neglected sub-leading terms of $O(\lambda^2)$. As can be noted, the observable receives a non-vanishing correction also in absence of spurion contributions ($\varepsilon \to 0$ limit), while the effect of the spurion is constructive for $\varepsilon > 0$. As is well known, the vector operators $O^\pm_{lq}$ lead to a universal shift in R_D and R_{D^*}, only the scalar operator differentiate among the two observables (see appendix).

As far as FCNC processes are concerned, it is easy to realize that $b \to s$ transitions are sensitive to the insertion of a single spurion (NP amplitude proportional to ε), while $s \to d$ modes are affected by the insertion of two spurions, with an amplitude proportional to $\varepsilon^2\kappa$. In the neutrino modes, NP modifies (at the tree level) the coefficients of the effective Lagrangian (see appendix A.1.1) involving tau neutrinos:

$$\begin{aligned} |C^{\rm SM}_{\tau,bs}| &\to \left| C^{\rm SM}_{\tau,bs} - \varepsilon\frac{\pi v^2}{\alpha} C^-_{lq} \right|\,, \\ |C^{\rm SM}_{\tau,sd}| &\to \left| C^{\rm SM}_{\tau,sd} + \kappa\varepsilon^2\frac{\pi v^2}{\alpha} C^-_{lq} \right|\,. \end{aligned} \tag{2.55}$$

The effect is potentially sizable, given the SM amplitude is loop suppressed. Note that, since $C^{\rm SM}_{\tau,bs} \approx C^{\rm SM}_{\tau,sd}$, the interference between SM and NP amplitude is opposite in the two modes in the limit $\kappa = 1$ and $\varepsilon > 0$. Since in our framework there are no scalar nor right-handed current operators affecting the di-neutrino modes, a firm prediction of this setup is a universal modification of $\mathcal{B}(B^+ \to K^+\nu\bar{\nu})$ and $\mathcal{B}(B \to K^*\nu\bar{\nu})$ relative to their SM values. This differs from what happens in more general beyond-SM frameworks [171, 172, 203].

The last flavor-violating effect we consider is the modification of the $b \to s\ell\bar{\ell}$ amplitude ($\ell = e, \mu$) which occurs from the QED running of the $(\bar{b}_L\gamma^\mu s_L)(\bar{\tau}_L\gamma_\mu\tau_L)$ operator into

$O_9 \propto (\bar{b}_L \gamma^\mu s_L)(\bar{\ell}\gamma_\mu \ell)$ [204, 205]. This results into a lepton-universal shift of the Wilson coefficient C_9, defined as in [204], which can be written as [206]

$$\frac{C_9^{\rm NP}}{C_9^{\rm SM}} \approx \frac{\varepsilon v^2}{3} \frac{C_{lq}^+}{C_9^{\rm SM}} \log\left(\frac{\Lambda^2}{m_\tau^2}\right) \approx 0.23 \times \varepsilon C_{lq}^+ \,. \tag{2.56}$$

The numerical expression has been obtained setting $\Lambda = 1$ TeV (see the appendix for more details). As for $R_{D^{(*)}}$, also in this case the NP effect can at most be a small correction with the respect to the SM, given both NP and SM amplitudes are loop suppressed.

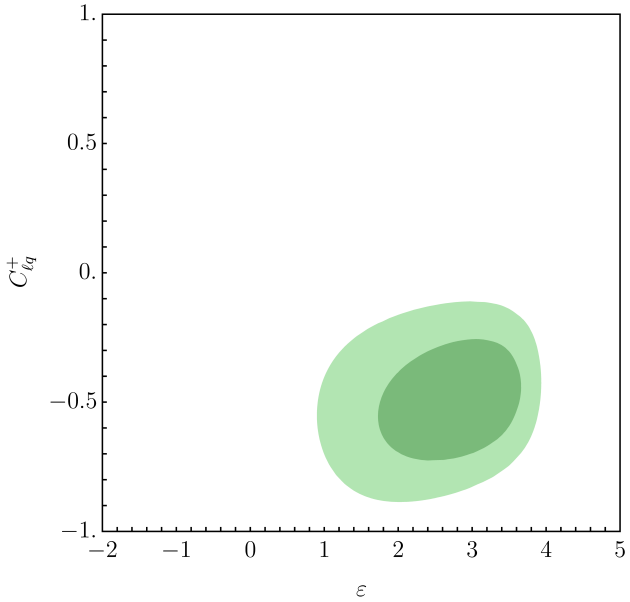


Figure 2.20: Constraints in the C_{lq}^+–ε plane. The green areas denote the parameter regions favored at 1σ and 2σ from a fit to all the observables but the two di-neutrino rare modes.

2.3.2 Numerical Analysis

We now proceed with a combined numerical analysis of the different observables listed in table 2.15. We can distinguish three classes of observables: i) EWPO and direct searches, which provide stringent bounds on $C_{lq}^\pm$ and C_S; ii) R_D, R_{D^*} and $\mathcal{B}(B \to K^{(*)}\mu\bar{\mu})$, where NP is at most a small correction with respect to the SM; iii) the two neutrino modes, where $O(1)$ modifications of the SM amplitude are possible.

There is a partial "factorization" of the different constraints: observables i) and ii) provide a stringent determination of C_{lq}^+ and ε, as illustrated in fig. 2.20. Obviously, the preference for non-vanishing values of C_{lq}^+ and ε is driven by the set ii). In particular, a positive value of ε is favored by eq. (2.54), since it allows a constructive interference between spurion and non-spurion terms in R_D and R_{D^*}, hence maximal contribution at fixed $C_{\ell q}^\pm$, whose absolute size is constrained by set i). The maximal value of ε is not determined by data but by model-dependent considerations: since we assume $\varepsilon = O(1)$, we have added a theoretical likelihood to suppresses values of $|\varepsilon|$ above 3. Scalar contribution do not alter this picture, being strongly constrained by direct searches (the best fit value of C_S is compatible with zero).

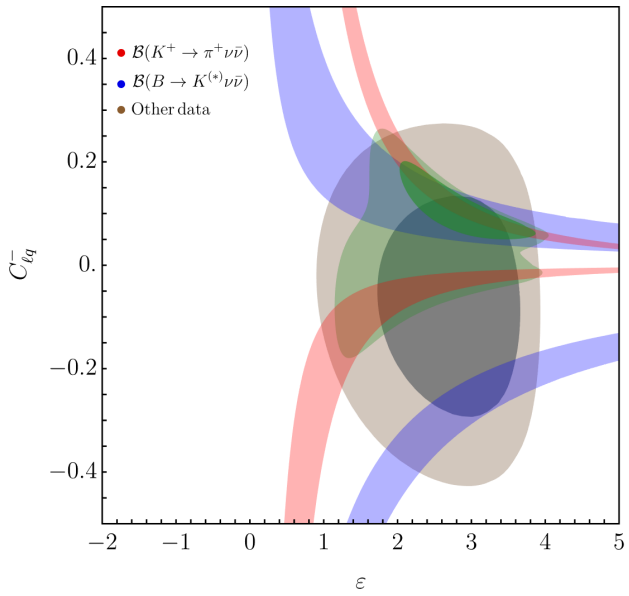


Figure 2.21: Constraints in the $C_{lq}^- - \varepsilon$ plane. The brown areas denote the parameter regions favored at 1σ and 2σ from a fit to all the observables but di-neutrino modes. The regions favored by $\mathcal{B}(B \to K^{(*)}\nu\bar{\nu})$ and $\mathcal{B}(K^+ \to \pi^+\nu\bar{\nu})$, separately, in the limit $\kappa = 1$, are indicated in blue and red, respectively (1σ bands). The green areas are the regions favored by all data at 1σ and 2σ (1σ only around the best fit point).

The two di-neutrino modes have a marginal role in constraining C_{lq}^+ and ε. On the other hand, despite their sizable experimental uncertainty, they already provide a significant constraint on the value of C_{lq}^-. As shown in fig. 2.21, the parameter C_{lq}^- is largely unconstrained by the observables in sets i) and ii), beside its maximal allowed size, while the information from the two di-neutrino modes provides a relevant constraint. Note that in fig. 2.21 the band denoted $\mathcal{B}(B \to K^{(*)}\nu\bar{\nu})$ corresponds to the combined constraint from $\mathcal{B}(B^+ \to K^+\nu\bar{\nu})$ and $\mathcal{B}(B \to K^*\nu\bar{\nu})$, which in our framework have the same functional dependence.

In the limit of minimal $U(2)_q$ breaking, i.e. setting $\kappa = 1$, there is good compatibility of the constraints from the two rare modes already at 1σ, in the parameter region for ε favored by the other data. This is non trivial given the decrease of $\mathcal{B}(K^+ \to \pi^+\nu\bar{\nu})$, compared to its SM value, for $0 < \varepsilon < 2$, as indicated in fig. 2.22. When all data are combined, a positive value of C_{lq}^- is preferred.

Discussion

From the numerical results presented above we can derive the following conclusions.

- The factorization of the constraints implies that the rank-one hypothesis we have implemented is not really tested by present data. As far as the observables i) and ii) are concerned, the only relevant spurion term is O_{lq}^+ (with one spurion): a generic coupling for this operator can thus be reabsorbed in the value of ε. As far as the two di-neutrino modes are concerned, possible $O(1)$ couplings in the relevant operators can be reabsorbed in the values of C_{lq}^- and κ. In other words, given current precision, five

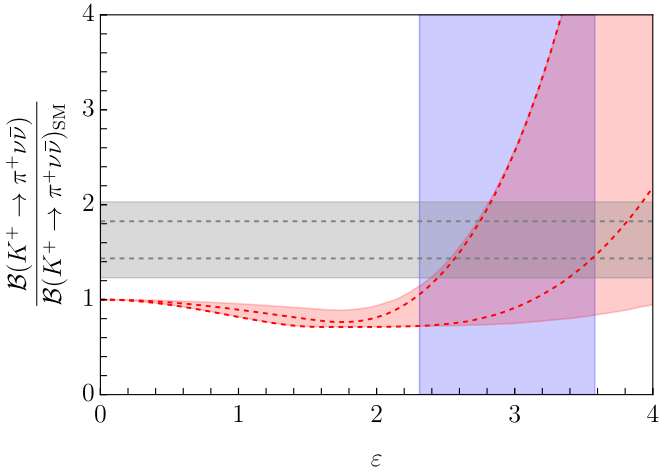


Figure 2.22: Prediction of $\mathcal{B}(K^+ \to \pi^+ \nu\bar{\nu})$ as function of ε, for $\kappa = 1$, using the value of C_{lq}^- determined from all the other observables at 1σ (red band). The blue band indicates the preferred ε values (1σ) from the global fit without $\mathcal{B}(K^+ \to \pi^+ \nu\bar{\nu})$. The gray band indicates the experimental determination of $\mathcal{B}(K^+ \to \pi^+ \nu\bar{\nu})$ at 1σ. The red and gray dashed lines illustrate the change of the respective regions assuming near-future experimental projections for $\mathcal{B}(K^+ \to \pi^+ \nu\bar{\nu})$ and $\mathcal{B}(B \to K^{(*)} \nu\bar{\nu})$ (see text). The red dashed lines are not centered with respect to the red band given the central value of C_{lq}^- changes with the projected branching fractions. We do not include a future projection on the ε (blue) band since this is not controlled only by the di-neutrino modes.

effective parameters are necessary to describe the system in full generality given the main dynamical assumptions of a mildly broken $U(2)^5$ flavor symmetry.

- A non trivial test we can perform with present data is the viability of the hypothesis of a minimal breaking of $U(2)_q$, combined with the rank-one relation between $\mathcal{B}(B \to K^{(*)} \nu\bar{\nu})$ and $\mathcal{B}(K^+ \to \pi^+ \nu\bar{\nu})$. Figs. 2.21–2.22 show that this hypothesis, which corresponds to fix $\kappa = 1$ and reduce the number of free parameters from 5 to 4, is well supported by present data. A further reduction from 4 to 3 parameters, obtained setting $C_S = 0$, is also well supported by data.

- The two di-neutrino modes test scales well above those directly probed at colliders. A clear illustration of this fact is shown in fig. 2.23, where the value of C_{lq}^- is expressed in term of the corresponding effective scale Λ. In principle, combining two modes could lead to a determination of ε completely independent from that obtained from the other flavor-changing observables. Right now this is not very significant given the large experimental uncertainties. Note that the study of normalised kinematic distributions for the di-neutrino modes would not add additional information since in our setup we generate only SM-like effective operators below the electroweak scale (see [203, 207] for non-SM like examples).

- Assuming minimal $U(2)_q$ breaking, the combination of the two di-neutrino modes leads to a 2σ hint of NP. This is evident in fig. 2.24, where we show the favored region in the $\mathcal{B}(B^+ \to K^+ \nu\bar{\nu})$–$\mathcal{B}(K^+ \to \pi^+ \nu\bar{\nu})$ plane from the global fit. As also shown in fig. 2.24,

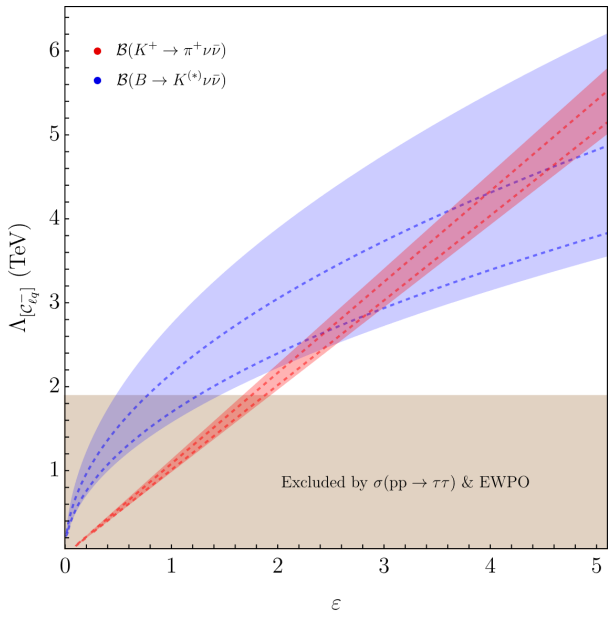


Figure 2.23: Λ vs. ε plane, where Λ is defined by $C_{lq}^- = 1/\Lambda^2$. The blue and red areas indicate present 1σ constraints from $\mathcal{B}(K^+ \to \pi^+\nu\bar{\nu})$ and $\mathcal{B}(B \to K^{(*)}\nu\bar{\nu})$, setting $\kappa = 1$. The 95% CL exclusion limit from direct searches and EWPO are also indicated. The dashed lines illustrate the change of the respective regions assuming near-future experimental projections for $\mathcal{B}(K^+ \to \pi^+\nu\bar{\nu})$ and $\mathcal{B}(B \to K^{(*)}\nu\bar{\nu})$.

relaxing the assumption of minimal $U(2)_q$ breaking the two modes become uncorrelated and the combined significance for a deviation from the SM drops below 95% CL.[16]

- In figs. 2.22–2.24 we illustrate how the individual constraints on the two modes, or the respective measurements, could change in the near future, assuming same central values but halved experimental errors. As can be seen in fig. 2.23, this would allow us to derive a stringent range for ε, testing the overall consistency of this framework and, in particular, the validity of the assumption $\varepsilon = O(1)$. As already stated, a firm prediction of this framework is a relative deviation from the SM identical in $\mathcal{B}(B^+ \to K^+\nu\bar{\nu})$ and $\mathcal{B}(B \to K^*\nu\bar{\nu})$, we thus expect the central value of $\mathcal{B}(B^+ \to K^+\nu\bar{\nu})$ to decrease, as indicated in fig. 2.24. If the central value of $\mathcal{B}(K^+ \to \pi^+\nu\bar{\nu})$ would remain unchanged, the combination of the two modes under the hypothesis of minimal $U(2)_q$ breaking, as in fig. 2.24, would point toward a deviation from the SM well above the 3σ level.

2.3.3 Comparison with explicit models

Vector leptoquark.

The non-vanishing values of $C_{lq}^{\pm}$ and ε are qualitatively in good agreement with the effects associated to a TeV-scale vector leptoquark coupled mainly to the third-generation (see e.g. [208–210]). While the values of C_{lq}^{+} and ε confirm previous findings along this direc-

[16] The small tension of the results of the global fits with the experimental determination of $\mathcal{B}(B^+ \to K^+\nu\bar{\nu})$ is caused by the inclusion of $\mathcal{B}(B \to K^*\nu\bar{\nu})$ data in the global fit.

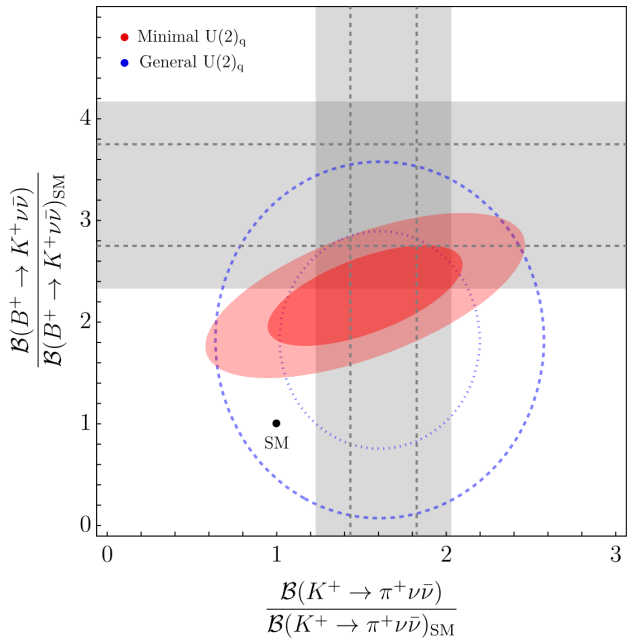


Figure 2.24: Correlation between $\mathcal{B}(B^+ \to K^+\nu\bar{\nu})$ and $\mathcal{B}(K^+ \to \pi^+\nu\bar{\nu})$, normalized to their SM predictions. The red areas denote the parameter regions favored at 1σ and 2σ from a global fit in the limit of minimal $U(2)_q$ breaking ($\kappa = 1$). The dashed and dotted blue curves are 1σ and 2σ regions from a global fit where κ is a free parameter. The gray bands indicate the current experimental constraints, while the dashed gray lines highlight near-future projections assuming halved experimental uncertainties.

tion [206], the di-neutrino modes provide an additional support to this picture indicating $|C_{lq}^+| \gg |C_{lq}^-|$. This is expected given $|C_{lq}^+|$ arises by the tree-level exchange of the leptoquark, while $|C_{lq}^-|$ is generated at the loop level [210].

It is worth stressing that both magnitudes and signs of the NP amplitudes are consistent with predictions made, before the observations of the two decay modes, in complete models where the leptoquark is a massive gauge boson arising from $SU(4)^{[3]} \times SU(3)^{[12]} \to SU(3)_c$ [210–213]. In this case, the constructive interference between SM and NP amplitudes in $B \to K^{(*)}\nu\bar{\nu}$ is unambiguously related to the enhancement of $R_{D^{(*)}}$, as shown first in [210] (based on the results in [211, 212]).

The $K \to \pi\nu\bar{\nu}$ amplitude is more complicated, since non-minimal $U(2)_q$ terms are naturally present; however, as shown in [213], constraints from $\Delta S = 2$ amplitudes point to a scenario that, once expressed in our notation, effectively corresponds to $1.0 \lesssim \mathrm{Re}(\kappa) \lesssim 1.5$. A discussion of the correlations between K and B decays under the $U(2)$ hypothesis in the scalar leptoquark scenario can be found in [159].

Z′ boson.

A generic Z' boson coupled to left-handed quarks and leptons provides a useful example to illustrate some of the challenges in generating large corrections to the di-neutrino widths in explicit models. Consider a massive Z' coupled to the following current

$$J^\mu_{Z'} = Q_q(\bar{q}^3_L + \tilde{V}_i^* \bar{q}^i_L)\gamma^\mu(q^3_L + \tilde{V}_i q^i_L) + Q_\tau \bar{l}^3_L \gamma^\mu l^3_L \,. \tag{2.57}$$

Integrating out the Z' leads to

$$C_{lq}^{-} = C_{lq}^{+} = -\frac{g^2}{M_{Z'}^2} Q_q Q_\tau \,, \tag{2.58}$$

$$C_{qq}^{(1)[3333]} = -\frac{g^2}{2M_{Z'}^2} Q_q^2 \,. \tag{2.59}$$

The term eq. (2.59) is the coefficient of the four-quark operator, in the notation of Ref. [214]. This is severely bounded by $\Delta F = 2$ amplitudes: generalising the up-aligned result of [214] (which corresponds to setting $|\varepsilon| = 1$ in our case), leads to

$$\left|C_{qq}^{(1)[3333]}\right| < (\varepsilon \Lambda_{Bs})^{-2} \,, \tag{2.60}$$

with $\Lambda_{Bs} = 7.6$ TeV. On the other hand, from fig. 2.23 we deduce that fitting the central values of the two di-neutrino modes requires

$$\left|C_{\ell q}^{-}\right| \approx \left[\varepsilon \times (1 \text{ TeV})\right]^{-2} \,. \tag{2.61}$$

Satisfying eqs. (2.58)–(2.61) is possible, but only if $|Q_\tau/Q_q| \gtrsim 30$, which appears a rather tuned choice. This excludes, for instance, the Z' bosons arising from flavor deconstruction of $U(1)$ gauge groups [215–217]. The difference with respect to the leptoquark case discussed above, also arising from flavor deconstruction, is that deconstructing the $SU(4)$ group one can conceive a flavor misalignment of charged currents (leptoquark-mediated) and neutral currents (Z'-mediated), avoiding the strong tree-level bounds from $\Delta F = 2$ transitions [218].

2.3.4 Summary

The recent observation of the $K^+ \to \pi^+ \nu\bar{\nu}$ decay by NA62 [219], and the evidence of $B^+ \to K^+ \nu\bar{\nu}$ reported by Belle-II [49], represent a major step forward in flavor physics. These long-sought rare decays are unique probes of short-range dynamics and, as pointed out in a number of recent works [2, 171, 172, 203, 220, 221], they are sensitive to a variety of SM extensions. Given the two neutrinos cannot be detected, also extensions of the SM with exotic invisible light states may affect these decay modes (see e.g. [180–182, 184, 185, 185, 186, 186, 187, 222]).

In this study, we have analyzed these processes in a specific class of SM extensions with heavy new particles. More precisely, we have considered an EFT based on the hypothesis of TeV-scale NP coupled mainly to quarks and leptons of the third generation. On general grounds, this hypothesis is particularly interesting for addressing both the hierarchy problem and the flavor hierarchies [214, 223] . Moreover, it is a setup where sizable deviations from the SM can consistently occur in the rare di-neutrino modes, despite the tight NP bounds derived from $B_s \to \mu^+\mu^-$ and other flavor-changing processes. Indeed, $K \to \pi\nu\bar{\nu}$ and $B \to K^{(*)}\nu\bar{\nu}$ are the only FCNC transitions involving third-generation leptons for which current measurements have reached the SM level.

In the motivated NP framework we have considered, $K \to \pi\nu\bar{\nu}$ and $B \to K^{(*)}\nu\bar{\nu}$ amplitudes are naturally linked. The link is non trivial and provides a key information to determine the flavor structure of the underlying dynamics. Despite affected by a significant uncertainty, present data hint to an enhancement of both decay rates compared to the corresponding SM expectations. As we have shown, this hint is compatible with being generated by a unique effective operator, with an alignment in flavor space following from the

hypothesis of a minimally broken $U(2)_q$ flavor symmetry. This flavor structure is also fully compatible, and naturally linked, with other hints of deviations from the SM in $B \to D^{(*)}\tau\nu$ and $B \to K^{(*)}\mu\bar{\mu}$ decays and, at the same time, is compatible with bounds from electroweak physics and direct searches. Enhanced rates for the two di-neutrino modes were indeed predicted [210, 213], before the recent measurements [49, 219], in complete UV models addressing these other observations. Needless to stress that future data on all these modes are needed to understand how solid this picture is. In the case of $B \to D^{(*)}\tau\nu$ and $B \to K^{(*)}\mu\bar{\mu}$, further theoretical scrutiny of the SM uncertainties is also needed.

Given their theoretical cleanliness, the di-neutrino modes plays a special role in shedding more light on this framework. As we have shown, already a reduction of a factor of two of present uncertainties could bring the evidence of NP, from the di-neutrino modes only, above the 3σ level (if the overall picture would not change significantly). More generally, the analysis we have presented provides a clear illustration of the high discovery potential and the unique discriminating power of these rare modes, especially when combined. They allow us to test high-scale NP in motivated models that are still inaccessible via direct searches. Their experimental study should be pursued up to the few % level, i.e. up to the level of the irreducible SM uncertainties, since they provide an invaluable tool to search or constrain new dynamics.

Chapter 3

Theoretical Tools for Future Colliders

The Standard Model of particle physics has achieved outstanding success, accurately describing a vast range of phenomena up to energies around the TeV scale. Above this threshold, the possiblity of new physics with $\mathcal{O}(1)$ couplings to SM fields remains an open, motivated possibility. Uncovering such physics is a key target for the next generation of collider experiments.

At present, the Large Hadron Collider at CERN is our only instrument for directly exploring physics at the electroweak scale and beyond, with its high-luminosity phase expected to run until the early 2040s. It has proven to be an outstanding machine, enabling both the search for new heavy states and precision measurements at the electroweak scale, most notably exemplified by the discovery of the Higgs boson and the study of its couplings. Nevertheless, the next major experiment in high-energy physics is likely to be a lepton collider. Proposed candidates include circular and linear electron-positron colliders (FCC-ee [224] and CEPC [225, 226] for the former; ILC [227], CLIC [228], and CCC [229] for the latter), as well as $\mu^+\mu^-$ [230, 231] colliders. Among these, the linear e^-e^+ machines and the muon colliders offer the possibility of reaching multi-TeV center-of-mass energies.

The Future Circular Collider (FCC) programme is structured in two main phases. The first phase, FCC-ee, involves an electron-positron collider designed to achieve maximum peak and integrated luminosities at four main working points, corresponding to the Z pole, the WW threshold, the $(Z)H$ production peak and the $t\bar{t}$ threshold. For example, integrated luminosity targets amount to the production of 6×10^{12} Z bosons, to be achieved over 15 years of run. With these luminosity goals, the FCC-ee is expected to improve the precision of electroweak observables by orders of magnitude compared to the LEP, significantly enhancing its sensitivity to indirect signs of new physics. The second phase, FCC-hh, envisions a proton-proton collider with a center-of-mass energy reaching up to about $\mathcal{O}(100)$ TeV, delivering a total integrated luminosity of roughly 20 ab^{-1} over 25 years of operation. For a comprehensive overview of the FCC project, we refer the reader to the original design reports, e.g. [232–237]. Numerous studies have also explored the physics opportunities enabled by these future machines, see e.g. [238–249] etc.

The Muon Collider concept is based on colliding two single-bunch muon beams of opposite charge. It represents a paradigm shift in collider design, being the first proposed machine to combine the high-energy reach of hadron colliders with the precision typically associated with lepton colliders. The Muon Collider programme envisions two main stages: an initial run at a center-of-mass energy of 3 TeV, followed by a stage at 10 TeV with an integrated luminosity

goal of $10\,\text{ab}^{-1}$. Calling $\sqrt{s}$ the center of mass energy in the initial state system, and $\sqrt{\hat{s}}$ its partonic center of mass energy, a key advantage of a muon collider over a proton-proton collider is that interactions occur across the full range of partonic center-of-mass energies up to $\sqrt{\hat{s}} = \sqrt{s}$, whereas pp collisions are predominantly characterized by $\sqrt{\hat{s}} \ll \sqrt{s}$ due to the proton's composite structure. For a comprehensive overview and technical details of the Muon Collider proposal, we refer the reader to [230, 231, 250–253]. Numerous studies on the associated physics potential, as well as comparisons between future lepton and hadron colliders, are available in the literature. See e.g. [254–263], and references therein.

The TeV energy range is not just significant for the potential discovery of new physics. At these scales, the effects of electroweak symmetry breaking diminish, leading to an effective restoration of the EW gauge symmetry. This restoration introduces a host of complex phenomena, making the physics case of future lepton colliders challenging, and exciting, on the theoretical side. For example, such effects are Sudakov double logarithmic corrections [264–271], EW radiation [272, 273], EW collinear splitting and EW parton distribution functions [257, 272, 274–283], etc. While some of these aspects are already relevant at the LHC [265, 271, 284–288], future high-energy colliders will probe this energy range directly, making it essential to develop a deep understanding of EW restoration and the related phenomenology to ensure accurate SM predictions. Among the proposed future colliders, this goal is particularly crucial in the case of TeV-scale muon colliders. In fact, the suppression of QCD effects, due to the non-colored nature of muons, promotes EW interactions to a leading role.

In this chapter we focus on a specific aspect of high energy lepton colliders: the description of EW initial state radiation (ISR). In a high-energy collision, the emission of ISR can be factorised from the hard scattering process if the emitted radiation is collinear, meaning its transverse momentum is much smaller than the typical energy of the hard scattering [1] [272, 286, 290–292]. Under this condition, the cross section for the entire process, inclusive over ISR, can be computed by convoluting the partonic cross section of the hard scattering with the parton distribution functions (PDFs) of the corresponding partons in the initial state, in a similar fashion to the treatment in protons collisions. The PDFs, $f_i(x, Q^2)$, describe then the probability that the parton i carries a longitudinal momentum fraction x of the initial beam momentum, with Q representing the factorization scale.

The content of this chapter is organized as follows. In section 3.1, we provide a basic introduction to parton distribution functions for leptons, beginning with a detailed review of electron–photon emission in pure QED and then generalizing the discussion to include the full set of Standard Model interactions. Expert readers may skip this review and proceed directly to section 3.2. Here, we turn our focus on the mixed Z/γ PDF and show that the leading-order approximation, often used in literature, is not suitable for an accurate description. On the other hand, extending the calculation to $\mathcal{O}(\alpha^2)$ allows us to derive an analytic expression that is in good agreement with the numerical result obtained in Ref. [282] by resumming at the leading-log order the full set of SM DGLAP equations. In section 3.3 we discuss a process, namely high-energy Compton scattering, that could allow to measure experimentally the impact of the Z/γ PDF, and we quantify the potential precision attainable. Then, in section 3.4 we study its effect in WH production, while in section 3.5 we show how also some new physics searches can be affected by this mixed PDF by focusing on single resonant

[1] A formalism that allows also to include the soft and soft-collinear regions of the splitting processes has recently been developed in Ref. [289]

production of axion-like scalar singlets (ALP). Finally, we conclude in section 3.6. Details of our computations are collected in the Appendices. Original results are based on [3].

3.1 Parton Distribution Functions at Muon Colliders

3.1.1 The equivalent photon approximation

While leptons are elementary particles in the Standard Model, the process of collinear emission of ISR, with transverse momentum p_T much smaller than the energy of the hard scattering process, can be factorized and a description in terms of parton distribution functions can be introduced, similarly to the case of proton colliders and the partonic structure of the proton. To introduce this formalism, we review the well-known example of the collinear splitting of an initial-state electron into an electron and a photon, a process understood at leading order for nearly a century [293–296].

Let us start by focusing on the diagram in fig. 3.1, *i.e.* on the initial splitting of $e \to e\gamma$ with subsequent hard scattering $\gamma X \to Y$. We want to show that in the limit of collinear emission ($E \gg p_T$), the intermediate photon can be treated as almost on-shell. In particular, replacing the numerator of the intermediate propagator with a sum over polarization vectors, we can decouple the electron emission vertex from the rest of the diagram. As a consequence, we will naturally identify a parton distribution function for the photon, which encodes the large logarithm due to collinear emission.

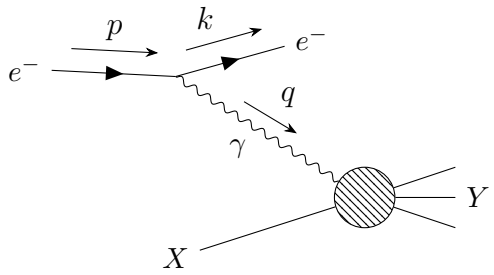


Figure 3.1: Sketch of initial state radiation from electron beam. The round blob represents the hard cross section, where the photon γ enters at order α. X and Y stand for generic initial and final states involved in the hard scattering.

Considering massless electrons, the three 4-momenta involved in the splitting vertex are, at leading orders in p_T

$$\begin{aligned} p =&(p, 0, 0, p)\,, \\ q \simeq&(zp, p_\perp, 0, zp + \frac{p_T^2}{2zp}) \\ k \simeq&((1-z)p, -p_\perp, 0, (1-z)p - \frac{p_T^2}{2zp})\,. \end{aligned} \tag{3.1}$$

In this way $p^2 = k^2 = 0$, while the intermediate photon has virtuality $q^2 = -p_T^2/(1-z)$. In order to factorize the total cross section we need to contract the electron emission vertex

and the remaining photon amplitude with physical transverse polarization vectors for the intermediate-state photon. Exploiting the Ward Identities in the limit of almost on-shell photon, it is straightforward to verify that it sufficies to implement the minimal propagator substitution

$$\frac{-ig^{\mu\nu}}{q^2} \to \frac{+1}{q^2}\sum_i \epsilon^{\mu}_{T,i}\epsilon^{*\nu}_{T,i}\,, \tag{3.2}$$

where ϵ_T is the transverse photon polarization. In this way, the total amplitude becomes

$$\mathcal{M}_{eX\to eY} \propto \mathcal{M}_{e\to e\gamma}\,\frac{i}{q^2}\,\mathcal{M}_{\gamma X\to Y}\,, \tag{3.3}$$

where we have called $\mathcal{M}_{e\to e\gamma}$ the splitting amplitude relative to the first collinear splitting of the electron, and $\mathcal{M}_{\gamma X\to Y}$ represent the matrix element for the scattering of the photon from X, that we assume for simplicity to be unpolarised. Using this last expression, together with the kinematic approximations in eq. (3.1), we can write the total cross section as follows:

$$\sigma(eX\to eY) = \frac{1}{(1+v_X)2p2E_X}\int\frac{d^3k}{(2\pi)^2}\frac{1}{2k_0}\int d\Pi_Y\frac{1}{2}\sum|\mathcal{M}_{e\to e\gamma}|^2\frac{1}{q^2}|\mathcal{M}_{\gamma X\to Y}|^2 \tag{3.4}$$

where v_X is the velocity of X and $\int d\Pi_Y$ is the phase space integral over Y. The integral has a singularity when k is collinear with the incident electron momentum p. However, via appropriate change of variables (at leading order in p_T) $d^3k = dk^3d^2k_T = pdz\cdot\pi dp_T^2$, we can isolate the singularity so that the cross section can be expressed as

$$\begin{aligned}\sigma &= \int\frac{pdzdp_T^2}{16\pi^2(1-z)p}[\frac{1}{2}\sum|\mathcal{M}_{e\to e\gamma}|^2]\frac{(1-z)^2}{p_T^4}\frac{z}{(1+v_X)2zp2E_X}\int d\Pi_Y|\mathcal{M}_{\gamma X}|^2 = \\ &= \int\frac{dzdp_T^2}{16\pi^2(1-z)}[\frac{1}{2}\sum|\mathcal{M}_{e\to e\gamma}|^2]\frac{z(1-z)^2}{p_T^4}\cdot\sigma(\gamma X\to Y)\,.\end{aligned} \tag{3.5}$$

Finally, it is easy to derive the explicit spin-averaged electron emission vertex

$$\frac{1}{2}\sum_{\text{pol}}|\mathcal{M}_{e\to e\gamma}|^2 = \frac{2e^2p_T^2}{z(1-z)}\left[\frac{1+(1-z)^2}{z}\right]\,, \tag{3.6}$$

and performing explicitely the integral over p_T^2, one finds the familiar Weizsacker-Williams equivalent photon approximation:

$$\sigma(eX\to eY) = \int_0^1 dz\frac{\alpha}{2\pi}\log\frac{s}{m^2}\left[\frac{1+(1-z)^2}{z}\right]\cdot\sigma(\gamma X\to Y)\,. \tag{3.7}$$

Here the cross section on the r.h.s is for a real photon with energy zp, and $\sqrt{s}$ is the center-of-mass energy of the electron-X system. Notice that we reintroduced the electron mass m as an IR cutoff for the divergent integral over p_T^2. Most importantly, we can recognize the Parton Distribution Function of the photon

$$f_\gamma(z) = \frac{\alpha}{2\pi}\log\frac{s}{m^2}\left[\frac{1+(1-z)^2}{z}\right]\,. \tag{3.8}$$

that can be interpreted as the probability to find a photon as parton content of the incident electron, carrying a fraction z of its energy.

Multiple emissions

In the previous computation, we focused on the case of an intermediate photon. However, it is also possible for the intermediate nearly on-shell particle entering the hard cross section to be the electron, while the emitted photon is real. In this case, we would find a leading order correction to the electron PDF

$$f_e^{(\alpha)}(x) = \frac{\alpha}{2\pi} \log \frac{s}{m^2} \left[\frac{1+x^2}{(1-x)_+} \right] , \tag{3.9}$$

where $x \equiv 1 - z$. Of course, this contribution has to be considered as an order-α correction to the zeroth-order $f_e^{(0)}(x) = \delta(1-x)$, which can be naively seen as the probability that an electron remains an electron in absence of ISR. When evaluating integrals involving the PDFs, divergences may arise and must be handled with care. A common approach involves treating the PDFs as the one in eq. (3.9) using the "+-distribution" prescription to properly manage the singular behavior, for example:

$$\begin{aligned} \int_x^1 dz \frac{f(z)}{(1-z)_+} &= \int_x^1 dz \frac{f(z) - f(1)}{1-z} - f(1) \int_0^x \frac{dz}{1-z} \\ &= \int_x^1 dz \frac{f(z) - f(1)}{1-z} + f(1) \log(1-x) \, . \end{aligned} \tag{3.10}$$

In general, multiple splittings can occur, leading to the emission of several particles as initial state radiation. For example, the intermediate photon in fig. 3.1 could further split into a collinear positron and another nearly on-shell electron that enters the hard scattering process. The same applies to the case of real emitted photons: multiple photons can be emitted from a sequence of intermediate, nearly on-shell electrons.

In the case of n collinear emissions, whether electrons or photons, it is easy to see that the total cross section involves n integrals over the virtualities $p_{T,i}^2$. The region of integration characterised by the ordering $p_{T,1}^2 \gg p_{T,2}^2 \gg p_{T,3}^2 \ldots \gg p_{T,n}^2$ gives a contribution that contains the factor

$$\left(\frac{\alpha}{2\pi}\right)^n \int_{m^2}^s \frac{dp_{T,1}^2}{p_{T,1}^2} \int_{m^2}^{p_{T,1}^2} \frac{dp_{T,2}^2}{p_{T,2}^2} \ldots \int_{m^2}^{p_{T,n-1}^2} \frac{dp_{T,n}^2}{p_{T,n}^2} = \frac{1}{n!} \left(\frac{\alpha}{2\pi}\right)^n \log^n \frac{s}{m^2} \, , \tag{3.11}$$

that is the leading-log (LL) term. The contributions that arise from different orderings provide instead terms with at least one less power of the large logarithm at the same order of α, *i.e.* the next-to-leading logs (NLL). To improve the accuracy of perturbation theory, it would then be useful to introduce a procedure for summing the LLs to all orders in α. Analogously to what is done with running couplings in QFT, it can be achieved by introducing a factorization scale Q inside the functions $f_e(x, Q)$ and $f_\gamma(x, Q)$. We do not discuss this in detail here and instead refer the reader to standard textbook treatments such as [7] for a comprehensive overview. However, we now provide a simple recipe to derive the role of the factorization scale Q in the simplified case of QED.

Let us consider again the total cross section of eq. (3.5). It can be written in general compact form as

$$\begin{aligned} \sigma_{e+X\to C+Y} &= \int \frac{dp_T^2 dz}{16\pi^2 p_T^4} \left|\mathcal{M}_{e\to CB}\right|^2 z\bar{z}\sigma_{B+X\to Y} \\ &\equiv \int dp_T^2 \int_0^1 dz \frac{d\mathcal{P}_{e\to B+C}}{dz dp_T^2}\left(z, p_T^2\right) \sigma_{B+X\to Y} \end{aligned} \tag{3.12}$$

where $\bar{z} \equiv 1 - z$ and now B, C can be both electrons or photons. As we have learned from the equivalent photon approximation, the total cross section involving an initial electron e can be also written as

$$\sigma_{e+X\to Y} = \sum_B \int_0^1 dx f_B(x) \sigma_{B+X\to Y}\,, \tag{3.13}$$

where B denotes any partonic constituent of the electron that is carrying a fraction x of its momentum, with $f_B(x)$ representing the corresponding PDF. Now, if we want to be fully inclusive about initial state radiation, we have to consider all the possible further splittings of the parton B. It can be proved that this is achieved by considering the general total cross section:

$$\begin{aligned}\sigma^{\rm TOT}_{eX\to Y} &= \sum_B \int_0^1 dx \left[f_B(x) + \sum_{A,C} \int_0^{Q^2} dp_T^2 \int_x^1 \frac{dz}{z} \frac{d\mathcal{P}_{A\to B+C}}{dz dp_T^2}\left(z, p_T^2\right) f_A\left(\frac{x}{z}, p_T^2\right)\right] \sigma_{B+X\to Y} \\ &\equiv \sum_B \int_0^1 dx f_B\left(x, Q^2\right) \sigma_{B+X\to Y}\,,\end{aligned} \tag{3.14}$$

where in the last step we have defined the dependence of f_B on the scale Q. Taking a derivative with respect to Q, and asking for cross sections to be invariant under this factorization scale, leads to the so-called DGLAP equations. They are a set of coupled differential equations which drive the evolution of the PDFs $f_e(x,Q)$, $f_{\bar{e}}(x,Q)$, and $f_\gamma(x,Q)$ as a function of the sliding scale Q, and provide solutions that automatically resum all the LLs arising from collinear emissions. In this simple example, where we just have QED with one electron, they read

$$\begin{aligned}\frac{d}{d\log Q} f_\gamma(x,Q) =& \frac{\alpha}{\pi}\int_x^1 \frac{dz}{z}\left\{P_{\gamma\leftarrow e}(z)\left[f_e\left(\frac{x}{z},Q\right) + f_{\bar{e}}\left(\frac{x}{z},Q\right)\right] + P_{\gamma\leftarrow\gamma}(z) f_\gamma\left(\frac{x}{z},Q\right)\right\} \\ \frac{d}{d\log Q} f_e(x,Q) =& \frac{\alpha}{\pi}\int_x^1 \frac{dz}{z}\left\{P_{e\leftarrow e}(z) f_e\left(\frac{x}{z},Q\right) + P_{e\leftarrow\gamma}(z) f_\gamma\left(\frac{x}{z},Q\right)\right\} \\ \frac{d}{d\log Q} f_{\bar{e}}(x,Q) =& \frac{\alpha}{\pi}\int_x^1 \frac{dz}{z}\left\{P_{e\leftarrow e}(z) f_{\bar{e}}\left(\frac{x}{z},Q\right) + P_{e\leftarrow\gamma}(z) f_\gamma\left(\frac{x}{z},Q\right)\right\}\end{aligned} \tag{3.15}$$

where the functions $P_{AB}(z)$ are called splitting functions and are simply derived from the splitting amplitudes, like the previously mentioned $\mathcal{M}_{e\to e\gamma}$. Instead, $P_{\gamma\leftarrow\gamma}(z)$ refers to the radiative correction consisting in a loop with internal fermion lines. Explicitely, they are

$$\begin{aligned} P_{e\leftarrow e}(z) &= \tfrac{1+z^2}{(1-z)_+} + \tfrac{3}{2}\delta(1-z), & P_{\gamma\leftarrow e}(z) &= \tfrac{1+(1-z)^2}{z}, \\ P_{e\leftarrow\gamma}(z) &= z^2 + (1-z)^2, & P_{\gamma\leftarrow\gamma}(z) &= -\tfrac{2}{3}\delta(1-z). \end{aligned} \tag{3.16}$$

When considering an initial electron beam, one should integrate the DGLAP equations with the initial conditions

$$f_e(x,m_e) = \delta(1-x) + \mathcal{O}(\alpha), \quad f_{\bar{e}}(x,m_e) = 0 + \mathcal{O}(\alpha), \quad f_\gamma(x,m_e) = 0 + \mathcal{O}(\alpha)\,. \tag{3.17}$$

3.1.2 The Standard Model PDFs

In the previous section, we derived the equivalent photon approximation in QED and introduced the main concepts underlying the use of parton distribution functions for leptons,

along with the DGLAP evolution equations. We now turn to the discussion of the full set of DGLAP equations within the Standard Model. For concreteness, we focus on muon initial beams, since the phenomenological applications discussed in this chapter pertain to processes occurring at muon colliders.

Since the Standard Model is significantly more complex and richer than QED, we now introduce a more general notation that will be useful throughout the rest of the chapter. We also highlight some features that are specific to non-Abelian gauge theories, the presence of the Higgs mechanism, and the inclusion of massive states.

In full analogy with the previous case, let us start considering a generic parton splitting $A \to B + C$ followed by the hard scattering $B + X \to Y$, as shown in the diagram in fig. 3.2. We can define z as the fraction of the energy of the initial particle A that is carried by the

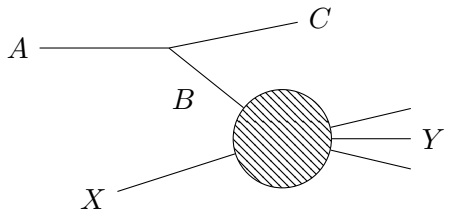


Figure 3.2: Schematic diagram for the process $AX \to CY$, with initial-state collinear splitting $A \to BC$, followed by a hard scattering $BX \to Y$.

particle B. The kinematics of the process, up to quadratic order in the transverse momentum p_T, is then

$$\begin{aligned} p_A^\mu &= \left(E_A, 0, 0, \sqrt{E_A^2 - m_A^2}\right), \\ p_B^\mu &= \left(zE_A, p_T, 0, \sqrt{E_A^2 - m_A^2} - \sqrt{\bar{z}^2 E_A^2 - m_C^2} + \frac{p_T^2}{2\sqrt{\bar{z}^2 E_A^2 - m_C^2}}\right), \\ p_C^\mu &= \left(\bar{z}E_A, -p_T, 0, \sqrt{\bar{z}^2 E_A^2 - m_C^2} - \frac{p_T^2}{2\sqrt{\bar{z}^2 E_A^2 - m_C^2}}\right), \end{aligned} \tag{3.18}$$

with, again, $\bar{z} = 1 - z$. At this order, the particle C is considered on-shell, such that $p_C^2 = m_C^2$, while for the particle B we can find

$$p_B^2 = m_A^2 + m_C^2 - 2\bar{z}E_A^2 + 2\sqrt{\left(E_A^2 - m_A^2\right)\left(\bar{z}^2 E_A^2 - m_C^2\right)} - \sqrt{\frac{\left(E_A^2 - m_A^2\right)}{\left(\bar{z}^2 E_A^2 - m_C^2\right)}} p_T^2. \tag{3.19}$$

We will be interested in the limit of high-energy beams such that $E_A \gg m$ and $E_A \gg p_T$, relevant for the future Muon Collider processes. With these working assumptions, we can write the virtuality of the particle B as

$$m_B^2 - p_B^2 = \frac{1}{\bar{z}}\left(p_T^2 + zm_C^2 + \bar{z}m_B^2 - z\bar{z}m_A^2\right) + \mathcal{O}\left(\frac{m^2}{E^2}, \frac{p_T^2}{E^2}\right) \equiv \frac{\tilde{p}_T^2}{\bar{z}}. \tag{3.20}$$

As in the QED case, we can define the splitting distribution

$$\frac{d\mathcal{P}_{A\to B+C}}{dz dp_T^2}\left(z, p_T^2\right) = \frac{1}{16\pi^2 \tilde{p}_T^4} z\bar{z}\left|\mathcal{M}_{A\to B+C}\right|^2 \tag{3.21}$$

and parametrize the Standard matrix elements, present also in the unbroken (massless) phase, as

$$|\mathcal{M}_{A\to B+C}|^2 \equiv 8\pi\alpha_{ABC}\frac{p_T^2}{z\bar{z}}P_{BA}^C(z)\,. \tag{3.22}$$

Here, P_{BA}^C is the splitting function associated to the process $A \to B + C$ and α_{ABC} is the corresponding coupling. In the presence of massive partons, the so-called ultra-collinear matrix elements appear, proportional to m^2 instead of p_T^2. In the SM, where all the masses of elementary particles are proportional to the Higgs vev v, they can be parametrized with some new splitting functions U_{BA}^C

$$|\mathcal{M}_{A\to B+C}|^2 = \frac{v^2}{z\bar{z}}U_{BA}^C(z)\,. \tag{3.23}$$

Putting all these pieces together, the evolution equation for a parton B in the SM, as part of the DGLAP equations, can be written as

$$\frac{df_B(x,t)}{dt} = \sum_{A,C}\frac{\alpha_{ABC}}{2\pi}\tilde{P}_{BA}^C \otimes f_A + \frac{v^2}{16\pi^2Q^2}\sum_{A,C}\tilde{U}_{BA}^C \otimes f_A, \tag{3.24}$$

where we introduce the variable $t = \log(Q^2/m_\mu^2)$ and for simplicity we defined the convolution

$$P \otimes f = f \otimes P \equiv \int_x^1 \frac{dz}{z}P(z)f\left(\frac{x}{z}\right) \tag{3.25}$$

$\tilde{P}$ and $\tilde{U}$ are the splitting functions for massive partons and are obtained from the massless ones by the rescaling

$$\tilde{P}_{BA}^C\left(z,Q^2\right) = \left(\frac{p_T^2}{\tilde{p}_T^2}\right)^2 P_{BA}^C(z). \tag{3.26}$$

One final ingredient required to obtain the complete set of evolution equations is the inclusion of virtual corrections, denoted as P_B^v, analogous to the $P_{\gamma\leftarrow\gamma}$ term in QED. The full DGLAP evolution equation for a parton B then reads:

$$\frac{df_B(x,t)}{dt} = P_B^v(x,t)\,f_B(x,t) + \sum_{A,C}\frac{\alpha_{ABC}}{2\pi}\tilde{P}_{BA}^C \otimes f_A + \frac{v^2}{16\pi^2Q^2}\sum_{A,C}\tilde{U}_{BA}^C \otimes f_A, \tag{3.27}$$

A useful trick to compute these radiative corrections is to exploit momentum conservation: the total momentum carried by all partons must equal the momentum of the initial beam. Since each parton carries a fraction x of the total momentum, this implies

$$\sum_A \int_0^1 dx\; x f_A(x,t) = 1 \quad \forall t \tag{3.28}$$

Taking the derivative of this relation with respect to t, and using eq. (3.27), one can straightforwardly derive

$$P_A^v(t) = -\sum_{B,C}\int_0^{z_{\max}^{ABC}(t)} dz z\left(\frac{\alpha_{ABC}}{2\pi}\tilde{P}_{BA}^C(z) + \frac{v^2}{16\pi^2Q^2}\tilde{U}_{BA}^C(z)\right) \tag{3.29}$$

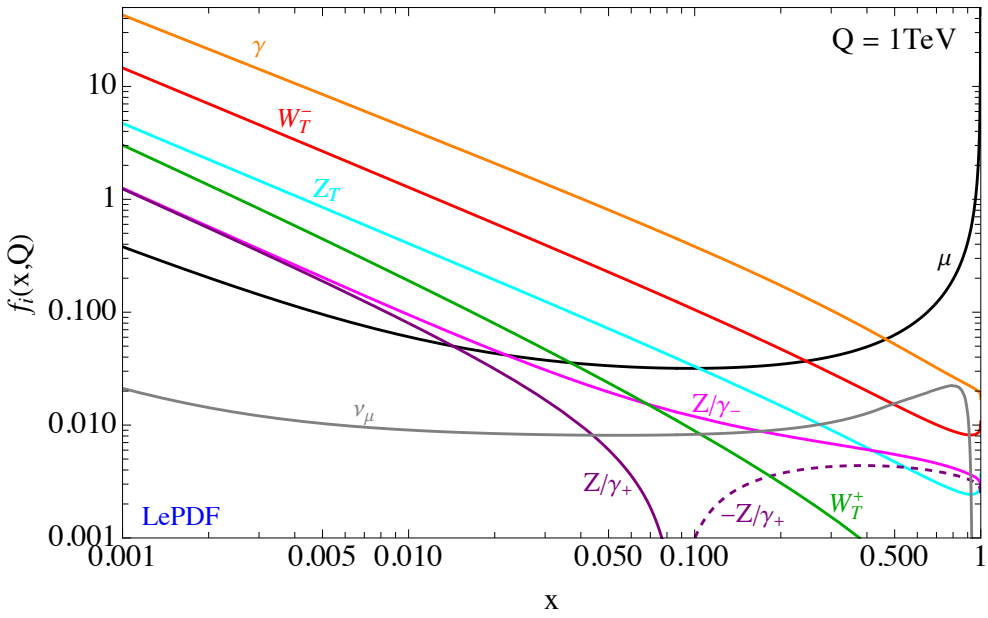


Figure 3.3: Examples of some SM PDFs of a muon obtained with LePDF [282], for a factorization scale $Q = 1\,\text{TeV}$. Except for the Z/γ PDF, the other are summed over the transverse helicities. The dashed line indicates that the PDF is negative, in which case we plot the absolute value.

where $z_{\text{max}}^{ABC} = 1$ in most cases, except for some special situations that will be discussed later. We refer the reader to Ref. [282] for the explicit list of the splitting functions and DGLAP equations for the SM particles, with same notation of eq. (3.27), taking into account all the effects we have mentioned in this introduction. In addition, they provide the complete numerical solutions of the DGLAP equations, which we employ in the following. In fig. 3.3 we show some examples of SM PDFs of a muon obtained with LePDF. Further details on the formalism can be found, e.g., in ref.s [257, 272, 274–278, 280–282].

Finally, a few comments are in order about the analogies with the common PDFs used for proton-proton collisions. In the case of proton colliders, QCD interactions dominate the phenomenology. Since this interaction becomes non-perturbative at low scales, PDFs of a proton can only be obtained by fitting experimental data. In lepton colliders, however, at low energy scales the leading interaction is QED, allowing for a derivation of PDFs of leptons from first principles by solving the differential DGLAP equations of eq. (3.27), [297–299] with boundary conditions set at the lepton mass scale [300]. When the factorisation scale Q rises above the EW scale, QED interactions should be substituted with the complete EW ones in order to resum also the possibly large logarithms due to collinear emission of electroweak radiation [275].

3.2 The mixed Z_T/γ PDF

EW interactions introduce several new phenomena in the evolution of PDFs like Sudakov double-logs [265, 267, 269], polarization effects [301], ultra-collinear splittings [276], and EW mass effects [276, 302], some of which we mentioned in the introduction. Another peculiar feature of SM PDFs is the necessary presence of PDFs describing mixed-states, due to the possible interference between the photon and the transverse polarizations of the Z boson, $f_{Z/\gamma_\pm}(x, Q^2)$, as well as between its longitudinal polarization and the Higgs [266, 275, 276]. Such mixed PDFs are not present in QCD or QED, and is therefore a specific EW effect, due to the fact that those states have the same quantum numbers under the unbroken gauge group.

In order to understand the presence of this mixed functions, it is intructive to start again from the the initial-state splitting and factorisation as in eq. (3.3). We follow the discussion of Ref. [272]. Consider a process $AX \to CY$, which can proceed through the exchange of a virtual particle B^* with electroweak-scale mass m as the emission $A \to CB^*$, with C having a transverse momentum $|\mathbf{p}_T|$ relative to the direction of A, followed by the hard scattering $BX \to Y$ of typical hard energy E, as depicted schematically in fig. 3.2. Collinear factorization states that if $\delta_m = m/E \ll 1$ and $\delta_T = |\mathbf{p}_T|/E \ll 1$ then the amplitude factorizes as

$$i\mathcal{M}(AX \to CY) = \sum_B i\mathcal{M}^{\text{split}}(A \to CB^*)\frac{i}{Q^2} i\mathcal{M}^{\text{hard}}(BX \to Y)\,(1 + \mathcal{O}(\delta_{m,\perp}))\ , \tag{3.30}$$

where in the hard scattering matrix element the state B is taken as approximately on-shell, and we are now interested in the general case in which the role of B could be played by several particles. The differential cross section $d\sigma$ is proportional to the modulus square of eq. (3.30) and therefore it contains the interference terms of different states B and B' that can enter the same splitting and hard processes, which in general could be different species or different helicities:

$$d\sigma \propto |\mathcal{M}(AX \to CY)|^2 \propto \sum_{B,B'} d\rho^{\text{split}}_{BB'}\, d\rho^{\text{hard}}_{B'B} = \text{Tr}\left[d\rho^{\text{split}} d\rho^{\text{hard}}\right]\ , \tag{3.31}$$

where the density matrices for the splitting and hard processes are proportional to

$$\begin{aligned} d\rho^{\text{split}}_{BB'} &\propto \text{Re}\left[\mathcal{M}^{\text{split}}(A \to CB^*)\mathcal{M}^{\text{split}}(A \to CB'^*)^*\right]\ , \\ d\rho^{\text{hard}}_{B'B} &\propto \text{Re}\left[\mathcal{M}^{\text{hard}}(B'X \to Y)^*\mathcal{M}^{\text{hard}}(BX \to Y)\right]\ , \end{aligned} \tag{3.32}$$

and we refer to [272] for details. Upon integrating over the azimutal angle of the collinear emission process, the interference between different helicity states vanishes.[2]

In order for the interference to be non-vanishing, the states B and B' should be interchangable in both the splitting and hard processes. This implies they should have the same conserved charges, i.e. same electric charge and color representation, but also same family lepton number $L_{e,\mu,\tau}$, baryon number and, if CKM-suppressed splitting processes are neglected, also individual baryon number for each generation $B_{1,2,3}$. With these constraints,

[2] As pointed out in [272, 286], upon integrating over the splitting azimutal angle the corrections to the factorization expression become of $\mathcal{O}(\delta^2_{m,T})$.

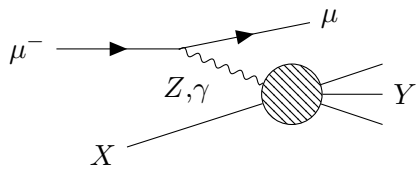


Figure 3.4: Sketch of initial state radiation from muon beam. The round blob represents the hard cross section, where the Z, γ and their interference enter at order α (one splittings). X and Y stand for generic initial and final states involved in the hard scattering.

in the SM the only possible non-vanishing interference terms are between the photon and the transverse Z boson, inducing the mixed Z/γ PDF, or between the longitudinal Z boson and the phyiscal Higgs, responsible for the mixed h/Z_L PDF [266, 272, 275, 276]. The mass difference between the two states is at most of order m, i.e. the EW scale, therefore the effects due to the different virtuality will be of $\mathcal{O}(\delta_m^2)$, compatible with the approximation on which factorization is based. In this work we focus on the mixed Z/γ case, since its effects are much larger than those due to the h/Z_L splitting.

3.2.1 Z_T/γ PDF at NLO

It is possible to derive some approximate analytical solutions to the DGLAP equations, obtained iteratively by solving them order-by-order in the coupling expansion. To get the leading order PDF for vector gauge bosons, similarly to the equivalent photon approximation, it is enough to start with the zeroth-order result

$$f^{(0)}_{\mu_L}(x,Q^2) = f^{(0)}_{\mu_R}(x,Q^2) = \frac{1}{2}\delta(1-x)\,, \qquad f^{(0)}_{i\neq\mu_{L,R}}(x,Q^2) = 0 \tag{3.33}$$

This is nothing but the assumption that, at zero order in the interacting couplings, the only non trivial partonic content of a muon beam is the muon itself. We can then plug this zeroth-order estimates in the r.h.s. of the DGLAP equation for the mixed Z/γ PDFs [282] (see also appendix B.1). In this way a single collinear splitting is considered and all the differential equations decouple, allowing for a straightforward analytical solution. This procedure was applied to the EW gauge bosons PDFs, resulting in what is also known as Effective Vector Boson Approximation (EVA) [295, 296, 302–309]. In the Z/γ case the only non trivial terms, corresponding to fig. 3.4, are:

$$\frac{d\, f^{(\alpha)}_{Z/\gamma_\pm}}{dt} \supset -\frac{\alpha_{\gamma 2}(t)}{2\pi}\frac{2}{c_W(t)}\left[Q^Z_{\mu_L}\tilde{P}^f_{V_+f_L}\otimes f_{f_L} + Q^Z_{\mu_R}\tilde{P}^f_{V_-f_L}\otimes f_{f_R}\right] \tag{3.34}$$

where by the $\pm$ subscript we denote the helicity and the splitting functions are

$$P^f_{V_+f_L}(x) = P^f_{V_-f_R}(x) = \frac{(1-x)^2}{x}\,, \qquad P^f_{V_-f_L}(x) = P^f_{V_+f_R}(x) = \frac{1}{x}\,. \tag{3.35}$$

For brevity, we defined $\alpha_{\gamma 2} = \sqrt{\alpha_\gamma \alpha_2}$, $Q^Z_{\mu_L} = -\frac{1}{2} + s^2_W$, $Q^Z_{\mu_R} = s^2_W$, and s_W is the sine of the Weinberg angle. Since only one collinear emission is considered, the approximate solution is

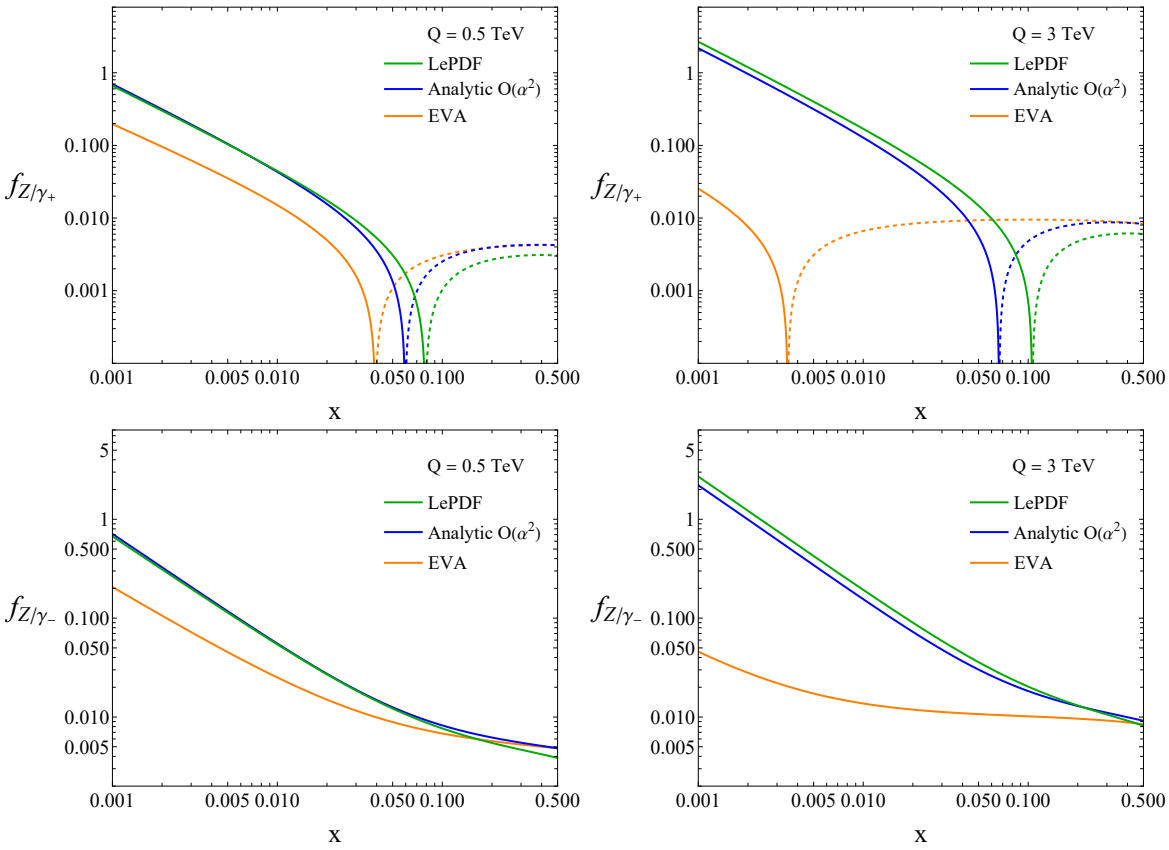


Figure 3.5: Comparison of the EVA $\mathcal{O}(\alpha)$ approximation in orange, the $\mathcal{O}(\alpha^2)$ approximation in blue and the numerical full solution to the DGLAP equation in green. Dashed lines represent negative values. In the upper (lower) panels, we show the Z/γ PDF for $+(-)$ helicity. In both cases, the factorization scale is fixed to $Q = 0.5$ TeV (left) and 3 TeV (right).

of linear $\mathcal{O}(\alpha)$ order in the coupling. An explicit computation of the integrals leads to

$$\begin{aligned} f^{(\alpha)}_{Z/\gamma_\pm}(x,Q^2) &= -\int_{m_\mu^2}^{Q^2} dp_T^2\, \frac{\alpha_{\gamma 2}}{2\pi c_W}\frac{1}{(p_T^2+(1-x)m_Z^2)}\left(P^f_{V_\pm f_L}(x)Q^Z_{\mu_L}+P^f_{V_\pm f_R}(x)Q^Z_{\mu_R}\right) = \\ &= -\frac{\alpha_{\gamma 2}}{2\pi c_W}\left(P^f_{V_\pm f_L}(x)Q^Z_{\mu_L}+P^f_{V_\pm f_R}(x)Q^Z_{\mu_R}\right)\log\frac{Q^2+(1-x)m_Z^2}{m_\mu^2+(1-x)m_Z^2}\,, \end{aligned} \tag{3.36}$$

As it was also pointed out in Ref. [282], this EVA result for the Z/γ PDF is accidentally suppressed due to the fact that, for $x \ll 1$, it is proportional to $Q^Z_{\mu_L}+Q^Z_{\mu_R} = -\frac{1}{2}+2s_W^2 \approx -0.038$, where we used $s_W^2(m_Z)\approx 0.231$ (at higher renormalization scales the $\overline{\text{MS}}$ Weinberg angle grows, making the cancellation even stronger). This well known accidental suppression, by at least one order of magnitude, of the vectorial couplings of a charged lepton to the Z boson enters our result because in the initial conditions $f^{(0)}_{\mu_{L,R}}$ it was assumed that the initial muon beam is not polarized. Conversely, this tuned cancellation is lifted in the full numerical evolution since a polarization is induced in the muon PDF by EW interactions and, more importantly, contributions from multiple splittings with other particles are considered. Eventually, the full numerical solution exhibits an enhancement of up to two orders of magnitude [282], as can be noticed by comparing the orange and green lines in fig. 3.5.

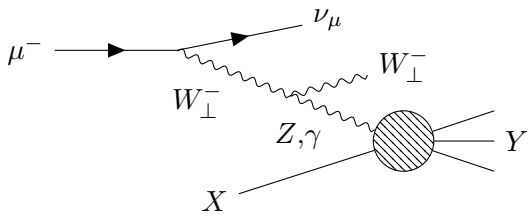


Figure 3.6: Sketch of initial state radiation from muon beam. The round blob represents the hard cross section, where the Z, γ and their interference enter at order α^2 (two splittings). X and Y stand for generic initial and final states involved in the hard scattering.

The origin of this enhancement can be understood also analytically, already at $\mathcal{O}(\alpha^2)$. For this purpose we solve iteratively the DGLAP equations at second order, using this time the $\mathcal{O}(\alpha)$ solutions for fermion and gauge boson PDFs appearing in the r.h.s. of eq. (3.27):[3]

$$\begin{aligned}\frac{df^{(\alpha^2)}_{Z/\gamma_+}(x,Q^2)}{dt} &= \frac{\alpha_{\gamma 2}(t)}{2\pi} 2c_W P^V_{V_+V_\pm} \otimes f^{(\alpha)}_{W^-_\pm} + \frac{\alpha_{\gamma 2}(t)}{2\pi}\frac{c_{2W}(t)}{c_W(t)} P^h_{V_+h} \otimes f^{(\alpha)}_{W^-_L} + \\ &+ \frac{\alpha_{\gamma 2}(t)}{2\pi}\frac{2}{c_W(t)} \sum_f Q_f \left[Q^Z_{f_L} P^f_{V_+f_L} \otimes f^{(\alpha)}_{f_L} + Q^Z_{f_R} P^f_{V_-f_L} \otimes f^{(\alpha)}_{f_R} \right] ,\end{aligned} \tag{3.37}$$

For example, let focus on the first term in the equation above, corresponding to the double emission of fig. 3.6. The transverse W^- boson PDF is, at leading order[4]

$$f^{(\alpha)}_{W^-_\pm}(x,Q^2) \approx \frac{\alpha_2}{8\pi} P^f_{V_\pm f_L}(x) \log\frac{Q^2}{m_Z^2} , \tag{3.38}$$

i.e., it is the EVA approximation derived following similar steps to what we did for eq. (3.36) and taking for simplicity the limit of small values of x and large Q^2. The convolutions involving $f^{(\alpha)}_{W^-_\pm}$ in eq. (3.37) are computed in detail in appendix B.1, where the proper treatment of Sudakov double logarithms is discussed. Then, an integral over t is performed starting from the EW scale, that we identify as m_Z, up to the factorization scale Q. The final analytic result is:

$$\begin{aligned} f^{(\alpha^2)P_{VV}}_{Z/\gamma_+}(x,Q) &= \frac{\alpha_2\alpha_{\gamma 2}}{96\pi^2 x}(t-t_Z)^2\, c_W \cdot \Big[4(t-t_Z)(1-x)^2 + J(x)\Big] , \\ f^{(\alpha^2)P_{VV}}_{Z/\gamma_-}(x,Q) &= \frac{\alpha_2\alpha_{\gamma 2}}{96\pi^2 x}(t-t_Z)^2\, c_W \cdot \Big[4(t-t_Z) + K(x)\Big] , \\ J(x) &= -31 + 60x - 33x^2 + 4x^3 + 12(1-x)^2\log(1-x) - \\ &\quad - 6(2-2x+x^2)\log(x) , \\ K(x) &= -31 - 12x + 39x^2 + 4x^3 + 12\log(1-x) - \\ &\quad - 6(2+6x+3x^2)\log(x) . \end{aligned} \tag{3.39}$$

where $t_Z = \log(m_Z^2/m_\mu^2)$. Notice the presence of some double Sudakov logs coming from the $P^V_{V_hV_h}\,(h=\pm)$ splittings, namely terms proportional to $\alpha^2(t-t_Z)^3 = \alpha^2\log^3(Q^2/m_Z^2)$,

[3] Note that the W^+ PDF receives no contributions at order α.

[4] For the sake of simplicity, we consider any EW splitting process starting from the EW scale $Q_{EW} \equiv m_Z$.

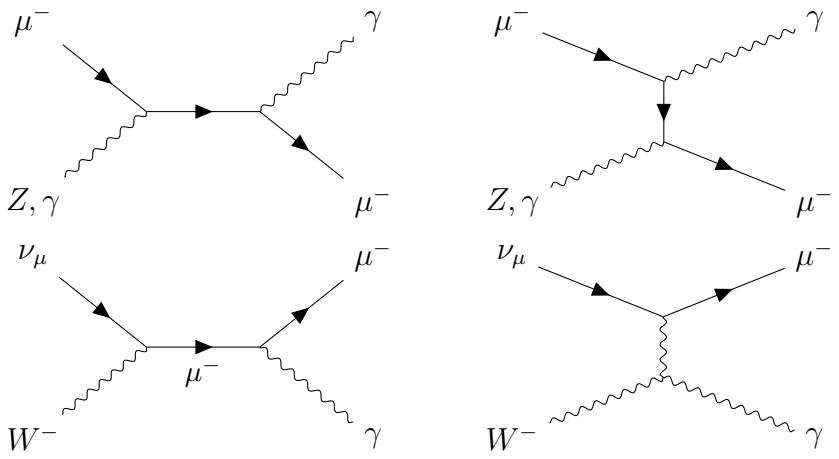


Figure 3.7: Top: leading-order partonic diagrams for Compton scattering at muon colliders: $\mu^-(Z,\gamma) \to \mu^-\gamma$. Bottom: leading-order partonic diagrams for the background process $\nu_\mu W^- \to \mu^-\gamma$

which we find to be the main responsible for the large enhancement in the mixed PDF. The comparison between the EVA estimation of eq. (3.36), the approximate $\mathcal{O}(\alpha^2)$ computation of eq. (3.37), and the leading-log resummed numerical solution is displayed in fig. 3.5, where we show the PDFs at fixed $Q = 0.5, 3$ TeV as function of x. The numerical $\mathcal{O}(\alpha^2)$ estimate in the plot contains also the other contributions of eq. (3.37), whose analytic expressions are fully reported in appendix B.1.

By comparing the different lines in fig. 3.5 it is clear that higher order splittings do have a large impact on the mixed $f_{Z/\gamma}$, with the main contribution captured by the W boson emission of fig. 3.6, that we computed analytically in eq. (3.39). The large difference between the $\mathcal{O}(\alpha)$ and $\mathcal{O}(\alpha^2)$ result could cause concerns regarding possible large corrections at $\mathcal{O}(\alpha^3)$. Such worries can be put to rest by observing that the large $\mathcal{O}(\alpha^2)$ effect is not due to anomalously large corrections but to an anomalously small contribution at leading order (due to the cancellation described above), and by comparing in fig. 3.5 the $\mathcal{O}(\alpha^2)$ line (blue) with the resummed one of LePDF (green).[5]

3.3 Compton scattering

As a first example to showcase the impact of the Z/γ PDF we consider the simple SM process of Compton scattering at muon colliders: $\mu^- + (\gamma, Z) \to \mu^-\gamma$, where the initial photon or Z boson comes from the PDF of the anti muon.[6] The leading-order partonic diagrams inducing this process are shown in the top row of fig. 3.7. The resulting helicity-dependent partonic cross sections for initial-state photon, Z boson, or mixed Z/γ state are reported in appendix B.2.1. This process, where a large new physics effect is not expected due to the

[5] For Z/γ_+, the relative difference between the two increases only near the region where the mixed PDF changes sign, which is to be expected since in that region the PDF is necessarily very small.

[6] The contribution to the process from picking up the μ^- PDF inside the anti-muon beam and γ, Z from the muon is negligible.

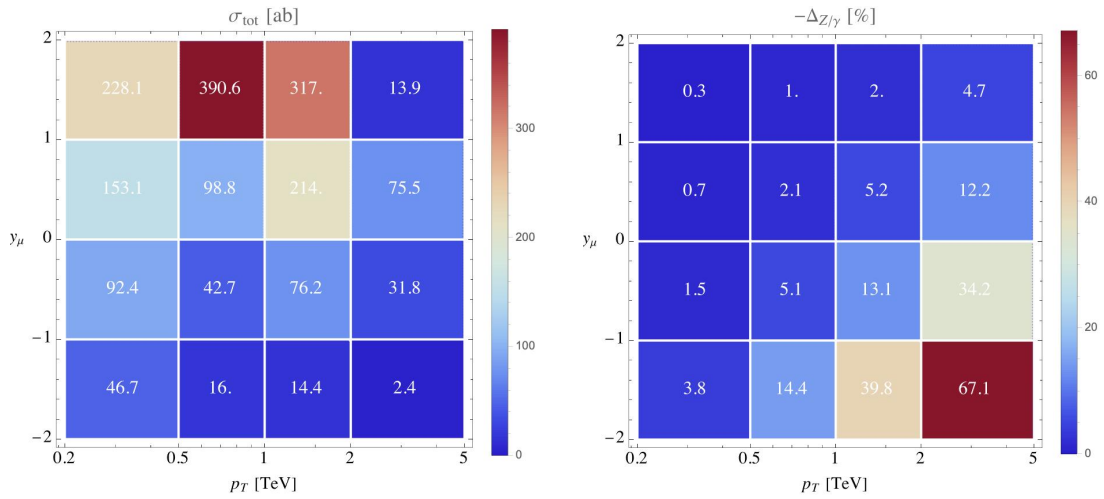


Figure 3.8: In the left panel we show the total cross section, in ab, for $\mu^-\gamma$ production at a 10 TeV MuC in bins of muon p_T and rapidity y_μ, integrating in the photon rapidity between $y_\gamma \in [-2, 2]$. The right panel shows the $\Delta_{Z/\gamma}$ ratio in percent for the same bins.

strong constraints on the coupling between the muon and the photon or the Z boson,[7] can be instead a suitable testing ground to study experimentally the effect of the mixed Z/γ PDF, by comparing the experimental results with the SM prediction. This is the perspective under which we study it, with the goal of obtaining the size of this novel contribution and estimating the potential experimental reach to measuring it.

To obtain cross section for $\mu^-\gamma$ production at a muon collider we multiply the partonic cross sections with the corresponding PDFs, as described in appendix B.2. To the partonic process of interest, however, we must also add the process $\nu_\mu W^- \to \mu^-\gamma$, since it has the same final state (see bottom row of fig. 3.7). We expect this to be subleading due to the suppression of the initial state's PDFs, compared to the one of μ^- and γ or Z. The sum of all contributions gives us the the fully differential cross section in the muon and photon rapidities and their p_T. In fig. 3.8 (left panel) we show the total cross section (in ab) in bins of p_T and muon rapidity y_μ, where we integrated over the photon rapidity between -2 and 2. We recall that the planned integrated luminosity for a 10TeV MuC is approximately 10ab^{-1}.

To evaluate the impact of the Z/γ PDF we define the ratio $\Delta_{Z/\gamma}$ of the Z/γ-PDF contribution to the total cross section, over the full result:

$$\Delta_{Z/\gamma} \equiv \frac{\sigma_{Z/\gamma}}{\sigma_{\rm tot}} \,, \tag{3.40}$$

where the ratio is taken either for the same bin or at the level of differential cross sections, depending on the plot. We observe that this ratio is almost independent on y_γ, which is the reason for integrating over the photon rapidity in fig. 3.8. In the right panel we report $-\Delta_{Z/\gamma}$ for the same bins. The impact of the Z/γ PDF is negative and ranges in size from about 1% up to tens of percent at large p_T and backward muons (negative rapidities). We note that the contribution due to the $\nu_\mu W^-$ initial state is about 2% of the total one in the bins with $1 < y_\mu < 2$, less than 1% for $0 < y_\mu < 2$, and at the per-mille level or smaller for $y_\mu < 0$.

[7] The same couplings could be tested also, with better sensitivity to heavy new physics, in $\mu^-\mu^+ \to \mu^-\mu^+$ and $\mu^-\mu^+ \to \ell^-\ell^+$, other than in precise low-energy measurements such as that of the muon $(g-2)$.

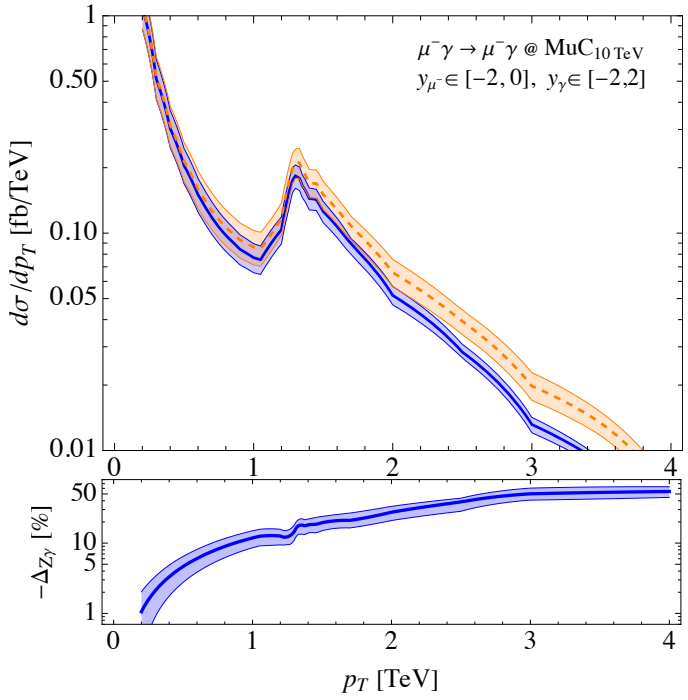


Figure 3.9: Differential cross section $d\sigma/dp_T$ for $\mu^-\gamma$ production at a 10TeV MuC, after having integrated over $y_\gamma \in [-2, 2]$ and $y_\mu \in [-2, 0]$. The solid blue (dashed orange) line include (exclude) the contribution from the Z/γ PDF. Its relative contribution, in percentage, is shown in the lower panel. The colored bands are obtained by varying the factorizaton scale in the PDFs as $Q \in [p_T/2, 2p_T]$.

In particular, it is completely negligible in all the bins where the Z/γ PDF gives the largest contribution.

In fig. 3.9 we plot the differential cross section in p_T, integrated in rapidities over the full experimental coverage for the photon, $y_\gamma \in [-2, 2]$, and for a backward-going muon, $y_\mu \in [-2, 0]$. We show in solid blue (dashed orange) the values obtained by including (excluding) the contribution due to the Z/γ PDF. The $\Delta_{Z/\gamma}$ ratio is shown in the bottom panel. We estimate the uncertainty in the PDF evaluation by varying the factorization scale around the central value $Q = p_T$ from $p_T/2$ to $2p_T$, and report the corresponding uncertainty bands. We note that the peak at around $p_T \sim 1350\,\mathrm{GeV}$, that is noticeable in fig. 3.9, is due to the fact that, for those values of p_T the kinematical configuration with $x_1 = 1$ (x_1 being the Bjorken variable for the incoming muon) enters the range of rapidities included in the integration. For $x_1 \approx 1$ the μ^- PDF gets the large enhancement due to it being the valence parton, remnant of the Dirac delta that describes the zeroth order PDF of the muon.

figs. 3.8 and 3.9 show that this process is very sensitivy to the Z/γ PDF, especially going to values of $p_T \gtrsim 500$GeV and backward-going muons. To better quantify this statement we can calculate the statistical significance of the Z/γ contribution over the null assumption, i.e. over the case where it is absent, for each of the (p_T, y_μ) bins assuming $\mathcal{L} = 10\,\mathrm{ab}^{-1}$ of

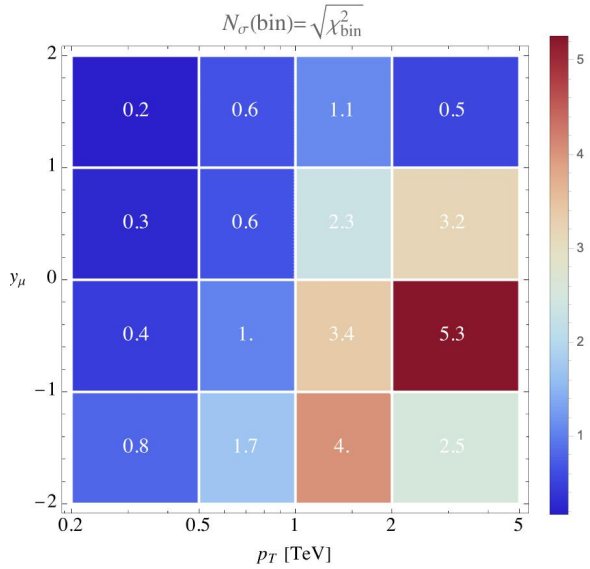


Figure 3.10: Statistical significance of the Z/γ contribution to the compton scattering process at a MuC10, in N_σ, for each (p_T, y_μ) bin.

integrated luminosity by computing[8]

$$N_\sigma(\text{bin}) \equiv \sqrt{\chi^2_{\text{bin}}} \approx \left(\mathcal{L}\frac{(\sigma_{\text{tot}} - \hat{\sigma})^2}{\hat{\sigma}}\right)^{1/2} , \tag{3.41}$$

where $\hat{\sigma} = \sigma_{\text{tot}} - \sigma_{Z/\gamma}$. The result is shown in fig. 3.10, where we see that in several bins the effect of the Z/γ PDF exceeds 3σ of statistical significance and even 5σ in the bin $p_T \in [2-5]$TeV and $y_\mu \in [-1, 0]$. While at present this effect might be diluted by the PDF scale uncertainty, future theory developements are expected to reduce it substantially since performing precise measurements of EW processes is one of the main goals of a future high-energy muon collider.

3.4 Associated Higgs plus W production

The large rate of emission of collinear photons and EW gauge bosons from high-energy initial-state leptons leads to the well known statement that *high energy muon colliders are vector boson colliders* [230, 252, 302]. Indeed, one of the main processes for the production of electroweakly charged final states in TeV-scale $\mu\bar{\mu}$ collision is through vector boson fusion. When the typical energy of the hard scattering process is much higher than the EW scale then collinear factorization can be applied and the process can be described in terms of the gauge bosons PDFs. While the most important channel for Higgs production at a MuC is single-production [230, 252, 310], associate production with a Z or W boson is also relevant and can offer additional handles to constrain Higgs couplings.

Our goal is to quantify the impact of the Z/γ PDF in WH production and compare it with the expected experimental precision. Contrary to the Compton scattering studied

[8]We only consider statistical uncertainties since they are of several percent in the most sensitive bins: a value larger than the expected future theoretical uncertainties, of about 1%.

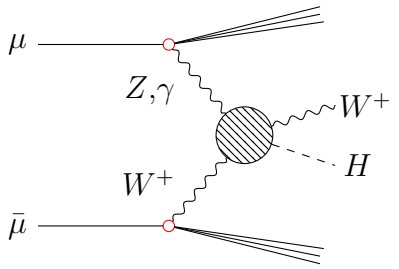


Figure 3.11: Sketch of a vector boson fusion process with production of a W^+H pair. The internal boson lines stand for Z, γ or their interference. The red empty dots emphasize that the boson PDFs are the results to the full DGLAP equations, not only a single splitting.

above, in this case one would like to use precise measurement of this process in order to test for small contributions due to new physics. To do that it is crucial to have a complete and precise SM prediction.

The cross section for $W^{\pm}H$ production at MuC, sketched in fig. 3.11, has already been investigated, for instance, in Ref. [309]. However, these studies employed the EVA approximation for the EW gauge bosons PDFs and totally neglected the mixed Z/γ term.

Total cross sections are computed by integrating the triply differential distribution defined in appendix B.2. For the case under consideration, the parton 2 is a W^+ while the parton of type 1 can either be either Z, γ, or the interference contribution. In the latter case, $f_1(x_1) = f_{Z/\gamma}(x_1)$ and the hard "cross section" appearing in eq. (B.12) is understood to be proportional to $\mathrm{Re}\,[\mathcal{M}(ZW^+ \to W^+H) \cdot \mathcal{M}(\gamma W^+ \to W^+H)^*]$, as explained in section 3.2. We compute the differential partonic cross section $d\sigma_{\mathrm{H}}/dt$ using the FeynCalc [311, 312] and FeynArts [313] packages. Then, the integrals of eq. (B.12) are evaluated numerically with the following domain restrictions:

$$|y_W| < 2\,, \quad |y_H| < 2\,, \quad m > 0.5\,\mathrm{TeV}\,, \tag{3.42}$$

where y are the rapidities of final state particles and m their total invariant mass. The rapidity cuts depend on the detector geometry [314] while the lower value for the energy in the center of mass frame is set in such a way that the factorization assumption is not spoiled. In Ref. [309], the authors computed the cross sections with a different choice of cuts, namely $|y_i| < 3, m > 1\,\mathrm{TeV}$. Employing the same setup, we find a good agreement with their results (see Table 4 in [309]), with small deviations ascribable to the use of the complete numerical PDFs.

As this channel could be potentially exploited to look for indirect signatures of new physics, we parameterize possible deviations in the ZZH and WWH couplings and investigate the way they affect the prediction of the total cross section.[9] Denoting by $\kappa_{W,Z}$ the multiplicative deviations in the tree-level SM Higgs couplings to EW gauge bosons [315], such that the SM case is obtained for $\kappa_{W,Z}^{\mathrm{SM}} = 1$, and fixing the factorization scale to $Q = m/2$ (we

[9] In principle, modified couplings should be employed in the computation of the PDFs as well. However, this effect is negligible since Higgs couplings induce a very small contribution to EW PDFs [282].

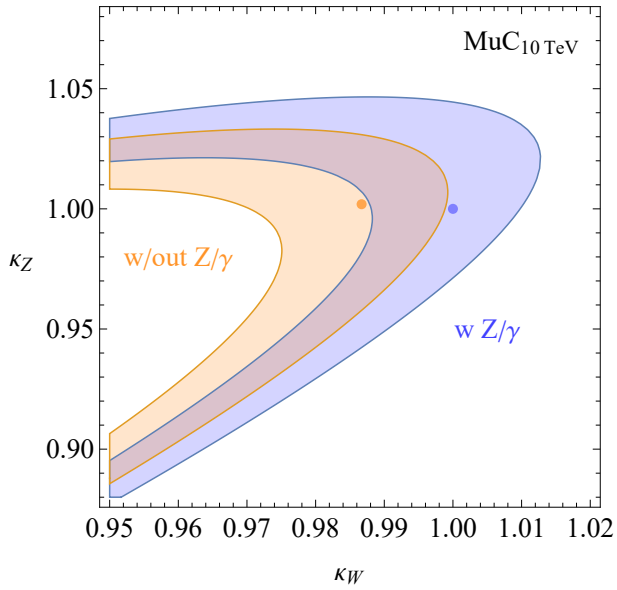


Figure 3.12: 95% CL bands for the effective couplings $\kappa_{W,Z}$ assuming the SM central value and a relative precision of the 1% level, for 10 TeV MuC. The factorization scale is $Q = m/2$, where m is the center of mass energy of the hard scattering.

study the impact of scale uncertainties below), we find the following cross sections:

$$\begin{aligned}
\sigma^{3\,\mathrm{TeV}}_{\text{no-}Z/\gamma}\,[\mathrm{fb}] &= 12.87\,\kappa_W^2 + 8.71\,\kappa_Z^2 - 17.79\,\kappa_W\kappa_Z\,, \\
\delta\sigma^{3\,\mathrm{TeV}}_{Z/\gamma}\,[\mathrm{fb}] &= -0.075\,\kappa_W^2 - 0.010\,\kappa_W\kappa_Z\,, \\
\sigma^{10\,\mathrm{TeV}}_{\text{no-}Z/\gamma}\,[\mathrm{fb}] &= 135.70\,\kappa_W^2 + 126.93\,\kappa_Z^2 - 255.82\,\kappa_W\kappa_Z\,, \\
\delta\sigma^{10\,\mathrm{TeV}}_{Z/\gamma}\,[\mathrm{fb}] &= -0.15\,\kappa_W^2 - 0.030\,\kappa_W\kappa_Z\,,
\end{aligned} \tag{3.43}$$

where $\sigma_{\text{no-}Z/\gamma}$ is the total cross section computed without taking into account the the Z/γ PDF. Its contribution is given by $\delta\sigma_{Z/\gamma}$. Remarkably, the Z/γ interference term mostly modifies the weight of the κ_W contribution. We can have a better insight on its effect by rewriting $\kappa_{W,Z}$ around the SM value, $\kappa_{W,Z} \equiv 1+\delta_{W,Z}$, and comparing the expressions without and with the mixed PDF:

$$\begin{aligned}
\sigma^{3\,\mathrm{TeV}}_{\text{no-}Z/\gamma}\,[\mathrm{fb}] &= 3.79 + 7.95\,\delta_W - 0.37\,\delta_Z + 12.9\delta_W^2 - 17.8\delta_W\delta_Z + 8.71\delta_Z^2, \\
\sigma^{3\,\mathrm{TeV}}_{\text{tot}}\,[\mathrm{fb}] &= 3.71 + 7.79\,\delta_W - 0.38\,\delta_Z + 12.8\delta_W^2 - 17.8\delta_W\delta_Z + 8.71\delta_Z^2, \\
\sigma^{10\,\mathrm{TeV}}_{\text{no-}Z/\gamma}\,[\mathrm{fb}] &= 6.81 + 15.58\,\delta_W - 1.96\,\delta_Z + 135.7\delta_W^2 - 255.8\delta_W\delta_Z + 126.9\delta_Z^2, \\
\sigma^{10\,\mathrm{TeV}}_{\text{tot}}\,[\mathrm{fb}] &= 6.63 + 15.25\,\delta_W - 1.99\,\delta_Z + 135.6\delta_W^2 - 255.9\delta_W\delta_Z + 126.9\delta_Z^2,
\end{aligned} \tag{3.44}$$

where $\sigma_{\text{tot}} = \sigma_{\text{no-}Z/\gamma} + \delta\sigma_{Z/\gamma}$. From these expressions one can understand that the main effect of the Z/γ contribution is to modify the SM prediction, by an amount of approximately 2% (3%) for the 3 (10) TeV MuC. Such percent effect is important to be taken into account given the expected future precision in such measurements. This is illustrated in fig. 3.12 for the 10 TeV MuC, where we perform a fit in the (κ_W, κ_Z) plane assuming a measurements

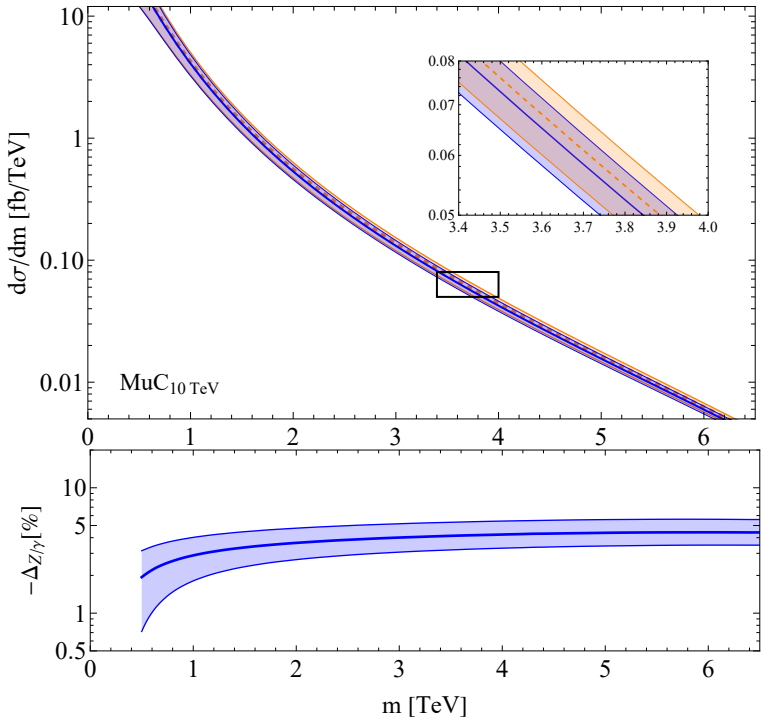


Figure 3.13: Differential cross section $d\sigma/dm$ for W^-H production at a 10 TeV MuC, after having integrated over $y_{W,H} \in [-2, 2]$. The solid blue (dashed orange) line include (exclude) the contribution from the Z/γ PDF. Its relative contribution, in percentage, is shown in the lower panel. The colored bands are obtained by varying the factorizaton scale in the PDFs as $Q \in [m/2, 2m]$.

of WH production cross section with 1% precision.[10] For the *truth* value we take the SM point including the Z/γ effect, then fit it with the expressions in eq. (3.43). It is worth emphasizing that the WH production receives a background contribution from the muon-neutrino scattering, whose total cross section is $\sigma^{3\,\text{TeV}\,(10\,\text{TeV})}_{\mu_L\,\nu\to W^+H} = 0.160\,(0.031)$ fb.[11]

By comparing the cross sections $\sigma_{\text{no-}Z/\gamma}$ in eq. (3.43) with the ones in eq. (3.44) one notices that near the SM point, $\kappa_{W,Z} \approx 1$, each of the three terms in $\sigma_{\text{no-}Z/\gamma}$ is larger than the overall result, signalling that a cancellation takes place in the SM limit. This cancellation is stronger at the 10 TeV MuC than at 3 TeV. Its origin lies in the Higgs's role in unitarising the scattering of longitudinally polarised gauge bosons. In fact, the leading contribution to each of the three terms in $\sigma_{\text{no-}Z/\gamma}$ in eq. (3.43) is due to the scattering of longitudinal helicities: $Z_L W_L^+ \to W_L^+ H$. Away from the SM limit, specifically for values that violate custodial symmetry (i.e. if $\kappa_Z \neq \kappa_W$) the corresponding scattering amplitude grows with the energy and at some point it would violate perturbative unitarity. In the SM limit this energy-growing behaviour is cancelled.[12]

In fig. 3.13 we plot the SM differential cross section $d\sigma/dm$ for a 10 TeV MuC, as a

[10] This is a reasonable estimate given the expected number of events in the $H \to b\bar{b}$ and $W \to \ell\nu$ decay channels, with 10ab^{-1} of integrated luminosity.

[11] A dedicated study on the effects due to the muon neutrino PDF inside the muon will is the focus of [254].

[12] In the SM Effective Field Theory, a dimension-6 operator that would induce such an effect in this channel is $\mathcal{O}_T = (H^\dagger \overset{\leftrightarrow}{D}_\mu H)^2$, where H is the Higgs doublet.

function of the hard scattering center of mass energy m. The colored bands are obtained by varying the factorization scale, akin to what we did in fig. 3.9. Compared with the Compton scattering, the Z/γ interference contribution has a weaker effect, so that the colored bands almost superpose. The relative size of the effect can be seen in the bottom panel, its size being of a few percent, confirming the result derived above for the integrated cross section.

3.5 ALP single production

As an example to showcase the importance of the Z/γ PDF also for BSM searches, we consider the process of single production of an axion-like pseudo-scalar particle (ALP), $\phi \sim (1,1)_0$ under the SM gauge group. Neglecting the coupling to gluons, which have a suppressed PDF at muon colliders [281, 282], the leading interactions with electroweak vector bosons are described by the dimension-five operators

$$\mathcal{L}_{\phi VV} = \frac{C_W}{\Lambda}\phi W^a_{\mu\nu}\widetilde{W}^{\mu\nu,a} + \frac{C_B}{\Lambda}\phi B_{\mu\nu}\widetilde{B}^{\mu\nu}\,. \tag{3.45}$$

Below the electroweak scale, the resulting couplings with physical EW bosons are:

$$\mathcal{L}^{eff}_{\phi VV} = \frac{c_{\phi ZZ}}{4\Lambda}\phi Z_{\mu\nu}\widetilde{Z}^{\mu\nu} + \frac{c_{\phi\gamma\gamma}}{4\Lambda}\phi F_{\mu\nu}\widetilde{F}^{\mu\nu} + \frac{c_{\phi\gamma Z}}{2\Lambda}\phi F_{\mu\nu}\widetilde{Z}^{\mu\nu} + \frac{c_{\phi WW}}{2\Lambda}\phi W^+_{\mu\nu}\widetilde{W}^{-\mu\nu}\,, \tag{3.46}$$

where

$$\begin{aligned} c_{\phi\gamma\gamma} &= 4(s^2_{\theta_W}C_W + c^2_{\theta_W}C_B), \quad c_{\phi ZZ} = 4(c^2_{\theta_W}C_W + s^2_{\theta_W}C_B), \\ c_{\phi\gamma Z} &= 4s_{\theta_W}c_{\theta_W}(C_W - C_B), \quad c_{\phi WW} = 4C_W\,. \end{aligned} \tag{3.47}$$

Within this model, it is straightforward to compute the partonic cross section for resonant production of a single heavy electroweak singlet in the high energy limit (*i.e.* massless vectors limit) and in the narrow-width approximation ($\Gamma_\phi \ll M_\phi$):

$$\sigma_H(V_1V_2 \to \phi)(\hat{s}) = \frac{\pi}{4}\frac{c^2_{\phi V_1V_2}}{\Lambda^2}M^2_\phi\delta(\hat{s} - M^2_\phi)\,, \tag{3.48}$$

where $V_{1,2} = Z, \gamma$ or $V_{1,2} = W^\pm$, and $\hat{s}$ is the energy in the center of mass frame. By angular momentum conservation, only amplitudes with both transverse vectors of same helicity are non-vanishing. The total cross section for a VBF process at MuC can then be computed by convoluting this with parton luminosities. The case of $W^\pm$ in the initial state follows as standard, however for Z and γ we should take into consideration also the possible interference in both initial legs, see fig. 3.14. To see how this should be implemented it is useful to extend the factorized amplitude of eq. (3.30) to both initial legs:

$$i\mathcal{M}(AD \to CE\phi) \propto \sum_{V_1}\sum_{V_2}\frac{\mathcal{M}^{\text{split}}(A \to CV_1^*)}{q_1^2 - m^2_{V_1}}\frac{\mathcal{M}^{\text{split}}(D \to EV_2^*)}{q_2^2 - m^2_{V_2}}\mathcal{M}^{\text{hard}}(V_1V_2 \to \phi)\,, \tag{3.49}$$

The cross section is obtained by squaring this expression. To describe it, we can introduce two splitting matrices, one each for μ and $\bar{\mu}$, and define

$$\rho^{\text{split}}_{\mu,V_1V_1'} = \begin{pmatrix} f^{(\mu)}_\gamma & f^{(\mu)}_{Z/\gamma} \\ f^{(\mu)}_{Z/\gamma} & f^{(\mu)}_Z \end{pmatrix}, \quad \rho^{\text{split}}_{\bar{\mu},V_2V_2'} = \begin{pmatrix} f^{(\bar{\mu})}_\gamma & f^{(\bar{\mu})}_{Z/\gamma} \\ f^{(\bar{\mu})}_{Z/\gamma} & f^{(\bar{\mu})}_Z \end{pmatrix}, \quad \sigma^{\text{hard}}_{V_1,V_1',V_2,V_2'} \propto \mathcal{M}^{\text{hard}}_{V_1,V_2}\cdot\mathcal{M}^{\text{hard}\,*}_{V_1',V_2'}\,, \tag{3.50}$$

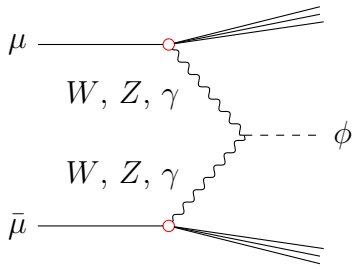


Figure 3.14: Sketch of the vector boson fusion production of a ϕ singlet. Interference effects are now possible for both the bosons entering the hard cross section. The red empty dots emphasize that the boson PDFs are the results to the full DGLAP equations, not only a single collinear emission.

where, given the definition of the couplings and for $M_\phi \gg m_Z$, the hard cross section can be written in full generality as:

$$\sigma^{\text{hard}}_{V_1,V_1',V_2,V_2'}(\hat{s}) = c_{\phi V_1 V_2}\; c_{\phi V_1' V_2'}\; \frac{\pi}{4}\frac{1}{\Lambda^2} M_\phi^2\; \delta(\hat{s} - M_\phi^2)\,. \tag{3.51}$$

The final cross section for this process at a muon collider at energy $\sqrt{s_0}$ is then obtained by summing over the $V_{1,2}^{(\prime)}$ indices, obtaining the right factorization between hard scatterings and PDFs:

$$\sigma^{Z,\gamma}_{\text{tot}}(s_0) = \sum_{V_1,V_1',V_2,V_2'} \int_{\hat{s}_{min}}^{s_0} d\hat{s} \frac{1}{s_0}\, \mathcal{L}_{V_1,V_1',V_2,V_2'}(\hat{s}, s_0) \cdot \sigma^{\text{hard}}_{V_1,V_1',V_2,V_2'}(\hat{s})\;, \tag{3.52}$$

where the parton luminosities are given by

$$\mathcal{L}_{V_1,V_1',V_2,V_2'}(\hat{s}, s_0) = \int_0^1 \frac{dz}{z} \rho^{\text{split}}_{\mu,V_1,V_1'}\left(z, \frac{\hat{s}}{4}\right) \cdot \rho^{\text{split}}_{\bar{\mu},V_2,V_2'}\left(\frac{\hat{s}}{z s_0}, \frac{\hat{s}}{4}\right). \tag{3.53}$$

Since in the narrow width approximation the hard cross section is proportional to a Dirac delta, the total cross section simplifies to

$$\sigma^{Z,\gamma}_{\text{tot}}(s_0) = \sum_{V_1,V_1',V_2,V_2'} \mathcal{L}_{V_1,V_1',V_2,V_2'}(M_\phi^2, s_0)\; c_{\phi V_1 V_2}\; c_{\phi V_1' V_2'}\; \frac{1}{s_0}\frac{\pi}{4}\frac{M_\phi^2}{\Lambda^2}\;. \tag{3.54}$$

To obtain the full cross section for single-ALP production, σ_{tot}, we should then also add the contribution from $W^\pm$ in the initial state, $\sigma_{\text{tot}} = \sigma^{Z,\gamma}_{\text{tot}} + \sigma^{W}_{\text{tot}}$, where

$$\sigma^{W}_{\text{tot}}(s_0) = \mathcal{L}_{W^-W^+}(M_\phi^2, s_0)\; c^2_{\phi WW}\; \frac{1}{s_0}\frac{\pi}{4}\frac{M_\phi^2}{\Lambda^2}\;. \tag{3.55}$$

With the aim of studying the importance of the mixed Z/γ PDF, we show in the left panel of fig. 3.15 the ratio between the contribution to σ_{tot} due to interference (*i.e.* that would vanish in the $f_{Z/\gamma} \to 0$ limit), and the complete σ_{tot}. Three cases are studied, depending on the interactions that we switch on in the UV. As it is clear from the plot, the effect becomes more and more important at higher mass scales where, however, we expect the total cross section to be suppressed. Indeed, we illustrate in the right panel of fig. 3.15 the total cross

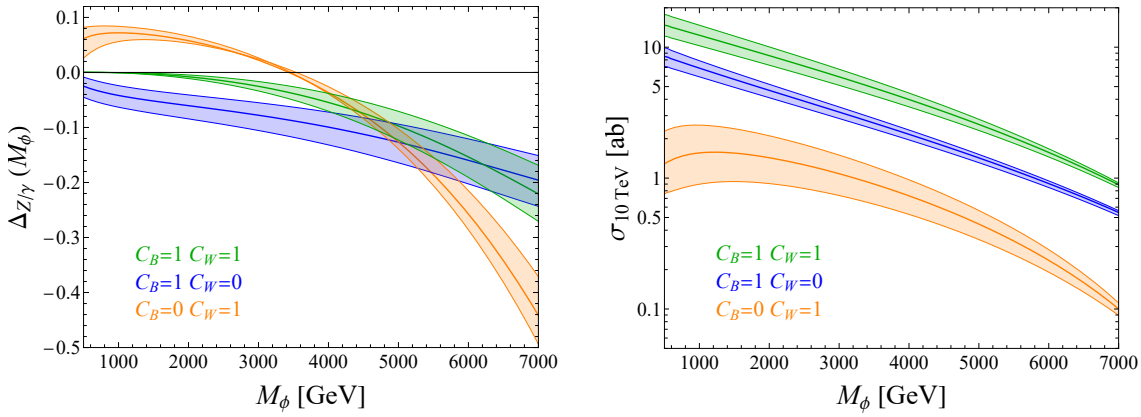


Figure 3.15: Left panel: ratio between the interference contribution to the cross section and the total $\sigma_{\rm tot}$. Right panel: total cross section as a function of the singlet mass M_ϕ. Three cases are shown depending on the WCs which are turned on in the UV, where we fix $\Lambda = 1$TeV. Uncertainty bands correspond to different choices of the factorization scale $Q = \xi \frac{\hat{s}}{2}$ with $\xi = 0.5, 1, 2$.

section in ab as a function of the EW singlet mass, for $\Lambda = 1\,\text{TeV}$. To estimate the mass reach, a reader should keep in mind that at a 10 TeV MuC the integrated luminosity is expected to be 10 ab^{-1}. We observe that, for ALP masses below ~ 4 TeV, the Z/γ PDF effect ranges from about $+10\%$ to -10%, and gives therefore a sizeable impact in the total production cross section.

3.6 Summary

The next generation of multi-TeV colliders offers a unique opportunity to probe EW interactions in a regime where SM gauge symmetries are effectively restored. Muon colliders, with their high luminosity, large center-of-mass energy available for hard scattering processes, suppressed QCD backgrounds, and relatively small footprint, are ideal for studying these phenomena.

In this study, we have provided a detailed analysis of the mixed Z/γ PDF, an exotic effect arising from EW interactions in collinear emission of initial-state radiation. Our study highlights the suppression of the LO EVA result, due to the well known accidental tuning in the vector-like muon coupling to the Z boson. By extending the EVA computation to $\mathcal{O}(\alpha^2)$, we have analytically shown how this suppression is lifted, offering a more accurate approximation to the numerical results.

We also explored the phenomenological implications of this PDF at muon colliders. Notably, we identified Compton scattering as a viable process to experimentally detect the Z/γ PDF with high precision, potentially achieving a significance greater than 5σ at a 10 TeV muon collider. Furthermore, we demonstrated that the Z/γ PDF can lead to a 2-3% modification in the SM WH production cross section, which is a substantial effect given the anticipated precision in this channel. Additionally, in the context of new physics, we showed that this PDF could modify the resonant single-production cross section of an ALP by up to 10% at a 10 TeV muon collider.

The work presented here is a step forward in understanding EW effects in parton distribution functions, a critical component of the broader effort to explore and understand electroweak interactions and their phenomenology in the unbroken regime. As muon colliders are expected to push the frontiers of high-energy physics, the precise study of such effects will be crucial in refining our understanding of the SM and unlocking new physics.

Chapter 4

Cosmological probes of BSM scenarios

Observational and conceptual evidence points to the existence of physics beyond the Standard Model. Yet, the nature and origin of such new physics remain elusive. It may manifest in high-energy collider experiments, at present or future machines, or in unexpected signals from astrophysical or cosmological observations. In this chapter, we focus on the latter possibility: exploring the high-energy frontier through cosmological probes.

The early universe acts as a natural high-energy laboratory, where physical processes at extreme energy scales may have left imprints that are still accessible today. A striking example of this is the production of gravitational waves (GWs) from cosmological sources [316], such as, for example, during cosmological first-order phase transitions (FOPTs) [317–321]. Detecting such a signal, either in current observations or in the next generation of GW detection experiments, would provide compelling evidence for new physics at the corresponding energy scale.

In the following, we study some aspects of FOPTs, with a particular focus on their interplay with dark matter physics. The origin of dark matter, regardless of its specific nature, is deeply tied to the thermal history of the universe. It is thus important to assess how modifications to the standard cosmological evolution may impact the mechanisms responsible for the generation of a dark matter relic. In particular, we focus on a class of FOPTs that feature a phase of supercooling, that is, a finite period of inflation characterized by a nearly constant Hubble rate and exponential expansion of the universe. As a consequence, both the thermal freeze-out regime, where dark matter was initially in thermal equilibrium, and the freeze-in regime, where dark matter production occurs through feeble interactions, are affected.

Supercooling epochs arise in several well-motivated BSM scenarios, linking modified thermal histories to well-known shortcomings of the Standard Model and to the need for new physics. For instance, supercooled phase transitions can be associated with the breaking of a Peccei–Quinn $U(1)$ symmetry [322, 323], either in weakly coupled extensions, where the axion is an elementary scalar, or in strongly coupled models where the axion emerges as a composite pseudo-Nambu–Goldstone boson. Other motivated frameworks involve classically conformal BSM extensions, often featuring additional gauge symmetries such as an Abelian $U(1)$ factor [324–332] or $SU(2)$ gauge groups [330, 333–344]. These models have been widely studied in relation to baryogenesis and neutrino physics, with symmetry breaking triggered by radiative corrections à la Coleman–Weinberg. Finally, supercooling can also arise in generic strongly coupled sectors undergoing a first-order transition [345–354]. Such dynamics can be

relevant for composite Higgs models, where new strong interactions above the TeV scale are employed to address the hierarchy problem. In general, supercooling can characterise phase transitions in hidden or visible sectors, at weak or strong coupling.

Supercooled transitions are especially compelling also from an experimental perspective. Among all classes of FOPTs, they are known to produce particularly strong gravitational wave signals. This makes them especially promising targets for current and upcoming GW experiments.

The structure of this chapter is as follows. In section 4.1, we briefly review the theory of cosmological first-order phase transitions. In section 4.2, we discuss the thermal history of a supercooled universe and the characteristic stages of such an evolution. Section 4.3 is devoted to the study of dark matter decoupling and relic abundance in this modified cosmological background, with an emphasis on scenarios that have received limited attention in previous literature. Finally, in section 4.4, we summarise the results and offer a few remarks on baryogenesis. The results presented in this chapter are preliminary and based on ongoing work.

4.1 Cosmological first order phase transitions

In cosmology, symmetries and their breaking are particularly important in determining the dynamics of the early universe. As it cooled down from the hot, dense conditions following the Big Bang, the universe may have undergone a series of phase transitions, driven by the changing temperature and environment. The main feature and consequences of each phase transition depend on how this symmetry breaking occurs.

Of particular interest are first-order phase transitions. These transitions typically involve a barrier separating the symmetric and broken minima in the effective potential, and are characterized by a discontinuous change in the order parameter, the release of latent heat, and the coexistence of multiple phases. Such transitions can lead to out-of-equilibrium dynamics with many phenomenological implications, from mechanisms for baryogenesis to the generation of gravitational waves and topological defects.

Within the Standard Model, two well-known transitions are the electroweak symmetry breaking and the QCD confinement transition. Neither of these is a first-order transition, but crossovers. However, this opens up an exciting window for new physics: many BSM scenarios predict that the electroweak transition could become first-order, or that additional FOPTs might occur at higher energy scales earlier in the cosmic history.

FOPTs proceed via tunneling processes, where the field initially trapped in the metastable (false) minimum of the potential tunnels through a barrier to the true vacuum. A typical example of such a potential is shown in fig. 4.1, where the scalar field ϕ, acting as the order parameter, sits initially in the false vacuum. Usually, $V(\phi)$ is the effective potential obtained taking into account radiative and thermal corrections, which may be the origin of the true vacuum, otherwise absent at higher scale.

FOPTs do not occur instantaneously and homogeneously everywhere in the universe, but they proceed instead through the nucleation of finite regions of true vacuum within the surrounding false vacuum. These nucleated bubbles then expand and eventually percolate, completing the transition throughout the universe.

The theoretical framework for describing these processes was established by Coleman in

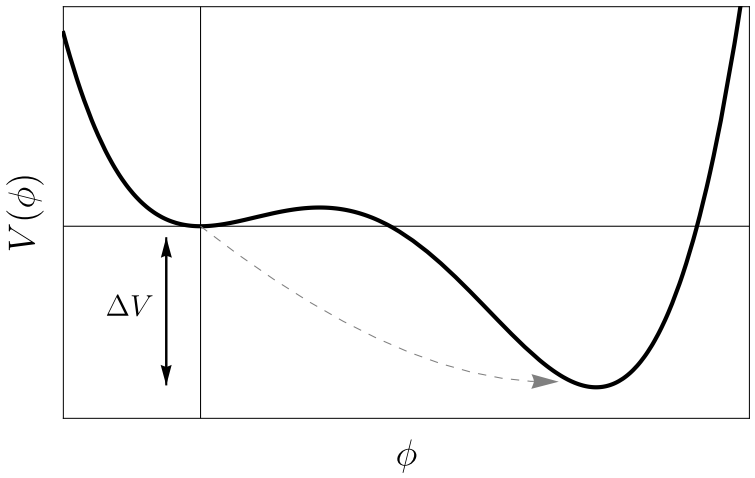


Figure 4.1: Sketch of the typical potential characterizing first order phase transitions. Tunneling through the potential barrier drives the scalar field, that is the order parameter of the transition, from the false vacuum and the true vacumm value. The gap between the two minima, ΔV, provides a vacuum energy component in the Friedmann equations prior to the completion of the phase transition.

his seminal works on tunneling in QFT [355, 356], later extended to include finite-temperature effects relevant for cosmology [357]. We now review a simplified treatment of this formalism, though we refer to ref.s [319, 358] for a comprehensive review.

To describe the tunneling process, we need to define the tunneling rate Γ, *i.e.* the probability per unit volume and unit time that a transition to true vacuum occurs and that a bubble is nucleated. It can be studied by using the Euclidean path integral approach and isolating its saddle point contribution, solving the equation of motion

$$\frac{\delta S_E[\phi]}{\delta \phi} = 0\,.$$

This classical solution is usually called *bounce*[1], corresponding to the field profile of the nucleated bubble. The vacuum decay rate can then be written as

$$\Gamma = A\, e^{-S_E} \tag{4.1}$$

where A has the dimension of energy to the fourth power[2], and S_E is the Euclidean action evaluated on the solution of the Euclidean eom. As Coleman showed, the bounce solution with minimal action at zero temperature exhibits a maximal spherical symmetry $O(d)$, where d is the total number of euclidean dimensions. Thus, the eom simplifies to

$$\frac{d^2\phi}{d\rho^2} + \frac{d-1}{\rho}\frac{d\phi}{d\rho} = \frac{dV}{d\phi}, \tag{4.2}$$

[1]The solution we are interested in is a saddle-point, with the presence of a negative eigenvalue of the second functional derivative of the action corresponding to instability of the false vacuum.

[2]The coefficient A displayed in eq. (4.1) is often estimated as $A \sim T^4$, however a rigorous treatment based on functional determinants can be employed for rigorous results [356, 358].

where ρ is the euclidean radius, and with boundary conditions

$$\frac{d\phi}{d\rho}(\rho = 0) = 0, \quad \phi(\rho = \infty) = 0\,. \tag{4.3}$$

At finite temperature $T > 0$, the euclidean time is compactified and periodic, with extension $\beta = 1/T$. In this case, there are both $O(d)$ solutions and $O(d-1)$ solutions, with the latter corresponding to spherical symmetry only in spatial directions, obtained from the same eom of eq. (4.2) after substituting $d \to d-1$. In general, for $d = 4$, the exponent of the tunelling rate in eq. (4.1) is dominated by one among the following four-dimensional and three-dimensional actions

$$\begin{aligned} S_4 &= 2\pi^2 \int_0^\infty d\rho\, \rho^3 \left[\frac{1}{2}\left(\frac{d\varphi^{(4)}}{d\rho}\right)^2 + V(\varphi^{(4)})\right], \\ \frac{S_3}{T} &= \frac{4\pi}{T} \int_0^\infty d\rho\, \rho^2 \left[\frac{1}{2}\left(\frac{d\varphi^{(3)}}{d\rho}\right)^2 + V(\varphi^{(3)})\right], \end{aligned} \tag{4.4}$$

where $\varphi^{(4)}$ and $\varphi^{(3)}$ denote respectivelly the $O(4)$ and $O(3)$ solutions, while ρ is understood to be the 4(3)-dimensional euclidean radius in the first(second) line. An example of a $O(4)$ bounce solution obtained from the quartic potential shown in fig. 4.1 is illustrated in fig. 4.2. If we look at this spherical solution, it is natural to identify the location of the bubble wall at a distance $\rho = R$, as the collection of points $(\tau, \vec{x})$ such that $R = \sqrt{\tau^2 + \vec{x}^2}$.

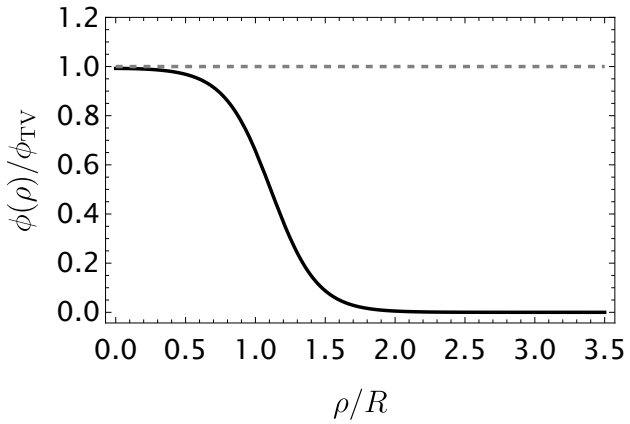


Figure 4.2: Typical bounce solution of the classical equation of motion in presence of potentials as the one in fig. 4.1. The transition region in which the field rapidly drops from the true vacuum value $\phi_{\rm TV}$ to the false vacuum value $\phi_{\rm F} = 0$ can be identified as the location of the bubble surface, with euclidean radius R.

Understanding how these bubbles expand and evolve in time involves moving back to Minkowski spacetime. When rotating back, the location of the bubble surface is identified by $R = \sqrt{\vec{x}^2 - t^2}$. Consequently, the bubble expands with the time t, characterized by an increasing radius given at any instant by $r(t) = |\vec{x}(t)| = \sqrt{R^2 + t^2}$. Following this equation, the bubble wall will asymptotically reach the speed of light. However, in most of realistic scenarios, a friction is applied by the sorrounding plasma of particles, and the bubble walls often reach some terminal velocities.

In the $O(3)$ case, the euclidean field profile only depends on the spherical radius of three-dimensional space. Thus, when rotating back to Minkowski, these solutions are stationary. It is generally believed that thermal fluctuations will slightly deform the radius $R \to R + \delta$, causing the expansion to begin.

Assuming that the nucleation rate is larger than Hubble $\Gamma > H^4$, the expanding bubbles will eventually merge, with the collision of regions of true vacuum giving rise to violent processes. Such phenomenon can lead to the production of gravitational waves. Calling $T_{ij}(x)$ the stress-energy tensor built out of $\phi(x,t)$, the total field describing the multi-bounces configuration, we can use Weinberg's master formula [359]

$$\frac{\mathrm{d}E}{\mathrm{d}\Omega_k\ \mathrm{d}\omega} = 2G\omega^2 \Lambda_{ij,lm}(\hat{k}) T^*_{ij}(\vec{k}) T_{lm}(\vec{k})\,, \tag{4.5}$$

that relates the evolution of the scalar field to the energy radiated as gravitational waves towards a direction $\hat{k}$, where $\Lambda_{ij,lm}(\hat{k})$ is the projector along this direction and Ω_k the solid angle. The fourier transform of the stress energy tensor in eq. (4.5) and the subsequent integration over angles can be performed numerically, despite being very demanding. For this reason, many semi-analytic techniques, based on approximate descriptions of the bubbles collisions, have been formulated. On general grounds, the final GWs spectrum can be expressed as [321, 360–362]

$$\Omega_{\mathrm{GW}}(\omega) \equiv \frac{1}{E_{\mathrm{tot}}} \frac{\mathrm{d}E}{\mathrm{d}\ln\omega} = \left(\frac{H}{\beta}\right)^2 \left(\frac{\alpha}{1+\alpha}\right)^2 S(\omega), \tag{4.6}$$

where $S(\omega)$ is a function describing the shape of the GW spectrum, that can be derived numerically or estimated via analytical approximations. In addition, we have introduced two key parameters that characterize the dynamics of a FOPT: the strength of the transition α, and the typical timescale of the transition β:

$$\alpha = \frac{\Delta V - T\frac{d\Delta V(\phi)}{dT}}{\rho_{\mathrm{rad}}} \approx \frac{\Delta V}{\rho_{\mathrm{rad}}}, \qquad \frac{\beta}{H} = T\frac{d(S_E/T)}{dT}\,. \tag{4.7}$$

We can observe that the signal strength is particularly enhanced in the cases in which the gap between the two vacua, ΔV, is particularly large compared to the energy density of the radiation bath ρ_{rad}. This is exactly the case of supercooling, which is described in the next section.

The collision of bubble profiles is not the only potential source of gravitational waves. It is known that two further sizable contributions come from sound waves and turbulance effects that characterize the thermal plasma. However, these contributions are negligible in the specific scenario of supercooling, since the period of inflation causes a strong dilution of the species present in the plasma.

Although there is a rich and extensive literature on the computation of the GW spectrum through numerical methods [360, 363–366] or analytic estimates [321, 361, 362, 367, 367, 368], they go well beyond the scope of this brief review and we do not comment further on this. We will consider FOPTs, and in particular supercooled transitions, as an interesting background scenario where the modified cosmology can have a sizable impact on the phenomenology of a dark sector.

4.2 Supercooling

Supercooled phase transitions occur when, due to a suppressed nucleation rate Γ, the system remains trapped in the metastable phase for extended periods, beyond the critical temperature at which a true vacuum develops. When the universe cools down and reaches the temperature $T_{\rm inf}$ defined by the equality

$$\frac{\pi^2}{30} g_* T_{\rm inf}^4 = \Delta V = 3 H_{\rm inf}^2 m_{\rm Pl}^2 \,, \tag{4.8}$$

the vacuum energy becomes the dominant component. From this point, the universe undergoes a period of inflation characterized by a constant Hubble rate $H_{\rm inf}$ and hence an exponential expansion

$$\frac{a(t)}{a(t_{\rm inf})} = e^{H_{\rm inf}\, t} \,, \quad \frac{T(t)}{T(t_{\rm inf})} = e^{-H_{\rm inf}\, t} \,. \tag{4.9}$$

The exponential decrease (growth) of the temperature (scale factor) can also be parametrized in terms of e-folds ΔN, defined by the relation $T = T_{\rm inf}\, e^{-\Delta N}$. The vacuum domination epoch lasts until when the universe reaches the nucleation temperature $T_{\rm nuc}$ such that the nucleation rate per volume is $\Gamma(T_{\rm nuc}) > H^4$, triggering enough bubbles formation and the completion of the transition. The subsequent release of latent heat then reheats the universe, restoring thermal equilibrium. This cosmological history is sketched in fig. 4.3.

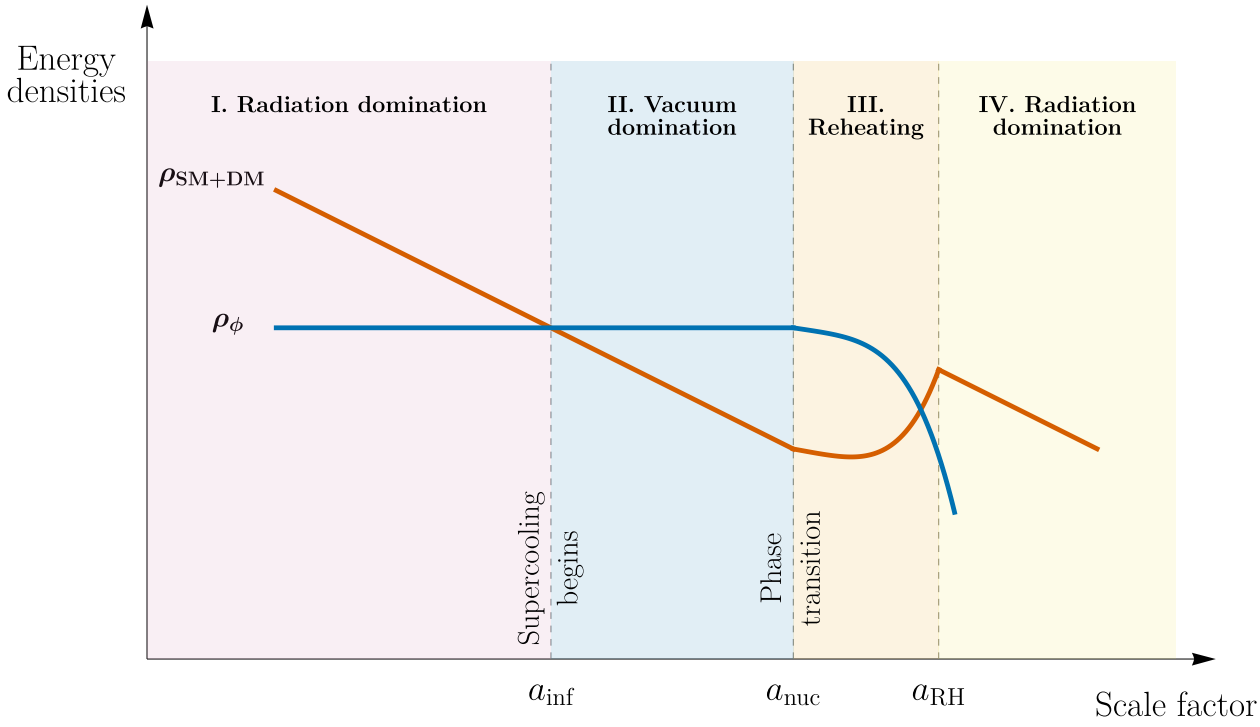


Figure 4.3: Cartoon of the evolution of energy densities in a supercooled universe, assuming Dark Matter was initially in thermal equilibrium with SM. DM freeze out and the implications of supercooling on DM freeze-in (and *phase-in* [369]) have been carefully studied in the regions I, III and IV. Here, we focus on the details of freeze-out happening in the region II.

Prior to supercooling, the number density of any particle species in thermal equilibrium with the radiation bath follows the standard thermal distribution:

$$n_i^{\rm eq} = \frac{\zeta(3)}{\pi^2} g_i T^3 \,, \tag{4.10}$$

and the total entropy density is given by

$$s = \frac{2\pi^2}{45} g_{\star s} T^3 \,. \tag{4.11}$$

Therefore, the abundance of any particle species at equilibrium reads:

$$Y_i^{\rm eq} = \frac{n_i^{\rm eq}}{s} = \frac{45\zeta(3) g_i}{2\pi^4 g_{\star s}} \,. \tag{4.12}$$

During the phase of inflation, both the number density and entropy density scale as a^{-3}, ensuring that the yield Y_i remains constant despite the exponential expansion of the Universe and the corresponding decrease in temperature. This applies also to relic abundance of decoupled species. On the other hand, the completion of the transition and the subsequent reheating lead to a significant entropy injection. Any pre-existing particle abundance is then diluted by the factor [370–372]

$$Y_i^{\rm SC} = Y_i \cdot \frac{T_{\rm nuc}^3 T_{\rm RH}}{T_{\rm inf}^4} \,. \tag{4.13}$$

Here, $T_{\rm RH}$ denotes the reheating temperature. By simple energy budget considerations, $T_{\rm RH}$ equals $T_{\rm inf}$ in the case of instantaneous reheating. On the other hand, it can be smaller if a period of matter domination occurs during the inflaton oscillations, before the thermal bath once again becomes the dominant component of the Universe. In general, $T_{\rm RH}$ should be determined by solving the coupled system: [373]

$$\dot\rho_{\rm rad} + 4H\rho_{\rm rad} = \gamma\,\rho_\phi, \quad \dot\rho_\phi + 3H\rho_\phi = -\gamma\,\rho_\phi, \quad H^2 = \frac{\rho_{\rm rad}+\rho_\phi}{3m_{\rm Pl}^2}, \tag{4.14}$$

where γ is the rate of energy transfer from the scalar into radiation. However, we can roughly estimate the reheating temperature as

$$T_{\rm RH} = T_{\rm inf}\,\min(1, \gamma/H_{\rm inf})^{1/2} \,. \tag{4.15}$$

Particles may be thermally regenerated in the radiation bath after reheating, provided that $T_{\rm RH} \gtrsim m_i$.[3] Consequently, the total abundance receives two contributions, schematically,

$$Y_i^{\rm tot} \simeq Y_i^{\rm SC} + Y_i^{\rm th}, \tag{4.16}$$

where $Y_i^{\rm th}$ is the sub-thermal contribution posterior to reheating, and $Y_i^{\rm SC}$ is the diluted particle abundance according to eq. (4.13). Depending on $T_{\rm RH}$, one of these contributions prevails above the other. In the following, we will focus on the case in which reheating is not very efficient, and the ratio $\gamma/H_{\rm inf} < 1$.

[3]The reheating temperature $T_{\rm RH}$ should be compared to the characteristic temperature at which particles normally decouple in a radiation-dominated universe. In the DM case, for example, it would be the freeze-out temperature $T_{\rm f.o.}$ or the freeze-in temperature $T_{\rm f.i.}$, depending on the specific model dynamics.

We conclude with a few remarks about the gravitational wave spectrum produced during supercooled FOPT. First, in supercooled FOPT, the collision of bubbles represent the main source of GWs, since the sorrounding plasma is highly diluted. Then, it is known that this class of PTs can produce some especially strong gravitational wave signals, due to the large values of the strength parameter $\alpha = \Delta V/\rho_{\rm rad}|_{T=T_{\rm nuc}}$ appearing in eq. (4.6). Moreover, as we briefly discussed, supercooled transitions can be followed by a period of matter domination occurring after the transition has completed and the gravitational wave spectrum has been generated. This feature imprints a distinctive tilt on the infrared tail of the spectrum, offering a potentially unique observational signature [374, 375]. Therefore, the observable GWs spectrum would also encode information about the ratio $\gamma/H_{\rm inf}$. Given the increase of interest in such strong phase transitions, it is interesting to study in detail the implications for the phenomenology of the Dark Matter.

4.3 DM relic in a supercooled universe

In general, supercooling epochs can potentially span significant portions of the Universe's thermal history, up to $\mathcal{O}(10)$ e-folds, without requiring much tuning [324]. Therefore, the dilution factor of eq. (4.13) can significantly suppress the thermal relic abundance of dark matter. As a result, the viable parameter space for mass and coupling values, such as those considered in the usual WIMP scenarios, can be drastically modified. It is therefore natural to ask, on general grounds, what impact such a non-standard cosmological epoch could have on dark matter, whether it be a minimal candidate or a light particle within a more complex dark sector. One should consider the possibility that the dynamical production of the DM relic occurs during any of the stages illustrated in fig. 4.3, and carefully account for the role of the reheating dynamics and entropy injection.

The phenomenological consequences of these non-standard scenarios on the DM thermal relic have already been investigated in a number of previous works. In particular, two scenarios that have been explored are *Inflatable Dark Matter* (e.g. [345, 370, 371]), where freeze-out occurs before supercooling and the relic is subsequently diluted by entropy injection as in eq. (4.13), and *Supercool Dark Matter* (e.g. [343, 345, 372]), where initially massless particles acquire a mass through the phase transition, forming either elementary or composite states that can be heavier or lighter than the reheating temperature. However, as we show in the following sections, there remain scenarios that have not been considered in previous literature, and for which a detailed analysis of the entropy budget and decoupling dynamics reveals new regions of parameter space. In detail, we discuss the possibility of DM relic production during the period of vacuum domination, region II in fig. 4.3, where the standard picture of particle decoupling as explained in section 1.3 is modified. During this phase, the Hubble rate no longer scales as T^2, but instead remains approximately constant, $H \simeq H_{\rm inf}$, as defined in eq. (4.8). As a result, for a given temperature dependence of $\Gamma_{\rm int}$, the decoupling condition $\Gamma_{\rm int} \approx H$ can be satisfied at a different temperature compared to the standard radiation-dominated case. This shift in the decoupling point alters the freeze-out dynamics and ultimately impacts the resulting relic abundance.

While the possibility of producing dark matter through the non-equilibrium dynamics of the first-order phase transition is certainly appealing[4], we focus here on scenarios in which

[4]In a first-order phase transition with runaway bubbles, the possibility exists to abundantly produce heavy

the dark sector is independent of the new physics responsible for the transition. Although this possibility may offer a less minimal solution, it is still interesting to explore the phenomenology of a dark sector under general assumptions. Moreover, ref. [372] pointed out that achieving the correct relic abundance of dark matter composite particles arising from a supercooled confining transition requires a prolonged period of supercooling, up to $\Delta N \approx 13$, which appears to be unlikely in light of recent studies on strongly coupled dynamics [353, 354].

We now present a quantitative analysis of how supercooling affects the freeze-out dynamics of Dark Matter. We also comment on the implications of these effects for secluded dark sectors. While these considerations apply with generality to any supercooling scenario, we illustrate throughout the discussion our results with applications to specific motivated models.

4.3.1 Freeze-out

In a standard radiation-dominated universe the Boltzmann equation can be written in the well-known compact form (see review in section 1.3):

$$\frac{dY}{dx} = \frac{\lambda}{x^2}\left(Y^2 - Y_{\rm eq}^2\right), \quad \text{where} \quad \lambda = m_{\rm Pl} m_{\rm DM} \langle \sigma_{\rm ann} v_{\rm rel} \rangle \sqrt{\frac{8\pi^2 g_{\star s}}{45}}, \tag{4.17}$$

where $m_{\rm Pl}$ denotes the reduced Planck mass and assuming $g_\star = g_{\star s}$. The $1/x^2$ dependence on the right-hand side reflects the fact that the Hubble rate decreases quadratically with temperature, i.e., $H \sim T^2$. However, if the cosmological history of the universe includes a period of supercooling, the form of the Boltzmann equation is modified. In particular, if freeze-out occurs during the phase of inflation the resulting dynamics differ substantially. As the Hubble parameter becomes constant from the time when the radiation and vacuum energy densities are equal, the Boltzmann equation takes the form:

$$\frac{dY}{dx} = \frac{\mu}{x^4}(Y^2 - Y_{\rm eq}^2), \quad \text{where} \quad \mu = \frac{2\pi^2}{45} g_{\star s} \frac{m_{\rm DM}^3 \langle \sigma_{\rm ann} v_{\rm rel} \rangle}{H_{\rm inf}}, \tag{4.18}$$

with the parametric difference coming from the different Jacobian factor in dt/dx. To see how this compare to the standard Boltzmann eq., it is useful to consider the ratio:

$$\frac{\lambda}{\mu} = \sqrt{\frac{90}{\pi^2 g_{\star s}}} \frac{m_{\rm Pl} H_{\rm inf}}{m_{\rm DM}^2} = \frac{T_{\rm inf}^2}{m_{\rm DM}^2} = x^{-2} \frac{T_{\rm inf}^2}{T^2} \simeq x^{-2} e^{2H_{\rm inf}\Delta t}, \tag{4.19}$$

where Δt denotes the time elapsed since the onset of inflation. Thus, to a first approximation, the two equations are similar, but the effective thermally averaged annihilation cross section during supercooling is exponentially decreasing in time, relative to that in a radiation-dominated universe:

$$\langle \sigma_{\rm ann} v_{\rm rel} \rangle_{\rm inf} \sim \langle \sigma_{\rm ann} v_{\rm rel} \rangle \, e^{-2H_{\rm inf}\Delta t}. \tag{4.20}$$

We can then expect that particles decouple earlier in an inflating universe compared to standard cosmology.

dark matter particles during the bubble collisions [350, 376–381] or due to interactions between the bubble wall and the plasma [382–385]. In addition, particle may be produced during the tachyonic or preheating stages of the oscillating scalar field [328, 386, 387].

When freeze-out occurs in the non-relativistic regime and in standard radiation dominated universe, the time at which the particle decouples from the bath scales approximately as $x_{\rm f.o.}^{\rm rad} \simeq \log(\lambda)$. Therefore, approximating $\mu/x^2 \to \mu/x_{\rm f.o.}^{\rm SC\,2}$ in the supercooled case, the shift in freeze-out between the two scenarios can be crudely estimated as:

$$\Delta x_{\rm f.o.} \propto \log\left(\frac{\lambda}{\mu/x_{\rm f.o.}^{\rm SC\,2}}\right) = 2H\Delta t_{\rm f.o.}^{\rm SC} = 2\Delta N_{\rm f.o.}^{\rm SC}\,, \tag{4.21}$$

where $\Delta N_{\rm f.o.}^{\rm SC}$ is the number of e-folds until the freeze out. This shift could be significant

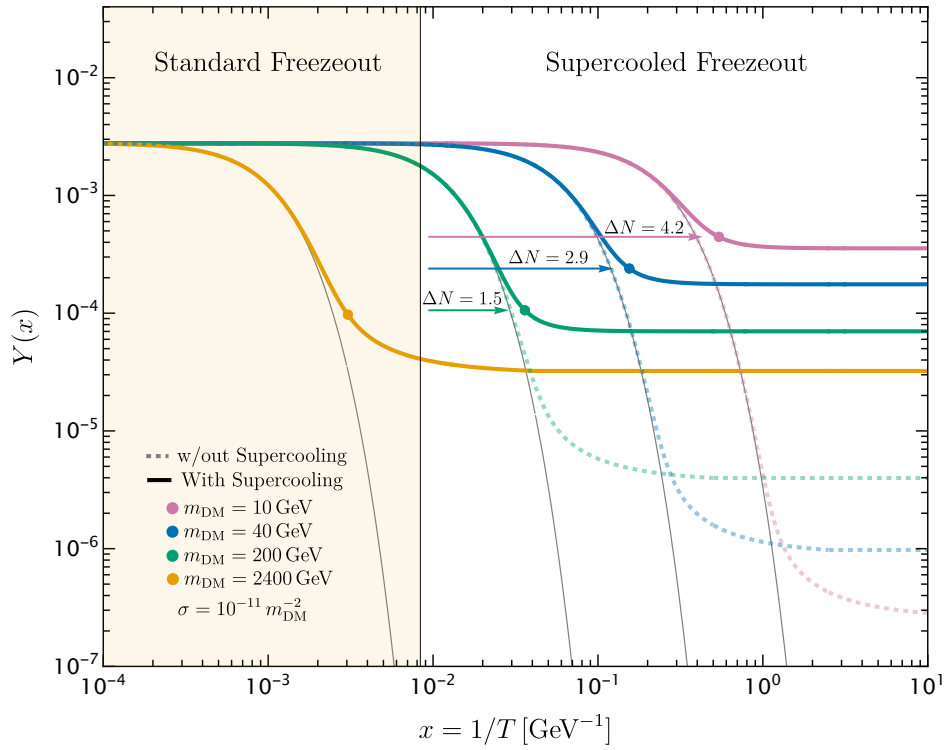


Figure 4.4: DM freeze-out for several masses. The plotted yield Y is evaluated before the end of supercooling and the consequent entropy injection, that dilutes Y by a factor $(T_{\rm nuc}/T_{\rm inf})^3$. The solid lines are the full solution to the Boltzmann equation while the circular dots indicate the moment where $\Delta Y(x)/Y_{\rm EQ}(x) = 2$, that we identify as freeze-out condition. For comparison, we show as dashed lines the solution that one would get for same mass and cross section in a standard radiation dominated universe. The vertical line describes the onset of supercooling while ΔN is the number of efolds elapsed since that moment. In these plots $T_{\rm inf} = 120\,{\rm GeV}$ and $\sigma = 10^{-11} m_{\rm DM}^{-2}$.

enough to yield a noticeable difference in the final relic abundance due to the exponential dependence of the Botlzmann distibution $n \simeq x^{3/2}\exp(-x)$. To have a rough estimate of this effect, we can use the cold relic approximation of eq. (1.100). We note that when freeze-out occurs in the non-relativistic regime, the final relic yield is approximately proportional to $x_{\rm f.o.}$ and inversely proportional to the annihilation cross section. Therefore, using the previous approximations, we can derive an estimate for the ratio between the relic abundances in the

supercooled scenario and the standard radiation-dominated case

$$\frac{Y_\infty^{\rm SC}}{Y_\infty^{\rm rad}} \approx \frac{x_{\rm f.o.}^{\rm SC}}{x_{\rm f.o.}^{\rm rad}} \cdot e^{2\Delta N_{\rm f.o.}^{\rm SC}} \approx \left(1 + \frac{2\Delta N_{\rm f.o.}^{\rm SC}}{x_{\rm f.o.}^{\rm SC}}\right)^{-1} e^{2\Delta N_{\rm f.o.}^{\rm SC}} \,. \tag{4.22}$$

As an illustrative example, some numerical solutions to the Boltzmann equations are presented in fig. 4.4, where we fix $T_{\rm inf} \simeq 120\,{\rm GeV}$ and analyze the freeze-out dynamics for a range of particle masses $m_{\rm DM} = \mathcal{O}(10)\,{\rm GeV}$–$\mathcal{O}(1)\,{\rm TeV}$. We assume a parametric dependence of the dominant s-wave annihilation cross section given by $\sigma \simeq 10^{-11} m_{\rm DM}^{-2}$ and fix the number of degrees of freedom to $g_\star = g_{\star s} = 150$. While these specific values correspond to particular models discussed in the following, we emphasize that the qualitative effects described here may be relevant across a broader class of scenarios involving higher temperature and mass scales.

The results in fig. 4.4 confirm the expectation that the final yield of a species experiencing a period of supercooling lasting ΔN efolds is exponentially enhanced by a factor proportional to $e^{2\Delta N}$ with respect to the standard freeze-out scenario. Indeed, eq. (4.22) provides reasonably good predictions: $Y_\infty^{\rm SC}/Y_\infty^{\rm rad} \simeq 1646, 176, 13$ respectively for the purple, blue, and green lines. Therefore, the particle mass required to achieve the correct relic abundance differs exponentially from the value expected in a radiation-dominated universe. Remarkably, smaller masses, despite corresponding to larger annihilation cross sections, lead to a larger relic abundance. This can be understood by inspecting eq. (4.20), as smaller masses imply a later freeze-out and a larger exponential suppression of the effective cross-section of the Boltzmann equation. This behavior is in stark contrast to the standard scenario in radiation domination, where a larger cross section would result in smaller relic abundances.

We briefly comment that a similar exponential effect also influences freeze-in scenarios, where the yield Y typically grows monotonically as $dY/dT \sim -1/T^2$ until it freezes-in [388]. In standard cosmology, it reaches a plateau for $T = \max(m_{\rm DM}, m_{\rm SM})$ where $m_{\rm SM}$ denotes SM species that may produce dark matter particles. However, if the DM mass falls within the supercooling region, the yield Y doesn't grow anymore as $1/T$, due to the constant Hubble rate. Instead, it reaches the freeze-in value at approximately $T_{\rm inf}$. The ratio of the final yield in the supercooled case to that in the standard radiation-dominated case is given by $Y_{\rm f.i.}^{\rm SC}/Y_{\rm f.i.}^{\rm rad} \approx T_{\rm f.i.}^{\rm rad}/T_{\rm inf} = \exp(-\Delta N_{\rm f.i.}^{\rm SC})$, where $T_{\rm f.i.}^{\rm rad}$ refers to the freeze-in temperature in the standard case. Remarkably, supercooling affects freeze-in in the opposite way compared to freeze-out, leading to a suppression rather than an enhancement of the final relic abundance. A detailed analysis of this case is left for future work.

Application: supercooling from strongly-coupled dynamics

We now analyze an explicit realization of these effects by considering the supercooled scenarios discussed in Refs. [345–347], within the framework of strongly coupled gauge extensions of the Standard Model motivated, for instance, by the idea of compositeness. In particular, we focus on nearly conformal theories characterized by a small, marginally relevant deformation

$$\Delta\mathcal{L} = g\,\mathcal{O}_g \,, \tag{4.23}$$

where the operator $\mathcal{O}_g$ has scaling dimension ${\rm Dim}[\mathcal{O}_g] = 4-\epsilon$, with $\epsilon \ll 1$. The impact of this deformation on the conformal dynamics is negligible in the deep ultraviolet UV. However,

as the coupling g evolves toward the infrared IR under the renormalization group flow, it eventually reaches a critical value g_c, at which point conformal symmetry is broken, and a mass gap Λ_c is generated. The theory then undergoes a transition to a confined phase.

It has been discussed, through studies of these classes of theories and their five-dimensional duals based on the AdS/CFT correspondence, that the transition from the deconfined to the confined phase can be a FOPT accompanied by a period of supercooling [345–354]. Whether, and under what conditions, such a period of supercooling can occur remains the subject of increasingly refined investigations [354, 389].

These scenarios can be qualitatively summarised as follows. Although the confined phase becomes energetically favorable below a certain critical temperature, the tunneling rate between the two phases can be highly suppressed, causing the theory to remain trapped in the deconfined phase. As the universe continues to cool, and undergoes supercooling, the temperature eventually drops to the QCD scale, where QCD itself confines and begins to influence the dynamics of the conformal sector. This interplay is expected on general grounds, as realistic models of compositeness typically feature couplings between Standard Model quarks and operators of the TeV-scale strong sector, interactions necessary for generating fermion masses after electroweak symmetry breaking. Therefore, QCD modifies the vacuum structure and triggers the completion of the phase transition.

We refer the reader to refs. [345, 346, 390] for detailed discussions on the treatment of these theories and the characterization of their phases. For practical purposes, we assume that the critical temperature marking the onset of the inflation epoch is approximately $T_{\rm inf} \sim \mathcal{O}(100)\,\text{GeV}$, while bubble nucleation is triggered at temperatures around $T_{\rm nuc} \sim \Lambda^{\rm dec}_{\rm QCD} \approx \mathcal{O}(1)\,\Lambda_{\rm QCD}$. Here, $\Lambda^{\rm dec}_{\rm QCD}$ denotes the QCD scale in the deconfined phase, which generally differs from its value in the Standard Model vacuum, $\Lambda_{\rm QCD}$, since the conformal sector, containing states charged under QCD, can modify the running of the strong coupling g_s.

We emphasize that supercooling periods spanning from the TeV scale down to the QCD scale can also arise in weakly coupled extensions of the Standard Model, see e.g. ref.s [328, 343, 391, 392].

Let us now assume that the Standard Model is extended by new degrees of freedom that give rise to a supercooled phase transition, as in the scenarios discussed above. In addition to this new dynamics, we consider the presence of a dark sector that remains in thermal equilibrium with the visible sector throughout the evolution of the universe, but whose impact on the spontaneous breaking of conformal invariance is negligible. We explore the possibility that some dark matter particles either decouple before the onset of supercooling or freeze out during the epoch of inflation. In the latter case, the effects illustrated in fig. 4.4 become relevant.

We show in fig. 4.5 the region of parameter space in the $m_{\rm DM}$–$(T_{\rm nuc}/T_{\rm inf})$ plane that is compatible with the observed dark matter relic abundance, for different values of the annihilation cross section. For concreteness, we fix $T_{\rm RH} = 0.05\,T_{\rm inf}$, which is indicated by the shaded orange region in the plot. We also assume a parametric dependence of the dominant s-wave annihilation cross section of the form $\sigma \sim m_{\rm DM}^{-2}$, as would arise, for example, in scenarios where dark matter annihilates via an s-channel exchange of a massive dark vector.

For heavy DM candidates, *i.e.* in the cold relic regime shown in fig. 4.5, freeze-out occurs prior to the onset of supercooling. In this case, the final relic abundance can be estimated

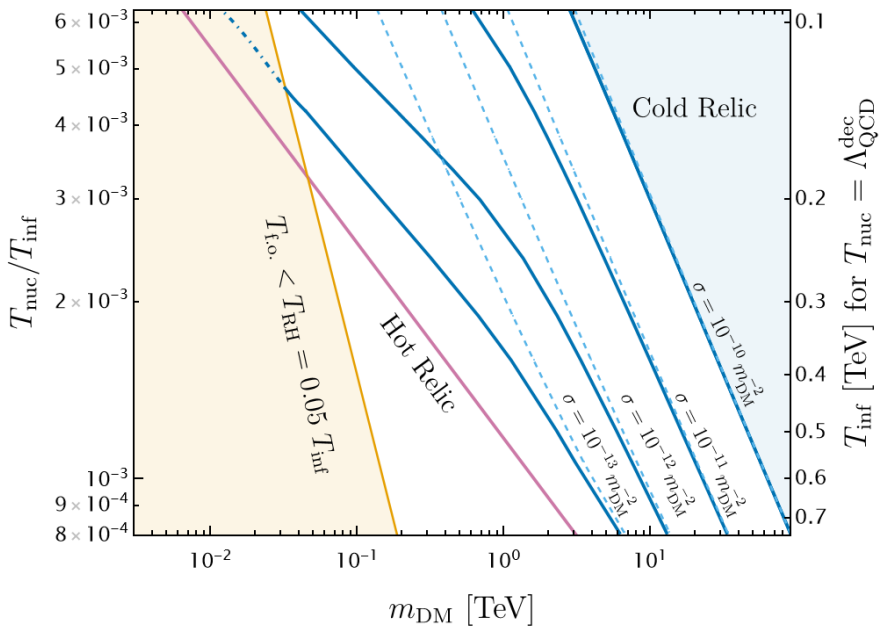


Figure 4.5: The dashed lines mark where the DM achieves the relic abundance if we only accounted for the dilution factor in eq. (4.13). The solid lines are the result of our numerical evaluation, accounting for the modification of the freeze-out dynamics during the supercooled phase. The cross-sections for this plot range from $10^{-13} m_{\rm DM}^{-2}$ to $10^{-10} m_{\rm DM}^{-2}$. The purple line shows the analytic approximation for the freeze-out of a hot relic before the supercooling. In this plot, $g_\star = g_{\star s} = 150$.

by

$$\Omega_{\rm DM}^{\rm cold} h^2 \simeq 1.07 \cdot 10^9 \frac{(n+1) x_{\rm f.o.}^{n+1}\, {\rm GeV}^{-1}}{(g_{\star s}/g_*^{1/2}) M_{\rm Pl}\, \sigma} \cdot \left(\frac{T_{\rm nuc}}{T_{\rm inf}}\right)^3 \cdot \left(\frac{T_{\rm RH}}{T_{\rm inf}}\right) . \tag{4.24}$$

Freeze-out may also occur before the supercooling phase in the case of a very small annihilation cross section, resulting in a hot relic, that we represent as a purple curve in fig. 4.5. This scenario is described by

$$\Omega_{\rm DM}^{\rm hot} h^2 \simeq 0.075 \cdot \left(\frac{m}{\rm eV}\right) \cdot \left(\frac{g_{\rm DM}}{g_{\star s}(x_f)}\right) \cdot \left(\frac{T_{\rm nuc}}{T_{\rm inf}}\right)^3 \cdot \left(\frac{T_{\rm RH}}{T_{\rm inf}}\right) , \tag{4.25}$$

where $g_{\rm DM}$ is the number of internal degrees of freedom of the DM particle. Besides these two limiting cases, we observe that for DM candidates with masses below $m_{\rm DM} \sim \mathcal{O}(1)$ TeV, and thus freeze-out temperatures $T_{\rm f.o.}$ expected within the supercooling window, a detailed numerical solution of the Boltzmann equation is required. The numerical results (solid lines) can indeed differ by an order of magnitude or more compared to including just the dilution factor (dashed lines), shifting the viable mass range. In general, smaller masses lead to freeze-out occurring earlier compared to standard cosmology (see also fig. 4.4), and so closer to the relativistic regime where the Boltzmann equilibrium distribution $Y(x)$ flattens at small x. As a result, the leftmost blue curves in fig. 4.5 resemble the behavior typical of hot dark matter. We may then conclude that supercooled dark matter, when decoupling during the

supercooling phase, displays a freeze-out closer to a warmer relic, compared to the standard freeze-out.

As discussed above, if the reheating temperature is large enough such that $T_{\rm RH} > T_{\rm f.o.}$, dark matter particles can be thermally regenerated and potentially reach equilibrium again. This limit is stressed by the dot-dashed curves in fig. 4.5. In such scenarios, reheating effectively erases any memory of the supercooling phase, and freeze-out proceeds through the standard dynamics of a radiation-dominated universe. Therefore, the characteristic enhancement of the DM relic abundance due to supercooling is only relevant within the temperature window $T_{\rm inf} - T_{\rm RH}$. The size of this window depends on the model-dependent reheating dynamics. However, in section 4.3.3 we will discuss a general situation in which reheating does not terminate the temperature range in which these supercooling-induced effects are relevant.

4.3.2 Implications on Direct Searches

Here we discuss the consequences of a supercooling epoch on the target parameter space for direct detection experiments. In addition to the well-known dilution of the DM relic abundance due to entropy injection, we stress, following the message of the previous section, that a detailed numerical solution of the Boltzmann equation is essential for accurate predictions.

We consider again a supercooled transition driven by strongly coupled dynamics and focus on a minimal dark sector model consisting of a massive Z' vector boson that couples to both DM fermions and Standard Model quarks[5]:

$$\mathcal{L}_{\text{fermion},Z'} \supset \sum_i Z'_\mu \bar{q}_i \gamma^\mu \left(g_q^V - g_q^A \gamma_5 \right) q_i \,. \tag{4.26}$$

where q_i denotes here all of the SM quarks. Assuming that the vector boson is heavier than the fermionic DM candidate χ ($M_{Z'} > 2m_{\rm DM}$), the annihilation cross section in the case of vector couplings reads [393][6]:

$$(\sigma v)(\chi\bar{\chi} \to Z' \to q\bar{q}) \approx \frac{3 m_{\rm DM}^2 N_c}{\pi \left[\left(M_{Z'}^2 - 4m_{\rm DM}^2 \right)^2 + \Gamma_{Z'}^2 M_{Z'}^2 \right]} \cdot \left(g_\chi^V \right)^2 \left(g_q^V \right)^2 \,. \tag{4.27}$$

This cross section enters the Boltzmann equation and governs the decoupling of DM particles in the early universe. If the vector mediator has a mass significantly larger than the DM particle, e.g. $M_{Z'} \simeq \mathcal{O}(100)\, m_{\rm DM}$, the annihilation cross section exhibits a parametric dependence $\sigma \propto m_{\rm DM}^{-2}$, with overall coefficients of the same order as those shown in fig. 4.5.

Once the couplings to fermions are fixed, the dark matter mass $m_{\rm DM}$ can be determined by requiring that the correct relic abundance is reproduced. One can then compute the spin-independent DM–nucleon cross section relevant for direct detection experiments:

$$\sigma_{\chi-N}^{\rm SI} = 1.13 \times 10^{-43}\ {\rm cm}^2 \cdot (g_\chi^V g_q^V)^2 \left(\frac{\mu_{\chi-N}}{1\,{\rm GeV}} \right)^2 \left(\frac{10\,{\rm TeV}}{M_{Z'}} \right)^4 , \tag{4.28}$$

[5] In partial compositeness scenarios, SM fermions are a mixture of composite and elementary states, such that both components need to carry a non-zero charge under the dark $U(1)_D$, similarly to the color charge in QCD. However, we implicitly assume that the Z' plays a negligible role in the phase transition occurring in the visible sector, contrary to the case of QCD-induced effects.

[6] Since our goal is to highlight a generic sizable effect rather than provide precise model-dependent predictions, we do not include possible contributions by BSM fermions here, and simply caution the reader about this limitation.

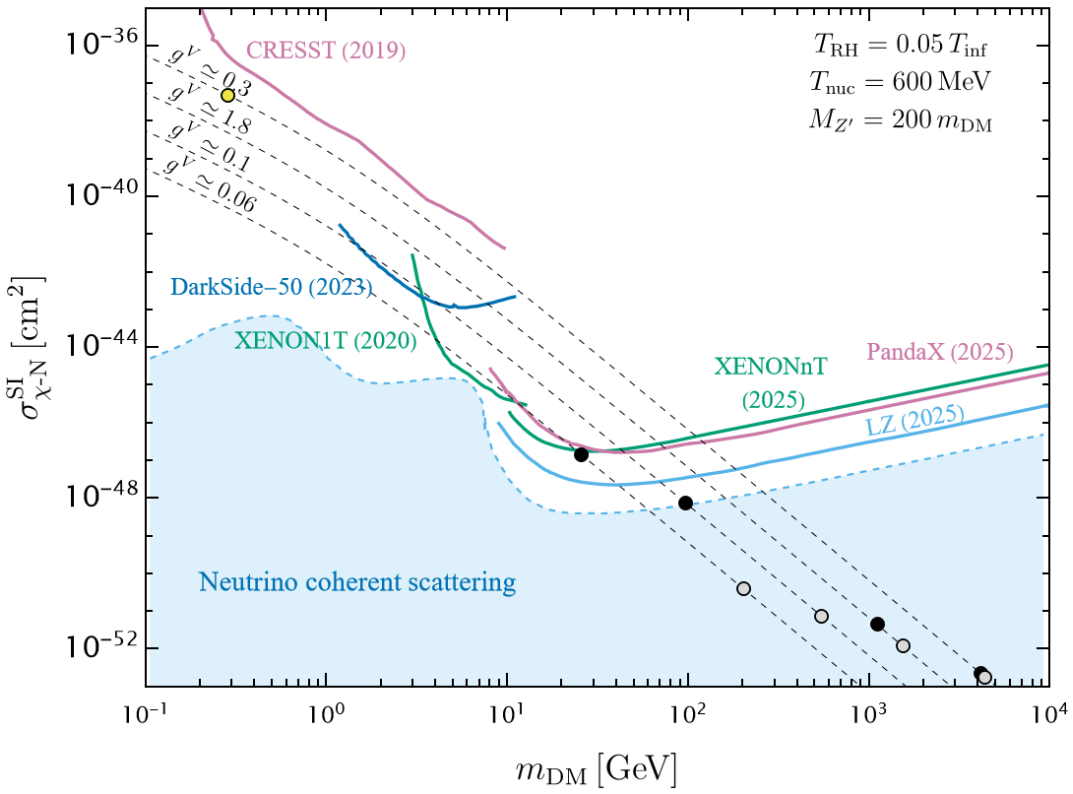


Figure 4.6: Constraints from direct detection experiments on the spin-independent dark matter–nucleon cross section as a function of the dark matter mass. The gray and black markers indicate the points that yield the correct relic abundance for fixed $T_{\rm nuc}/T_{\rm inf} = 5{\cdot}10^{-3}$, considering, respectively, just the naive dilution factor or solving the full numerical freeze-out during supercooling. The yellow marker indicates the dark matter mass required in the absence of supercooling for this model. Neutrino "fog" defined according to [394].

where $\mu_{\chi-N}$ is the reduced mass of the DM–nucleon system. Results for several choices of the coupling $g^V_\chi = g^V_q \equiv g^V$ are shown in fig. 4.6. The gray and black points correspond to the values of $m_{\rm DM}$ required to match the observed relic abundance when considering, respectively, the naive dilution factor and the full numerical solution of freeze-out during supercooling.

In the case of a standard radiation-dominated cosmology, the same model yields dark matter masses around $m_{\rm DM} \leq 0.1\,{\rm GeV}$, as the yellow dot in Fig. 4.6. For sub-GeV dark matter, constraints from direct detection via electron scattering become relevant. However, we do not discuss these bounds, nor collider limits in that region, as our focus lies outside the standard cosmological scenario.

The effect discussed in section 4.3.1 becomes even more significant in the context of direct detection. Since the spin-independent nuclear scattering cross section scales as $M_V^{-4} \propto m_{\rm DM}^{-4}$, a mismatch of just one order of magnitude in the predicted dark matter mass can translate into a four-order-of-magnitude deviation in the expected nuclear cross section. Parametrically, the correction to the cross section is enhanced by a factor roughly proportional to $e^{8\Delta N}$.

If one estimates the relic abundance using only the naive entropy dilution factor, the

resulting DM mass tends to be relatively large, which in turn yields extremely suppressed nuclear cross sections. These predictions often fall deep into the so-called neutrino fog, where coherent neutrino scattering obscures dark matter signals. In contrast, when the freeze-out process is treated accurately by solving the Boltzmann equation within the proper supercooled cosmological background, the predicted dark matter mass can be significantly lower. This leads to enhanced cross sections that can lie within the reach of current or near-future direct detection experiments. This underscores the importance of a precise treatment of freeze-out in cosmologies featuring non-standard thermal histories [395].

4.3.3 Freeze-out in secluded Dark Sector

If reheating is nearly instantaneous and the reheating temperature $T_{\rm RH}$ is high enough to repopulate the thermal bath with dark sector particles, then the effects illustrated in fig. 4.4 become irrelevant. In this case, the relic abundance generated during the supercooling window is strongly diluted and overshadowed by the subsequent thermal production. Dark matter particles would re-enter thermal equilibrium and evolve as in the standard radiation-dominated scenario, eventually decoupling at later times and effectively erasing any memory of the preceding supercooling phase.

However, there exist scenarios in which the portal between the dark and visible sectors is sufficiently weak that thermal production after reheating is negligible or entirely absent. In such cases, the dark sector does not efficiently rethermalize after the transition, and the relic abundance generated during supercooling can remain relevant. This opens the possibility for the dynamics illustrated in fig. 4.4 to have a sizable impact, even in the absence of a matter-dominated epoch and despite the consequent high reheating temperature.

Consider a hidden dark sector that is internally thermalized at a temperature T_D, related to the visible sector temperature by the parameter $\xi \equiv T/T_D$. The dark sector may interact with the Standard Model through a feeble portal interaction, but we assume it is insufficient to establish thermal equilibrium between the two sectors, so that ξ remains approximately constant. If this dark sector features a non-trivial spectrum with interacting species, some of them may decouple from equilibrium and serve as viable dark matter candidates. In such a setup, one typically obtains a standard freeze-out scenario within the hidden sector, where dark matter abundance is determined by the annihilations among dark species. However, the Hubble expansion rate that governs this freeze-out receives contributions from both the visible and hidden energy densities—and, in the case of a supercooled phase transition, also from the vacuum energy component. This makes the dynamics sensitive to the thermal history of the visible sector, even if the dark sector is otherwise secluded. Explicitely, the Hubble rate would read,

$$H(T,T_D)^2 = \frac{\frac{\pi^2}{30}(g_{*D}T_D^4 + g_* T^4) + \Delta V}{3\,m_{\rm Pl}^2} = \frac{\frac{\pi^2}{30}(g_{*D} + \xi^4 g_*)T_D^4 + \Delta V}{3\,m_{\rm Pl}^2}\,. \tag{4.29}$$

In a standard radiation-dominated universe, solving the Boltzmann equation within the hidden sector shows that, if $g_*^D \ll g_*\,\xi^4$, the final relic density can be estimated using the standard cold relic approximation with the rescaling $\Omega_{\rm DM}h^2 \to \xi^{-1}\Omega_{\rm DM}h^2$ [396]. If the thermal history also includes an epoch of supercooling, two main effects arise:

- The supercooling phase during which the Hubble rate remains constant, from $T_{\rm inf}$ to

$T_{\rm nuc}$ in the SM bath, spans in the dark sector a range of temperature from $T_{\rm inf}/\xi$ to $T_{\rm nuc}/\xi$, thereby shifting the relevant supercooling scales for dark sector dynamics.

- The characteristic features of freeze-out during supercooling, as illustrated in fig. 4.4, are no longer confined to the temperature window $T_{\rm inf}$–$T_{\rm RH}$, but extend down to $T_{\rm nuc}$, since reheating does not affect the hidden sector.

For concreteness, we mention a well-studied model of dark matter where this mechanism may be relevant. Consider a secluded dark sector consisting of a minimal dark Abelian $U(1)_D$ gauge symmetry with a single Dirac fermion. This dark sector can interact with the Standard Model via a kinetic mixing portal:

$$\mathcal{L} \supset -\frac{\varepsilon}{2} B^{\mu\nu} F'_{\mu\nu} \,, \tag{4.30}$$

where $B^{\mu\nu}$ is the SM hypercharge field strength tensor and $F'_{\mu\nu}$ is the field strength of the dark photon. The key parameters of the model are the dark gauge coupling $\alpha' = e'^2/4\pi$ and the mass of the dark fermion $m_{e'}$. As usual, one can rotate to a basis where the kinetic terms are canonically normalized. Following [396], the relevant Lagrangian terms involving the SM photon γ, the SM Z boson, and the dark photon γ' read:

$$\begin{aligned} \mathcal{L} \supset & - e J^{\mu}_{\rm EM} \gamma_{\mu} + e' \frac{\varepsilon \cos\theta_{\varepsilon}}{\sqrt{1-\varepsilon^2}} J^{\mu}_{\rm DM} \gamma_{\mu} - e' J^{\mu}_{\rm DM} \gamma'_{\mu} - \\ & - e' \frac{\varepsilon \sin\theta_{\varepsilon}}{\sqrt{1-\varepsilon^2}} J^{\mu}_{\rm DM} Z_{\mu} - g \frac{\cos\theta_W}{\cos\theta_{\varepsilon}} J^{\mu}_{Z} Z_{\mu} \,, \end{aligned} \tag{4.31}$$

where θ_{ε} is defined by $\tan\theta_{\epsilon} = \tan\theta_W/\sqrt{1-\epsilon^2}$, while $\hat{\epsilon}$ is proportional to the original kinetic mixing parameter ϵ, rescaled by mixing angles arising from the diagonalization, namely $\hat{\epsilon} = \epsilon\cos\theta_W/\sqrt{1-\epsilon^2}$. With this choice, dark fermions are coupled to ordinary photon and Z bosons.

If the dark sector possesses a non-negligible energy density and evolves in thermal equilibrium along with the temperature T_D, freeze-out of the dark fermions could eventually occur through the annihilation channel $e'e' \to \gamma'\gamma'$, with a cross section proportional to $\alpha'^2/m^2_{\rm DM}$. After the completion of the supercooled transition in the visible sector, any subsequent thermal production of dark particles, even at temperatures $T_{\rm RH} > T_{\rm f.o.}$, will be strongly suppressed due to the smallness of the mixing parameter $\hat{\epsilon}$ and thus negligible. We emphasize that such a tiny value of the mixing parameter is smaller than in the pure freeze-in scenario.

4.4 Discussion

First-order phase transitions have attracted growing interest in recent years, particularly in light of the observed stochastic gravitational wave background at nanohertz frequencies [397–400] and the anticipated sensitivity of future gravitational wave observatories [401–405]. Within this exciting context, it is interesting to investigate the occurrence of FOPTs in well-motivated extensions of the Standard Model. Among the various potential connections, a particularly compelling one is the interplay between cosmological FOPTs and dark matter physics.

In this chapter we focused on the way a non-standard thermal history, induced by a supercooled FOPT in the visible sector, can impact the phenomenology of dark matter, even if the dark sector is not directly involved in the transition. We showed that when decoupling occurs during the period of inflation, a careful treatment of the freeze-out (or freeze-in) process is essential. Under certain conditions, the resulting relic abundance can differ exponentially from that obtained in the standard radiation-dominated scenario. This significantly alters the viable mass ranges for dark matter candidates and shifts the corresponding targets for direct detection experiments. We presented explicit examples, identified the key parameters controlling these effects, and discussed under what assumptions they become phenomenologically relevant. Our findings motivate further investigation into supercooled phase transitions, focusing on reheating dynamics and the imprints of the related period of matter domination on the gravitational wave spectrum, sensitive to the difference between $T_{\rm inf}$ and $T_{\rm RH}$.

A modified thermal history also has important implications for the baryon asymmetry of the universe. If baryogenesis occurs at energy scales above the onset of supercooling, $\Lambda_{\not B} > T_{\rm inf}$, the initial baryon asymmetry $\eta_B^{(0)}$ is then diluted by the injection of entropy down to the value η_B that we observe today:

$$\eta_B = \frac{n_B - n_{\bar{B}}}{s} = \eta_B^{(0)} \times \left(\frac{T_{\rm nuc}}{T_{\rm inf}}\right)^3 \left(\frac{T_{\rm RH}}{T_{\rm inf}}\right) = (8.7 \pm 0.1) \times 10^{-11} \,. \tag{4.32}$$

The required size of the primordial asymmetry $\eta_B^{(0)}$ thus depends on the amount of supercooling and the duration of the inflation phase. However, this explanation requires a rather large initial asymmetry, which poses a challenge. It could potentially arise from out-of-equilibrium decays with maximal CP violation, or from resonant decays of nearly degenerate particles. Alternatively, mechanisms like spontaneous baryogenesis or the Affleck-Dine scenario might generate a sufficient asymmetry without excessive fine-tuning. A detailed exploration of these possibilities is left for future work. It is also conceivable that the baryon asymmetry is generated after the supercooled transition. In this case, one avoids the need for large initial asymmetries and the risk of washout due to entropy injection. However, producing an asymmetry at low energies could also be challenging [406].

Exploring the interplay between FOPTs, dark sectors, and baryogenesis mechanisms may also offer a compelling framework to address the observed coincidence between dark matter and baryon abundances.

Conclusions and Outlook

The Standard Model of particle physics stands as one of the most successful achievements of quantum field theory and a cornerstone of our understanding of nature. Nevertheless, it is an incomplete theory and the path toward discovering new physics is not unique. There are multiple well-motivated avenues to explore, each worthy of careful theoretical and experimental investigation. In this thesis, we have explored several facets of one such direction: the study of new degrees of freedom that may exist above the electroweak scale and couple to the SM with $\mathcal{O}(1)$ couplings.

In chapter 2, motivated by the current experimental scenario and theoretical considerations, we investigated within the SMEFT framework the possibility of new physics predominantly coupled to the third generation of SM fermions. In particular, in section 2.1, we presented a comprehensive analysis of effective operators involving top quarks, providing a complementary approach with respect to direct constraints based on high-energy data [141, 143, 407, 408]. Then, in section 2.2 and section 2.3, we studied the implications of the latest measurements of $B \to K\bar{\nu}\nu$ and $K \to \pi\bar{\nu}\nu$, highlighting the consequences of these results for flavor physics, should they prove to be more than statistical fluctuations, and the relevance of future sensitivity improvements.

Regarding the SMEFT framework, there are numerous future directions. In spite of being a well-established framework, there is room for improvement, both in its formal QFT aspects and in practical strategies for performing SMEFT analyses, including the use of new algorithms [409] or machine learning techniques [410–415]. As we have discussed, the SMEFT framework, despite being a bottom-up approach, requires certain assumptions to remain predictive and to avoid the proliferation of operators and coefficients without a motivated underlying structure. In this sense, efforts in SMEFT should be complemented by model-building activities. Finally, it is interesting to explore the potential of future colliders, such as the FCC running at the Z pole (the so-called Tera-Z stage), in probing extensions of the Standard Model via precise measurements of flavor-changing processes and EWPO [245, 416, 417]. The SMEFT framework, as well as explicit models, are fundamental to understand which regions of parameter space will be probed by future facilities.

Concerning future colliders, in chapter 3 we discussed some theoretical challenges associated with the next-generation machines. We reviewed the possibility of describing initial state radiation phenomena using the PDFs formalism in the case of lepton colliders. In particular, we provided a phenomenological analysis based on Muon Collider processes, highlighting the role of a peculiar effect: the mixed Z/γ PDF. We presented NLO analytic approximations and emphasized the importance of including this effect for precise computations and predictions, essential both for testing the Standard Model and for exploring indirect signatures of new degrees of freedom, as well as for direct new physics discovery channels.

There are several future directions for these kinds of studies: higher-order computations [418, 419], a better characterization of both the collinear and soft emission regions [289], the inclusion of both ISR and FSR for complete fixed-order computations [254], and more. In general, the physics opportunities at muon colliders, as well as at the FCC, require careful attention and scrutiny. Even though the expected timeline for these colliders spans several decades, it is important to discuss now what the opportunities at these machines are, and to have a clear roadmap of investigations and studies so that, by the time new data become available, we are equipped with the theoretical tools needed to compare observations with accurate predictions and models.

In chapter 4, we scrutinized some aspects of cosmological phase transitions, namely the occurrence of periods of supercooling in the early universe and their connection to the dynamics and evolution of dark sectors. We discussed the consequences of a finite period of inflation on the way dark matter particles decouple, and its consequence on viable candidates and targets for detection experiments.

There are several future directions to be explored in this area. For example, in the context of supercooling, recent studies revisited the features of confining phase transitions in strongly coupled sectors [353, 354, 389], whose dynamics cannot be treated with perturbative methods. For this class of models, both the transition dynamics and the associated particle production mechanisms still require deeper investigation. More broadly, the production of gravitational wave signatures from first-order phase transitions is the subject of increasingly refined studies, both through numerical simulations and through improved analytic modeling of the relevant processes. Future experiments and sensitivity improvements will enhance our understanding of these phenomena, hopefully detecting new signals or constraining regions of parameter space. Regarding the discussion in chapter 4, the next decade will see new experiments focusing on gravitational waves along with advancements in dark matter direct detection experiments [420, 421]. In addition, future colliders will provide stronger bounds on dark matter interactions with the Standard Model, both through precision tests [422–424] and resonant production[425]. In this context, it is important to explore all well-motivated BSM scenarios and to improve our understanding of the various types of signatures that may be hiding at the high-energy frontier.

Overall, in this thesis we investigated the phenomenology of physics beyond the Standard Model by examining present hints, future opportunities, and signals from the early universe. This approach, drawing on inputs of various nature, is guided by a single goal: to hopefully lead to a major discovery in particle physics in the coming years.

Appendix A

In this appendix, we collect a number of definitions, discussions, calculations, and results that, for simplicity, were not included in the main text of chapter 2.

A.1 Observables

We present the low-energy EFT parametrization for most of the observables that were relevant to the analysis discussed in the main text of chapter 2. We note that the content of this appendix is not meant to be an exhaustive review; rather, we refer the reader to more comprehensive references throughout. Our focus is on the observables and effective operators relevant to the specific scenarios and assumptions considered in our analysis.

In each section, we define the infrared (IR) effective Hamiltonian relevant to a given process, explicitly introducing the contributing operators and their coefficients. We primarily follow the standard Weak Effective Theory (WET) basis and conventions. However, for the sake of clarity when comparing with existing literature, we occasionally adopt alternative conventions, such as the so-called Low-Energy EFT (LEFT) basis. The full list of operators and Wilson coefficients used in this latter basis is reported in appendix A.1.14.

Although we omit certain contributions that are not relevant for the purposes of this thesis, we emphasize that the low-energy effective descriptions are independent of the SMEFT assumptions at the UV scale and of any specific matching procedure or basis choice. Consequently, the formulae provided in this appendix are applicable to all three analyses discussed in sections 2.1 to 2.3. Nonetheless, we occasionally comment on the role of specific observables within a given SMEFT framework. So, for the sake of clarity, we briefly summarise below the main assumptions adopted in each case:

- In section 2.1, we work in the up-type quark mass basis and assume that only operators involving top quarks are generated at the UV scale. Lepton flavor indices are left generic, and lepton-flavor violating (LFV) effects are allowed. Our focus is on the impact of the operators listed in table 2.1 on low-energy observables. Relevant matchings and runnings are discussed in the main text.

- In section 2.2, we adopt the down-type quark basis and consider both lepton flavor universal (LFU) and τ-philic scenarios on the leptonic side. Relevant operators, matchings and runnings are mentioned in main text.

- In section 2.3, we continue using the down-type quark basis. Operators involving light quarks are assumed to be proportional to those involving the third generation, with the proportionality dictated by a $U(2)_q$-breaking spurion $\tilde{V}$. So, in this case, we use only

the coefficients of the operators involving third-generation fermions, omitting flavor indices, and describing the couplings to light families in terms of the parameters ε and κ. On the leptonic side we restrict to operators coupled to τ leptons. Overall, we only have the five parameters of table 2.15

A.1.1 $P \to M\nu_\alpha\nu_\beta$

Here we recollect the decay channels of mesons $P = \{B, K\}$ into $M = \{K, \pi, \rho\}$ and two neutrinos. The BSM contribution to these processes is described by the Hamiltonian:

$$\begin{aligned}
&\mathcal{H}_{eff}^{BSM} = -\frac{4G_F}{\sqrt{2}}\frac{\alpha}{4\pi}\sum_{i,j,\alpha,\beta} V_{ti}^* V_{tj}\left(C_L^{ij\alpha\beta}\mathcal{O}_L^{ij\alpha\beta} + C_R^{ij\alpha\beta}\mathcal{O}_R^{ij\alpha\beta}\right) , \\
&\mathcal{O}_L^{ij\alpha\beta} = (\bar{d}_L^i\gamma_\mu d_L^j)(\bar{\nu}^\alpha\gamma^\mu(1-\gamma_5)\nu^\beta) , \quad \mathcal{O}_R^{ij\alpha\beta} = (\bar{d}_R^i\gamma_\mu d_R^j)(\bar{\nu}^\alpha\gamma^\mu(1-\gamma_5)\nu^\beta) .
\end{aligned} \tag{A.33}$$

$B \to K^{(*)}\nu\bar{\nu}$

The short-distance EFT coefficients in the Standard Model are given by $C_L^{sb\alpha\beta} = C_{L,\mathrm{SM}}^{sb}\delta_{\alpha\beta}$ and $C_R^{sb\alpha\beta} = 0$, with $C_{L,\mathrm{SM}}^{sb} = -6.32(7)$. Theoretical predictions of these modes have been updated with latest lattice results in Ref. [48], providing $\mathcal{B}(B^+ \to K^+\nu\bar{\nu})_{\mathrm{SM}} = (4.44 \pm 0.30) \times 10^{-6}$, $\mathcal{B}(B^+ \to K^{*+}\nu\bar{\nu})_{\mathrm{SM}} = (9.8 \pm 1.4) \times 10^{-6}$, $\mathcal{B}(B^0 \to K_S\nu\bar{\nu})_{\mathrm{SM}} = (2.05 \pm 0.14) \times 10^{-6}$, where the tree-level contribution has been removed. It is common to define the ratios

$$R_{K^{(*)}}^{\nu} \equiv \frac{\mathcal{B}(B \to K^{(*)}\nu\bar{\nu})}{\mathcal{B}(B \to K^{(*)}\nu\bar{\nu})_{\mathrm{SM}}} = 1 + \Delta R_{K^{(*)}}^{\nu} , \tag{A.34}$$

where the deviation from the SM expectation induced by New Physics can be parametrized as

$$\begin{aligned}
\Delta R_{K^{(*)}}^{\nu} = &\sum_\alpha \frac{2\mathrm{Re}[C_{L,\mathrm{SM}}^{sb}(C_L^{sb\alpha\alpha} + C_R^{sb\alpha\alpha})]}{3|C_{L,\mathrm{SM}}^{sb}|^2} + \sum_{\alpha,\beta}\frac{|C_L^{sb\alpha\beta} + C_R^{sb\alpha\beta}|^2}{3|C_{L,\mathrm{SM}}^{sb}|^2} - \\
&- \eta_{K^{(*)}}\sum_{\alpha,\beta}\frac{\mathrm{Re}[C_R^{sb\alpha\beta}(C_{L,\mathrm{SM}}^{sb} + C_L^{sb\alpha\beta})]}{3|C_{L,\mathrm{SM}}^{sb}|^2} .
\end{aligned} \tag{A.35}$$

In the formula above $\eta_K = 0$ and $\eta_{K^*} = 3.33(7)$, so that the decay mode to the K meson only depends on the vector current, *i.e.* on the combination $C_V = C_L + C_R$.

Within the EFT framework discussed in section 2.3, the only relevant coefficient is $C_L^{sb\tau\tau}$. Its tree-level matching onto the SMEFT basis, expressed in terms of the $U(2)_q$-breaking spurion, is given by

$$C_L^{sb\tau\tau} = -\varepsilon\frac{\pi v^2}{\alpha}C_{lq}^- , \tag{A.36}$$

where all flavor indices in C_{lq}^- are implicitly understood to refer to third-generation fermions.

$K \to \pi\nu\bar{\nu}$

Decays of K_L and K_0 to pions and neutrinos have been discussed in Refs. [159, 167, 426]. The branching ratios read:

$$\begin{aligned}\mathcal{B}(K^+ \to \pi^+\nu\bar{\nu})_{th} = \mathcal{B}(K^+ \to \pi^+\nu_e\bar{\nu}_e)_{\rm SM} \sum_{\alpha,\beta=1,2} \left|\delta_{\alpha\beta} + \frac{C_V^{ds\alpha\beta}}{C_{L,\rm SM}^{ds11}}\right|^2 \\ + \mathcal{B}(K^+ \to \pi^+\nu_\tau\bar{\nu}_\tau)_{\rm SM} \left[\left|1 + \frac{C_V^{ds33}}{C_{L,\rm SM}^{ds33}}\right|^2 + \sum_{\alpha=1,2}\left(\left|\frac{C_V^{ds\alpha3}}{C_{L,\rm SM}^{ds33}}\right|^2 + \left|\frac{C_V^{ds3\alpha}}{C_{L,\rm SM}^{ds33}}\right|^2\right)\right],\end{aligned} \tag{A.37}$$

$$\begin{aligned}\mathcal{B}(K_L \to \pi^0\nu\bar{\nu})_{th} = \frac{1}{3}\mathcal{B}(K_L \to \pi^0\nu\bar{\nu})_{\rm SM}\left[\sum_{\alpha,\beta=1,2}\left(\delta_{\alpha\beta} + \frac{\mathrm{Im}[N_{ds}C_V^{ds\alpha\beta}]}{\mathrm{Im}[N_{ds}C_{L,\rm SM}^{ds11}]}\right)^2\right. \\ \left. + \left(1 + \frac{\mathrm{Im}[N_{ds}C_V^{ds33}]}{\mathrm{Im}[N_{ds}C_{L,\rm SM}^{ds33}]}\right) + \sum_{\alpha=1,2}\left(\left(\frac{\mathrm{Im}[N_{ds}C_V^{ds\alpha3}]}{\mathrm{Im}[N_{ds}C_{L,\rm SM}^{ds33}]}\right) + \left(\frac{\mathrm{Im}[N_{ds}C_V^{ds3\alpha}]}{\mathrm{Im}[N_{ds}C_{L,\rm SM}^{ds33}]}\right)\right)\right],\end{aligned} \tag{A.38}$$

where we defined $N_{ds} = (G_F\alpha V_{td}^* V_{ts}/\sqrt{2}\pi)$, $C_V = C_L + C_R$ and the SM values for the branching ratios and Wilson coefficients are

$$\begin{aligned}\mathcal{B}(K^+ \to \pi^+\nu_e\bar{\nu}_e)_{\rm SM} &= 3.06 \times 10^{-11}\,, \\ \mathcal{B}(K^+ \to \pi^+\nu_\tau\bar{\nu}_\tau)_{\rm SM} &= 2.52 \times 10^{-11}\,, \\ \mathcal{B}(K_L \to \pi^0\nu\bar{\nu})_{\rm SM} &= 3.4 \times 10^{-11}\,,\end{aligned} \tag{A.39}$$

$$C_{L,\rm SM}^{ds\alpha\beta} = -\frac{1}{s_W^2}\left(X_t + \frac{V_{cd}^* V_{cs}}{V_{td}^* V_{ts}} X_c^\alpha\right)\delta_{\alpha\beta}\,, \quad C_{R,\rm SM}^{ds\alpha\beta} = 0\,, \tag{A.40}$$

with $X_t = 1.481$, $X_c^e = X_c^\mu = 1.053 \times 10^{-3}$ and $X_c^\tau = 0.711 \times 10^{-3}$.

Within the EFT framework discussed in section 2.3, the only relevant coefficient is $C_L^{ds\,\tau\tau}$. Its tree-level matching onto the SMEFT basis, expressed in terms of the $U(2)_q$-breaking spurions, is given by

$$C_L^{ds\,\tau\tau} = \varepsilon^2\kappa\,\frac{\pi v^2}{\alpha}\,C_{lq}^-\,, \tag{A.41}$$

where all flavor indices in C_{lq}^- are implicitly understood to refer to third-generation.

$B \to \pi\nu\bar{\nu}, \rho\nu\bar{\nu}$

Differential and total branching ratios of $B \to \pi\nu\bar{\nu}$ and $B \to \rho\nu\bar{\nu}$ are studied, e.g., in Ref. [221]. The general formula for this processes is:

$$\mathcal{B}(B \to F_d\nu\bar{\nu}) = A_+^{BF_d} x_{bd}^+ + A_-^{BF_d} x_{bd}^-\,, \tag{A.42}$$

with

$$x_{bd}^\pm = \sum_{\alpha,\beta}\left|2V_{td}^* V_{tb}\left(C_{L,\rm SM}^{db}\delta_{\alpha\beta} + C_L^{db\alpha\beta} \pm C_R^{db\alpha\beta}\right)\right|^2\,, \tag{A.43}$$

and where we have defined the coefficients in such a way that $C_{L,\rm SM}^{db} = -6.32$. The coefficients A_-^{BP} are zero for pseudoscalar mesons while, in general, $A_-^{BV} \gg A_+^{BV}$ for vectors. They are given in table A.1.

$B \to F_d$	$A_+^{BF}\,[10^{-8}]$	$A_-^{BF}\,[10^{-8}]$
$B^+ \to \pi^+$	332 ± 34	0
$B^0 \to \pi^0$	154 ± 16	0
$B^+ \to \rho^+$	126 ± 26	1236 ± 502
$B^0 \to \rho^0$	59 ± 12	573 ± 233

Table A.1: Coefficients $A_\pm^{BF_d}$ as in eq. (A.42).

A.1.2 $B_s \to \ell_\alpha^- \ell_\beta^+$ and $K_{L,S} \to \ell_\alpha^- \ell_\beta^+$

The branching ratio for rare leptonic B decays is discussed, for example, in Ref. [427] and the same description holds also for kaons. In our analyses, these processes are induced by the operators

$$\begin{aligned} O_9^{ij\alpha\beta} &= (\bar{d}_i \gamma_\mu P_L d_j)(\bar{\ell}_\alpha \gamma^\mu \ell_\beta)\,, \quad O_{10}^{ij\alpha\beta} = (\bar{d}_i \gamma_\mu P_L d_j)(\bar{\ell}_\alpha \gamma^\mu \gamma_5 \ell_\beta)\,, \\ O_9'^{ij\alpha\beta} &= (\bar{d}_i \gamma_\mu P_L d_j)(\bar{\ell}_\alpha \gamma^\mu \ell_\beta)\,, \quad O_{10}'^{ij\alpha\beta} = (\bar{d}_i \gamma_\mu P_L d_j)(\bar{\ell}_\alpha \gamma^\mu \gamma_5 \ell_\beta)\,. \end{aligned} \tag{A.44}$$

appearing in the effective Hamiltonian

$$\mathcal{H}_{eff} = -\frac{4G_F}{\sqrt{2}} \frac{\alpha}{4\pi} \sum_k V_{ti}^* V_{tj} \mathcal{C}_k^{ij\alpha\beta} \mathcal{O}_k^{ij\alpha\beta}. \tag{A.45}$$

In our analyses of sections 2.1 and 2.2, we do not consider the usual scalar and pseudoscalar operators O_S and O_P (see e.g. in Ref. [427]), since they are generated with negligible coefficients with respect to $O_9^{(\prime)}$ and $O_{10}^{(\prime)}$. The relation between these coefficients and the LEFT ones is

$$C_{9(10)}^{ij\alpha\beta} = \frac{\sqrt{2}\pi}{G_F \alpha V_{ti}^* V_{tj}} \left(L_{\substack{de \\ ij\alpha\beta}}^{V,LR} \pm L_{\substack{ed \\ \alpha\beta ij}}^{V,LL} \right), \quad C_{9(10)}'^{ij\alpha\beta} = \frac{\sqrt{2}\pi}{G_F \alpha V_{ti}^* V_{tj}} \left(L_{\substack{ed \\ \alpha\beta ij}}^{V,RR} \pm L_{\substack{ed \\ \alpha\beta ij}}^{V,LR} \right). \tag{A.46}$$

The branching ratio for the leptonic B_s decays is given by

$$\begin{aligned} \mathcal{B}(B_s \to \ell_\alpha^- \ell_\beta^+)_{th} = {} & \frac{\tau_{B_s}}{64\pi^3} \frac{\alpha^2 G_F^2}{m_{B_s}^3} f_{B_s}^2 |V_{tb} V_{ts}^*|^2 \lambda^{1/2}(m_{B_s}, m_\alpha, m_\beta) \times \\ & \times \Bigg[\left[m_{B_s}^2 - (m_\alpha + m_\beta)^2 \right] \times \left| (C_{9,\mathrm{SM}}^{sb\alpha\beta} + C_9^{sb\alpha\beta} - C_9'^{sb\alpha\beta})(m_\alpha - m_\beta) \right|^2 + \\ & + \left[m_{B_s}^2 - (m_\alpha - m_\beta)^2 \right] \times \left| (C_{10,\mathrm{SM}}^{sb\alpha\beta} + C_{10}^{sb\alpha\beta} - C_{10}'^{sb\alpha\beta})(m_\alpha + m_\beta) \right|^2 \Bigg], \end{aligned} \tag{A.47}$$

where $\lambda(a,b,c) = [a^2 - (b-c)^2][a^2 - (b+c)^2]$. When comparing the theoretical prediction of B decays to untagged experimental data, the sizeable decay width differences in the $B_s^0 - \bar{B}_s^0$ system must be taken into account. This is done by using an effective lifetime. To a good approximation one has [428, 429]

$$\mathcal{B}(B_s \to \ell_\alpha^- \ell_\beta^+)_{\mathrm{eff}} \simeq \frac{1}{1 - y_s} \mathcal{B}(B_s \to \ell_\alpha^- \ell_\beta^+)_{\mathrm{th}}\,, \tag{A.48}$$

with $y_s = \Delta\Gamma_{B_s}/(2\Gamma_{B_s}) = 0.064(4)$, according to the current PDG and HFLAV average [51]. Numerical values for couplings and parameters appearing in the formula can be found in Refs. [51, 430]. The expression in eq. (A.47) can be applied to $B_d \to \ell_\alpha^- \ell_\beta^+$ with the obvious $s \to d$ replacement. For $\ell_\alpha = \ell_\beta = \ell$, as expected, the coefficients $C_9^{(\prime)}$ do not contribute. The experimental value for this decay mode to muon-antimuon pair is

$$\mathcal{B}(B_s \to \mu^-\mu^+) = (3.01 \pm 0.35) \times 10^{-9} \text{ [51]}\,. \tag{A.49}$$

The leptonic kaon decays are instead given by

$$\begin{aligned}\mathcal{B}(K_{L(S)} \to \ell_\alpha^- \ell_\beta^+)_{th} = {}& \frac{\tau_{K_L}}{128\pi^3}\frac{\alpha^2 G_F^2}{m_{K_0}^3} f_K^2 |V_{td}V_{ts}^*|^2 \lambda^{1/2}(m_K, m_\alpha, m_\beta)\times \\ \times \Bigg[& \left[m_{K_0}^2 - (m_\alpha + m_\beta)^2\right] \times \left|\left(C_{9,\text{SM}}^{ds\alpha\beta} \pm C_{9,\text{SM}}^{sd\alpha\beta} + C_9^{ds\alpha\beta} \pm C_9^{sd\alpha\beta}\right)\right|^2 (m_\alpha - m_\beta)^2 + \\ & + \left[m_{K_0}^2 - (m_\alpha - m_\beta)^2\right] \times \left|\left(C_{10,\text{SM}}^{ds\alpha\beta} \pm C_{10,\text{SM}}^{sd\alpha\beta} + C_{10}^{ds\alpha\beta} \pm C_{10}^{sd\alpha\beta}\right)\right|^2 (m_\alpha + m_\beta)^2 \Bigg]\,.\end{aligned} \tag{A.50}$$

where, in case of non vanishing $C'_{9(10)}$ coefficients, we should perform the shift $C_{9(10)} \to C_{9(10)} - C'_{9(10)}$. Notice that for kaons both ds and sd indices appear, since $K_{L,S}$ are linear combinations of K^0 and $\bar{K}^0$

$$\left|K_{L(S)}\right\rangle = \frac{|K^0\rangle \pm \left|\bar{K}^0\right\rangle}{\sqrt{2}}\,. \tag{A.51}$$

The standard model contribution to SD physics is discussed in [431]. For K_S, whose SM contribution is dominated by long distance effects, we use the estimate of Ref. [64]: $\mathcal{B}(K_S \to \mu^+\mu^-)_{\text{LD}} \approx 4.99 \cdot 10^{-12}$, which is orders of magnitude below present sensitivity. The bounds on these observables are:

$$\begin{aligned}\mathcal{B}(K_L \to \mu^+\mu^-)_{\text{SD}} &< 2.5 \cdot 10^{-9} \text{ [64]}\,, \\ \mathcal{B}(K_S \to \mu^+\mu^-) &< 2.1 \cdot 10^{-10}\,(90\%\text{CL}) \text{ [63]}\end{aligned} \tag{A.52}$$

A.1.3 $B \to K^{(*)}\ell^+\ell^-$

In Ref. [432], the leading contributions to the decay width of $B \to K^{(*)}\ell^+\ell^-$ are computed. Under some justified assumptions, the R_K and R_{K^*} ratios read

$$\begin{aligned}R_K([1.1,6]) \approx {}& 1.00 + 0.24\text{Re}[C_9 - C_{10}] + 0.24\text{Re}[C'_9 - C'_{10}] + 0.058\text{Re}[C_9^* C'_9 + \\ & + C_{10}^* C'_{10}] + 0.029\left(|C_9|^2 + |C'_9|^2 + |C_{10}|^2 + |C'_{10}|^2\right)\,,\end{aligned}$$

$$\begin{aligned}R_{K^*}([1.1,6]) \approx {}& 1.00 + 0.24\text{Re}[C_9 - C_{10}] - 0.18\text{Re}[C'_9] + 0.17\text{Re}[C'_{10}] - 0.042\text{Re}[C_9^* C'_9 + \\ & + C_{10}^* C'_{10}] + +0.029\left(|C_9|^2 + |C'_9|^2 + |C_{10}|^2 + |C'_{10}|^2\right)\,,\end{aligned}$$

where the operators and the Hamiltonian are defined as in eqs. (A.44) and (A.45). The numerical coefficients are compatible with the ones computed, for example, in Refs. [433–435] and with our calculation of R_{K^*}, derived using expressions and form factors provided in Refs. [436, 437].

Within the approach of section 2.3, New Physics induces vanishing tree-level contributions to all the C_i coefficients in eq. (A.44) that involve light fermions. However, a sizable RG-induced contribution arises from the QED running of the operator $(\bar{b}_L\gamma^\mu s_L)(\bar{\tau}_L\gamma_\mu\tau_L)$ into O_9 [204, 205].

In terms of the $U(2)_q$-breaking spurions, this leads to [206]:

$$\Delta C_9 \doteq C_9^{\rm NP} \approx \frac{\varepsilon v^2}{3} C^+_{\ell q} \log\left(\frac{\Lambda^2}{m_\tau^2}\right), \tag{A.53}$$

where all the indices in C^+_{lq} are implicitly assumed to refer to the third generation of fermions. This contribution should be compared to the SM value $C_9^{\rm SM} \approx 4.2$.

Based on recent analyses of $B \to K^{(*)}\mu\bar{\mu}$ data [438, 439], including SM uncertainties associated with charm-loop rescattering effects [440], we adopt the value

$$\Delta C_9^{\rm exp} = C_9^{\rm exp} - C_9^{\rm SM} = -0.6 \pm 0.2\,. \tag{A.54}$$

A.1.4 $K_L \to \pi^0\ell^+\ell^-$

Rearranging the formula given in Ref. [441] to fit our notation, we obtain for the branching ratio

$$\mathcal{B}(K_L \to \pi^0\ell^+\ell^-)_{th} = a_\ell\left[(\omega^\ell_{7V})^2 + (\omega^\ell_{7A})^2\right] + b_\ell\omega^\ell_{7V} + c_\ell, \tag{A.55}$$

where

$$\begin{aligned}
\omega^\ell_{7V} &= \frac{1}{2\pi}\frac{1}{1.407\times10^{-4}}\left[P_0{\rm Im}(V^*_{ts}V_{td}) + {\rm Im}(C^{sd\ell\ell}_{9,\rm SM} + C^{sd\ell\ell}_9)\right], \\
\omega^\ell_{7A} &= \frac{1}{2\pi}\frac{1}{1.407\times10^{-4}}{\rm Im}(C^{sd\ell\ell}_{10,\rm SM} + C^{sd\ell\ell}_{10}).
\end{aligned} \tag{A.56}$$

The numerical coefficients a, b and c are given by

$$\begin{aligned}
a_e &= 4.62\times10^{-12}, & a_\mu &= 1.09\times10^{-12}, \\
b_e &= 13.56\times10^{-12}, & b_\mu &= 3.156\times10^{-12}, \\
c_e &= 20.88\times10^{-12}, & c_\mu &= 10.0384\times10^{-12}.
\end{aligned} \tag{A.57}$$

A.1.5 $P \to M\ell^-_\alpha\ell^+_\beta$

We consider here the semileptonic decay of a meson $P = \{B, K_L, K^+\}$ into $M = \{K^{(*)}, \pi\}$ and two different leptons. The branching ratios for the decays are [427, 442]

$$\mathcal{B}(P \to M\ell^-_\alpha\ell^+_\beta)_{th} = \frac{1}{8G_F^2}\left(\alpha^+_V\left|L^{V,LR}_{\substack{de\\ij\alpha\beta}} + L^{V,LL}_{\substack{ed\\\alpha\beta ij}}\right|^2 + \alpha^-_V\left|L^{V,LR}_{\substack{de\\ij\alpha\beta}} - L^{V,LL}_{\substack{ed\\\alpha\beta ij}}\right|^2\right). \tag{A.58}$$

Numerical values for the multiplicative coefficients are given in table A.2. The indices ij correspond to the transition $q_j \to q_i\ell^-_\alpha\ell^+_\beta$ and for K_L it is understood the average $(ds+sd)/2$.

Process	α_V^+	α_V^-
$B \to K e^+ \mu^-$	8.2(6)	8.2(6)
$B \to K e^+ \tau^-$	5.3(2)	5.3(2)
$B \to K \mu^+ \tau^-$	5.2(2)	5.2(2)
$B \to K^* e^+ \mu^-$	2.8(5)	2.8(5)
$B \to K^* e^+ \tau^-$	1.4(2)	1.4(2)
$B \to K^* \mu^+ \tau^-$	1.5(2)	1.3(2)
$K^+ \to \pi^+ e^+ \mu^-$	0.596(4)	0.598(4)
$K_L \to \pi^0 e^+ \mu^-$	2.75(2)	2.76(2)

Table A.2: Values for the factors defined in eq. (A.58), for all the possible final states. Details on their computation can be found in ref. [442].

A.1.6 $B \to X_s\gamma$

The inclusive radiative B decays can be parametrized in terms of the operators

$$O_7 = \frac{e}{16\pi^2} m_b (\bar{s}\sigma_{\alpha\beta} P_{R(L)} b) F^{\alpha\beta} \,, \quad O_8 = \frac{g}{16\pi^2} m_b (\bar{s}\sigma_{\alpha\beta} P_{R(L)} T^a b) G_a^{\alpha\beta} \,, \tag{A.59}$$

and the effective Hamiltonian

$$\mathcal{H}_{eff} = -\frac{4G_F}{\sqrt{2}} V_{ts}^* V_{tb} \sum_i \mathcal{C}_i \mathcal{O}_i \,. \tag{A.60}$$

The branching ratio is given then by [443, 444]

$$\mathcal{B}(\bar{B} \to X_s\gamma)_{E_\gamma > 1.6\,\text{GeV}} = 10^{-4} \times (3.36 \pm 0.23 - 8.22 C_7 - 1.99 C_8) \,, \tag{A.61}$$

where the coefficients are defined at the matching scale $\mu_0 = 160$ GeV [443]. In terms of LEFT coefficients, we have:

$$\begin{gathered} C_7 = \frac{N_{sb}^{-1} e}{m_b} \times L^{d\gamma}_{sb} \,, \qquad C_8 = \frac{N_{sb}^{-1} e^2}{g m_b} L^{dG}_{sb} \,, \\ N_{sb} = \frac{4G_F}{\sqrt{2}} \frac{\alpha_{em}}{4\pi} V_{ts}^* V_{tb} \,. \end{gathered} \tag{A.62}$$

A.1.7 $R(D^{(*)})$

Semileptonic charged-current $b \to c\ell\nu$ transitions can be tested through the LFU ratios

$$R_{D^{(*)}} = \frac{\mathcal{B}\left(B \to D^{(*)}\tau\nu\right)}{\mathcal{B}\left(B \to D^{(*)}\ell\nu\right)} \,.$$

We use the HFLAV values [445] for both the experimental averages and the SM predictions of $R_{D^{(*)}}$, namely:

$$\begin{aligned} R_D^{\text{SM}} &= 0.298 \pm 0.004 \,, \quad & R_{D^*}^{\text{SM}} &= 0.254 \pm 0.005 \,, \\ R_D^{\text{exp}} &= 0.342 \pm 0.026 \,, \quad & R_{D^*}^{\text{exp}} &= 0.287 \pm 0.012 \,, \\ & & \rho &= -0.39 \,. \end{aligned} \tag{A.63}$$

Following Ref.[446, 447], we define the effective Lagrangian

$$\begin{aligned}\mathcal{L}_{\text{eff}} = -\frac{4G_F V_{cb}}{\sqrt{2}}\Big[&(1+C_{V_L})(\bar{c}\gamma^\mu P_L b)(\bar{\tau}\gamma_\mu P_L \nu_\tau) + \\ &+ C_{S_R}(\bar{c}P_R b)(\bar{\tau}P_L\nu_\tau)\Big]\,,\end{aligned} \tag{A.64}$$

and simply parametrize the EFT dependence of these observables, normalized to the SM prediction, as:

$$\begin{aligned}\frac{R_D}{R_D^{\text{SM}}} &= |1+C_{V_L}|^2 + 1.01|C_{S_R}|^2 + 1.49\,\text{Re}[(1+C_{V_L})C_{S_R}^*]\,,\\ \frac{R_{D^*}}{R_{D^*}^{\text{SM}}} &= |1+C_{V_L}|^2 + 0.04|C_{S_R}|^2 - 0.11\,\text{Re}[(1+C_{V_L})C_{S_R}^*]\,.\end{aligned} \tag{A.65}$$

Within the EFT setup of section 2.3, these low-energy coefficients can be matched onto our SMEFT basis in terms of the $U(2)_q$-breaking spurions as follows:

$$\begin{aligned}C_{V_L} &= \frac{v^2}{V_{cb}}\left(V_{cd}V_{td}^*\,\kappa\,\varepsilon\,C_{lq}^3 + V_{cs}V_{ts}^*\,\varepsilon\,C_{lq}^3 - V_{cb}\,C_{lq}^3\right)\,,\\ C_{S_R} &= \frac{v^2}{2V_{cb}}\left(V_{cd}V_{td}^*\,\kappa\,\varepsilon\,C_S + V_{cs}V_{ts}^*\,\varepsilon\,C_S - V_{cb}\,C_S\right)^*\,.\end{aligned} \tag{A.66}$$

Here, $C_{lq}^3 = (C_{lq}^+ - C_{lq}^-)/2$. In these expressions, all indices are implicitly understood to refer to third-generation fermions. The CKM factors V_{ci} appear due to the choice of working in a down-quark-aligned basis, while the V_{ti}^* terms arise from the spurion insertions. The complex conjugation in C_{S_R} reflects the fact that, by convention, the Wilson coefficient C_S multiplies the hermitian conjugate of the operator associated with C_{S_R}. Renormalization group effects are particularly relevant in the presence of scalar operators and must therefore not be neglected for this observable.

A.1.8 LFU in τ decays

We consider lepton flavor universality in leptonic τ decays. The relevant observables are the ratios $\left|g_\tau/g_{\mu(e)}\right|$, defined as

$$\left|\frac{g_\tau}{g_{\mu(e)}}\right| = \frac{\mathcal{B}(\tau\to e(\mu)\nu\bar{\nu})/\mathcal{B}(\tau\to e(\mu)\nu\bar{\nu})_{\text{SM}}}{\mathcal{B}(\mu\to e\nu\bar{\nu})/\mathcal{B}(\mu\to e\nu\bar{\nu})_{\text{SM}}}\,. \tag{A.67}$$

The corresponding experimental values are reported by HFLAV [445]:

$$\left|\frac{g_\tau}{g_\mu}\right|^{\text{exp}} = (0.9\pm1.4)\,10^{-3}\,,\quad \left|\frac{g_\tau}{g_e}\right|^{\text{exp}} = (2.7\pm1.4)\,10^{-3}\,,$$

with a correlation $\rho_\tau = 0.51$. NP effects can modify these ratios through effective four leptons operators. In general, in terms of LEFT operators

$$\begin{aligned}\frac{g_\tau}{g_e} - 1 &= \frac{v^2}{2}\left(L^{V,LL}_{\substack{\nu e\\ \mu e e\mu}} - L^{V,LL}_{\substack{\nu e\\ \tau\mu\mu\tau}}\right)\,,\\ \frac{g_\tau}{g_\mu} - 1 &= \frac{v^2}{2}\left(L^{V,LL}_{\substack{\nu e\\ \mu e e\mu}} - L^{V,LL}_{\substack{\nu e\\ \tau e e\tau}}\right)\,.\end{aligned} \tag{A.68}$$

Within the top-philic scenario of section 2.1, this is matched at the SMEFT level onto:

$$\begin{aligned}\frac{g_\tau}{g_e} - 1 &= 0.0038\,(C_{lq}^{(3),33} - C_{lq}^{(3),11})\,,\\ \frac{g_\tau}{g_\mu} - 1 &= 0.0038\,(C_{lq}^{(3),33} - C_{lq}^{(3),22})\,,\end{aligned} \tag{A.69}$$

where C_{lq} is expressed in TeV^{-2} units.

On the other hand, within the framework of Section 2.3, the operators considered there (see eq. (2.51)) can contribute to these observables only through RG mixing effects. Taking into account the leading-log evolution in the SMEFT:

$$\left|\frac{g_\tau}{g_{e(\mu)}}\right| - 1 \simeq -\frac{m_t^2 N_c}{16\pi^2}\log\left(\frac{\Lambda^2}{m_t^2}\right) C_{lq}^3(\Lambda)\,, \tag{A.70}$$

where $\Lambda = 1$ TeV is the UV scale , and $C_{lq}^3 = (C_{lq}^+ - C_{lq}^-)/2$, where all the indices are omitted as they are understood to refer to third generation of fermions.

A.1.9 Charged lepton flavor violation

For charged lepton flavor violation processes, considered in section 2.1, we employ the expressions from Refs. [125, 130], after translating them to the LEFT basis. In the following we give the explicit expressions used in this work.

- $\ell_H \to \ell_L \gamma$

  We may take a reference renormalization scale $\mu = 2\,\text{GeV}$, where the LEFT is yet well defined. One has [125, 130, 448]

  $$\Gamma_{\ell\to\ell'\gamma} = \frac{m_\ell^3}{4\pi}[|L_{\underset{\ell'\ell}{e\gamma}}|^2 + |L_{\underset{\ell\ell'}{e\gamma}}|^2]\,. \tag{A.71}$$

  The (nonperturbative) effect of four-fermion operators involving tensor light-quark currents can be taken into account by making the following transformations

  $$L_{\underset{\ell'\ell}{e\gamma}} \to L_{\underset{\ell'\ell}{e\gamma}} - e\left(c_3^{\ell'\ell} + \frac{c_8^{\ell'\ell}}{\sqrt{3}}\right) i\Pi_{VT}(0)\,, \tag{A.72}$$

  $$L_{\underset{\ell\ell'}{e\gamma}} \to L_{\underset{\ell\ell'}{e\gamma}} + e\left(c_3^{\ell\ell'} + \frac{c_8^{\ell\ell'}}{\sqrt{3}}\right) i\Pi_{VT}(0)\,, \tag{A.73}$$

  with

  $$c_3^{ij} = L_{\underset{ij11}{eu}}^{T,RR} - L_{\underset{ij11}{ed}}^{T,RR}\,, \tag{A.74}$$

  $$c_8^{ij} = \frac{1}{\sqrt{3}}\left[L_{\underset{ij11}{eu}}^{T,RR} + L_{\underset{ij11}{ed}}^{T,RR} - 2L_{\underset{ij22}{ed}}^{T,RR}\right]\,. \tag{A.75}$$

  As in Ref. [130] we take $i\Pi_{VT}(0) \approx 0.04\,\text{GeV}$.

- $\tau \to 3e$, $\tau \to 3\mu$, $\mu \to 3e$

  We use the analytic expressions given in Ref. [130], adapting them to the LEFT normalization of this work. Numerically we find, in GeV units,

$$\begin{aligned}\mathcal{B}(\tau \to 3e) \approx\ & 1.6 \times 10^8 (|L^{S,RR}_{\substack{ee\\1113}}|^2 + |L^{V,LR}_{\substack{ee\\1113}}|^2 + |L^{V,LR}_{\substack{ee\\1311}}|^2) \\ & + 1.3 \times 10^9 (|L^{V,LL}_{\substack{ee\\1311}}|^2 + |L^{V,RR}_{\substack{ee\\1311}}|^2) + 2.1 \times 10^9 (|L_{\substack{e\gamma\\31}}|^2 + |L_{\substack{e\gamma\\13}}|^2) \\ & + [L_{\substack{e\gamma\\31}} (-4.5 \times 10^8 L^{V,LL}_{\substack{ee\\1113}} - 1.1 \times 10^8 L^{V,LR}_{\substack{ee\\1311}}) + c.c.] \\ & + [L^*_{\substack{e\gamma\\13}} (-4.5 \times 10^8 L^{V,RR}_{\substack{ee\\1113}} - 1.1 \times 10^8 L^{V,LR}_{\substack{ee\\1113}}) + c.c.] \,. \end{aligned} \tag{A.76}$$

  The analytic expressions trivially generalize for $\tau \to 3\mu$, $\mu \to 3e$. Numerically one finds

$$\begin{aligned}\mathcal{B}(\tau \to 3\mu) \approx\ & 1.6 \times 10^8 (|L^{S,RR}_{\substack{ee\\1123}}|^2 + |L^{V,LR}_{\substack{ee\\1123}}|^2 + |L^{V,LR}_{\substack{ee\\2311}}|^2) \\ & + 1.3 \times 10^9 (|L^{V,LL}_{\substack{ee\\2311}}|^2 + |L^{V,RR}_{\substack{ee\\2311}}|^2) + 4.4 \times 10^8 (|L_{\substack{e\gamma\\32}}|^2 + |L_{\substack{e\gamma\\23}}|^2) \\ & + [L_{\substack{e\gamma\\32}} (-4.5 \times 10^8 L^{V,LL}_{\substack{ee\\1123}} - 1.1 \times 10^8 L^{V,LR}_{\substack{ee\\2311}}) + c.c.] \\ & + [L^*_{\substack{e\gamma\\23}} (-4.5 \times 10^8 L^{V,RR}_{\substack{ee\\1123}} - 1.1 \times 10^8 L^{V,LR}_{\substack{ee\\1123}}) + c.c.] \,, \end{aligned} \tag{A.77}$$

  and

$$\begin{aligned}\mathcal{B}(\mu \to 3e) \approx\ & 9.2 \times 10^8 (|L^{S,RR}_{\substack{ee\\1112}}|^2 + |L^{V,LR}_{\substack{ee\\1112}}|^2 + |L^{V,LR}_{\substack{ee\\1211}}|^2) \\ & + 7.4 \times 10^9 (|L^{V,LL}_{\substack{ee\\1211}}|^2 + |L^{V,RR}_{\substack{ee\\1211}}|^2) + 1.9 \times 10^{12} (|L_{\substack{e\gamma\\21}}|^2 + |L_{\substack{e\gamma\\12}}|^2) \\ & + [L_{\substack{e\gamma\\21}} (-4.2 \times 10^{10} L^{V,LL}_{\substack{ee\\1112}} - 1.1 \times 10^{10} L^{V,LR}_{\substack{ee\\1211}}) + c.c.] \\ & + [L^*_{\substack{e\gamma\\12}} (-4.2 \times 10^{10} L^{V,RR}_{\substack{ee\\1112}} - 1.1 \times 10^{10} L^{V,LR}_{\substack{ee\\1112}}) + c.c.] \,, \end{aligned} \tag{A.78}$$

- $\tau \to e\bar{\mu}\mu$, $\tau \to \mu\bar{e}e$.

  Once again we adapt the analytic results as given in Ref. [130], finding

$$\begin{aligned}\mathcal{B}(\tau \to e\bar{\mu}\mu) \approx\ & 2.5 \times 10^9 (|L^{V,LL}_{\substack{ee\\1223}}|^2 + |L^{V,RR}_{\substack{ee\\1223}}|^2) \\ & + 1.6 \times 10^8 (|L^{V,LR}_{\substack{ee\\2213}}|^2 + |L^{V,LR}_{\substack{ee\\1322}}|^2) + 1.0 \times 10^8 (|L_{\substack{e\gamma\\31}}|^2 + |L_{\substack{e\gamma\\13}}|^2) \\ & - 2.1 \times 10^8 [L_{\substack{e\gamma\\31}} L^{V,LL}_{\substack{ee\\1223}} + c.c.] \\ & + [L^*_{\substack{e\gamma\\13}} (-5.2 \times 10^7 L^{*V,LR}_{\substack{ee\\1322}} - 2.6 \times 10^8 L^{V,RR}_{\substack{ee\\1223}}) + c.c.] \,, \end{aligned} \tag{A.79}$$

  and

$$\begin{aligned}\mathcal{B}(\tau \to \mu\bar{e}e) \approx\ & 2.6 \times 10^9 (|L^{V,LL}_{\substack{ee\\1123}}|^2 + |L^{V,RR}_{\substack{ee\\1123}}|^2) \\ & + 1.6 \times 10^8 (|L^{V,LR}_{\substack{ee\\1123}}|^2 + |L^{V,LR}_{\substack{ee\\2311}}|^2) + 5.0 \times 10^8 (|L_{\substack{e\gamma\\32}}|^2 + |L_{\substack{e\gamma\\23}}|^2) \\ & - 2.2 \times 10^8 [L_{\substack{e\gamma\\32}} L^{V,LL}_{\substack{ee\\1123}} + c.c.] \\ & + [L^*_{\substack{e\gamma\\23}} (-5.5 \times 10^7 L^{*V,LR}_{\substack{ee\\2311}} - 2.8 \times 10^8 L^{V,RR}_{\substack{ee\\1123}}) + c.c.] \,. \end{aligned} \tag{A.80}$$

- $\mu\text{Au} \to e\text{Au}$.

  We adapt the results of Ref. [125], neglecting the power-suppressed contributions from c and b quarks. In principle they are given at a $\mu = 1\,\text{GeV}$, but within the theoretical uncertainties the same expressions can also be used at $\mu = 2\,\text{GeV}$.[7] We have also checked that we agree with the adaptation given in Ref. [448]. The numerical result is rather large. For reference, the first quadratic coefficients are

$$\mathcal{B}(\mu\text{Au} \to e\text{Au}) \approx 1.1 \times 10^{13}[(L^{S,RL}_{\substack{ed\\1211}})^2 + (L^{S,RL}_{\substack{ed\\2111}})^2 + (L^{S,RR}_{\substack{ed\\2111}})^2 + (L^{S,RR}_{\substack{ed\\1211}})^2 + (d \to u)] \tag{A.81}$$

- $\tau \to \ell\pi^0$

  We take the numerical result of Ref. [130]. Adapting it to the normalization of this work we have

$$\mathcal{B}(\tau \to \ell\pi^0) \approx B_1(\tau \to \ell\pi^0) + B_2(\tau \to \ell\pi^0)\,,$$

  with

$$\begin{aligned}\mathcal{B}_1(\tau \to \ell\pi^0) \approx{}& 1.3 \times 10^8 |L^{S,RL}_{\substack{ed\\\ell 311}} - L^{S,RL}_{\substack{eu\\\ell 311}} - L^{S,RR}_{\substack{ed\\\ell 311}} + L^{S,RR}_{\substack{eu\\\ell 311}}|^2 \\ &+ 5.1 \times 10^7 |L^{V,LL}_{\substack{ed\\3\ell 11}} - L^{V,LL}_{\substack{eu\\3\ell 11}} - L^{V,LR}_{\substack{ed\\3\ell 11}} + L^{V,LR}_{\substack{eu\\3\ell 11}}|^2\,,\end{aligned} \tag{A.82}$$

  and $\mathcal{B}_2(\tau \to \ell\pi^0)$ can be obtained from the $B_1(\tau \to \ell\pi^0)$ expression by making the following transformations

$$L^{V,LL}_{\substack{eq\\3\ell 11}} \to L^{V,RR}_{\substack{eq\\3\ell 11}}, L^{V,LR}_{\substack{eq\\3\ell 11}} \to L^{V,LR}_{\substack{qe\\113\ell}}, L^{S,RR}_{\substack{eq\\\ell 3qq}} \to L^{S,RR^*}_{\substack{eq\\3\ell qq}}, L^{S,RL}_{\substack{eq\\\ell 3qq}} \to L^{S,RL^*}_{\substack{eq\\3\ell qq}}. \tag{A.83}$$

- $\tau \to \ell\pi^+\pi^-$

  Once again we use the numerical results from Ref. [130]. We find

$$\mathcal{B}(\tau \to \ell\pi\pi) = \mathcal{B}_1(\tau \to \ell\pi\pi) + \mathcal{B}_2(\tau \to \ell\pi\pi)\,.$$

$$\begin{aligned}\mathcal{B}_1(\tau \to \ell\pi\pi) \approx{}& 9.2 \times 10^8 |L^{T,RR}_{\substack{ed\\3\ell 11}} - L^{T,RR}_{\substack{eu\\3\ell 11}}|^2 + 4.6 \times 10^8 |L^{V,LL}_{\substack{ed\\3\ell 11}} - L^{V,LL}_{\substack{eu\\3\ell 11}} + L^{V,LR}_{\substack{ed\\3\ell 11}} - L^{V,LR}_{\substack{eu\\3\ell 11}}|^2 \\ &+ 5.0 \times 10^8 |L_{\substack{e\gamma\\3\ell}}|^2 + 1.6 \times 10^8 |L^{S,RL}_{\substack{ed\\3\ell 11}} + L^{S,RL}_{\substack{eu\\3\ell 11}} + L^{S,RR}_{\substack{ed\\3\ell 11}} + L^{S,RR}_{\substack{eu\\3\ell 11}}|^2 \\ &+ 1.2 \times 10^8 |L^{S,RL}_{\substack{ed\\3\ell 22}} + L^{S,RR}_{\substack{ed\\3\ell 22}}|^2\,,\end{aligned} \tag{A.84}$$

  and $\mathcal{B}_2(\tau \to \ell\pi\pi)$ can be obtained from the $B_1(\tau \to \ell\pi\pi)$ expression by making the following transformations

$$\begin{aligned}&L^{T,RR}_{\substack{eq\\3\ell 11}} \to L^{T,RR}_{\substack{eq\\\ell 311}}, L^{V,LL}_{\substack{eq\\3\ell 11}} \to L^{V,RR}_{\substack{eq\\3\ell 11}}, L^{V,LR}_{\substack{eq\\3\ell 11}} \to L^{V,LR}_{\substack{qe\\113\ell}}, \\ &L_{\substack{e\gamma\\3\ell}} \to L_{\substack{e\gamma\\\ell 3}}, L^{S,RR}_{\substack{eq\\3\ell qq}} \to L^{S,RR^*}_{\substack{eq\\\ell 3qq}}, L^{S,RL}_{\substack{eq\\3\ell qq}} \to L^{S,RL^*}_{\substack{eq\\\ell 3qq}}.\end{aligned} \tag{A.85}$$

$\tau \to \ell\eta, \tau \to \ell\eta', \tau \to \ell K, \tau \to \ell\pi K, \tau \to \ell K K$ are also included in our χ^2, adapting the compilation of Ref. [130]. However they play a marginal phenomenological role in our analysis and thus we refrain from giving the explicit expressions.

[7] The large QCD running of the scalar quark current is fully taken into account by simply taking as input $m_q(\mu = 2\,\text{GeV})$ instead of $m_q(\mu = 1\,\text{GeV})$.

A.1.10 Matching relations for the Cabibbo angle observables

The running of the chirality-flipping low-energy couplings to the M_Z mass is large and needs to be taken into account. From Ref. [449], which includes higher-order QCD running effects, one has

$$\begin{pmatrix}\epsilon_S\\ \epsilon_P\\ \epsilon_T\end{pmatrix}_{\mu=2\,\text{GeV}} = \begin{pmatrix}1.72 & 2.46\times10^{-6} & -0.0242\\ 2.46\times10^{-6} & 1.72 & -0.0242\\ -2.17\times10^{-4} & -2.17\times10^{-4} & 0.825\end{pmatrix}\begin{pmatrix}\epsilon_S\\ \epsilon_P\\ \epsilon_T\end{pmatrix}_{\mu=M_Z}. \tag{A.86}$$

At M_Z at tree-level one has

$$\begin{aligned}
-\frac{2\hat{V}_{ud}}{v^2}\epsilon_L^{dse} &= 2\left(C^{(3)}_{\substack{Hl\\22}} - C^{(3)}_{\substack{Hq\\11}} - C_{\substack{ll\\1221}} + C^{(3)}_{\substack{lq\\1111}}\right)\\
-\frac{2\hat{V}_{ud}}{v^2}\epsilon_L^{d\ell'/\ell} &= L^{V,LL}_{\substack{\nu edu\\ \ell'\ell'11}} - L^{V,LL}_{\substack{\nu edu\\ \ell\ell11}} = 2V_{ud}(C^{(3)}_{\substack{Hl\\ \ell\ell}} - C^{(3)}_{\substack{Hl\\ \ell'\ell'}} - C^{(3)}_{\substack{lq\\ \ell\ell11}} + C^{(3)}_{\substack{lq\\ \ell'\ell'11}}) - 2V_{us}(-C^{(3)}_{\substack{lq\\ \ell\ell21}} + C^{(3)}_{\substack{lq\\ \ell'\ell'21}}),\\
-\frac{2\hat{V}_{us}}{v^2}\epsilon_L^{s\ell'/\ell} &= L^{V,LL}_{\substack{\nu edu\\ \ell'\ell'21}} - L^{V,LL}_{\substack{\nu edu\\ \ell\ell21}} = 2V_{us}(C^{(3)}_{\substack{Hl\\ \ell\ell}} - C^{(3)}_{\substack{Hl\\ \ell'\ell'}} - C^{(3)}_{\substack{lq\\ \ell\ell11}} + C^{(3)}_{\substack{lq\\ \ell'\ell'11}}) + 2V_{ud}(-C^{(3)}_{\substack{lq\\ \ell\ell21}} + C^{(3)}_{\substack{lq\\ \ell'\ell'21}}),\\
-\frac{2\hat{V}_{uD}}{v^2}\epsilon_R^{D} &= L^{V,LR}_{\substack{\nu edu\\ \ell\ell D1}} = -C_{\substack{Hud\\1D}},\\
-\frac{2\hat{V}_{ud}}{v^2}\epsilon_S^{d\ell} &= L^{S,RR}_{\substack{\nu edu\\ \ell\ell11}} + L^{S,RL}_{\substack{\nu edu\\ \ell\ell11}} = C_{\substack{ledq\\ \ell\ell11}} + V_{ud}C^{(1)}_{\substack{lequ\\ \ell\ell11}} - V_{us}C^{(1)}_{\substack{lequ\\ \ell\ell21}},\\
-\frac{2\hat{V}_{us}}{v^2}\epsilon_S^{s\ell} &= L^{S,RR}_{\substack{\nu edu\\ \ell\ell21}} + L^{S,RL}_{\substack{\nu edu\\ \ell\ell21}} = C_{\substack{ledq\\ \ell\ell21}} + V_{us}C^{(1)}_{\substack{lequ\\ \ell\ell11}} + V_{ud}C^{(1)}_{\substack{lequ\\ \ell\ell21}},\\
-\frac{2\hat{V}_{ud}}{v^2}\epsilon_P^{d\ell} &= L^{S,RR}_{\substack{\nu edu\\ \ell\ell11}} - L^{S,RL}_{\substack{\nu edu\\ \ell\ell11}} = -C_{\substack{ledq\\ \ell\ell11}} + V_{ud}C^{(1)}_{\substack{lequ\\ \ell\ell11}} - V_{us}C^{(1)}_{\substack{lequ\\ \ell\ell21}},\\
-\frac{2\hat{V}_{us}}{v^2}\epsilon_P^{s\ell} &= L^{S,RR}_{\substack{\nu edu\\ \ell\ell21}} - L^{S,RL}_{\substack{\nu edu\\ \ell\ell21}} = -C_{\substack{ledq\\ \ell\ell21}} + V_{us}C^{(1)}_{\substack{lequ\\ \ell\ell11}} + V_{ud}C^{(1)}_{\substack{lequ\\ \ell\ell21}},\\
-\frac{2\hat{V}_{ud}}{v^2}\frac{1}{4}\hat{\epsilon}_T^{d\ell} &= L^{T,RR}_{\substack{\nu edu\\ \ell\ell11}} = V_{ud}C^{(3)}_{\substack{lequ\\ \ell\ell11}} - V_{us}C^{(3)}_{\substack{lequ\\ \ell\ell21}},\\
-\frac{2\hat{V}_{us}}{v^2}\frac{1}{4}\hat{\epsilon}_T^{s\ell} &= L^{T,RR}_{\substack{\nu edu\\ \ell\ell21}} = V_{us}C^{(3)}_{\substack{lequ\\ \ell\ell11}} + V_{ud}C^{(3)}_{\substack{lequ\\ \ell\ell21}}.
\end{aligned} \tag{A.87}$$

The leading mechanism to generate a top operator, relevant for section 2.1, is through the large mixing of $C^{(3)}_{\substack{Hl\\ \alpha\alpha}}$ with $C^{(3)}_{\substack{lq\\ \alpha\alpha33}}$ through a double top-Yukawa insertion [33],[8]

$$v^2 C^{(3)}_{\substack{Hl\\ \alpha\alpha}}(M_Z^2) \approx v^2 4N_c\frac{m_t^2}{(4\pi v)^2}C^{(3)}_{\substack{lq\\ \alpha\alpha33}}(\Lambda^2_{\text{UV}})\log\frac{\Lambda_{\text{UV}}}{M_Z} = \left[\frac{N_c}{4\pi^2}\frac{m_t^2}{\Lambda^2_{\text{UV}}}\log\frac{\Lambda_{\text{UV}}}{M_Z}\right]\Lambda^2_{\text{UV}}C^{(3)}_{\substack{lq\\ \alpha\alpha33}}(\Lambda^2_{\text{UV}}). \tag{A.88}$$

[8] As in the rest of this work, the DSixTools package has been used to perform the full one-loop running. We have also checked that the loop-induced top operators in the SMEFT-LEFT matching play a marginal role in this sector and, in first approximation, can be neglected.

A.1.11 Higgs basis used for EWPT and Higgs fit

The fit performed in Ref. [134] employs a specific combinations of Wilson coefficients of the Warsaw basis, called *Higgs basis*. This allows to reduce the correlations between the directions mostly constrained by EW precision data and those constrained by Higgs data, which differ strongly in the precision. The combinations used are the following:

$$\begin{aligned}
\delta g_L^{W\ell} &= C_{Hl}^{(3)} + f(1/2,0) - f(-1/2,-1),\\
\delta g_L^{Z\ell} &= -\frac{1}{2}C_{Hl}^{(3)} - \frac{1}{2}C_{Hl}^{(1)} + f(-1/2,-1),\\
\delta g_R^{Z\ell} &= -\frac{1}{2}C_{He}^{(1)} + f(0,-1),\\
\delta g_L^{Zu} &= \frac{1}{2}C_{Hq}^{(3)} - \frac{1}{2}C_{Hq}^{(1)} + f(1/2,2/3),\\
\delta g_L^{Zd} &= -\frac{1}{2}C_{Hq}^{(3)} - \frac{1}{2}C_{Hq}^{(1)} + f(-1/2,-1/3),\\
\delta g_R^{Zu} &= -\frac{1}{2}C_{Hu} + f(0,2/3),\\
\delta g_R^{Zd} &= -\frac{1}{2}C_{Hd} + f(0,-1/3),\\
\delta c_z &= C_{H\Box} - \frac{1}{4}C_{HD} - \frac{3}{2}\Delta_{G_F},\\
c_{z\Box} &= \frac{1}{2g_L^2}\left(C_{HD} + 2\Delta_{G_F}\right),\\
c_{gg} &= \frac{4}{g_s^2}C_{HG},\\
c_{\gamma\gamma} &= 4\left(\frac{1}{g_L^2}C_{HW} + \frac{1}{g_Y^2}C_{HB} - \frac{1}{g_L g_Y}C_{HWB}\right),\\
c_{zz} &= 4\left(\frac{g_L^2 C_{HW} + g_Y^2 C_{HB} + g_L g_Y C_{HWB}}{(g_L^2+g_Y^2)^2}\right),\\
c_{z\gamma} &= 4\left(\frac{C_{HW} - C_{HB} - \frac{g_L^2-g_Y^2}{2g_L g_Y}C_{HWB}}{g_L^2+g_Y^2}\right),
\end{aligned} \tag{A.89}$$

where

$$f(T^3,Q) \equiv \left\{ -Q\frac{g_L g_Y}{g_L^2-g_Y^2}C_{HWB} - \mathbf{1}\left(\frac{1}{4}C_{HD} + \frac{1}{2}\Delta_{G_F}\right)\left(T^3 + Q\frac{g_Y^2}{g_L^2-g_Y^2}\right)\right\}\mathbf{1}\,, \tag{A.90}$$

and $\Delta_{G_F} = [C_{Hl}^{(3)}]_{11} + [C_{Hl}^{(3)}]_{22} - \frac{1}{2}[C_{ll}]_{1221}$. To these coefficients, the fit in Ref. [134] also adds those for the dimension-6 Yukawa-like operators of top, bottom, muon and tau fermions, as well as the one responsible for modifying the muon decay: $[C_{uH}]_{33}$, $[C_{dH}]_{33}$, $[C_{eH}]_{22}$, $[C_{eH}]_{33}$, $[C_{ll}]_{1221}$.

The set of $\delta g_{V\psi}$ parametrize the corresponding vertex corrections of Z and W bosons, and are mostly constrained by electroweak data from LEP. As mentioned, the coefficient $[C_{ll}]_{1221}$ enters the EW fit by its impact in the muon decay. Finally, the other coefficients do not affect EW observables at tree level and are only constrained by Higgs data.

Class	Coefficients	Warsaw basis	95% CL Individual	95% CL Marginalised
Dipoles	c_{tG}	C_{uG}	[0.01,0.11]	[0.01,0.23]
	c_{tW}	C_{uW}	[-0.085,0.030]	[-0.28,0.13]
	c_{tZ}	$-\mathrm{s}_\theta\, C_{uB} + \mathrm{c}_\theta\, C_{uW}$	[-0.038,0.090]	[-0.50,0.14]
Higgs-Top	c^3_{HQ}	$C^{(3)}_{Hq}$	[-0.39,0.34]	[-0.42,0.31]
	$c^{(-)}_{HQ}$	$C^{(1)}_{Hq} - C^{(3)}_{Hq}$	[-1.1,1.5]	[-2.7,2.7]
	c_{Ht}	C_{Hu}	[-2.8,2.2]	[-15,4]
	c_{tH}	C_{uH}	[-1.3,0.4]	[-0.5,2.9]
4 quarks	c^1_{QQ}	$2C^{(1)}_{qq} - \frac{2}{3}C^{(3)}_{qq}$	[-2.3,2.0]	[-3.7,4.4]
	c^8_{QQ}	$8C^{(3)}_{qq}$	[-6.8,5.9]	[-13,10]
	c^1_{Qt}	$C^{(1)}_{qu}$	[-1.8,1.9]	[-1.5,1.4]
	c^8_{Qt}	$C^{(8)}_{qu}$	[-4.3,3.3]	[-3.4,2.5]
	c^1_{tt}	C_{uu}	[-1.1,1.0]	[-0.88,0.81]

Table A.3: The 95% CL bounds from SMEFiT for individual and global fits obtained using quadratic EFT calculations. Top quark, Higgs and diboson data have been used, as discussed in Ref. [143]. Coefficients are expressed in both the SMEFiT and the Warsaw basis conventions.

For the explicit expressions of the observables in terms of SMEFT coefficients in the third-generation-philic framework, see also [450].

A.1.12 High-p_T tails

We consider High-p_T Drell-Yan tails, using LHC Run-II di-tau and mono-tau data. The likelihood is constructed using `HighPT` [195], and running effects for these observables are neglected.

A.1.13 Direct constraints from LHC

Here we provide the 95% CL bounds on Wilson coefficients, from both individual and global marginalised fits obtained from SMEFiT [143]. These are illustrated in table A.3. Single parameter fits match the findings of Ref. [143] (see Table 5.4 therein).

Even though it is reasonable to expect that individual bounds are comparable or more severe than the global ones, we observe the latter to be stronger in the case of the $C^{(1/8)}_{qu}$ and C_{uu} coefficients. This surprising trend was also observed in Ref. [143], where the global analysis involved a larger set of operators.

The direct bounds shown in table A.3 are compared to the indirect limits computed in this work in section 2.1.4.

A.1.14 LEFT Operator Basis

$\nu\nu + h.c.$	
$\mathcal{O}_\nu$	$(\nu_{Lp}^T C \nu_{Lr})$

$(\nu\nu)X + h.c.$	
$\mathcal{O}_{\nu\gamma}$	$(\nu_{Lp}^T C \sigma^{\mu\nu} \nu_{Lr}) F_{\mu\nu}$

$(\overline{L}R)X + h.c.$	
$\mathcal{O}_{e\gamma}$	$\bar{e}_{Lp} \sigma^{\mu\nu} e_{Rr} \, F_{\mu\nu}$
$\mathcal{O}_{u\gamma}$	$\bar{u}_{Lp} \sigma^{\mu\nu} u_{Rr} \, F_{\mu\nu}$
$\mathcal{O}_{d\gamma}$	$\bar{d}_{Lp} \sigma^{\mu\nu} d_{Rr} \, F_{\mu\nu}$
$\mathcal{O}_{uG}$	$\bar{u}_{Lp} \sigma^{\mu\nu} T^A u_{Rr} \, G^A_{\mu\nu}$
$\mathcal{O}_{dG}$	$\bar{d}_{Lp} \sigma^{\mu\nu} T^A d_{Rr} \, G^A_{\mu\nu}$

X^3	
$\mathcal{O}_G$	$f^{ABC} G_\mu^{A\nu} G_\nu^{B\rho} G_\rho^{C\mu}$
$\mathcal{O}_{\widetilde{G}}$	$f^{ABC} \widetilde{G}_\mu^{A\nu} G_\nu^{B\rho} G_\rho^{C\mu}$

$(\overline{L}L)(\overline{L}L)$	
$\mathcal{O}_{\nu\nu}^{V,LL}$	$(\bar{\nu}_{Lp} \gamma^\mu \nu_{Lr})(\bar{\nu}_{Ls} \gamma_\mu \nu_{Lt})$
$\mathcal{O}_{ee}^{V,LL}$	$(\bar{e}_{Lp} \gamma^\mu e_{Lr})(\bar{e}_{Ls} \gamma_\mu e_{Lt})$
$\mathcal{O}_{\nu e}^{V,LL}$	$(\bar{\nu}_{Lp} \gamma^\mu \nu_{Lr})(\bar{e}_{Ls} \gamma_\mu e_{Lt})$
$\mathcal{O}_{\nu u}^{V,LL}$	$(\bar{\nu}_{Lp} \gamma^\mu \nu_{Lr})(\bar{u}_{Ls} \gamma_\mu u_{Lt})$
$\mathcal{O}_{\nu d}^{V,LL}$	$(\bar{\nu}_{Lp} \gamma^\mu \nu_{Lr})(\bar{d}_{Ls} \gamma_\mu d_{Lt})$
$\mathcal{O}_{eu}^{V,LL}$	$(\bar{e}_{Lp} \gamma^\mu e_{Lr})(\bar{u}_{Ls} \gamma_\mu u_{Lt})$
$\mathcal{O}_{ed}^{V,LL}$	$(\bar{e}_{Lp} \gamma^\mu e_{Lr})(\bar{d}_{Ls} \gamma_\mu d_{Lt})$
$\mathcal{O}_{\nu edu}^{V,LL}$	$(\bar{\nu}_{Lp} \gamma^\mu e_{Lr})(\bar{d}_{Ls} \gamma_\mu u_{Lt}) + h.c.$
$\mathcal{O}_{uu}^{V,LL}$	$(\bar{u}_{Lp} \gamma^\mu u_{Lr})(\bar{u}_{Ls} \gamma_\mu u_{Lt})$
$\mathcal{O}_{dd}^{V,LL}$	$(\bar{d}_{Lp} \gamma^\mu d_{Lr})(\bar{d}_{Ls} \gamma_\mu d_{Lt})$
$\mathcal{O}_{ud}^{V1,LL}$	$(\bar{u}_{Lp} \gamma^\mu u_{Lr})(\bar{d}_{Ls} \gamma_\mu d_{Lt})$
$\mathcal{O}_{ud}^{V8,LL}$	$(\bar{u}_{Lp} \gamma^\mu T^A u_{Lr})(\bar{d}_{Ls} \gamma_\mu T^A d_{Lt})$

$(\overline{R}R)(\overline{R}R)$	
$\mathcal{O}_{ee}^{V,RR}$	$(\bar{e}_{Rp} \gamma^\mu e_{Rr})(\bar{e}_{Rs} \gamma_\mu e_{Rt})$
$\mathcal{O}_{eu}^{V,RR}$	$(\bar{e}_{Rp} \gamma^\mu e_{Rr})(\bar{u}_{Rs} \gamma_\mu u_{Rt})$
$\mathcal{O}_{ed}^{V,RR}$	$(\bar{e}_{Rp} \gamma^\mu e_{Rr})(\bar{d}_{Rs} \gamma_\mu d_{Rt})$
$\mathcal{O}_{uu}^{V,RR}$	$(\bar{u}_{Rp} \gamma^\mu u_{Rr})(\bar{u}_{Rs} \gamma_\mu u_{Rt})$
$\mathcal{O}_{dd}^{V,RR}$	$(\bar{d}_{Rp} \gamma^\mu d_{Rr})(\bar{d}_{Rs} \gamma_\mu d_{Rt})$
$\mathcal{O}_{ud}^{V1,RR}$	$(\bar{u}_{Rp} \gamma^\mu u_{Rr})(\bar{d}_{Rs} \gamma_\mu d_{Rt})$
$\mathcal{O}_{ud}^{V8,RR}$	$(\bar{u}_{Rp} \gamma^\mu T^A u_{Rr})(\bar{d}_{Rs} \gamma_\mu T^A d_{Rt})$

$(\overline{L}L)(\overline{R}R)$	
$\mathcal{O}_{\nu e}^{V,LR}$	$(\bar{\nu}_{Lp} \gamma^\mu \nu_{Lr})(\bar{e}_{Rs} \gamma_\mu e_{Rt})$
$\mathcal{O}_{ee}^{V,LR}$	$(\bar{e}_{Lp} \gamma^\mu e_{Lr})(\bar{e}_{Rs} \gamma_\mu e_{Rt})$
$\mathcal{O}_{\nu u}^{V,LR}$	$(\bar{\nu}_{Lp} \gamma^\mu \nu_{Lr})(\bar{u}_{Rs} \gamma_\mu u_{Rt})$
$\mathcal{O}_{\nu d}^{V,LR}$	$(\bar{\nu}_{Lp} \gamma^\mu \nu_{Lr})(\bar{d}_{Rs} \gamma_\mu d_{Rt})$
$\mathcal{O}_{eu}^{V,LR}$	$(\bar{e}_{Lp} \gamma^\mu e_{Lr})(\bar{u}_{Rs} \gamma_\mu u_{Rt})$
$\mathcal{O}_{ed}^{V,LR}$	$(\bar{e}_{Lp} \gamma^\mu e_{Lr})(\bar{d}_{Rs} \gamma_\mu d_{Rt})$
$\mathcal{O}_{ue}^{V,LR}$	$(\bar{u}_{Lp} \gamma^\mu u_{Lr})(\bar{e}_{Rs} \gamma_\mu e_{Rt})$
$\mathcal{O}_{de}^{V,LR}$	$(\bar{d}_{Lp} \gamma^\mu d_{Lr})(\bar{e}_{Rs} \gamma_\mu e_{Rt})$
$\mathcal{O}_{\nu edu}^{V,LR}$	$(\bar{\nu}_{Lp} \gamma^\mu e_{Lr})(\bar{d}_{Rs} \gamma_\mu u_{Rt}) + h.c.$
$\mathcal{O}_{uu}^{V1,LR}$	$(\bar{u}_{Lp} \gamma^\mu u_{Lr})(\bar{u}_{Rs} \gamma_\mu u_{Rt})$
$\mathcal{O}_{uu}^{V8,LR}$	$(\bar{u}_{Lp} \gamma^\mu T^A u_{Lr})(\bar{u}_{Rs} \gamma_\mu T^A u_{Rt})$
$\mathcal{O}_{ud}^{V1,LR}$	$(\bar{u}_{Lp} \gamma^\mu u_{Lr})(\bar{d}_{Rs} \gamma_\mu d_{Rt})$
$\mathcal{O}_{ud}^{V8,LR}$	$(\bar{u}_{Lp} \gamma^\mu T^A u_{Lr})(\bar{d}_{Rs} \gamma_\mu T^A d_{Rt})$
$\mathcal{O}_{du}^{V1,LR}$	$(\bar{d}_{Lp} \gamma^\mu d_{Lr})(\bar{u}_{Rs} \gamma_\mu u_{Rt})$
$\mathcal{O}_{du}^{V8,LR}$	$(\bar{d}_{Lp} \gamma^\mu T^A d_{Lr})(\bar{u}_{Rs} \gamma_\mu T^A u_{Rt})$
$\mathcal{O}_{dd}^{V1,LR}$	$(\bar{d}_{Lp} \gamma^\mu d_{Lr})(\bar{d}_{Rs} \gamma_\mu d_{Rt})$
$\mathcal{O}_{dd}^{V8,LR}$	$(\bar{d}_{Lp} \gamma^\mu T^A d_{Lr})(\bar{d}_{Rs} \gamma_\mu T^A d_{Rt})$
$\mathcal{O}_{uddu}^{V1,LR}$	$(\bar{u}_{Lp} \gamma^\mu d_{Lr})(\bar{d}_{Rs} \gamma_\mu u_{Rt}) + h.c.$
$\mathcal{O}_{uddu}^{V8,LR}$	$(\bar{u}_{Lp} \gamma^\mu T^A d_{Lr})(\bar{d}_{Rs} \gamma_\mu T^A u_{Rt}) + h.c.$

$(\overline{L}R)(\overline{L}R) + h.c.$	
$\mathcal{O}_{ee}^{S,RR}$	$(\bar{e}_{Lp} e_{Rr})(\bar{e}_{Ls} e_{Rt})$
$\mathcal{O}_{eu}^{S,RR}$	$(\bar{e}_{Lp} e_{Rr})(\bar{u}_{Ls} u_{Rt})$
$\mathcal{O}_{eu}^{T,RR}$	$(\bar{e}_{Lp} \sigma^{\mu\nu} e_{Rr})(\bar{u}_{Ls} \sigma_{\mu\nu} u_{Rt})$
$\mathcal{O}_{ed}^{S,RR}$	$(\bar{e}_{Lp} e_{Rr})(\bar{d}_{Ls} d_{Rt})$
$\mathcal{O}_{ed}^{T,RR}$	$(\bar{e}_{Lp} \sigma^{\mu\nu} e_{Rr})(\bar{d}_{Ls} \sigma_{\mu\nu} d_{Rt})$
$\mathcal{O}_{\nu edu}^{S,RR}$	$(\bar{\nu}_{Lp} e_{Rr})(\bar{d}_{Ls} u_{Rt})$
$\mathcal{O}_{\nu edu}^{T,RR}$	$(\bar{\nu}_{Lp} \sigma^{\mu\nu} e_{Rr})(\bar{d}_{Ls} \sigma_{\mu\nu} u_{Rt})$
$\mathcal{O}_{uu}^{S1,RR}$	$(\bar{u}_{Lp} u_{Rr})(\bar{u}_{Ls} u_{Rt})$
$\mathcal{O}_{uu}^{S8,RR}$	$(\bar{u}_{Lp} T^A u_{Rr})(\bar{u}_{Ls} T^A u_{Rt})$
$\mathcal{O}_{ud}^{S1,RR}$	$(\bar{u}_{Lp} u_{Rr})(\bar{d}_{Ls} d_{Rt})$
$\mathcal{O}_{ud}^{S8,RR}$	$(\bar{u}_{Lp} T^A u_{Rr})(\bar{d}_{Ls} T^A d_{Rt})$
$\mathcal{O}_{dd}^{S1,RR}$	$(\bar{d}_{Lp} d_{Rr})(\bar{d}_{Ls} d_{Rt})$
$\mathcal{O}_{dd}^{S8,RR}$	$(\bar{d}_{Lp} T^A d_{Rr})(\bar{d}_{Ls} T^A d_{Rt})$
$\mathcal{O}_{uddu}^{S1,RR}$	$(\bar{u}_{Lp} d_{Rr})(\bar{d}_{Ls} u_{Rt})$
$\mathcal{O}_{uddu}^{S8,RR}$	$(\bar{u}_{Lp} T^A d_{Rr})(\bar{d}_{Ls} T^A u_{Rt})$

$(\overline{L}R)(\overline{R}L) + h.c.$	
$\mathcal{O}_{eu}^{S,RL}$	$(\bar{e}_{Lp} e_{Rr})(\bar{u}_{Rs} u_{Lt})$
$\mathcal{O}_{ed}^{S,RL}$	$(\bar{e}_{Lp} e_{Rr})(\bar{d}_{Rs} d_{Lt})$
$\mathcal{O}_{\nu edu}^{S,RL}$	$(\bar{\nu}_{Lp} e_{Rr})(\bar{d}_{Rs} u_{Lt})$

Table A.4: LEFT operators of dimension three and five, as well as LEFT operators of dimension six that conserve baryon and lepton number, reproduced from Ref. [29].

A.2 Four-quark operators and $\Delta F = 2$ observables

In this Appendix we recollect the list of four-quark operators generated at tree or loop level by the mediators considered in section 2.2.3. The relevant operators are

$$\begin{aligned}
\mathcal{O}_{qq}^{(1)ijkl} &= \left(\bar{q}_L^i \gamma_\mu q_L^j\right)\left(\bar{q}_L^k \gamma^\mu q_L^l\right) \ , \\
\mathcal{O}_{qq}^{(3)ijkl} &= \left(\bar{q}_L^i \gamma_\mu \sigma_a q_L^j\right)\left(\bar{q}_L^k \gamma^\mu \sigma_a q_L^l\right) \ , \\
\mathcal{O}_{dd}^{ijkl} &= \left(\bar{d}_R^i \gamma_\mu d_R^j\right)\left(\bar{d}_R^k \gamma^\mu d_R^l\right) \ , \\
\mathcal{O}_{qd}^{(1)ijkl} &= \left(\bar{q}_L^i \gamma_\mu q_L^j\right)\left(\bar{d}_R^k \gamma^\mu d_R^l\right) \ ,
\end{aligned} \tag{A.91}$$

and are highly constrained by $\Delta F = 2$ observables like meson-antimeson mixing. These operators are generated at tree level by the exchange of colorless vector mediator like V' or Z'. The matching of the non-vanishing corresponding SMEFT coefficients reads

$$C_{qq}^{(3)ijkl} = -\frac{1}{8}\frac{g_q^{ij} g_q^{kl}}{M_{V'}^2} \tag{A.92}$$

for the Lagrangian eq. (2.37) and

$$C_{qq}^{(1)ijkl} = -\frac{1}{2}\frac{g_L^{ij} g_L^{kl}}{M_{Z'}^2}, \quad C_{qd}^{(1)ijkl} = -\frac{g_L^{ij} g_R^{kl}}{M_{Z'}^2}, \quad C_{dd}^{ijkl} = -\frac{1}{2}\frac{g_R^{ij} g_R^{kl}}{M_{Z'}^2} \ , \tag{A.93}$$

for the Lagrangian eq. (2.45). Leptoquarks instead generate four-quark operators only at loop level, arising from the same interaction terms shown in table 2.14. One can easily compute the non vanishing SMEFT coefficient of the loop-induced four-quark operators for scalar leptoquarks, getting by direct calculation [152, 160, 451]

$$C_{qq}^{(1)ijkl} = C_{qq}^{(3)ijkl} = -\frac{\lambda_{i\tau}\lambda_{j\tau}^* \lambda_{k\tau}\lambda_{l\tau}^*}{256\pi^2 m_{LQ}^2} \quad \text{for } S_1 \ , \tag{A.94}$$

$$C_{qq}^{(1)ijkl} = 9C_{qq}^{(3)ijkl} = -\frac{9\lambda_{i\tau}\lambda_{j\tau}^* \lambda_{k\tau}\lambda_{l\tau}^*}{256\pi^2 m_{LQ}^2} \quad \text{for } S_3 \ , \tag{A.95}$$

$$C_{dd}^{ijkl} = -\frac{\lambda_{i\tau}\lambda_{j\tau}^* \lambda_{k\tau}\lambda_{l\tau}^*}{64\pi^2 m_{LQ}^2} \quad \text{for } \tilde{R}_2 \ ,$$

while the loop diagram with vector LQ is UV divergent and requires a complete UV model to be calculable. However, in order to evaluate the impact of the four-quark operators on the phenomenological analysis we aim to perform, we estimate the loop-induced SMEFT coefficients by considering just the $g_{\mu\nu}$-term of the vector LQ propagator inside the loop, which leads to a finite, although incomplete, result (the same procedure has been followed for example in Ref. [452]). The matching of the non-vanishing corresponding SMEFT coefficients thus evaluated then reads

$$C_{qq}^{(1)ijkl} = 9C_{qq}^{(3)ijkl} = -\frac{9\lambda_{i\tau}\lambda_{j\tau}^* \lambda_{k\tau}\lambda_{l\tau}^*}{64\pi^2 m_{LQ}^2} \quad \text{for } U_3 \ ,$$

$$C_{dd}^{ijkl} = -\frac{\lambda_{i\tau}\lambda_{j\tau}^* \lambda_{k\tau}\lambda_{l\tau}^*}{16\pi^2 m_{LQ}^2} \quad \text{for } V_2 \ . \tag{A.96}$$

We employ the expressions of NP contributions to meson mixing observables from Ref. [71]. Notice that they are provided in terms of WCs evolved up to a scale $\mu = 5$ TeV, while we set our NP scale at 1 TeV. We neglect this difference, hiding the small effect in the uncertainty of working with a leading log resummation in the RG evolution. For the numerical constraints we take the results of the fit, updated in summer 2023, by the UTfit collaboration [196, 197].

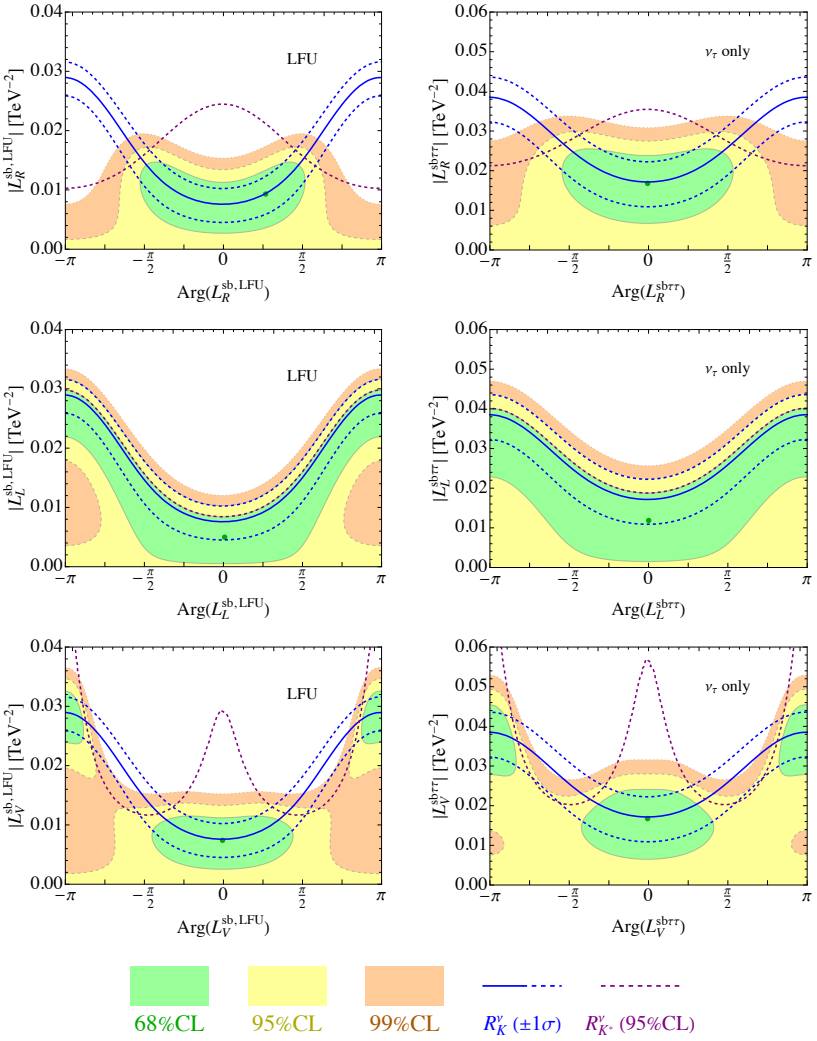


Figure A.7: 2D fit in the $\text{Arg}(L^{sb\alpha\beta}) - |L^{sb\alpha\beta}|$ for NP coupled to right-handed, left-handed, vector quark current while assuming LFU (on the left) or coupling only to tau neutrinos (on the right). The solid (dashed) blue line refers to the central value ($\pm1\sigma$ value) of $R^\nu_{K^+}$ observable. The dashed purple line refers to the upper limit at 95% of $R^\nu_{K^*}$ observable.

A.3 Fits of $b \to s\nu\bar{\nu}$

In this Appendix we discuss the 2D fits of the EFT coefficients related to the $b \to s\nu\bar{\nu}$ transition, independently on the ROFV assumption. While, at the level of LEFT the EFT

coefficient responsible for $b \to s\nu\bar{\nu}$ transitions does not impact other classes of observables, in case of the SMEFT it does. We discuss each case individually in the following.

A.3.1 LEFT

At the level of the LEFT, non-trivial correlations among the coefficients of different operators are absent, so we have to consider only $B \to K^{(*)}\nu\bar{\nu}$ observables. We study scenarios of NP coupled to right, left or vector quark current while assuming either LFU or only tau flavor on the lepton side. We plot in Fig. A.7 the regions at 1σ, 2σ and 3σ in the plane $\text{Arg}(L^{sb\alpha\beta}) - |L^{sb\alpha\beta}|$. The coefficient explicitly reads

$$L^{sb\alpha\beta}_{L,R,V} = C_{L,R,V}\ e^{i\alpha_{sb}}\ \cos\theta \sin\theta \sin\phi \times \begin{cases} \delta^{\alpha\beta} & \text{for LFU ,} \\ \delta^{\tau\alpha}\delta^{\tau\beta} & \text{for only tau flavor ,} \end{cases} \tag{A.97}$$

which means that, for any given θ and ϕ, the overall coefficient C and the phase α_{sb} are univocally determined. We note that in all the cases we consider the fits favour a real and positive value of the LEFT coefficient. We thus evaluate the best-fit value at vanishing complex phase and report the obtained values in the main text.

A.3.2 SMEFT and simplified models

In this Section, we discuss the 2D fits of the coefficient related to the $b \to s\nu\bar{\nu}$ transition in the SMEFT. Among the observables of the fit, additionally to the LEFT case, we must include also the $B_s \to \mu^+\mu^-$ decay, the $R_{K^{(*)}}$ ratios and, where explicitly specified, the ΔM_{B_s} meson mass mixing, whose information would otherwise be lost as they are mainly affected, trough the correlations coming from the SMEFT or the underlying UV structure, by the same SMEFT coefficients related to $R^{\nu}_{K^{(*)}}$.

Vector-like quarks

We list in table A.5 some examples of heavy BSM states, such as vector-like quarks, that can generate Higgs-quark coefficients in the EFT when integrated out. The 2D fits in the $\text{Arg}(C^{(+)sb}_{Hq}(C^{sb}_{Hd})) - |C^{(+)sb}_{Hq}(C^{sb}_{Hd})|$ plane are illustrated in fig. A.8, displaying also the bounds from $B_s \to \mu^+\mu^-$ and ΔM_{B_s}. As can be seen, none of these models allows to fit the measured value of R^K_ν.

Vector triplet V' and vector singlet Z'

We discussed in the main text the case of a vector triplet V' and the vector singlets $Z'_{L,R}$ coupled to the third family of leptons, see section 2.2.3. Here, instead, we illustrate in fig. A.9 the 2D fits for a V' and a Z'_L that are universally coupled to all the lepton families. We do not show the Z'_R, as this case is similar to V'. Indeed, they generate a contribution of the same sign to the Wilson Coefficients in eq. (A.47), getting a strong contraint from the $B_s \to \mu^+\mu^-$ decay. As a result, we find these UV states to be unable to address the Belle II excess. The LFU Z'_L could fit reasonably well the R^{ν}_K excess, with a large phase in the EFT coefficient. This phase implies constraints from B_s-mixing even stronger than those discussed in the main text for V' or Z's only coupled to tau doublet, therefore we do not consider it further.

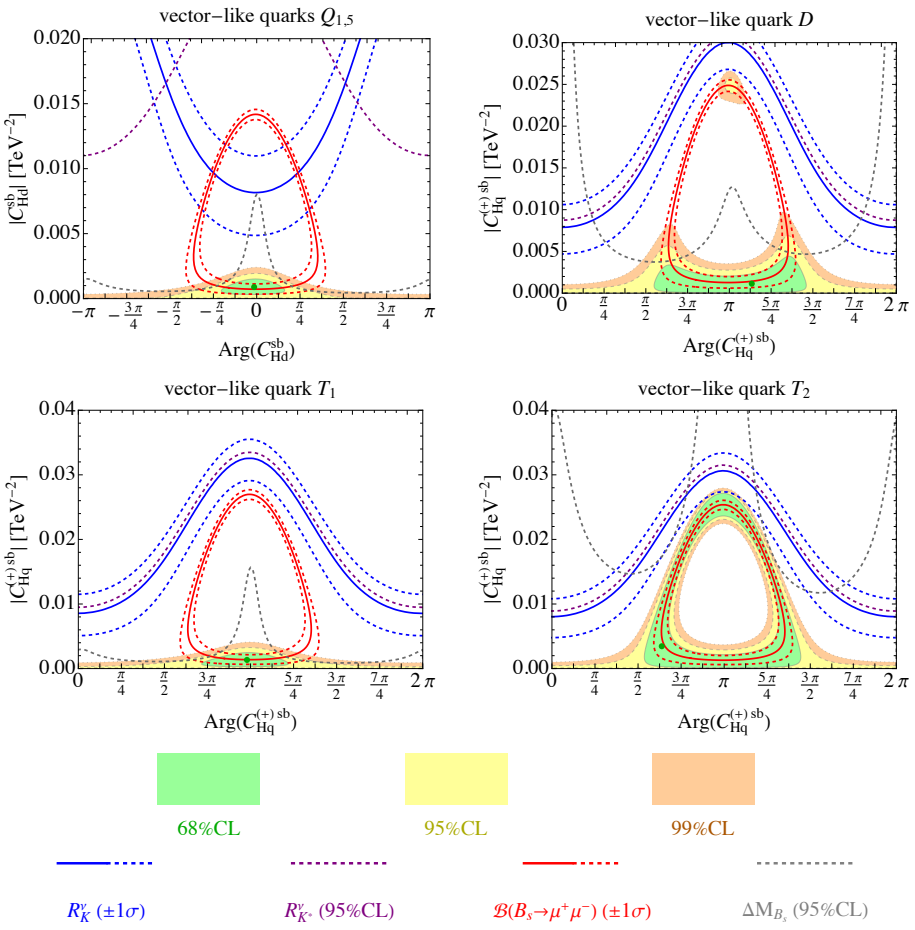


Figure A.8: 2D fit in the $|C_{Hq}^{(+)sb}(C_{Hd}^{sb})| - \text{Arg}(C_{Hq}^{(+)sb}(C_{Hd}^{sb}))$ plane for several vector-like quarks models. The solid (dashed) blue lines refer to the central value ($\pm1\sigma$ contours) of the $R_{K^+}^\nu$ observable. The solid (dashed) red lines refer to the central value ($\pm1\sigma$ contours) of the $B_s \to \mu^+\mu^-$ observable. The region above the dashed gray lines is excluded at 95% from the ΔM_{B_s} observable. The dashed purple line refers to the upper limit at 95% of $R_{K^*}^\nu$ observable.

Simplified model	**Spin**	**SM irrep**	**SMEFT couplings**
D	1/2	$(\mathbf{3},\mathbf{1},-1/3)$	$C_{Hq}^{(1)} = C_{Hq}^{(3)}$
T_1	1/2	$(\mathbf{3},\mathbf{3},-1/3)$	$C_{Hq}^{(1)} = -3C_{Hq}^{(3)}$
T_2	1/2	$(\mathbf{3},\mathbf{3},2/6)$	$C_{Hq}^{(1)} = 3C_{Hq}^{(3)}$
Q_1	1/2	$(\mathbf{3},\mathbf{2},1/6)$	C_{Hd}
Q_5	1/2	$(\mathbf{3},\mathbf{2},-5/6)$	C_{Hd}

Table A.5: List of vector-like quark mediators and the corresponding Higgs-quark couplings generated when when integrating them out at the tree level.

Leptoquarks

Regard the LQs, since in our analysis we choose to fix the mass (at 2 TeV), the SMEFT coefficient of the four-quark operator $\mathcal{O}_{qq}^{(1,3)\tau\tau sb}$ ($\mathcal{O}_{dd}^{\tau\tau sb}$), see appendix A.2, turns out to be

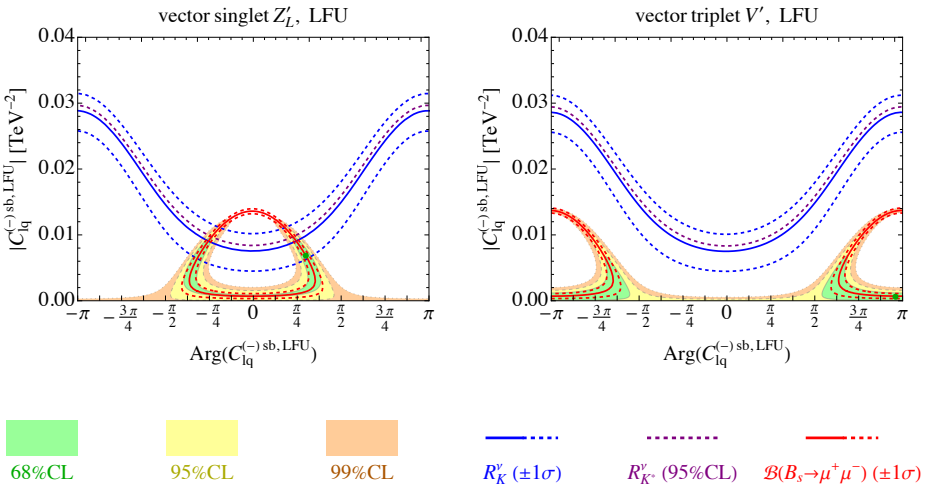


Figure A.9: 2D fit in the $\text{Arg}(C_{lq}^{(-)\alpha\beta sb}) - |C_{lq}^{(-)\alpha\beta sb}|$ for Z'_L (on the left) and for V' (on the right) assuming LFU. The solid (dashed) blue line refers to the central value ($\pm1\sigma$ value) of $R^\nu_{K^+}$ observable. The solid (dashed) red lines refer to the central value ($\pm1\sigma$ contours) of the $B_s \to \mu^+\mu^-$ observable. The dashed purple line refers to the upper limit at 95% of $R^\nu_{K^*}$ observable.

exactly proportional to the square of the semileptonic ones $\mathcal{O}_{lq}^{(1,3)\tau\tau sb}$ ($\mathcal{O}_{ld}^{\tau\tau sb}$), e.g.:

$$C_{lq}^{(1,3)\tau\tau sb} \propto \lambda_{b\tau}\lambda^*_{s\tau}\,, \qquad C_{qq}^{(1,3)\tau\tau sb} \propto (\lambda_{b\tau}\lambda^*_{s\tau})^2 \propto \left(C_{lq}^{(1,3)\tau\tau sb}\right)^2\,. \tag{A.98}$$

Fixing the semileptonic operator to fit R^ν_K would therefore fix also the coefficient responsible for B_s mixing. Hence, we have to include ΔM_{B_s} among the observables of the 2D fits. We plot in fig. A.10 the resulting 1σ, 2σ and 3σ regions of the 2D fits for the LQs simplified models. Note that $\tilde{R}_2$ and V_2 generate the same semileptonic coefficient $C_{ld}^{\tau\tau sb}$ and thus same four-quark coefficient $C_{dd}^{\tau\tau sb}$ at fixed value of the mass, so they produce the same 2D fit. We conclude that the best scenarios appear to be $\tilde{R}_2$ and V_2, slightly favoured over S_1 and S_3, while U_3 has to be discarded. This result is in agreement with the results of the LEFT analysis where we observe a preference over NP coupled to right-handed quarks. Hence, assuming for simplicity the coefficient to be real, we report the best-fit value of $\tilde{R}_2$ and V_2, together with S_1 as an example of LQ coupled to left-handed quarks, in the main text.

A.3.3 LNV operators

The role of $\Delta L = 2$ operators in the context of rare meson decays has been studied in several works: implications for kaon decays have been considered in Refs. [453, 454], while Ref. [455] discussed their impact on B-meson (semi)invisible modes. Recently, Ref. [456] provided a comprehensive study of dim-7 $\Delta L = 2$ SMEFT operators, considering both low-energy observables and high-energy collider limits. Following the analysis of [456], we update the limits from $B \to K^{(*)}\nu\bar{\nu}$ in light of the Belle II measurement.

At the level of LEFT, the effective (dim-6) operators relevant for $d_i \to d_j\nu\nu$ transitions

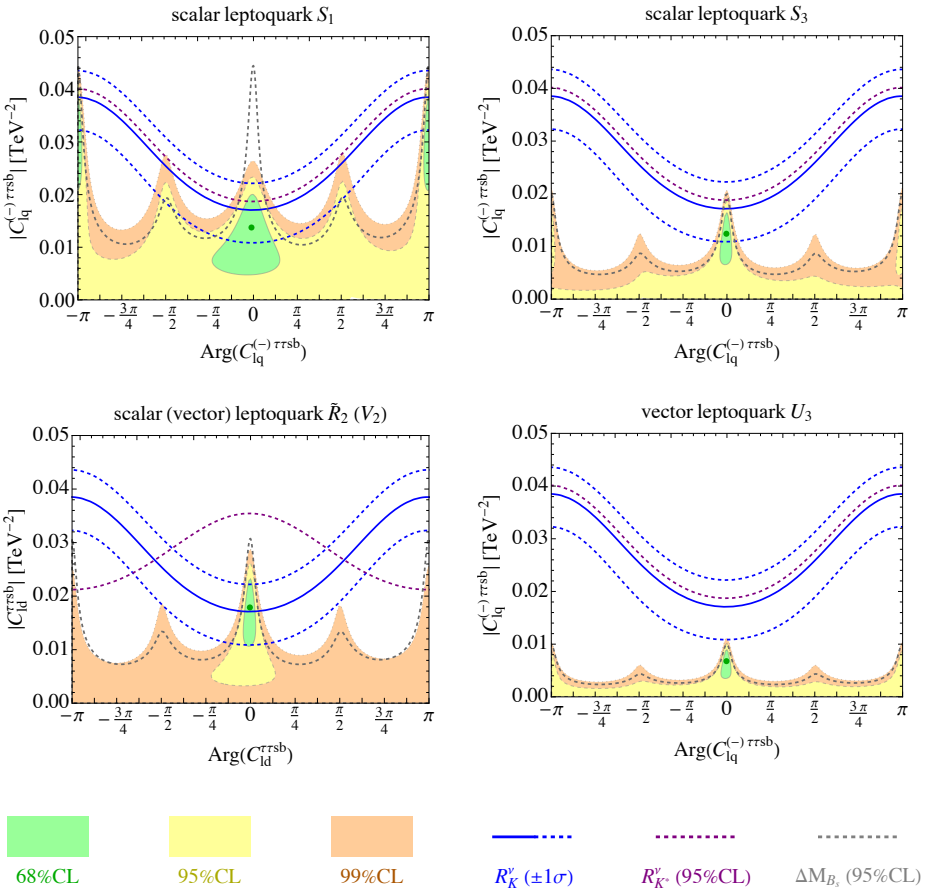


Figure A.10: 2D fit in the $\text{Arg}(C_{lq}^{(-)\tau\tau sb}(C_{ld}^{\tau\tau sb})) - |C_{lq}^{(-)\tau\tau sb}(C_{ld}^{\tau\tau sb})|$ plane assuming coupling only to tau sector. UV mediators that can give rise to these effective operators are outlined. The solid (dashed) blue lines refer to the central value ($\pm1\sigma$ contours) of the $R_{K^+}^\nu$ observable. The dashed purple line refers to the upper limit at 95% of $R_{K^*}^\nu$ observable. The region above the dashed gray line is excluded at 95% by ΔM_{B_s} observable.

are:

$$\begin{aligned}
\mathcal{O}_{d\nu}^{S,LL} &= (\overline{d_R} d_L)(\overline{\nu^C}\nu) + \text{h.c.}\,, \\
\mathcal{O}_{d\nu}^{S,LR} &= (\overline{d_L} d_R)(\overline{\nu^C}\nu) + \text{h.c.}\,, \\
\mathcal{O}_{d\nu}^{T,LL} &= (\overline{d_R}\sigma^{\mu\nu} d_L)(\overline{\nu^C}\sigma_{\mu\nu}\nu) + \text{h.c.}\,,
\end{aligned} \tag{A.99}$$

employing the basis of Ref. [38]. The dim-5 dipole operator $\overline{\nu^C}\sigma_{\mu\nu}\nu F^{\mu\nu}$is not considered, as it can only appear with the down quark dipole operator $\overline{d_L}\sigma^{\mu\nu} d_R F_{\mu\nu}$, bringing a double loop suppression. In addition, there are stringent bounds from neutrino magnetic moment searches. We also neglect the operator $\mathcal{O}_{d\nu}^{S,LR}$, since it is not generated at tree level by any dim-7 $\Delta L = 2$ SMEFT operator. The tree level matching expressions for the remaining two coefficients are:

$$\begin{aligned}
L_{d\nu,prst}^{S,LL} &= -\frac{\sqrt{2}v}{8} V_{xr} \left(C_{\bar{d}LQLH1}^{ptxs} + C_{\bar{d}LQLH1}^{psxt} \right) , \\
L_{d\nu,prst}^{T,LL} &= -\frac{\sqrt{2}v}{32} V_{xr} \left(C_{\bar{d}LQLH1}^{ptxs} - C_{\bar{d}LQLH1}^{psxt} \right) ,
\end{aligned} \tag{A.100}$$

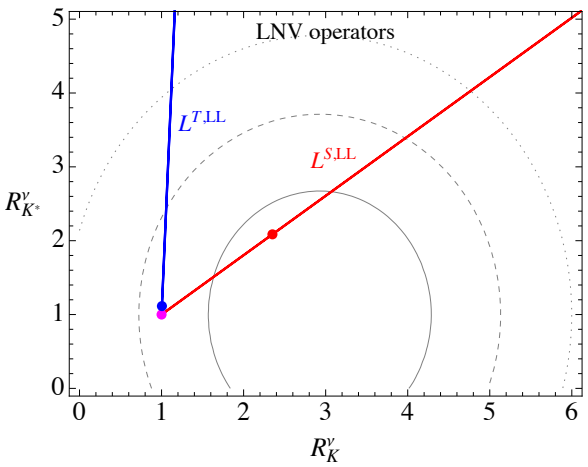


Figure A.11: Fit of available data on all $B \to K^{(*)}\nu\bar{\nu}$ channels. Solid, dashed, and dotted gray lines represent 68, 95, and 99% CL contours.

where the dim-7 SMEFT operator appearing in these expressions is

$$O^{prst}_{\bar{d}LQLH1} = \epsilon_{ji}\epsilon_{mn}\left(\overline{d}_p L^i_r\right)\left(\overline{Q^c_s}^j L^m_t\right) H^n \,. \tag{A.101}$$

The dependence of the $B \to K^{(*)}\nu\nu$ branching ratios on the LNV LEFT coefficients is:

$$\begin{aligned}
\mathcal{B}(B^+ \to K^+\nu_\alpha\nu_\beta) &= \frac{10^{10}\,\mathrm{GeV}^2}{1+\delta^\beta_\alpha}\Big[4.01\left(|L^{S,LL}_{d\nu,sb\alpha\beta} + L^{S,LR}_{d\nu,sb\alpha\beta}|^2 + \mathrm{perm}\right) \\
&\qquad\qquad 6.15\left(|L^{T,LL}_{d\nu,sb\alpha\beta}|^2 + \mathrm{perm}\right)\Big] \,, \\
\mathcal{B}(B^0 \to K^{*0}\nu_\alpha\nu_\beta) &= \frac{10^{10}\,\mathrm{GeV}^2}{1+\delta^\beta_\alpha}\Big[1.49\left(|L^{S,LL}_{d\nu,sb\alpha\beta} - L^{S,LR}_{d\nu,sb\alpha\beta}|^2 + \mathrm{perm}\right) \\
&\qquad\qquad 72.3\left(|L^{T,LL}_{d\nu,sb\alpha\beta}|^2 + \mathrm{perm}\right)\Big] \,,
\end{aligned} \tag{A.102}$$

where the EFT coefficients are evaluated at the m_b scale. The QCD RG evolution up to m_Z is given by: $L^{S,LL}_{d\nu}(m_b) = 1.137 L^{S,LL}_{d\nu}(m_Z)$, $L^{S,LR}_{d\nu}(m_b) = 1.137 L^{S,LR}_{d\nu}(m_Z)$, and $L^{T,LL}_{d\nu}(m_b) = 0.900 L^{T,LL}_{d\nu}(m_Z)$. The expressions in eq. (A.102) have been derived integrating the differential rate of Ref. [456] in q^2. For the K mode we employed the form factors fit from Ref. [48], while for the K^* mode we used the results from Ref. [437].

The dependence of the two modes on the LEFT coefficients is shown in fig. A.11. We see that the scalar operator allows a better fit than the tensor one, the preferred values being $L^{S,LL}_{d\nu,sb\tau\tau}(m_b) = (1.22 \pm 0.34) \times 10^{-8}\mathrm{GeV}^{-2}$ (the best-fit point is shown as a red dot). In terms of the dim-7 SMEFT operator, evaluated at the m_Z scale, the best-fit point corresponds to a scale of $|C^{sb\tau\tau}_{\bar{d}LQLH1}|^{-1/3} \approx 1.6$ TeV. The tensor operator (blue line and blue dot for the best-fit point) does not improve the fit over the Standard Model (magenta dot).

Appendix B

B.1 Derivation of the Z/γ PDF at order α^2

In this appendix we review the analytical computation of the $f_{Z/\gamma}(x, Q^2)$ PDF by solving iteratively the DGLAP equations at $\mathcal{O}(\alpha^2)$. We focus here on the positive polarization, but analogous calculation steps can be performed for the negative helicity state, for which the results are reported at the end of the appendix.

We compute the PDF at next-to-leading-order iteratively: we substitute in the DGLAP equation of $f_{Z/\gamma_+}(x, Q^2)$ the leading order $\mathcal{O}(\alpha)$ expressions of the other PDFs appearing therein. Namely, we study the equation

$$\begin{aligned}\frac{df^{(\alpha^2)}_{Z/\gamma_+}(x,Q^2)}{dt} &= \frac{\alpha_{\gamma 2}(t)}{2\pi} 2c_W P^V_{V_+V_\pm} \otimes f^{(\alpha)}_{W^-_\pm} + \frac{\alpha_{\gamma 2}(t)}{2\pi}\frac{c_{2W}(t)}{c_W(t)} P^h_{V_+h} \otimes f^{(\alpha)}_{W^-_L} + \\ &+ \frac{\alpha_{\gamma 2}(t)}{2\pi}\frac{2}{c_W(t)}(-1)\left[Q^Z_{\mu_L} P^f_{V_+f_L} \otimes f^{(\alpha)}_{\mu_L} + Q^Z_{\mu_R} P^f_{V_-f_L} \otimes f^{(\alpha)}_{\mu_R}\right],\end{aligned} \tag{B.1}$$

where we consider the leading order expressions:

$$\begin{aligned}
f^{(\alpha)}_{W^-_+}(x,Q^2) &\approx \frac{\alpha_2}{8\pi}\frac{(1-x)^2}{x}(t-t_Z)\,,\\
f^{(\alpha)}_{W^-_-}(x,Q^2) &\approx \frac{\alpha_2}{8\pi}\frac{1}{x}(t-t_Z)\,,\\
f^{(\alpha)}_{W^-_L}(x,Q^2) &\approx \frac{\alpha_2}{8\pi}\frac{1-x}{x}\,,\\
f^{(\alpha)}_{\mu_L}(x,Q^2) &= +\frac{1}{2}\delta(1-x) + \frac{\alpha_2}{16\pi}\delta(1-x)\left(3(t-t_Z)-(t-t_Z)^2\right) + \\
&\quad + \frac{1}{4\pi}\left(\frac{1+x^2}{1-x}+\frac{3}{2}\delta(1-x)\right)\left(\alpha_\gamma t + \alpha_2\left(\frac{(1-2s^2_W)^2}{4c^2_W}\right)(t-t_Z)\right)\,,\\
f^{(\alpha)}_{\mu_R}(x,Q^2) &= +\frac{1}{2}\delta(1-x) + \frac{1}{4\pi}\left(\frac{1+x^2}{1-x}+\frac{3}{2}\delta(1-x)\right)\left(\alpha_\gamma t + \alpha_2\frac{s^4_W}{c^2_W}(t-t_Z)\right)\,,
\end{aligned} \tag{B.2}$$

and we defined $t = \log(Q^2/m^2_\mu)$ and $t_Z = \log(m^2_Z/m^2_\mu)$. These leading order formulas can be easily derived and are often used in literature, see e.g. Ref. [282] for a detailed introduction.

Regarding the vector boson PDFs, we employ some simplifying approximations. First, all the electroweak ISR effects are considered starting from a unique EW scale, that we identify as m_Z (for both collinear emissions involving W and Z boson vertices). In addition,

the above expressions are valid in the limit of high energy $Q^2 \gg m_Z^2$ and small x. These approximations do not jeopardise the goal of section 3.2.1, since the most important effects that arise at NLO are anyway captured (see fig. 3.5), allowing for an analytic understanding of the NLO enhancement. In the rest of the paper, full numerical solutions of DGLAP equations from LePDF [282] were used to compute predictions.

In the next subsections, we discuss in more detail the convolutions appearing in eq. (B.1), the origin of the Sudakov logarithms, and we display the full analytic results. We split the computation in three pieces, depending on the states involved in the initial splitting: $P^V_{VV}, P^f_{Vf}, P^h_{Vh}$. We follow the notation and conventions of Ref. [282], to which we refer the reader for a complete introduction.

P_{VV} contribution at $\mathcal{O}(\alpha^2)$

Here we discuss the contribution to eq. (B.1) due to the collinear emission of a $W^-_\pm$ gauge boson, as depicted in fig. 3.6. The convolution with the W boson PDF reads:

$$P^V_{V_+V_\pm} \otimes f^{(\alpha)}_{W^-_\pm} = \int_x^1 \frac{dz}{z} \frac{(1-z)^3}{z} f^{(\alpha)}_{W^-_-}\left(\frac{x}{z}, Q^2\right) + \int_x^{z_{max}(Q)} \frac{dz}{z} \frac{1+z^4}{z(1-z)} f^{(\alpha)}_{W^-_+}\left(\frac{x}{z}, Q^2\right) . \quad \text{(B.3)}$$

Noticeably, following Ref. [277], we set the upper limit in the second integral to $z_{max}(Q) = 1 - m_Z/Q$. This plays the role of an explicit IR cutoff to the $1/(1-z)$ pole, alternative to the usual +-distribution prescription. This procedure can be used in processes where the emitted radiation (e.g. a $W^\pm$ boson) changes the $\mathrm{SU}(2)_L$ component of the initial state and allows to reproduce, to a double log approximation, the Sudakov factor for ISR expected in these cases. More discussions on these effects can be found in [264, 271, 274, 277, 278]. The $(1-z)$ pole in this splitting, responsible for the Sudakov log, hints at the importance of the soft region $z \approx 1$. Thus, an interesting future development could be the application of the formalism of Ref. [289] to this calculation.

Upon performing the integrals in eq. (B.3) and further integrating over t, the total contribution to the NLO Z/γ_+ PDF is:

$$\begin{aligned} f^{(\alpha^2)P_{VV}}_{Z/\gamma_+}(x,Q) &= \frac{\alpha_2\alpha_{\gamma 2}}{96\pi^2 x}(t-t_Z)^2\, c_W \cdot \Big[4(t-t_Z)(1-x)^2 + J(x)\Big] , \\ J(x) &= -31 + 60x - 33x^2 + 4x^3 + 12(1-x)^2\log(1-x) - \\ &\quad - 6(2-2x+x^2)\log(x) . \end{aligned} \quad \text{(B.4)}$$

The $\alpha^2(t-t_Z)^3$ terms appearing in this formula contain the Sudakov double logs mentioned above. Due to the gap between the EW scale and the multi-TeV energy scales explored at a MuC, these additional powers of $\log(Q^2/m_Z^2)$ provide a remarkable enhancement. The contribution described in this section is indeed the largest one appearing at α^2 order.

P_{Vf} contribution at $\mathcal{O}(\alpha^2)$

We now discuss the NLO contribution due to the P_{Vf} splitting. The zeroth order $f^{(0)}_{\mu_L} = f^{(0)}_{\mu_R} = \frac{1}{2}\delta(1-x)$ appearing in eq. (B.2) lead to the EVA approximation of the Z/γ PDF that we have already discussed in section 3.2.1. Therefore, we now focus only on the other terms

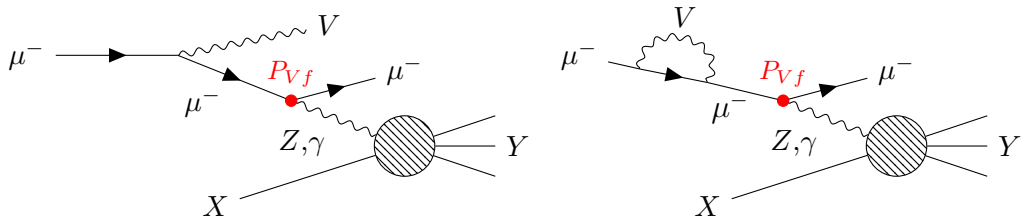


Figure B.1: Sketch of the contribution due to the P_{Vf} splitting at $\mathcal{O}(\alpha^2)$, accounting for a double emission or virtual correction plus one collinear emission.

appearing at $\mathcal{O}(\alpha)$ order in $f_{\mu_{L/R}}$, *i.e.* on the double emission diagrams (or virtual correction plus emission) sketched in fig. B.1. These convolutions in eq. (B.1) are, precisely

$$\begin{aligned} &Q^Z_{\mu_L} P^f_{V_+ f_L} \otimes f^{(\alpha)}_{\mu_L} + Q^Z_{\mu_R} P^f_{V_- f_L} \otimes f^{(\alpha)}_{\mu_R} = \\ &= \Big(-\frac{1}{2} + s_W^2 \Big) \int_x^1 \frac{dz}{z} \frac{(1-z)^2}{z} f^{(\alpha)}_{\mu_L}\Big(\frac{x}{z}, Q^2\Big) + (0 + s_W^2) \int_x^1 \frac{dz}{z} \frac{1}{z} f^{(\alpha)}_{\mu_R}\Big(\frac{x}{z}, Q^2\Big) . \end{aligned} \tag{B.5}$$

After performing these integrals and further integrating over the evolution scale, we find

$$\begin{aligned} f^{(\alpha^2) P_{Vf}}_{Z/\gamma_+}(x, Q^2) = &\frac{\alpha_{\gamma 2}\alpha_2}{48 c_W \pi^2} (t - t_Z)^3 \frac{(1-x)^2}{x} \Big(-\frac{1}{2} + s_W^2 \Big) - \\ &- \frac{\alpha_{\gamma 2}\alpha_2}{64 c_W^3 \pi^2 x} (t - t_Z)^2 S(x) - \frac{\alpha_{\gamma 2}\alpha_\gamma}{16 c_W \pi^2 x} (t^2 - t_Z^2) P(x) , \end{aligned} \tag{B.6}$$

where $P(x)$ and $S(x)$ explicitely read

$$\begin{aligned} S(x) = &-3c_W^2 + 6c_W^2 s_W^2 - x + 6c_W^2 x + 6s_W^2 x - 12 c_W^2 s_W^2 x - 12 s_W^4 x + \\ &+ 16 s_W^6 x + x^2 - 3c_W^2 x^2 - 6 s_W^2 x^2 + 6 c_W^2 s_W^2 x^2 + 12 s_W^4 x^2 - 4 s_W^6 x^2 + \\ &+ 2(-(-1+x)^2 + 6 s_W^2 (-1+x)^2 - 12 s_W^4 (-1+x)^2 + 8 s_W^6 (2 - 2x + \\ &+ x^2)) \log(1-x) - (-1 + 2 s_W^2)^3 (-2 + x) x \log(x) , \\ P(x) = &(-2(-1+x)^2 + 4 s_W^2 (2 - 2x + x^2)) \log(1-x) + x(-1 - s_W^2(-4 + x) + \\ &+ x - (-1 + 2 s_W^2)(-2 + x) \log(x)) . \end{aligned} \tag{B.7}$$

It can be noted the presence of a double Sudakov logarithm $\alpha^2 (t - t_Z)^3$. It is originated in the virtual correction to the μ_L PDF due to a W boson loop, as in the right diagram of fig. B.1.

P_{Vh} contribution at $\mathcal{O}(\alpha^2)$

Finally, we discuss the contribution due to the collinear emission of a longitudinally polarized W_L^- boson, sketched in fig. B.2. Explicitely, the convolution in eq. (B.1) describing this process reads

$$\begin{aligned} P^h_{V_+ h} \otimes f^{(\alpha)}_{W_L^-} &= \int_x^1 \frac{dz}{z} \frac{(1-z)}{z} f^{(\alpha)}_{W_L^-}\Big(\frac{x}{z}, Q^2\Big) = \\ &= \int_x^1 \frac{dz}{z} \frac{(1-z)}{z} \frac{(z-x)\alpha_2}{4\pi x} = -\frac{\alpha_2}{4\pi} \frac{(2 - 2x + (x+1)\log(x))}{x} . \end{aligned} \tag{B.8}$$

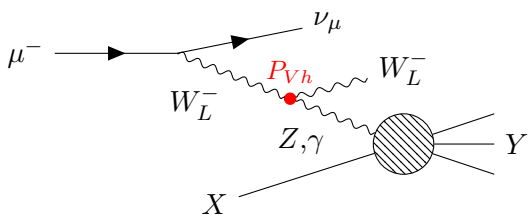


Figure B.2: Sketch of the contribution due to the P_{Vh} splitting at $\mathcal{O}(\alpha^2)$.

Then, the integral over the factorization scale t is trivial and amounts to the overall contribution

$$f_{Z/\gamma_+}^{(\alpha^2)P_{Vh}}(x,Q^2) = -\frac{\alpha_2\alpha_{\gamma 2}}{8\pi^2 x\, c_W}\left(c_W^2 - s_W^2\right)(t-t_Z)(2-2x+(x+1)\log(x))\,. \tag{B.9}$$

The three contributions described in these sections, added to the EVA approximation of $f_{Z/\gamma}$, were used in section 3.2.1 to plot the $\mathcal{O}(\alpha^2)$ PDFs of fig. 3.5.

Analytic expressions for $f_{Z/\gamma_-}(x,Q^2)$

We report here the analytic contributions at order $\mathcal{O}(\alpha^2)$ to the $f_{Z/\gamma_-}(x,Q^2)$ PDF. These have been determined following the same procedure outlined above for the positive helicity:

$$\begin{aligned}
f_{Z/\gamma_-}^{(\alpha^2)P_{VV}}(x,Q) =& \frac{\alpha_2\alpha_{\gamma 2}}{96\pi^2 x}(t-t_Z)^2\, c_W\cdot\Big[4(t-t_Z)+K(x)\Big]\,,\\
f_{Z/\gamma_-}^{(\alpha^2)P_{Vf}}(x,Q) =& \frac{\alpha_{\gamma 2}\alpha_2}{48 c_W\pi^2}(t-t_Z)^3\frac{1}{x}\Big(-\frac{1}{2}+s_W^2\Big)-\\
&-\frac{\alpha_{\gamma 2}\alpha_2}{128 c_W^3\pi^2 x}(t-t_Z)^2 R(x) - \frac{\alpha_{\gamma 2}\alpha_\gamma}{32 c_W\pi^2 x}(t^2-t_Z^2)T(x)\,,\\
f_{Z/\gamma_-}^{(\alpha^2)P_{Vh}}(x,Q) =& -\frac{\alpha_2\alpha_{\gamma 2}}{8\pi^2 x\, c_W}\left(c_W^2 - s_W^2\right)(t-t_Z)(2-2x+(x+1)\log(x))\,,
\end{aligned} \tag{B.10}$$

where we defined

$$\begin{aligned}
K(x) =& -31-12x+39x^2+4x^3+12\log(1-x)-6(2+6x+3x^2)\log(x)\,,\\
R(x) =& -6c_W^2+12c_W^2s_W^2-2x+12s_W^2x-24s_W^4x+32s_W^6x-x^2+6s_W^2x^2-\\
&-12s_W^4x^2-8s_W^6x^2+4(-1+6s_W^2-12s_W^4+8s_W^6(2-2x+x^2))\cdot\\
&\cdot\log(1-x)-16s_W^6(-2+x)x\log(x)\,,\\
T(x) =& 4(-1+2s_W^2(2-2x+x^2))\log(1-x)-x(2+2s_W^2(-4+x)+\\
&+x+4s_W^2(-2+x)\log(x))\,.
\end{aligned} \tag{B.11}$$

The Sudakov double logarithms in this formulas originate from the same source as those discussed in the preceding sections. The contribution given by the emission of a longitudinal W_L boson has the same form as in the positive helicity case, since this splitting function is independent of the vector boson's polarization, $P_{V_+h}(z) = P_{V_-h}(z)$.

B.2 Differential cross section

The differential cross section for a generic partonic process $1\,2 \to 3\,4$ can be written, in the lab frame and in the high energy limit, as:

$$\frac{d^3\sigma_{\rm tot}}{dy_3 dy_4 dm} = f_1(x_1) f_2(x_2) \frac{m^3}{2s} \frac{1}{\cosh^2 y_*} \frac{d\sigma_{\rm H}}{dt}(1\,2 \to 3\,4)\,. \tag{B.12}$$

where $f_i(x_i)$ are the PDFs, σ_H is the hard cross section, m is the energy in the center of mass frame, y_i is the rapidity of the state i and we defined

$$x_{1,2} = \frac{m}{\sqrt{s}} e^{\pm \frac{y_3+y_4}{2}}\,, \quad y_* = \frac{1}{2}(y_3 - y_4)\,, \quad t = -\frac{m^2}{2}(1-\cos\theta_*)\,, \quad \theta_* = \arcsin\left(\frac{1}{\cosh y_*}\right)\,. \tag{B.13}$$

The relation $m = 4\,p_T^2 \cosh^2 y_*$ allows to express the total cross section as a function of the transverse momentum p_T:

$$\frac{d^3\sigma_{\rm tot}}{dy_3 dy_4 dp_T} = f_1(x_1) f_2(x_2) \frac{2m\,p_T}{s} \frac{1}{\cosh^2 y_*} \frac{d\sigma_{\rm H}}{dt}(1\,2 \to 3\,4)\,. \tag{B.14}$$

A step by step derivation of the above formulas can be found in [7].

B.2.1 Partonic cross sections for Compton scattering

In the following, we report the helicity-dependent partonic hard cross section for Compton scattering, on which the results of section 3.3 are based:

$$\begin{aligned}
\frac{d\sigma}{dt}(\mu^-_{L,R}\gamma_{\mp} \to \mu^-\gamma) &= \frac{4\pi\alpha^2(s+t)}{s^3}\,, \\
\frac{d\sigma}{dt}(\mu^-_{L,R}\gamma_{\pm} \to \mu^-\gamma) &= \frac{4\pi\alpha^2}{s(s+t)}\,,
\end{aligned} \tag{B.15}$$

$$\begin{aligned}
\frac{d\sigma}{dt}(\mu^-_L Z_- \to \mu^-\gamma) &= \frac{\pi\alpha^2\left(1-2s_W^2\right)^2}{c_W^2 s_W^2} \frac{s\left(s+t-m_Z^2\right)}{\left(s-m_Z^2\right)^4}\,, \\
\frac{d\sigma}{dt}(\mu^-_L Z_+ \to \mu^-\gamma) &= \frac{\pi\alpha^2\left(1-2s_W^2\right)^2}{c_W^2 s_W^2} \frac{\left(t^2 m_Z^4 + \left(s-m_Z^2\right)^4\right)}{s\left(s-m_Z^2\right)^4\left(s+t-m_Z^2\right)}\,, \\
\frac{d\sigma}{dt}(\mu^-_L Z_L \to \mu^-\gamma) &= -\frac{2\pi\alpha^2\left(1-2s_W^2\right)^2}{c_W^2 s_W^2} \frac{m_Z^2 t}{s^2\left(s-m_Z^2\right)^4}\,, \\
\frac{d\sigma}{dt}(\mu^-_R Z_- \to \mu^-\gamma) &= \frac{4\pi\alpha^2 s_W^2}{c_W^2} \frac{\left(t^2 m_Z^4 + \left(s-m_Z^2\right)^4\right)}{s\left(s-m_Z^2\right)^4\left(s+t-m_Z^2\right)}\,, \\
\frac{d\sigma}{dt}(\mu^-_R Z_+ \to \mu^-\gamma) &= \frac{4\pi\alpha^2 s_W^2}{c_W^2} \frac{s\left(s+t-m_Z^2\right)}{\left(s-m_Z^2\right)^4}\,, \\
\frac{d\sigma}{dt}(\mu^-_R Z_L \to \mu^-\gamma) &= -\frac{8\pi\alpha^2 s_W^2}{c_W^2} \frac{m_Z^2 t}{\left(s-m_Z^2\right)^4}\,,
\end{aligned} \tag{B.16}$$

$$
\begin{aligned}
\frac{d\sigma}{dt}(\mu_L^- Z/\gamma_- \to \mu^- \gamma) &= -\frac{4\pi\alpha^2\left(1-2s_W^2\right)}{c_W s_W}\frac{s\left(s+t-m_Z^2\right)}{\left(s-m_Z^2\right)^4}\ , \\
\frac{d\sigma}{dt}(\mu_L^- Z/\gamma_+ \to \mu^- \gamma) &= -\frac{4\pi\alpha^2\left(1-2s_W^2\right)}{c_W s_W}\frac{\left(t^2 m_Z^4+\left(s-m_Z^2\right)^4\right)}{s\left(s-m_Z^2\right)^4\left(s+t-m_Z^2\right)}\ , \\
\frac{d\sigma}{dt}(\mu_R^- Z/\gamma_- \to \mu^- \gamma) &= \frac{8\pi\alpha^2 s_W}{c_W}\frac{\left(t^2 m_Z^4+\left(s-m_Z^2\right)^4\right)}{s\left(s-m_Z^2\right)^4\left(s+t-m_Z^2\right)}\ , \\
\frac{d\sigma}{dt}(\mu_R^- Z/\gamma_+ \to \mu^- \gamma) &= \frac{8\pi\alpha^2 s_W}{c_W}\frac{s\left(s+t-m_Z^2\right)}{\left(s-m_Z^2\right)^4}\ .
\end{aligned}
\tag{B.17}
$$

Bibliography

[1] F. Garosi, D. Marzocca, A. R. Sánchez and A. Stanzione, *Indirect constraints on top quark operators from a global SMEFT analysis*, *JHEP* **12** (2023) 129, [2310.00047].

[2] D. Marzocca, M. Nardecchia, A. Stanzione and C. Toni, *Implications of $B \to K\nu\bar{\nu}$ under rank-one flavor violation hypothesis*, *Eur. Phys. J. C* **84** (2024) 1217, [2404.06533].

[3] D. Marzocca and A. Stanzione, *On the impact of the mixed Z/γ PDF at muon colliders*, *JHEP* **03** (2025) 171, [2408.13191].

[4] L. Allwicher, M. Bordone, G. Isidori, G. Piazza and A. Stanzione, *Probing third-generation New Physics with $K\to\pi\nu\nu^{-}$ and $B\to K(*)\nu\nu^{-}$*, *Phys. Lett. B* **861** (2025) 139295, [2410.21444].

[5] M. D'Elia, L. Maio, F. Sanfilippo and A. Stanzione, *Phase diagram of QCD in a magnetic background*, *Phys. Rev. D* **105** (2022) 034511, [2111.11237].

[6] M. D'Elia, L. Maio, F. Sanfilippo and A. Stanzione, *Confining and chiral properties of QCD in extremely strong magnetic fields*, *Phys. Rev. D* **104** (2021) 114512, [2109.07456].

[7] M. E. Peskin and D. V. Schroeder, *An Introduction to quantum field theory*. Addison-Wesley, Reading, USA, 1995.

[8] M. D. Schwartz, *Quantum Field Theory and the Standard Model*. Cambridge University Press, 3, 2014.

[9] Particle Data Group collaboration, S. Navas et al., *Review of particle physics*, *Phys. Rev. D* **110** (2024) 030001.

[10] A. Falkowski, "GGI lectures on EFT." https://agenda.infn.it/event/39074/sessions/30445/attachments/122631/179708/ggi.pdf, 2024.

[11] B. Grzadkowski, M. Iskrzynski, M. Misiak and J. Rosiek, *Dimension-Six Terms in the Standard Model Lagrangian*, *JHEP* **10** (2010) 085, [1008.4884].

[12] G. Isidori, F. Wilsch and D. Wyler, *The standard model effective field theory at work*, *Rev. Mod. Phys.* **96** (2024) 015006, [2303.16922].

[13] J. Aebischer, A. J. Buras and J. Kumar, *SMEFT ATLAS: The Landscape Beyond the Standard Model*, 2507.05926.

[14] D. Baumann, *Cosmology*. Cambridge University Press, 7, 2022, 10.1017/9781108937092.

[15] S. L. Glashow, J. Iliopoulos and L. Maiani, *Weak Interactions with Lepton-Hadron Symmetry*, *Phys. Rev. D* **2** (1970) 1285–1292.

[16] R. Franceschini, *Beyond-Standard-Model Physics Associated with the Top Quark*, 2301.04407.

[17] R. Barbieri, G. Isidori, J. Jones-Perez, P. Lodone and D. M. Straub, *$U(2)$ and Minimal Flavour Violation in Supersymmetry*, *Eur. Phys. J.* **C71** (2011) 1725, [1105.2296].

[18] R. Barbieri, D. Buttazzo, F. Sala and D. M. Straub, *Flavour physics from an approximate $U(2)^3$ symmetry*, *JHEP* **07** (2012) 181, [1203.4218].

[19] R. Barbieri, D. Buttazzo, F. Sala, D. M. Straub and A. Tesi, *A 125 GeV composite Higgs boson versus flavour and electroweak precision tests*, *JHEP* **05** (2013) 069, [1211.5085].

[20] D. A. Faroughy, G. Isidori, F. Wilsch and K. Yamamoto, *Flavour symmetries in the SMEFT*, *JHEP* **08** (2020) 166, [2005.05366].

[21] P. J. Fox, Z. Ligeti, M. Papucci, G. Perez and M. D. Schwartz, *Deciphering top flavor violation at the LHC with B factories*, *Phys. Rev. D* **78** (2008) 054008, [0704.1482].

[22] B. Grzadkowski and M. Misiak, *Anomalous Wtb coupling effects in the weak radiative B-meson decay*, *Phys. Rev. D* **78** (2008) 077501, [0802.1413]. [Erratum: Phys.Rev.D 84, 059903 (2011)].

[23] J. Drobnak, S. Fajfer and J. F. Kamenik, *Probing anomalous tWb interactions with rare B decays*, *Nucl. Phys. B* **855** (2012) 82–99, [1109.2357].

[24] J. Brod, A. Greljo, E. Stamou and P. Uttayarat, *Probing anomalous $t\bar{t}Z$ interactions with rare meson decays*, *JHEP* **02** (2015) 141, [1408.0792].

[25] W. Altmannshofer, S. Gori, B. V. Lehmann and J. Zuo, *UV physics from IR features: New prospects from top flavor violation*, *Phys. Rev. D* **107** (2023) 095025, [2303.00781].

[26] V. Cirigliano, W. Dekens, J. de Vries and E. Mereghetti, *Constraining the top-Higgs sector of the Standard Model Effective Field Theory*, *Phys. Rev. D* **94** (2016) 034031, [1605.04311].

[27] S. Bißmann, J. Erdmann, C. Grunwald, G. Hiller and K. Kröninger, *Constraining top-quark couplings combining top-quark and $\boldsymbol{B}$ decay observables*, *Eur. Phys. J. C* **80** (2020) 136, [1909.13632].

[28] S. Bißmann, C. Grunwald, G. Hiller and K. Kröninger, *Top and Beauty synergies in SMEFT-fits at present and future colliders*, *JHEP* **06** (2021) 010, [2012.10456].

[29] E. E. Jenkins, A. V. Manohar and P. Stoffer, *Low-Energy Effective Field Theory below the Electroweak Scale: Operators and Matching*, *JHEP* **03** (2018) 016, [1709.04486]. [Erratum: JHEP 12, 043 (2023)].

[30] A. Celis, J. Fuentes-Martin, A. Vicente and J. Virto, *DsixTools: The Standard Model Effective Field Theory Toolkit*, *Eur. Phys. J. C* **77** (2017) 405, [1704.04504].

[31] J. Fuentes-Martin, P. Ruiz-Femenia, A. Vicente and J. Virto, *DsixTools 2.0: The Effective Field Theory Toolkit*, *Eur. Phys. J. C* **81** (2021) 167, [2010.16341].

[32] E. E. Jenkins, A. V. Manohar and M. Trott, *Renormalization Group Evolution of the Standard Model Dimension Six Operators I: Formalism and lambda Dependence*, *JHEP* **10** (2013) 087, [1308.2627].

[33] E. E. Jenkins, A. V. Manohar and M. Trott, *Renormalization Group Evolution of the Standard Model Dimension Six Operators II: Yukawa Dependence*, *JHEP* **01** (2014) 035, [1310.4838].

[34] R. Alonso, E. E. Jenkins, A. V. Manohar and M. Trott, *Renormalization Group Evolution of the Standard Model Dimension Six Operators III: Gauge Coupling Dependence and Phenomenology*, *JHEP* **04** (2014) 159, [1312.2014].

[35] J. Braathen, M. D. Goodsell, M. E. Krauss, T. Opferkuch and F. Staub, *N-loop running should be combined with N-loop matching*, *Phys. Rev. D* **97** (2018) 015011, [1711.08460].

[36] W. Dekens and P. Stoffer, *Low-energy effective field theory below the electroweak scale: matching at one loop*, *JHEP* **10** (2019) 197, [1908.05295]. [Erratum: JHEP 11, 148 (2022)].

[37] J. Aebischer, A. Crivellin, M. Fael and C. Greub, *Matching of gauge invariant dimension-six operators for $b \to s$ and $b \to c$ transitions*, *JHEP* **05** (2016) 037, [1512.02830].

[38] E. E. Jenkins, A. V. Manohar and P. Stoffer, *Low-Energy Effective Field Theory below the Electroweak Scale: Anomalous Dimensions*, *JHEP* **01** (2018) 084, [1711.05270].

[39] T. van Ritbergen, J. A. M. Vermaseren and S. A. Larin, *The Four loop beta function in quantum chromodynamics*, *Phys. Lett. B* **400** (1997) 379–384, [hep-ph/9701390].

[40] J. A. M. Vermaseren, S. A. Larin and T. van Ritbergen, *The four loop quark mass anomalous dimension and the invariant quark mass*, *Phys. Lett. B* **405** (1997) 327–333, [hep-ph/9703284].

[41] P. A. Baikov, K. G. Chetyrkin and J. H. Kühn, *Five-loop fermion anomalous dimension for a general gauge group from four-loop massless propagators*, *JHEP* **04** (2017) 119, [1702.01458].

[42] K. G. Chetyrkin, J. H. Kuhn and M. Steinhauser, *RunDec: A Mathematica package for running and*

decoupling of the strong coupling and quark masses, Comput. Phys. Commun. **133** (2000) 43–65, [hep-ph/0004189].

[43] A. V. Bednyakov, A. F. Pikelner and V. N. Velizhanin, *Anomalous dimensions of gauge fields and gauge coupling beta-functions in the Standard Model at three loops*, JHEP **01** (2013) 017, [1210.6873].

[44] A. V. Bednyakov, A. F. Pikelner and V. N. Velizhanin, *Yukawa coupling beta-functions in the Standard Model at three loops*, Phys. Lett. B **722** (2013) 336–340, [1212.6829].

[45] A. V. Bednyakov, A. F. Pikelner and V. N. Velizhanin, *Higgs self-coupling beta-function in the Standard Model at three loops*, Nucl. Phys. B **875** (2013) 552–565, [1303.4364].

[46] A. V. Bednyakov, A. F. Pikelner and V. N. Velizhanin, *Three-loop SM beta-functions for matrix Yukawa couplings*, Phys. Lett. B **737** (2014) 129–134, [1406.7171].

[47] LHCb collaboration, R. Aaij et al., *Test of lepton universality in $b \to s\ell^+\ell^-$ decays*, Phys. Rev. Lett. **131** (2023) 051803, [2212.09152].

[48] D. Bečirević, G. Piazza and O. Sumensari, *Revisiting $B \to K^{(*)}\nu\bar{\nu}$ decays in the Standard Model and beyond*, Eur. Phys. J. C **83** (2023) 252, [2301.06990].

[49] Belle-II collaboration, I. Adachi et al., *Evidence for $B+ \to K+\nu\nu^-$ decays*, Phys. Rev. D **109** (2024) 112006, [2311.14647].

[50] Belle collaboration, J. Grygier et al., *Search for $\boldsymbol{B \to h\nu\bar{\nu}}$ decays with semileptonic tagging at Belle*, Phys. Rev. D **96** (2017) 091101, [1702.03224]. [Addendum: Phys.Rev.D 97, 099902 (2018)].

[51] Particle Data Group collaboration, R. L. Workman and Others, *Review of Particle Physics*, PTEP **2022** (2022) 083C01.

[52] BELLE collaboration, S. Choudhury et al., *Test of lepton flavor universality and search for lepton flavor violation in $B \to K\ell\ell$ decays*, JHEP **03** (2021) 105, [1908.01848].

[53] BaBar collaboration, J. P. Lees et al., *A search for the decay modes $B^{+-} \to h^{+-}\tau^{+-}l$*, Phys. Rev. D **86** (2012) 012004, [1204.2852].

[54] LHCb collaboration, R. Aaij et al., *Search for the lepton flavour violating decay $B^+ \to K^+\mu^-\tau^+$ using B^{*0}_{s2} decays*, JHEP **06** (2020) 129, [2003.04352].

[55] LHCb collaboration, R. Aaij et al., *Search for the Rare Decays $B^0_s \to e^+e^-$ and $B^0 \to e^+e^-$*, Phys. Rev. Lett. **124** (2020) 211802, [2003.03999].

[56] LHCb collaboration, R. Aaij et al., *Measurement of the $B^0_s \to \mu^+\mu^-$ decay properties and search for the $B^0 \to \mu^+\mu^-$ and $B^0_s \to \mu^+\mu^-\gamma$ decays*, Phys. Rev. D **105** (2022) 012010, [2108.09283].

[57] LHCb collaboration, R. Aaij et al., *Search for the decays $B^0_s \to \tau^+\tau^-$ and $B^0 \to \tau^+\tau^-$*, Phys. Rev. Lett. **118** (2017) 251802, [1703.02508].

[58] LHCb collaboration, R. Aaij et al., *Search for the lepton-flavour violating decays $B^0_{(s)} \to e^\pm\mu^\mp$*, JHEP **03** (2018) 078, [1710.04111].

[59] LHCb collaboration, R. Aaij et al., *Search for the lepton-flavour-violating decays $B^0_s \to \tau^\pm\mu^\mp$ and $B^0 \to \tau^\pm\mu^\mp$*, Phys. Rev. Lett. **123** (2019) 211801, [1905.06614].

[60] NA62 collaboration, E. Cortina Gil et al., *Measurement of the very rare $K^+ \to \pi^+\nu\bar{\nu}$ decay*, JHEP **06** (2021) 093, [2103.15389].

[61] E949 collaboration, A. V. Artamonov et al., *New measurement of the $K^+ \to \pi^+\nu\bar{\nu}$ branching ratio*, Phys. Rev. Lett. **101** (2008) 191802, [0808.2459].

[62] KOTO collaboration, J. K. Ahn et al., *Search for the $K_L \to \pi^0\nu\bar{\nu}$ and $K_L \to \pi^0 X^0$ decays at the J-PARC KOTO experiment*, Phys. Rev. Lett. **122** (2019) 021802, [1810.09655].

[63] LHCb collaboration, R. Aaij et al., *Constraints on the $K^0_S \to \mu^+\mu^-$ Branching Fraction*, Phys. Rev. Lett. **125** (2020) 231801, [2001.10354].

[64] G. Isidori and R. Unterdorfer, *On the short distance constraints from K(L,S) —> mu+ mu-*, JHEP **01** (2004) 009, [hep-ph/0311084].

[65] BNL collaboration, D. Ambrose et al., *New limit on muon and electron lepton number violation from K0(L) —> mu+- e-+ decay*, *Phys. Rev. Lett.* **81** (1998) 5734–5737, [hep-ex/9811038].

[66] KTEV collaboration, A. Alavi-Harati et al., *Search for the Decay $K_L \to \pi^0\mu^+\mu^-$*, *Phys. Rev. Lett.* **84** (2000) 5279–5282, [hep-ex/0001006].

[67] KTeV collaboration, A. Alavi-Harati et al., *Search for the rare decay K(L) —> pi0 e+ e-*, *Phys. Rev. Lett.* **93** (2004) 021805, [hep-ex/0309072].

[68] KTeV collaboration, E. Abouzaid et al., *Search for lepton flavor violating decays of the neutral kaon*, *Phys. Rev. Lett.* **100** (2008) 131803, [0711.3472].

[69] NA62 collaboration, E. Cortina Gil et al., *Search for Lepton Number and Flavor Violation in K^+ and π^0 Decays*, *Phys. Rev. Lett.* **127** (2021) 131802, [2105.06759].

[70] A. J. Buras and E. Venturini, *The exclusive vision of rare K and B decays and of the quark mixing in the standard model*, *Eur. Phys. J. C* **82** (2022) 615, [2203.11960].

[71] J. Aebischer, C. Bobeth, A. J. Buras and J. Kumar, *SMEFT ATLAS of $\Delta F = 2$ transitions*, *JHEP* **12** (2020) 187, [2009.07276].

[72] V. Cirigliano, D. Díaz-Calderón, A. Falkowski, M. González-Alonso and A. Rodríguez-Sánchez, *Semileptonic tau decays beyond the Standard Model*, *JHEP* **04** (2022) 152, [2112.02087].

[73] M. González-Alonso and J. Martin Camalich, *Global Effective-Field-Theory analysis of New-Physics effects in (semi)leptonic kaon decays*, *JHEP* **12** (2016) 052, [1605.07114].

[74] A. Falkowski, M. González-Alonso and O. Naviliat-Cuncic, *Comprehensive analysis of beta decays within and beyond the Standard Model*, *JHEP* **04** (2021) 126, [2010.13797].

[75] Heavy Flavor Averaging Group, HFLAV collaboration, Y. S. Amhis et al., *Averages of b-hadron, c-hadron, and τ-lepton properties as of 2021*, *Phys. Rev. D* **107** (2023) 052008, [2206.07501].

[76] J. Aebischer, W. Dekens, E. E. Jenkins, A. V. Manohar, D. Sengupta and P. Stoffer, *Effective field theory interpretation of lepton magnetic and electric dipole moments*, *JHEP* **07** (2021) 107, [2102.08954].

[77] L. Morel, Z. Yao, P. Cladé and S. Guellati-Khélifa, *Determination of the fine-structure constant with an accuracy of 81 parts per trillion*, *Nature* **588** (2020) 61–65.

[78] R. H. Parker, C. Yu, W. Zhong, B. Estey and H. Müller, *Measurement of the fine-structure constant as a test of the Standard Model*, *Science* **360** (2018) 191, [1812.04130].

[79] T. Aoyama et al., *The anomalous magnetic moment of the muon in the Standard Model*, *Phys. Rept.* **887** (2020) 1–166, [2006.04822].

[80] T. Aoyama, M. Hayakawa, T. Kinoshita and M. Nio, *Complete Tenth-Order QED Contribution to the Muon g-2*, *Phys. Rev. Lett.* **109** (2012) 111808, [1205.5370].

[81] T. Aoyama, T. Kinoshita and M. Nio, *Theory of the Anomalous Magnetic Moment of the Electron*, *Atoms* **7** (2019) 28.

[82] A. Czarnecki, W. J. Marciano and A. Vainshtein, *Refinements in electroweak contributions to the muon anomalous magnetic moment*, *Phys. Rev. D* **67** (2003) 073006, [hep-ph/0212229]. [Erratum: Phys.Rev.D 73, 119901 (2006)].

[83] C. Gnendiger, D. Stöckinger and H. Stöckinger-Kim, *The electroweak contributions to $(g-2)_\mu$ after the Higgs boson mass measurement*, *Phys. Rev. D* **88** (2013) 053005, [1306.5546].

[84] M. Davier, A. Hoecker, B. Malaescu and Z. Zhang, *Reevaluation of the hadronic vacuum polarisation contributions to the Standard Model predictions of the muon $g-2$ and $\alpha(m_Z^2)$ using newest hadronic cross-section data*, *Eur. Phys. J. C* **77** (2017) 827, [1706.09436].

[85] A. Keshavarzi, D. Nomura and T. Teubner, *Muon $g-2$ and $\alpha(M_Z^2)$: a new data-based analysis*, *Phys. Rev. D* **97** (2018) 114025, [1802.02995].

[86] G. Colangelo, M. Hoferichter and P. Stoffer, *Two-pion contribution to hadronic vacuum polarization*, *JHEP* **02** (2019) 006, [1810.00007].

[87] M. Hoferichter, B.-L. Hoid and B. Kubis, *Three-pion contribution to hadronic vacuum polarization*, *JHEP* **08** (2019) 137, [1907.01556].

[88] M. Davier, A. Hoecker, B. Malaescu and Z. Zhang, *A new evaluation of the hadronic vacuum polarisation contributions to the muon anomalous magnetic moment and to* $\boldsymbol{\alpha(m_Z^2)}$, *Eur. Phys. J. C* **80** (2020) 241, [1908.00921]. [Erratum: Eur.Phys.J.C 80, 410 (2020)].

[89] A. Keshavarzi, D. Nomura and T. Teubner, $g-2$ *of charged leptons,* $\alpha(M_Z^2)$ *, and the hyperfine splitting of muonium*, *Phys. Rev. D* **101** (2020) 014029, [1911.00367].

[90] A. Kurz, T. Liu, P. Marquard and M. Steinhauser, *Hadronic contribution to the muon anomalous magnetic moment to next-to-next-to-leading order*, *Phys. Lett. B* **734** (2014) 144–147, [1403.6400].

[91] K. Melnikov and A. Vainshtein, *Hadronic light-by-light scattering contribution to the muon anomalous magnetic moment revisited*, *Phys. Rev. D* **70** (2004) 113006, [hep-ph/0312226].

[92] P. Masjuan and P. Sanchez-Puertas, *Pseudoscalar-pole contribution to the* $(g_\mu - 2)$*: a rational approach*, *Phys. Rev. D* **95** (2017) 054026, [1701.05829].

[93] G. Colangelo, M. Hoferichter, M. Procura and P. Stoffer, *Dispersion relation for hadronic light-by-light scattering: two-pion contributions*, *JHEP* **04** (2017) 161, [1702.07347].

[94] M. Hoferichter, B.-L. Hoid, B. Kubis, S. Leupold and S. P. Schneider, *Dispersion relation for hadronic light-by-light scattering: pion pole*, *JHEP* **10** (2018) 141, [1808.04823].

[95] A. Gérardin, H. B. Meyer and A. Nyffeler, *Lattice calculation of the pion transition form factor with* $N_f = 2 + 1$ *Wilson quarks*, *Phys. Rev. D* **100** (2019) 034520, [1903.09471].

[96] J. Bijnens, N. Hermansson-Truedsson and A. Rodríguez-Sánchez, *Short-distance constraints for the HLbL contribution to the muon anomalous magnetic moment*, *Phys. Lett. B* **798** (2019) 134994, [1908.03331].

[97] G. Colangelo, F. Hagelstein, M. Hoferichter, L. Laub and P. Stoffer, *Longitudinal short-distance constraints for the hadronic light-by-light contribution to* $(g-2)_\mu$ *with large-*N_c *Regge models*, *JHEP* **03** (2020) 101, [1910.13432].

[98] T. Blum, N. Christ, M. Hayakawa, T. Izubuchi, L. Jin, C. Jung et al., *Hadronic Light-by-Light Scattering Contribution to the Muon Anomalous Magnetic Moment from Lattice QCD*, *Phys. Rev. Lett.* **124** (2020) 132002, [1911.08123].

[99] G. Colangelo, M. Hoferichter, A. Nyffeler, M. Passera and P. Stoffer, *Remarks on higher-order hadronic corrections to the muon g−2*, *Phys. Lett. B* **735** (2014) 90–91, [1403.7512].

[100] S. Borsanyi et al., *Leading hadronic contribution to the muon magnetic moment from lattice QCD*, *Nature* **593** (2021) 51–55, [2002.12347].

[101] C. Lehner and A. S. Meyer, *Consistency of hadronic vacuum polarization between lattice QCD and the R-ratio*, *Phys. Rev. D* **101** (2020) 074515, [2003.04177].

[102] M. Cè, A. Gérardin, G. von Hippel, H. B. Meyer, K. Miura, K. Ottnad et al., *The hadronic running of the electromagnetic coupling and the electroweak mixing angle from lattice QCD*, *JHEP* **08** (2022) 220, [2203.08676].

[103] M. Cè et al., *Window observable for the hadronic vacuum polarization contribution to the muon g-2 from lattice QCD*, *Phys. Rev. D* **106** (2022) 114502, [2206.06582].

[104] chiQCD collaboration, G. Wang, T. Draper, K.-F. Liu and Y.-B. Yang, *Muon g-2 with overlap valence fermions*, *Phys. Rev. D* **107** (2023) 034513, [2204.01280].

[105] Extended Twisted Mass collaboration, C. Alexandrou et al., *Lattice calculation of the short and intermediate time-distance hadronic vacuum polarization contributions to the muon magnetic moment using twisted-mass fermions*, *Phys. Rev. D* **107** (2023) 074506, [2206.15084].

[106] G. Colangelo, A. X. El-Khadra, M. Hoferichter, A. Keshavarzi, C. Lehner, P. Stoffer et al.,

Data-driven evaluations of Euclidean windows to scrutinize hadronic vacuum polarization, Phys. Lett. B **833** (2022) 137313, [2205.12963].

[107] C. Aubin, T. Blum, M. Golterman and S. Peris, *Muon anomalous magnetic moment with staggered fermions: Is the lattice spacing small enough?*, Phys. Rev. D **106** (2022) 054503, [2204.12256].

[108] T. Blum et al., *An update of Euclidean windows of the hadronic vacuum polarization*, 2301.08696.

[109] Fermilab Lattice, HPQCD„ MILC collaboration, A. Bazavov et al., *Light-quark connected intermediate-window contributions to the muon g-2 hadronic vacuum polarization from lattice QCD*, Phys. Rev. D **107** (2023) 114514, [2301.08274].

[110] M. Davier, D. Díaz-Calderón, B. Malaescu, A. Pich, A. Rodríguez-Sánchez and Z. Zhang, *The Euclidean Adler function and its interplay with* $\Delta\alpha^{had}_{QED}$ *and* α_s, JHEP **04** (2023) 067, [2302.01359].

[111] CMD-3 collaboration, F. V. Ignatov et al., *Measurement of the* $e^+e^- \to \pi^+\pi^-$ *cross section from threshold to 1.2 GeV with the CMD-3 detector*, 2302.08834.

[112] G. Benton, D. Boito, M. Golterman, A. Keshavarzi, K. Maltman and S. Peris, *Data-driven determination of the light-quark connected component of the intermediate-window contribution to the muon* $g-2$, 2306.16808.

[113] M. Davier, Z. Fodor, A. Gerardin, L. Lellouch, B. Malaescu, F. M. Stokes et al., *Hadronic vacuum polarization: comparing lattice QCD and data-driven results in systematically improvable ways*, 2308.04221.

[114] A. Pich, *Precision Tau Physics*, Prog. Part. Nucl. Phys. **75** (2014) 41–85, [1310.7922].

[115] MEG collaboration, A. M. Baldini et al., *Search for the lepton flavour violating decay* $\mu^+ \to e^+\gamma$ *with the full dataset of the MEG experiment*, Eur. Phys. J. C **76** (2016) 434, [1605.05081].

[116] SINDRUM collaboration, U. Bellgardt et al., *Search for the Decay mu+ —> e+ e+ e-*, Nucl. Phys. B **299** (1988) 1–6.

[117] SINDRUM II collaboration, W. H. Bertl et al., *A Search for muon to electron conversion in muonic gold*, Eur. Phys. J. C **47** (2006) 337–346.

[118] BaBar collaboration, B. Aubert et al., *Searches for Lepton Flavor Violation in the Decays tau+- —> e+- gamma and tau+- —> mu+- gamma*, Phys. Rev. Lett. **104** (2010) 021802, [0908.2381].

[119] K. Hayasaka et al., *Search for Lepton Flavor Violating Tau Decays into Three Leptons with 719 Million Produced Tau+Tau- Pairs*, Phys. Lett. B **687** (2010) 139–143, [1001.3221].

[120] Belle collaboration, Y. Miyazaki et al., *Search for lepton flavor violating tau- decays into l- eta, l- eta-prime and l- pi0*, Phys. Lett. B **648** (2007) 341–350, [hep-ex/0703009].

[121] Belle collaboration, Y. Miyazaki et al., *Search for Lepton-Flavor-Violating and Lepton-Number-Violating* $\tau \to \ell hh'$ *Decay Modes*, Phys. Lett. B **719** (2013) 346–353, [1206.5595].

[122] Belle collaboration, A. Abdesselam et al., *Search for lepton-flavor-violating tau-lepton decays to* $\ell\gamma$ *at Belle*, JHEP **10** (2021) 19, [2103.12994].

[123] BaBar collaboration, B. Aubert et al., *Search for Lepton Flavor Violating Decays* $\tau^\pm \to \ell^\pm\pi^0$, $\ell^\pm\eta$, $\ell^\pm\eta'$, Phys. Rev. Lett. **98** (2007) 061803, [hep-ex/0610067].

[124] S. Davidson, B. Echenard, R. H. Bernstein, J. Heeck and D. G. Hitlin, *Charged Lepton Flavor Violation*, 2209.00142.

[125] A. Crivellin, S. Davidson, G. M. Pruna and A. Signer, *Renormalisation-group improved analysis of* $\mu \to e$ *processes in a systematic effective-field-theory approach*, JHEP **05** (2017) 117, [1702.03020].

[126] MEG II collaboration, A. M. Baldini et al., *The design of the MEG II experiment*, Eur. Phys. J. C **78** (2018) 380, [1801.04688].

[127] Mu2e collaboration, L. Bartoszek et al., *Mu2e Technical Design Report*, 1501.05241.

[128] Mu3e collaboration, K. Arndt et al., *Technical design of the phase I Mu3e experiment*, Nucl. Instrum. Meth. A **1014** (2021) 165679, [2009.11690].

[129] A. Celis, V. Cirigliano and E. Passemar, *Model-discriminating power of lepton flavor violating τ decays*, *Phys. Rev. D* **89** (2014) 095014, [1403.5781].

[130] V. Cirigliano, K. Fuyuto, C. Lee, E. Mereghetti and B. Yan, *Charged Lepton Flavor Violation at the EIC*, *JHEP* **03** (2021) 256, [2102.06176].

[131] T. Husek, K. Monsalvez-Pozo and J. Portoles, *Lepton-flavour violation in hadronic tau decays and $\mu - \tau$ conversion in nuclei*, *JHEP* **01** (2021) 059, [2009.10428].

[132] S. Banerjee et al., *Snowmass 2021 White Paper: Charged lepton flavor violation in the tau sector*, 2203.14919.

[133] Belle-II collaboration, L. Aggarwal et al., *Snowmass White Paper: Belle II physics reach and plans for the next decade and beyond*, 2207.06307.

[134] A. Falkowski and D. Straub, *Flavourful SMEFT likelihood for Higgs and electroweak data*, *JHEP* **04** (2020) 066, [1911.07866].

[135] A. Efrati, A. Falkowski and Y. Soreq, *Electroweak constraints on flavorful effective theories*, *JHEP* **07** (2015) 018, [1503.07872].

[136] P. Janot and S. Jadach, *Improved Bhabha cross section at LEP and the number of light neutrino species*, *Phys. Lett. B* **803** (2020) 135319, [1912.02067].

[137] D. Barducci et al., *Interpreting top-quark LHC measurements in the standard-model effective field theory*, 1802.07237.

[138] F. Maltoni, L. Mantani and K. Mimasu, *Top-quark electroweak interactions at high energy*, *JHEP* **10** (2019) 004, [1904.05637].

[139] I. Brivio, S. Bruggisser, F. Maltoni, R. Moutafis, T. Plehn, E. Vryonidou et al., *O new physics, where art thou? A global search in the top sector*, *JHEP* **02** (2020) 131, [1910.03606].

[140] G. Durieux, A. Irles, V. Miralles, A. Peñuelas, R. Pöschl, M. Perelló et al., *The electro-weak couplings of the top and bottom quarks — Global fit and future prospects*, *JHEP* **12** (2019) 98, [1907.10619]. [Erratum: JHEP 01, 195 (2021)].

[141] N. P. Hartland, F. Maltoni, E. R. Nocera, J. Rojo, E. Slade, E. Vryonidou et al., *A Monte Carlo global analysis of the Standard Model Effective Field Theory: the top quark sector*, *JHEP* **04** (2019) 100, [1901.05965].

[142] S. Bruggisser, R. Schäfer, D. van Dyk and S. Westhoff, *The Flavor of UV Physics*, *JHEP* **05** (2021) 257, [2101.07273].

[143] SMEFiT collaboration, J. J. Ethier, G. Magni, F. Maltoni, L. Mantani, E. R. Nocera, J. Rojo et al., *Combined SMEFT interpretation of Higgs, diboson, and top quark data from the LHC*, *JHEP* **11** (2021) 089, [2105.00006].

[144] V. Miralles, M. M. López, M. M. Llácer, A. Peñuelas, M. Perelló and M. Vos, *The top quark electro-weak couplings after LHC Run 2*, *JHEP* **02** (2022) 032, [2107.13917].

[145] G. Durieux, A. G. Camacho, L. Mantani, V. Miralles, M. M. López, M. Llácer Moreno et al., *Snowmass White Paper: prospects for the measurement of top-quark couplings*, in *Snowmass 2021*, 5, 2022, 2205.02140.

[146] J. de Blas, Y. Du, C. Grojean, J. Gu, V. Miralles, M. E. Peskin et al., *Global SMEFT Fits at Future Colliders*, in *Snowmass 2021*, 6, 2022, 2206.08326.

[147] S. Bruggisser, D. van Dyk and S. Westhoff, *Resolving the flavor structure in the MFV-SMEFT*, *JHEP* **02** (2023) 225, [2212.02532].

[148] T. Giani, G. Magni and J. Rojo, *SMEFiT: a flexible toolbox for global interpretations of particle physics data with effective field theories*, *Eur. Phys. J. C* **83** (2023) 393, [2302.06660].

[149] Z. Kassabov, M. Madigan, L. Mantani, J. Moore, M. Morales Alvarado, J. Rojo et al., *The top quark legacy of the LHC Run II for PDF and SMEFT analyses*, *JHEP* **05** (2023) 205, [2303.06159].

[150] C. Grunwald, G. Hiller, K. Kröninger and L. Nollen, *More Synergies from Beauty, Top, Z and Drell-Yan Measurements in SMEFT*, 2304.12837.

[151] B. M. Gavela, E. E. Jenkins, A. V. Manohar and L. Merlo, *Analysis of General Power Counting Rules in Effective Field Theory*, *Eur. Phys. J. C* **76** (2016) 485, [1601.07551].

[152] I. Doršner, S. Fajfer, A. Greljo, J. F. Kamenik and N. Košnik, *Physics of leptoquarks in precision experiments and at particle colliders*, *Phys. Rept.* **641** (2016) 1–68, [1603.04993].

[153] J. de Blas, J. C. Criado, M. Perez-Victoria and J. Santiago, *Effective description of general extensions of the Standard Model: the complete tree-level dictionary*, *JHEP* **03** (2018) 109, [1711.10391].

[154] P. Arnan, D. Becirevic, F. Mescia and O. Sumensari, *Probing low energy scalar leptoquarks by the leptonic W and Z couplings*, *JHEP* **02** (2019) 109, [1901.06315].

[155] A. Crivellin, D. Müller and F. Saturnino, *Flavor Phenomenology of the Leptoquark Singlet-Triplet Model*, *JHEP* **06** (2020) 020, [1912.04224].

[156] S. Saad, *Combined explanations of $(g-2)_\mu$, $R_{D^{(*)}}$, $R_{K^{(*)}}$ anomalies in a two-loop radiative neutrino mass model*, *Phys. Rev. D* **102** (2020) 015019, [2005.04352].

[157] A. Crivellin, D. Müller and F. Saturnino, *Leptoquarks in oblique corrections and Higgs signal strength: status and prospects*, *JHEP* **11** (2020) 094, [2006.10758].

[158] V. Gherardi, D. Marzocca and E. Venturini, *Low-energy phenomenology of scalar leptoquarks at one-loop accuracy*, *JHEP* **01** (2021) 138, [2008.09548].

[159] D. Marzocca, S. Trifinopoulos and E. Venturini, *From B-meson anomalies to Kaon physics with scalar leptoquarks*, *Eur. Phys. J. C* **82** (2022) 320, [2106.15630].

[160] V. Gherardi, D. Marzocca and E. Venturini, *Matching scalar leptoquarks to the SMEFT at one loop*, *JHEP* **07** (2020) 225, [2003.12525]. [Erratum: JHEP 01, 006 (2021)].

[161] ATLAS collaboration, G. Aad et al., *Search for new phenomena in pp collisions in final states with tau leptons, b-jets, and missing transverse momentum with the ATLAS detector*, *Phys. Rev. D* **104** (2021) 112005, [2108.07665].

[162] B. Belfatto, R. Beradze and Z. Berezhiani, *The CKM unitarity problem: A trace of new physics at the TeV scale?*, *Eur. Phys. J. C* **80** (2020) 149, [1906.02714].

[163] V. Cirigliano, W. Dekens, J. de Vries, E. Mereghetti and T. Tong, *Beta-decay implications for the W-boson mass anomaly*, *Phys. Rev. D* **106** (2022) 075001, [2204.08440].

[164] A. Crivellin, *Explaining the Cabibbo Angle Anomaly*, 7, 2022, 2207.02507.

[165] W. Altmannshofer, A. J. Buras, D. M. Straub and M. Wick, *New strategies for New Physics search in $B \to K^* \nu\bar{\nu}$, $B \to K\nu\bar{\nu}$ and $B \to X_s \nu\bar{\nu}$ decays*, *JHEP* **04** (2009) 022, [0902.0160].

[166] A. J. Buras, J. Girrbach-Noe, C. Niehoff and D. M. Straub, *$B \to K^{(*)} \nu\bar{\nu}$ decays in the Standard Model and beyond*, *JHEP* **02** (2015) 184, [1409.4557].

[167] A. J. Buras, D. Buttazzo and R. Knegjens, *$K \to \pi\nu\bar{\nu}$ and ε'/ε in simplified new physics models*, *JHEP* **11** (2015) 166, [1507.08672].

[168] T. Blake, G. Lanfranchi and D. M. Straub, *Rare B Decays as Tests of the Standard Model*, *Prog. Part. Nucl. Phys.* **92** (2017) 50–91, [1606.00916].

[169] HPQCD collaboration, W. G. Parrott, C. Bouchard and C. T. H. Davies, *Standard Model predictions for $B \to K\ell^+\ell^-$, $B \to K\ell^1\ell^2$ and $B \to K\nu\bar{\nu}$ using form factors from Nf=2+1+1 lattice QCD*, *Phys. Rev. D* **107** (2023) 014511, [2207.13371]. [Erratum: Phys.Rev.D 107, 119903 (2023)].

[170] Belle-II collaboration, W. Altmannshofer et al., *The Belle II Physics Book*, *PTEP* **2019** (2019) 123C01, [1808.10567]. [Erratum: PTEP 2020, 029201 (2020)].

[171] R. Bause, H. Gisbert and G. Hiller, *Implications of an enhanced $B \to K\nu\bar{\nu}$ branching ratio*, *Phys. Rev. D* **109** (2024) 015006, [2309.00075].

[172] L. Allwicher, D. Becirevic, G. Piazza, S. Rosauro-Alcaraz and O. Sumensari, *Understanding the first*

measurement of $B(B\to K\nu\nu^-)$, *Phys. Lett. B* **848** (2024) 138411, [2309.02246].

[173] P. Athron, R. Martinez and C. Sierra, *B meson anomalies and large $B^+ \to K^+\nu\bar{\nu}$ in non-universal U(1)′ models*, *JHEP* **02** (2024) 121, [2308.13426].

[174] A. Greljo and A. E. Thomsen, *Rising Through the Ranks: Flavor Hierarchies from a Gauged* **SU(2)** *Symmetry*, *Eur. Phys. J. C* **84** (2024) 213, [2309.11547].

[175] F.-Z. Chen, Q. Wen and F. Xu, *Correlating $B \to K^{(*)}\nu\bar{\nu}$ and flavor anomalies in SMEFT*, 2401.11552.

[176] A. D'Alise, G. Fabiano, D. Frattulillo, D. Iacobacci, F. Sannino, P. Santorelli et al., *New Physics Pathways from B Processes*, 2403.17614.

[177] T. Felkl, A. Giri, R. Mohanta and M. A. Schmidt, *When energy goes missing: new physics in $b \to s\nu\nu$ with sterile neutrinos*, *Eur. Phys. J. C* **83** (2023) 1135, [2309.02940].

[178] X.-G. He, X.-D. Ma and G. Valencia, *Revisiting models that enhance $B^+ \to K^+\nu\bar{\nu}$ in light of the new Belle II measurement*, 2309.12741.

[179] A. Berezhnoy and D. Melikhov, *$B \to K^* M_X$ vs $B \to K M_X$ as a probe of a scalar-mediator dark matter scenario*, *EPL* **145** (2024) 14001, [2309.17191].

[180] W. Altmannshofer, A. Crivellin, H. Haigh, G. Inguglia and J. Martin Camalich, *Light new physics in $B\to K(*)\nu\nu^-$?*, *Phys. Rev. D* **109** (2024) 075008, [2311.14629].

[181] D. McKeen, J. N. Ng and D. Tuckler, *Higgs portal interpretation of the Belle II $B+\to K+\nu\nu$ measurement*, *Phys. Rev. D* **109** (2024) 075006, [2312.00982].

[182] K. Fridell, M. Ghosh, T. Okui and K. Tobioka, *Decoding the $B\to K\nu\nu$ excess at Belle II: Kinematics, operators, and masses*, *Phys. Rev. D* **109** (2024) 115006, [2312.12507].

[183] S.-Y. Ho, J. Kim and P. Ko, *Recent $B^+ \to K^+\nu\bar{\nu}$ Excess and Muon $g-2$ Illuminating Light Dark Sector with Higgs Portal*, 2401.10112.

[184] E. Gabrielli, L. Marzola, K. Müürsepp and M. Raidal, *Explaining the $B^+ \to K^+\nu\bar{\nu}$ excess via a massless dark photon*, *Eur. Phys. J. C* **84** (2024) 460, [2402.05901].

[185] B.-F. Hou, X.-Q. Li, M. Shen, Y.-D. Yang and X.-B. Yuan, *Deciphering the Belle II data on $B \to K\nu\bar{\nu}$ decay in the (dark) SMEFT with minimal flavour violation*, *JHEP* **06** (2024) 172, [2402.19208].

[186] X.-G. He, X.-D. Ma, M. A. Schmidt, G. Valencia and R. R. Volkas, *Scalar dark matter explanation of the excess in the Belle II $B^+\to K^+$ + invisible measurement*, *JHEP* **07** (2024) 168, [2403.12485].

[187] P. D. Bolton, S. Fajfer, J. F. Kamenik and M. Novoa-Brunet, *Signatures of light new particles in $B\to K(*)$Emiss*, *Phys. Rev. D* **110** (2024) 055001, [2403.13887].

[188] A. Datta, D. Marfatia and L. Mukherjee, *$B\to K\nu\nu^-$, MiniBooNE and muon g-2 anomalies from a dark sector*, *Phys. Rev. D* **109** (2024) L031701, [2310.15136].

[189] V. Gherardi, D. Marzocca, M. Nardecchia and A. Romanino, *Rank-One Flavor Violation and B-meson anomalies*, *JHEP* **10** (2019) 112, [1903.10954].

[190] NA62 collaboration, E. Cortina Gil et al., *An investigation of the very rare $K^+ \to \pi^+\nu\bar{\nu}$ decay*, *JHEP* **11** (2020) 042, [2007.08218].

[191] Joel Christopher Swallow (for the NA62 collaboration), "New measurement of the $K^+ \to \pi^+\nu\bar{\nu}$ decay by the NA62 Experiment." https://indico.cern.ch/event/1447422/, Set., 2024.

[192] NA62 collaboration, M. Piccini, *Status of the NA62 Experiment*, *EPJ Web Conf.* **234** (2020) 01012.

[193] HIKE collaboration, M. U. Ashraf et al., *High Intensity Kaon Experiments (HIKE) at the CERN SPS Proposal for Phases 1 and 2*, 2311.08231.

[194] K. Aoki et al., *Extension of the J-PARC Hadron Experimental Facility: Third White Paper*, 2110.04462.

[195] L. Allwicher, D. A. Faroughy, F. Jaffredo, O. Sumensari and F. Wilsch, *HighPT: A tool for high-p_T Drell-Yan tails beyond the standard model*, *Comput. Phys. Commun.* **289** (2023) 108749, [2207.10756].

[196] UTfit collaboration, "New physics fit results: Summer 2023." http://utfit.org/UTfit/ResultsSummer2023NP.

[197] UTfit collaboration, M. Bona et al., *New UTfit Analysis of the Unitarity Triangle in the Cabibbo-Kobayashi-Maskawa scheme*, *Rend. Lincei Sci. Fis. Nat.* **34** (2023) 37–57, [2212.03894].

[198] D. Barducci, M. Nardecchia and C. Toni, *Perturbative unitarity constraints on generic vector interactions*, *JHEP* **09** (2023) 134, [2306.11533].

[199] ATLAS collaboration, G. Aad et al., *A search for high-mass resonances decaying to $\tau^+\tau^-$ in pp collisions at $\sqrt{s} = 8$ TeV with the ATLAS detector*, *JHEP* **07** (2015) 157, [1502.07177].

[200] ATLAS collaboration, G. Aad et al., *Search for heavy Higgs bosons decaying into two tau leptons with the ATLAS detector using pp collisions at $\sqrt{s} = 13$ TeV*, *Phys. Rev. Lett.* **125** (2020) 051801, [2002.12223].

[201] ATLAS collaboration, M. Aaboud et al., *Search for the direct production of charginos and neutralinos in final states with tau leptons in $\sqrt{s} = 13$ TeV pp collisions with the ATLAS detector*, *Eur. Phys. J. C* **78** (2018) 154, [1708.07875].

[202] L. Allwicher, P. Arnan, D. Barducci and M. Nardecchia, *Perturbative unitarity constraints on generic Yukawa interactions*, *JHEP* **10** (2021) 129, [2108.00013].

[203] A. J. Buras, J. Harz and M. A. Mojahed, *Disentangling new physics in $K \to \pi\bar{\nu}\nu$ and $B \to K(K^*)\bar{\nu}\nu$ observables*, 2405.06742.

[204] J. Aebischer, M. Fael, C. Greub and J. Virto, *B physics Beyond the Standard Model at One Loop: Complete Renormalization Group Evolution below the Electroweak Scale*, *JHEP* **09** (2017) 158, [1704.06639].

[205] A. Crivellin, C. Greub, D. Müller and F. Saturnino, *Importance of Loop Effects in Explaining the Accumulated Evidence for New Physics in B Decays with a Vector Leptoquark*, *Phys. Rev. Lett.* **122** (2019) 011805, [1807.02068].

[206] J. Aebischer, G. Isidori, M. Pesut, B. A. Stefanek and F. Wilsch, *Confronting the vector leptoquark hypothesis with new low- and high-energy data*, *Eur. Phys. J. C* **83** (2023) 153, [2210.13422].

[207] M. Gorbahn, U. Moldanazarova, K. H. Sieja, E. Stamou and M. Tabet, *The anatomy of $K^+ \to \pi^+\nu\bar{\nu}$ distributions*, *Eur. Phys. J. C* **84** (2024) 680, [2312.06494].

[208] R. Barbieri, G. Isidori, A. Pattori and F. Senia, *Anomalies in B-decays and $U(2)$ flavour symmetry*, *Eur. Phys. J.* **C76** (2016) 67, [1512.01560].

[209] L. Di Luzio, A. Greljo and M. Nardecchia, *Gauge leptoquark as the origin of B-physics anomalies*, *Phys. Rev. D* **96** (2017) 115011, [1708.08450].

[210] J. Fuentes-Martín, G. Isidori, M. König and N. Selimović, *Vector Leptoquarks Beyond Tree Level III: Vector-like Fermions and Flavor-Changing Transitions*, *Phys. Rev. D* **102** (2020) 115015, [2009.11296].

[211] J. Fuentes-Martín, G. Isidori, M. König and N. Selimović, *Vector Leptoquarks Beyond Tree Level*, *Phys. Rev. D* **101** (2020) 035024, [1910.13474].

[212] J. Fuentes-Martín, G. Isidori, M. König and N. Selimović, *Vector leptoquarks beyond tree level. II. $\mathcal{O}(\alpha_s)$ corrections and radial modes*, *Phys. Rev. D* **102** (2020) 035021, [2006.16250].

[213] O. L. Crosas, G. Isidori, J. M. Lizana, N. Selimovic and B. A. Stefanek, *Flavor non-universal vector leptoquark imprints in $K \to \pi\nu\nu^-$ and $\Delta F=2$ transitions*, *Phys. Lett. B* **835** (2022) 137525, [2207.00018].

[214] L. Allwicher, C. Cornella, G. Isidori and B. A. Stefanek, *New physics in the third generation. A comprehensive SMEFT analysis and future prospects*, *JHEP* **03** (2024) 049, [2311.00020].

[215] M. Fernández Navarro and S. F. King, *Tri-hypercharge: a separate gauged weak hypercharge for each fermion family as the origin of flavour*, *JHEP* **08** (2023) 020, [2305.07690].

[216] J. Davighi and B. A. Stefanek, *Deconstructed hypercharge: a natural model of flavour*, *JHEP* **11** (2023) 100, [2305.16280].

[217] R. Barbieri and G. Isidori, *Minimal flavour deconstruction*, *JHEP* **05** (2024) 033, [2312.14004].

[218] L. Di Luzio, J. Fuentes-Martin, A. Greljo, M. Nardecchia and S. Renner, *Maximal Flavour Violation: a Cabibbo mechanism for leptoquarks*, *JHEP* **11** (2018) 081, [1808.00942].

[219] NA62 collaboration, J. Swallow, *New measurement of the $K^+ \to \pi^+ \nu\bar{\nu}$ decay by the NA62 Experiment*, 2024.

[220] G. Anzivino et al., *Workshop summary: Kaons@CERN 2023*, *Eur. Phys. J. C* **84** (2024) 377, [2311.02923].

[221] R. Bause, H. Gisbert, M. Golz and G. Hiller, *Interplay of dineutrino modes with semileptonic rare B-decays*, *JHEP* **12** (2021) 061, [2109.01675].

[222] C. S. Kim, D. Sahoo and K. N. Vishnudath, *Searching for signatures of new physics in $B \to K \nu \overline{\nu}$ to distinguish between Dirac and Majorana neutrinos*, *Eur. Phys. J. C* **84** (2024) 882, [2405.17341].

[223] J. Davighi and G. Isidori, *Non-universal gauge interactions addressing the inescapable link between Higgs and flavour*, *JHEP* **07** (2023) 147, [2303.01520].

[224] FCC collaboration, A. Abada et al., *FCC-ee: The Lepton Collider: Future Circular Collider Conceptual Design Report Volume 2*, *Eur. Phys. J. ST* **228** (2019) 261–623.

[225] CEPC Study Group collaboration, M. Dong et al., *CEPC Conceptual Design Report: Volume 2 - Physics & Detector*, 1811.10545.

[226] X. Ai et al., *Flavor Physics at CEPC: a General Perspective*, 2412.19743.

[227] *The International Linear Collider Technical Design Report - Volume 1: Executive Summary*, 1306.6327.

[228] CLIC collaboration, J. de Blas et al., *The CLIC Potential for New Physics*, 1812.02093.

[229] M. Bai et al., *C^3: A "Cool" Route to the Higgs Boson and Beyond*, in *Snowmass 2021*, 10, 2021, 2110.15800.

[230] C. Accettura et al., *Towards a muon collider*, *Eur. Phys. J. C* **83** (2023) 864, [2303.08533]. [Erratum: Eur.Phys.J.C 84, 36 (2024)].

[231] International Muon Collider collaboration, C. Accettura et al., *The Muon Collider*, 2504.21417.

[232] FCC collaboration, M. Benedikt et al., *Future Circular Collider Feasibility Study Report: Volume 1, Physics, Experiments, Detectors*, 2505.00272.

[233] FCC collaboration, M. Benedikt et al., *Future Circular Collider Feasibility Study Report: Volume 2, Accelerators, Technical Infrastructure and Safety*, 2505.00274.

[234] FCC collaboration, M. Benedikt et al., *Future Circular Collider Feasibility Study Report: Volume 3, Civil Engineering, Implementation and Sustainability*, 2505.00273.

[235] FCC-ee collaboration, K. D. J. André, M. Benedikt, K. Oide and F. Zimmermann, *FCC-ee Collider Design Overview*, *PoS* **ICHEP2024** (2025) 830.

[236] FCC collaboration, *Collision-energy calibration and monochromatisation studies at FCC-ee*, .

[237] G. Broggi, A. Abramov, M. Boscolo, R. Bruce, D. Mirarchi and S. Redaelli, *First studies of crystal collimation for the FCC-ee*, *Nucl. Instrum. Meth. A* **1076** (2025) 170479.

[238] FCC collaboration, *Prospects in BSM physics at FCC*, .

[239] FCC collaboration, J. Burridge et al., *Prospects for physics at FCC-hh*, .

[240] FCC collaboration, *Prospects in electroweak, Higgs and Top physics at FCC*, .

[241] V. Maura, B. A. Stefanek and T. You, *The Higgs Self-Coupling at FCC-ee*, 2503.13719.

[242] V. Maura, B. A. Stefanek and T. You, *Accuracy complements energy: electroweak precision tests at Tera-Z*, 2412.14241.

[243] B. A. Stefanek, *Non-universal probes of composite Higgs models: new bounds and prospects for FCC-ee*, *JHEP* **09** (2024) 103, [2407.09593].

[244] A. Valenti and L. Vecchi, *Perturbative running of the topological angles*, *JHEP* **01** (2023) 131, [2210.09328].

[245] M. Bordone, C. Cornella and J. Davighi, *Precision Tests in $b \to s\ell^+\ell^-$ ($\ell = e, \mu$) at FCC-ee*, 2503.22635.

[246] A. Greljo, B. A. Stefanek and A. Valenti, *Cornering Natural SUSY at a Tera-Z Factory*, 2507.03073.

[247] Muon Collider collaboration, D. Stratakis et al., *A Muon Collider Facility for Physics Discovery*, 2203.08033.

[248] Muon Collider collaboration, S. Jindariani et al., *Promising Technologies and R&D Directions for the Future Muon Collider Detectors*, 2203.07224.

[249] Muon Collider collaboration, J. de Blas et al., *The physics case of a 3 TeV muon collider stage*, 2203.07261.

[250] Muon Collider collaboration, D. Stratakis et al., *A Muon Collider Facility for Physics Discovery*, 2203.08033.

[251] Muon Collider collaboration, S. Jindariani et al., *Promising Technologies and R&D Directions for the Future Muon Collider Detectors*, 2203.07224.

[252] C. Aime et al., *Muon Collider Physics Summary*, 2203.07256.

[253] Muon Collider collaboration, J. de Blas et al., *The physics case of a 3 TeV muon collider stage*, 2203.07261.

[254] R. Capdevilla, F. Garosi, D. Marzocca and B. Stechauner, *Testing the neutrino content of the muon at muon colliders*, *JHEP* **04** (2025) 168, [2410.21383].

[255] D. Marzocca and A. Stanzione, *On the impact of the mixed Z/γ PDF at muon colliders*, *JHEP* **03** (2025) 171, [2408.13191].

[256] D. Marzocca, M. Szewc and M. Tammaro, *Direct CKM determination from W decays at future lepton colliders*, *JHEP* **11** (2024) 017, [2405.08880].

[257] A. Azatov, F. Garosi, A. Greljo, D. Marzocca, J. Salko and S. Trifinopoulos, *New physics in $b \to s\mu\mu$: FCC-hh or a muon collider?*, *JHEP* **10** (2022) 149, [2205.13552].

[258] M. Ruhdorfer, E. Salvioni and A. Wulzer, *Building the case for forward muon detection at a muon collider*, *Phys. Rev. D* **111** (2025) 053010, [2411.00096].

[259] M. Ruhdorfer, E. Salvioni and A. Wulzer, *Invisible Higgs boson decay from forward muons at a muon collider*, *Phys. Rev. D* **107** (2023) 095038, [2303.14202].

[260] T. Han, M. Low, T. A. Wu and K. Xie, *Colorful particle production at high-energy muon colliders*, *JHEP* **06** (2025) 109, [2502.20443].

[261] T. Han, D. Liu and S. Wang, *Top quark electroweak dipole moment at a high energy muon collider*, *Phys. Rev. D* **111** (2025) 035015, [2410.11015].

[262] Y. Ma, E. Celada, T. Han, W. Kilian, N. Kreher, F. Maltoni et al., *Higgs-muon interactions at a multi-TeV muon collider*, *PoS* **ICHEP2024** (2024) 092, [2410.06991].

[263] T. Han, D. Liu, I. Low and X. Wang, *Electroweak scattering at the muon shot*, *Phys. Rev. D* **110** (2024) 013005, [2312.07670].

[264] D. Amati, A. Bassetto, M. Ciafaloni, G. Marchesini and G. Veneziano, *A Treatment of Hard Processes Sensitive to the Infrared Structure of QCD*, *Nucl. Phys. B* **173** (1980) 429–455.

[265] P. Ciafaloni and D. Comelli, *Sudakov enhancement of electroweak corrections*, *Phys. Lett. B* **446** (1999) 278–284, [hep-ph/9809321].

[266] M. Ciafaloni, P. Ciafaloni and D. Comelli, *Electroweak double logarithms in inclusive observables for a generic initial state*, *Phys. Lett. B* **501** (2001) 216–222, [hep-ph/0007096].

[267] M. Ciafaloni, P. Ciafaloni and D. Comelli, *Bloch-Nordsieck violating electroweak corrections to inclusive TeV scale hard processes*, *Phys. Rev. Lett.* **84** (2000) 4810–4813, [hep-ph/0001142].

[268] M. Ciafaloni, P. Ciafaloni and D. Comelli, *Electroweak Bloch-Nordsieck violation at the TeV scale: 'Strong' weak interactions?*, *Nucl. Phys. B* **589** (2000) 359–380, [hep-ph/0004071].

[269] M. Ciafaloni, P. Ciafaloni and D. Comelli, *Bloch-Nordsieck violation in spontaneously broken Abelian theories*, *Phys. Rev. Lett.* **87** (2001) 211802, [hep-ph/0103315].

[270] M. Ciafaloni, P. Ciafaloni and D. Comelli, *Electroweak double-logs at small x*, *JHEP* **05** (2008) 039, [0802.0168].

[271] A. V. Manohar and W. J. Waalewijn, *Electroweak Logarithms in Inclusive Cross Sections*, *JHEP* **08** (2018) 137, [1802.08687].

[272] G. Cuomo, L. Vecchi and A. Wulzer, *Goldstone Equivalence and High Energy Electroweak Physics*, *SciPost Phys.* **8** (2020) 078, [1911.12366].

[273] S. Chen, A. Glioti, R. Rattazzi, L. Ricci and A. Wulzer, *Learning from radiation at a very high energy lepton collider*, *JHEP* **05** (2022) 180, [2202.10509].

[274] M. Ciafaloni, P. Ciafaloni and D. Comelli, *Towards collinear evolution equations in electroweak theory*, *Phys. Rev. Lett.* **88** (2002) 102001, [hep-ph/0111109].

[275] P. Ciafaloni and D. Comelli, *Electroweak evolution equations*, *JHEP* **11** (2005) 022, [hep-ph/0505047].

[276] J. Chen, T. Han and B. Tweedie, *Electroweak Splitting Functions and High Energy Showering*, *JHEP* **11** (2017) 093, [1611.00788].

[277] C. W. Bauer, N. Ferland and B. R. Webber, *Standard Model Parton Distributions at Very High Energies*, *JHEP* **08** (2017) 036, [1703.08562].

[278] C. W. Bauer, N. Ferland and B. R. Webber, *Combining initial-state resummation with fixed-order calculations of electroweak corrections*, *JHEP* **04** (2018) 125, [1712.07147].

[279] B. Fornal, A. V. Manohar and W. J. Waalewijn, *Electroweak Gauge Boson Parton Distribution Functions*, *JHEP* **05** (2018) 106, [1803.06347].

[280] T. Han, Y. Ma and K. Xie, *High energy leptonic collisions and electroweak parton distribution functions*, *Phys. Rev. D* **103** (2021) L031301, [2007.14300].

[281] T. Han, Y. Ma and K. Xie, *Quark and gluon contents of a lepton at high energies*, *JHEP* **02** (2022) 154, [2103.09844].

[282] F. Garosi, D. Marzocca and S. Trifinopoulos, *LePDF: Standard Model PDFs for high-energy lepton colliders*, *JHEP* **09** (2023) 107, [2303.16964].

[283] P. Ciafaloni, G. Co', D. Colferai and D. Comelli, *Electroweak evolution equations and isospin conservation*, *JHEP* **07** (2024) 237, [2403.08583].

[284] A. Denner and S. Pozzorini, *One loop leading logarithms in electroweak radiative corrections. 1. Results*, *Eur. Phys. J. C* **18** (2001) 461–480, [hep-ph/0010201].

[285] A. Denner, *Electroweak radiative corrections at high-energies*, *PoS* **HEP2001** (2001) 129, [hep-ph/0110155].

[286] P. Borel, R. Franceschini, R. Rattazzi and A. Wulzer, *Probing the Scattering of Equivalent Electroweak Bosons*, *JHEP* **06** (2012) 122, [1202.1904].

[287] D. Pagani and M. Zaro, *One-loop electroweak Sudakov logarithms: a revisitation and automation*, *JHEP* **02** (2022) 161, [2110.03714].

[288] J. Chay and T. Kwon, *N-jettiness for muon jet pairs in electroweak high-energy processes*, *JHEP* **12** (2022) 091, [2207.05425].

[289] F. Nardi, L. Ricci and A. Wulzer, *Low-virtuality splitting in the Standard Model*, *JHEP* **10** (2024) 215, [2405.08220].

[290] Z. Kunszt and D. E. Soper, *On the Validity of the Effective W Approximation*, *Nucl. Phys. B* **296** (1988) 253–289.

[291] D. Buttazzo, D. Redigolo, F. Sala and A. Tesi, *Fusing Vectors into Scalars at High Energy Lepton Colliders*, *JHEP* **11** (2018) 144, [1807.04743].

[292] A. Costantini, F. De Lillo, F. Maltoni, L. Mantani, O. Mattelaer, R. Ruiz et al., *Vector boson fusion at multi-TeV muon colliders*, *JHEP* **09** (2020) 080, [2005.10289].

[293] E. Fermi, *Über die Theorie des Stoßes zwischen Atomen und elektrisch geladenen Teilchen*, *Zeitschrift fur Physik* **29** (Dec., 1924) 315–327.

[294] C. F. V. Weizsäcker, *Ausstrahlung bei Stößen sehr schneller Elektronen*, *Zeitschrift fur Physik* **88** (Sept., 1934) 612–625.

[295] E. J. Williams, *Nature of the high-energy particles of penetrating radiation and status of ionization and radiation formulae*, *Phys. Rev.* **45** (1934) 729–730.

[296] L. D. Landau and E. M. Lifschitz, *ON THE PRODUCTION OF ELECTRONS AND POSITRONS BY A COLLISION OF TWO PARTICLES*, *Phys. Z. Sowjetunion* **6** (1934) 244.

[297] V. N. Gribov and L. N. Lipatov, *Deep inelastic e p scattering in perturbation theory*, *Sov. J. Nucl. Phys.* **15** (1972) 438–450.

[298] Y. L. Dokshitzer, *Calculation of the Structure Functions for Deep Inelastic Scattering and e+ e- Annihilation by Perturbation Theory in Quantum Chromodynamics.*, *Sov. Phys. JETP* **46** (1977) 641–653.

[299] G. Altarelli and G. Parisi, *Asymptotic Freedom in Parton Language*, *Nucl. Phys. B* **126** (1977) 298–318.

[300] S. Frixione, *Initial conditions for electron and photon structure and fragmentation functions*, *JHEP* **11** (2019) 158, [1909.03886].

[301] C. W. Bauer and B. R. Webber, *Polarization Effects in Standard Model Parton Distributions at Very High Energies*, *JHEP* **03** (2019) 013, [1808.08831].

[302] H. Al Ali et al., *The muon Smasher's guide*, *Rept. Prog. Phys.* **85** (2022) 084201, [2103.14043].

[303] E. Fermi, *On the Theory of the impact between atoms and electrically charged particles*, *Z. Phys.* **29** (1924) 315–327.

[304] C. F. von Weizsacker, *Radiation emitted in collisions of very fast electrons*, *Z. Phys.* **88** (1934) 612–625.

[305] R. N. Cahn and S. Dawson, *Production of Very Massive Higgs Bosons*, *Phys. Lett. B* **136** (1984) 196. [Erratum: Phys.Lett.B 138, 464 (1984)].

[306] S. Dawson, *The Effective W Approximation*, *Nucl. Phys. B* **249** (1985) 42–60.

[307] M. S. Chanowitz and M. K. Gaillard, *Multiple Production of W and Z as a Signal of New Strong Interactions*, *Phys. Lett. B* **142** (1984) 85–90.

[308] G. L. Kane, W. W. Repko and W. B. Rolnick, *The Effective W+-, Z0 Approximation for High-Energy Collisions*, *Phys. Lett. B* **148** (1984) 367–372.

[309] R. Ruiz, A. Costantini, F. Maltoni and O. Mattelaer, *The Effective Vector Boson Approximation in high-energy muon collisions*, *JHEP* **06** (2022) 114, [2111.02442].

[310] M. Forslund and P. Meade, *High precision higgs from high energy muon colliders*, *JHEP* **08** (2022) 185, [2203.09425].

[311] V. Shtabovenko, R. Mertig and F. Orellana, *FeynCalc 9.3: New features and improvements*, *Comput. Phys. Commun.* **256** (2020) 107478, [2001.04407].

[312] V. Shtabovenko, R. Mertig and F. Orellana, *FeynCalc 10: Do multiloop integrals dream of computer codes?*, 2312.14089.

[313] T. Hahn, *Generating Feynman diagrams and amplitudes with FeynArts 3*, *Comput. Phys. Commun.* **140** (2001) 418–431, [hep-ph/0012260].

[314] C. Accettura et al., *Interim report for the International Muon Collider Collaboration (IMCC)*, 2407.12450.

[315] LHC Higgs Cross Section Working Group collaboration, A. David, A. Denner, M. Duehrssen, M. Grazzini, C. Grojean, G. Passarino et al., *LHC HXSWG interim recommendations to explore the coupling structure of a Higgs-like particle*, 1209.0040.

[316] C. Caprini and D. G. Figueroa, *Cosmological Backgrounds of Gravitational Waves*, *Class. Quant. Grav.* **35** (2018) 163001, [1801.04268].

[317] A. Kosowsky, M. S. Turner and R. Watkins, *Gravitational waves from first order cosmological phase transitions*, *Phys. Rev. Lett.* **69** (1992) 2026–2029.

[318] A. Kosowsky, M. S. Turner and R. Watkins, *Gravitational radiation from colliding vacuum bubbles*, *Phys. Rev. D* **45** (1992) 4514–4535.

[319] P. Athron, C. Balázs, A. Fowlie, L. Morris and L. Wu, *Cosmological phase transitions: From perturbative particle physics to gravitational waves*, *Prog. Part. Nucl. Phys.* **135** (2024) 104094, [2305.02357].

[320] C. J. Hogan, *Gravitational radiation from cosmological phase transitions*, *Monthly Notices of the Royal Astronomical Society* **218** (02, 1986) 629–636, [https://academic.oup.com/mnras/article-pdf/218/4/629/3299141/mnras218-0629.pdf].

[321] S. J. Huber and T. Konstandin, *Gravitational Wave Production by Collisions: More Bubbles*, *JCAP* **09** (2008) 022, [0806.1828].

[322] L. Delle Rose, G. Panico, M. Redi and A. Tesi, *Gravitational Waves from Supercool Axions*, *JHEP* **04** (2020) 025, [1912.06139].

[323] B. Von Harling, A. Pomarol, O. Pujolàs and F. Rompineve, *Peccei-Quinn Phase Transition at LIGO*, *JHEP* **04** (2020) 195, [1912.07587].

[324] N. Levi, T. Opferkuch and D. Redigolo, *The supercooling window at weak and strong coupling*, *JHEP* **02** (2023) 125, [2212.08085].

[325] J. Ellis, M. Lewicki and V. Vaskonen, *Updated predictions for gravitational waves produced in a strongly supercooled phase transition*, *JCAP* **11** (2020) 020, [2007.15586].

[326] R. Jinno and M. Takimoto, *Probing a classically conformal B-L model with gravitational waves*, *Phys. Rev. D* **95** (2017) 015020, [1604.05035].

[327] M. Lewicki, O. Pujolàs and V. Vaskonen, *Escape from supercooling with or without bubbles: gravitational wave signatures*, *Eur. Phys. J. C* **81** (2021) 857, [2106.09706].

[328] D. Schmitt and L. Sagunski, *QCD-sourced tachyonic phase transition in a supercooled Universe*, *JCAP* **02** (2025) 075, [2409.05851].

[329] M. Lewicki, P. Toczek and V. Vaskonen, *Black holes and gravitational waves from phase transitions in realistic models*, 2412.10366.

[330] I. Baldes and C. Garcia-Cely, *Strong gravitational radiation from a simple dark matter model*, *JHEP* **05** (2019) 190, [1809.01198].

[331] L. Marzola, A. Racioppi and V. Vaskonen, *Phase transition and gravitational wave phenomenology of scalar conformal extensions of the Standard Model*, *Eur. Phys. J. C* **77** (2017) 484, [1704.01034].

[332] C. Marzo, L. Marzola and V. Vaskonen, *Phase transition and vacuum stability in the classically*

conformal B–L model, *Eur. Phys. J. C* **79** (2019) 601, [1811.11169].

[333] T. Prokopec, J. Rezacek and B. Świeżewska, *Gravitational waves from conformal symmetry breaking*, *JCAP* **02** (2019) 009, [1809.11129].

[334] D. Marfatia and P.-Y. Tseng, *Gravitational wave signals of dark matter freeze-out*, *JHEP* **02** (2021) 022, [2006.07313].

[335] M. Kierkla, B. Swiezewska, T. V. I. Tenkanen and J. van de Vis, *Gravitational waves from supercooled phase transitions: dimensional transmutation meets dimensional reduction*, *JHEP* **02** (2024) 234, [2312.12413].

[336] T. Hambye and A. Strumia, *Dynamical generation of the weak and Dark Matter scale*, *Phys. Rev. D* **88** (2013) 055022, [1306.2329].

[337] C. D. Carone and R. Ramos, *Classical scale-invariance, the electroweak scale and vector dark matter*, *Phys. Rev. D* **88** (2013) 055020, [1307.8428].

[338] V. V. Khoze, C. McCabe and G. Ro, *Higgs vacuum stability from the dark matter portal*, *JHEP* **08** (2014) 026, [1403.4953].

[339] G. M. Pelaggi, *Predictions of a model of weak scale from dynamical breaking of scale invariance*, *Nucl. Phys. B* **893** (2015) 443–458, [1406.4104].

[340] A. Karam and K. Tamvakis, *Dark matter and neutrino masses from a scale-invariant multi-Higgs portal*, *Phys. Rev. D* **92** (2015) 075010, [1508.03031].

[341] V. V. Khoze and A. D. Plascencia, *Dark Matter and Leptogenesis Linked by Classical Scale Invariance*, *JHEP* **11** (2016) 025, [1605.06834].

[342] L. Chataignier, T. Prokopec, M. G. Schmidt and B. Świeżewska, *Systematic analysis of radiative symmetry breaking in models with extended scalar sector*, *JHEP* **08** (2018) 083, [1805.09292].

[343] T. Hambye, A. Strumia and D. Teresi, *Super-cool Dark Matter*, *JHEP* **08** (2018) 188, [1805.01473].

[344] M. Kierkla, A. Karam and B. Swiezewska, *Conformal model for gravitational waves and dark matter: a status update*, *JHEP* **03** (2023) 007, [2210.07075].

[345] P. Baratella, A. Pomarol and F. Rompineve, *The Supercooled Universe*, *JHEP* **03** (2019) 100, [1812.06996].

[346] B. von Harling and G. Servant, *QCD-induced Electroweak Phase Transition*, *JHEP* **01** (2018) 159, [1711.11554].

[347] L. Randall and G. Servant, *Gravitational waves from warped spacetime*, *JHEP* **05** (2007) 054, [hep-ph/0607158].

[348] G. Nardini, M. Quiros and A. Wulzer, *A Confining Strong First-Order Electroweak Phase Transition*, *JHEP* **09** (2007) 077, [0706.3388].

[349] T. Konstandin, G. Nardini and M. Quiros, *Gravitational Backreaction Effects on the Holographic Phase Transition*, *Phys. Rev. D* **82** (2010) 083513, [1007.1468].

[350] T. Konstandin and G. Servant, *Natural Cold Baryogenesis from Strongly Interacting Electroweak Symmetry Breaking*, *JCAP* **07** (2011) 024, [1104.4793].

[351] T. Konstandin and G. Servant, *Cosmological Consequences of Nearly Conformal Dynamics at the TeV scale*, *JCAP* **12** (2011) 009, [1104.4791].

[352] E. Megías, G. Nardini and M. Quirós, *Cosmological Phase Transitions in Warped Space: Gravitational Waves and Collider Signatures*, *JHEP* **09** (2018) 095, [1806.04877].

[353] R. K. Mishra and L. Randall, *Phase transition to RS: cool, not supercool*, *JHEP* **06** (2024) 099, [2401.09633].

[354] P. Agrawal, G. R. Kane, V. Loladze and M. Reig, *Supercooled Confinement*, 2504.00199.

[355] S. R. Coleman, *The Fate of the False Vacuum. 1. Semiclassical Theory*, *Phys. Rev. D* **15** (1977)

2929–2936. [Erratum: Phys.Rev.D 16, 1248 (1977)].

[356] C. G. Callan, Jr. and S. R. Coleman, *The Fate of the False Vacuum. 2. First Quantum Corrections*, *Phys. Rev. D* **16** (1977) 1762–1768.

[357] A. D. Linde, *Decay of the False Vacuum at Finite Temperature*, *Nucl. Phys. B* **216** (1983) 421. [Erratum: Nucl.Phys.B 223, 544 (1983)].

[358] F. Devoto, S. Devoto, L. Di Luzio and G. Ridolfi, *False vacuum decay: an introductory review*, *J. Phys. G* **49** (2022) 103001, [2205.03140].

[359] S. Weinberg, *Gravitation and Cosmology: Principles and Applications of the General Theory of Relativity*. John Wiley and Sons, New York, 1972.

[360] D. J. Weir, *Revisiting the envelope approximation: gravitational waves from bubble collisions*, *Phys. Rev. D* **93** (2016) 124037, [1604.08429].

[361] O. Gould, S. Sukuvaara and D. Weir, *Vacuum bubble collisions: From microphysics to gravitational waves*, *Phys. Rev. D* **104** (2021) 075039, [2107.05657].

[362] R. Jinno and M. Takimoto, *Gravitational waves from bubble collisions: An analytic derivation*, *Phys. Rev. D* **95** (2017) 024009, [1605.01403].

[363] D. Cutting, M. Hindmarsh and D. J. Weir, *Gravitational waves from vacuum first-order phase transitions: from the envelope to the lattice*, *Phys. Rev. D* **97** (2018) 123513, [1802.05712].

[364] M. Lewicki and V. Vaskonen, *Gravitational wave spectra from strongly supercooled phase transitions*, *Eur. Phys. J. C* **80** (2020) 1003, [2007.04967].

[365] M. Lewicki and V. Vaskonen, *Gravitational waves from colliding vacuum bubbles in gauge theories*, *Eur. Phys. J. C* **81** (2021) 437, [2012.07826]. [Erratum: Eur.Phys.J.C 81, 1077 (2021)].

[366] D. Cutting, E. G. Escartin, M. Hindmarsh and D. J. Weir, *Gravitational waves from vacuum first order phase transitions II: from thin to thick walls*, *Phys. Rev. D* **103** (2021) 023531, [2005.13537].

[367] R. Jinno, T. Konstandin and M. Takimoto, *Relativistic bubble collisions—a closer look*, *JCAP* **09** (2019) 035, [1906.02588].

[368] R. Jinno and M. Takimoto, *Gravitational waves from bubble dynamics: Beyond the Envelope*, *JCAP* **01** (2019) 060, [1707.03111].

[369] C. Benso, F. Kahlhoefer and H. Mansour, *Dark matter phase-in: producing feebly-interacting particles after a first-order phase transition*, 2504.10593.

[370] H. Davoudiasl, D. Hooper and S. D. McDermott, *Inflatable Dark Matter*, *Phys. Rev. Lett.* **116** (2016) 031303, [1507.08660].

[371] T. Cohen, D. E. Morrissey and A. Pierce, *Changes in Dark Matter Properties After Freeze-Out*, *Phys. Rev. D* **78** (2008) 111701, [0808.3994].

[372] I. Baldes, Y. Gouttenoire and F. Sala, *String Fragmentation in Supercooled Confinement and Implications for Dark Matter*, *JHEP* **04** (2021) 278, [2007.08440].

[373] G. F. Giudice, E. W. Kolb and A. Riotto, *Largest temperature of the radiation era and its cosmological implications*, *Phys. Rev. D* **64** (2001) 023508, [hep-ph/0005123].

[374] A. Hook, G. Marques-Tavares and D. Racco, *Causal gravitational waves as a probe of free streaming particles and the expansion of the Universe*, *JHEP* **02** (2021) 117, [2010.03568].

[375] A. Gonstal, M. Lewicki and B. Swiezewska, *Reconstructing early universe evolution with gravitational waves from supercooled phase transitions*, 2502.18436.

[376] A. Falkowski and J. M. No, *Non-thermal Dark Matter Production from the Electroweak Phase Transition: Multi-TeV WIMPs and 'Baby-Zillas'*, *JHEP* **02** (2013) 034, [1211.5615].

[377] A. Katz and A. Riotto, *Baryogenesis and Gravitational Waves from Runaway Bubble Collisions*, *JCAP* **11** (2016) 011, [1608.00583].

[378] M. Cataldi and B. Shakya, *Leptogenesis via bubble collisions*, *JCAP* **11** (2024) 047, [2407.16747].

[379] G. F. Giudice, H. M. Lee, A. Pomarol and B. Shakya, *Nonthermal heavy dark matter from a first-order phase transition*, *JHEP* **12** (2024) 190, [2403.03252].

[380] B. Shakya, *Aspects of particle production from bubble dynamics at a first order phase transition*, *Phys. Rev. D* **111** (2025) 023521, [2308.16224].

[381] H. Mansour and B. Shakya, *Particle production from phase transition bubbles*, *Phys. Rev. D* **111** (2025) 023520, [2308.13070].

[382] A. Azatov, X. Nagels, M. Vanvlasselaer and W. Yin, *Populating secluded dark sector with ultra-relativistic bubbles*, *JHEP* **11** (2024) 129, [2406.12554].

[383] A. Azatov, M. Vanvlasselaer and W. Yin, *Baryogenesis via relativistic bubble walls*, *JHEP* **10** (2021) 043, [2106.14913].

[384] A. Azatov, M. Vanvlasselaer and W. Yin, *Dark Matter production from relativistic bubble walls*, *JHEP* **03** (2021) 288, [2101.05721].

[385] A. Azatov and M. Vanvlasselaer, *Bubble wall velocity: heavy physics effects*, *JCAP* **01** (2021) 058, [2010.02590].

[386] G. N. Felder, L. Kofman and A. D. Linde, *Tachyonic instability and dynamics of spontaneous symmetry breaking*, *Phys. Rev. D* **64** (2001) 123517, [hep-th/0106179].

[387] S. Girmohanta, Y. Nakai and Z. Zhang, *Post-Sphaleron Darkogenesis*, 2507.03747.

[388] L. J. Hall, K. Jedamzik, J. March-Russell and S. M. West, *Freeze-In Production of FIMP Dark Matter*, *JHEP* **03** (2010) 080, [0911.1120].

[389] T. Gherghetta, A. Paul and A. Shkerin, *Holographic phase transitions via thermally-assisted tunneling*, 2504.12437.

[390] Z. Chacko and R. K. Mishra, *Effective Theory of a Light Dilaton*, *Phys. Rev. D* **87** (2013) 115006, [1209.3022].

[391] L. Sagunski, P. Schicho and D. Schmitt, *Supercool exit: Gravitational waves from QCD-triggered conformal symmetry breaking*, *Phys. Rev. D* **107** (2023) 123512, [2303.02450].

[392] H.-X. Zhang, K. Hashino, H. Ishida and S. Matsuzaki, *Significance of soft-scale breaking on primordial black hole production in Coleman-Weinberg type supercooling-phase transition*, 2506.23752.

[393] J. Abdallah et al., *Simplified Models for Dark Matter Searches at the LHC*, *Phys. Dark Univ.* **9-10** (2015) 8–23, [1506.03116].

[394] C. A. J. O'Hare, *New Definition of the Neutrino Floor for Direct Dark Matter Searches*, *Phys. Rev. Lett.* **127** (2021) 251802, [2109.03116].

[395] G. Arcadi, M. Lindner and S. Profumo, *Beyond the Veil: Charting WIMP Territories at the Neutrino Floor*, 2507.16987.

[396] X. Chu, T. Hambye and M. H. G. Tytgat, *The Four Basic Ways of Creating Dark Matter Through a Portal*, *JCAP* **05** (2012) 034, [1112.0493].

[397] NANOGrav collaboration, G. Agazie et al., *The NANOGrav 15 yr Data Set: Evidence for a Gravitational-wave Background*, *Astrophys. J. Lett.* **951** (2023) L8, [2306.16213].

[398] EPTA, InPTA: collaboration, J. Antoniadis et al., *The second data release from the European Pulsar Timing Array - III. Search for gravitational wave signals*, *Astron. Astrophys.* **678** (2023) A50, [2306.16214].

[399] D. J. Reardon et al., *Search for an Isotropic Gravitational-wave Background with the Parkes Pulsar Timing Array*, *Astrophys. J. Lett.* **951** (2023) L6, [2306.16215].

[400] H. Xu et al., *Searching for the Nano-Hertz Stochastic Gravitational Wave Background with the Chinese Pulsar Timing Array Data Release I*, *Res. Astron. Astrophys.* **23** (2023) 075024, [2306.16216].

[401] C. Caprini et al., *Science with the space-based interferometer eLISA. II: Gravitational waves from cosmological phase transitions*, *JCAP* **04** (2016) 001, [1512.06239].

[402] C. Caprini et al., *Detecting gravitational waves from cosmological phase transitions with LISA: an update*, *JCAP* **03** (2020) 024, [1910.13125].

[403] A. Abac et al., *The Science of the Einstein Telescope*, 2503.12263.

[404] M. Punturo et al., *The Einstein Telescope: A third-generation gravitational wave observatory*, *Class. Quant. Grav.* **27** (2010) 194002.

[405] S. Kawamura et al., *Current status of space gravitational wave antenna DECIGO and B-DECIGO*, *PTEP* **2021** (2021) 05A105, [2006.13545].

[406] H. Bagherian, M. Ekhterachian and S. Stelzl, *The Bearable Inhomogeneity of the Baryon Asymmetry*, 2505.15904.

[407] J. J. Ethier, R. Gomez-Ambrosio, G. Magni and J. Rojo, *SMEFT analysis of vector boson scattering and diboson data from the LHC Run II*, *Eur. Phys. J. C* **81** (2021) 560, [2101.03180].

[408] E. Celada, T. Giani, J. ter Hoeve, L. Mantani, J. Rojo, A. N. Rossia et al., *Mapping the SMEFT at high-energy colliders: from LEP and the (HL-)LHC to the FCC-ee*, *JHEP* **09** (2024) 091, [2404.12809].

[409] M. Hirsch, L. Mantani and V. Sanz, *Can SMEFT discover New Physics?*, 2507.11109.

[410] S. Chen, A. Glioti, G. Panico and A. Wulzer, *Parametrized classifiers for optimal EFT sensitivity*, *JHEP* **05** (2021) 247, [2007.10356].

[411] J. Brehmer, K. Cranmer, G. Louppe and J. Pavez, *Constraining Effective Field Theories with Machine Learning*, *Phys. Rev. Lett.* **121** (2018) 111801, [1805.00013].

[412] R. T. D'Agnolo, G. Grosso, M. Pierini, A. Wulzer and M. Zanetti, *Learning multivariate new physics*, *Eur. Phys. J. C* **81** (2021) 89, [1912.12155].

[413] R. Gomez Ambrosio, J. ter Hoeve, M. Madigan, J. Rojo and V. Sanz, *Unbinned multivariate observables for global SMEFT analyses from machine learning*, *JHEP* **03** (2023) 033, [2211.02058].

[414] G. Barenboim, J. Hirn and V. Sanz, *Symmetry meets AI*, *SciPost Phys.* **11** (2021) 014, [2103.06115].

[415] M. Morales-Alvarado, D. Conde, J. Bendavid, V. Sanz and M. Ubiali, *Symbolic regression for precision LHC physics*, in *38th conference on Neural Information Processing Systems*, 12, 2024, 2412.07839.

[416] L. Allwicher, M. McCullough and S. Renner, *New physics at Tera-Z: precision renormalised*, *JHEP* **02** (2025) 164, [2408.03992].

[417] L. Allwicher, G. Isidori and M. Pesut, *Flavored circular collider: cornering New Physics at FCC-ee via flavor-changing processes*, *Eur. Phys. J. C* **85** (2025) 631, [2503.17019].

[418] S. Frixione, F. Maltoni, D. Pagani and M. Zaro, *Double neutral-current corrections to NLO electroweak leptonic cross sections*, 2506.10732.

[419] S. Frixione, F. Maltoni, D. Pagani and M. Zaro, *Precision phenomenology at multi-TeV muon colliders*, 2506.10733.

[420] L. Baudis, *DARWIN/XLZD: A future xenon observatory for dark matter and other rare interactions*, *Nucl. Phys. B* **1003** (2024) 116473, [2404.19524].

[421] XLZD collaboration, J. Aalbers et al., *The XLZD Design Book: Towards the Next-Generation Liquid Xenon Observatory for Dark Matter and Neutrino Physics*, 2410.17137.

[422] A. Belyaev, A. Freegard, I. F. Ginzburg, D. Locke and A. Pukhov, *Decoding dark matter at future e+e- colliders*, *Phys. Rev. D* **106** (2022) 015016, [2112.15090].

[423] R. Capdevilla, F. Meloni and J. Zurita, *Discovering Electroweak Interacting Dark Matter at Muon Colliders Using Soft Tracks*, *Phys. Rev. Lett.* **134** (2025) 181802, [2405.08858].

[424] P. Olgoso, P. Paradisi and N. Selimovic, *The Dark Side of a Tera-Z Factory*, 2507.17803.

[425] S. Bottaro, A. Strumia and N. Vignaroli, *Minimal Dark Matter bound states at future colliders*, *JHEP* **06** (2021) 143, [2103.12766].

[426] A. J. Buras, D. Buttazzo, J. Girrbach-Noe and R. Knegjens, $K^+ \to \pi^+ \nu\bar{\nu}$ *and* $K_L \to \pi^0 \nu\bar{\nu}$ *in the Standard Model: status and perspectives*, *JHEP* **11** (2015) 033, [1503.02693].

[427] D. Bečirević, O. Sumensari and R. Zukanovich Funchal, *Lepton flavor violation in exclusive* $b \to s$ *decays*, *Eur. Phys. J. C* **76** (2016) 134, [1602.00881].

[428] K. De Bruyn, R. Fleischer, R. Knegjens, P. Koppenburg, M. Merk and N. Tuning, *Branching Ratio Measurements of* B_s *Decays*, *Phys. Rev. D* **86** (2012) 014027, [1204.1735].

[429] K. De Bruyn, R. Fleischer, R. Knegjens, P. Koppenburg, M. Merk, A. Pellegrino et al., *Probing New Physics via the* $B_s^0 \to \mu^+\mu^-$ *Effective Lifetime*, *Phys. Rev. Lett.* **109** (2012) 041801, [1204.1737].

[430] S. Aoki et al., *Review of lattice results concerning low-energy particle physics*, 1607.00299.

[431] G. D'Ambrosio, A. M. Iyer, F. Mahmoudi and S. Neshatpour, *Anatomy of kaon decays and prospects for lepton flavour universality violation*, *JHEP* **09** (2022) 148, [2206.14748].

[432] G. Hiller and M. Schmaltz, *Diagnosing lepton-nonuniversality in* $b \to s\ell\ell$, *JHEP* **02** (2015) 055, [1411.4773].

[433] M. Ciuchini, A. M. Coutinho, M. Fedele, E. Franco, A. Paul, L. Silvestrini et al., *New Physics in* $b \to s\ell^+\ell^-$ *confronts new data on Lepton Universality*, *Eur. Phys. J. C* **79** (2019) 719, [1903.09632].

[434] G. Hiller and I. Nisandzic, R_K *and* R_{K^*} *beyond the standard model*, *Phys. Rev. D* **96** (2017) 035003, [1704.05444].

[435] L.-S. Geng, B. Grinstein, S. Jger, J. Martin Camalich, X.-L. Ren and R.-X. Shi, *Towards the discovery of new physics with lepton-universality ratios of* $b \to s\ell\ell$ *decays*, 1704.05446.

[436] W. Altmannshofer, P. Ball, A. Bharucha, A. J. Buras, D. M. Straub and M. Wick, *Symmetries and Asymmetries of* $B \to K^*\mu^+\mu^-$ *Decays in the Standard Model and Beyond*, *JHEP* **01** (2009) 019, [0811.1214].

[437] A. Bharucha, D. M. Straub and R. Zwicky, $B \to V\ell^+\ell^-$ *in the Standard Model from light-cone sum rules*, *JHEP* **08** (2016) 098, [1503.05534].

[438] M. Algueró, J. Matias, B. Capdevila and A. Crivellin, *Disentangling lepton flavor universal and lepton flavor universality violating effects in* $b \to s\ell+\ell-$ *transitions*, *Phys. Rev. D* **105** (2022) 113007, [2205.15212].

[439] M. Bordone, G. isidori, S. Mächler and A. Tinari, *Short- vs. long-distance physics in* $B \to K^{(*)}\ell^+\ell^-$*: a data-driven analysis*, *Eur. Phys. J. C* **84** (2024) 547, [2401.18007].

[440] G. Isidori, Z. Polonsky and A. Tinari, *An explicit estimate of charm rescattering in* $B^0 \to K^0\bar{\ell}\ell$, 2405.17551.

[441] J. Aebischer, A. J. Buras and J. Kumar, *On the Importance of Rare Kaon Decays: A Snowmass 2021 White Paper*, in *Snowmass 2021*, 3, 2022, 2203.09524.

[442] A. Angelescu, D. A. Faroughy and O. Sumensari, *Lepton Flavor Violation and Dilepton Tails at the LHC*, *Eur. Phys. J. C* **80** (2020) 641, [2002.05684].

[443] M. Misiak et al., *Updated NNLO QCD predictions for the weak radiative B-meson decays*, *Phys. Rev. Lett.* **114** (2015) 221801, [1503.01789].

[444] M. Czakon, P. Fiedler, T. Huber, M. Misiak, T. Schutzmeier and M. Steinhauser, *The* $(Q_7, Q_{1,2})$ *contribution to* $\overline{B} \to X_s\gamma$ *at* $\mathcal{O}\left(\alpha_s^2\right)$, *JHEP* **04** (2015) 168, [1503.01791].

[445] HFLAV collaboration, Y. S. Amhis et al., *Averages of b-hadron, c-hadron, and* τ*-lepton properties as of 2021*, *Phys. Rev. D* **107** (2023) 052008, [2206.07501].

[446] S. Iguro, T. Kitahara and R. Watanabe, *Global fit to* $b \to c\tau\nu$ *anomalies 2022 mid-autumn*, 2210.10751.

[447] W.-F. Duan, S. Iguro, X.-Q. Li, R. Watanabe and Y.-D. Yang, *Sum rules for semi-leptonic $b \to c$ and $b \to u$ decays: accuracy checks and implications*, 2410.21384.

[448] W. Dekens, E. E. Jenkins, A. V. Manohar and P. Stoffer, *Non-perturbative effects in $\mu \to e\gamma$*, *JHEP* **01** (2019) 088, [1810.05675].

[449] M. González-Alonso, J. Martin Camalich and K. Mimouni, *Renormalization-group evolution of new physics contributions to (semi)leptonic meson decays*, *Phys. Lett. B* **772** (2017) 777–785, [1706.00410].

[450] L. Allwicher, G. Isidori, J. M. Lizana, N. Selimovic and B. A. Stefanek, *Third-family quark-lepton Unification and electroweak precision tests*, *JHEP* **05** (2023) 179, [2302.11584].

[451] C. Bobeth and A. J. Buras, *Leptoquarks meet ε'/ε and rare Kaon processes*, *JHEP* **02** (2018) 101, [1712.01295].

[452] S. Davidson, D. C. Bailey and B. A. Campbell, *Model independent constraints on leptoquarks from rare processes*, *Z. Phys. C* **61** (1994) 613–644, [hep-ph/9309310].

[453] T. Li, X.-D. Ma and M. A. Schmidt, *Implication of $K \to \pi\nu\bar{\nu}$ for generic neutrino interactions in effective field theories*, *Phys. Rev. D* **101** (2020) 055019, [1912.10433].

[454] F. F. Deppisch, K. Fridell and J. Harz, *Constraining lepton number violating interactions in rare kaon decays*, *JHEP* **12** (2020) 186, [2009.04494].

[455] T. Felkl, S. L. Li and M. A. Schmidt, *A tale of invisibility: constraints on new physics in $b \to s\nu\nu$*, *JHEP* **12** (2021) 118, [2111.04327].

[456] K. Fridell, L. Gráf, J. Harz and C. Hati, *Probing Lepton Number Violation: A Comprehensive Survey of Dimension-7 SMEFT*, 2306.08709.